Laser Powder Bed Fusion of Ti-6Al-4V: A Round Robin Analysis of Mechanical Property Variability

Reid Schur

A dissertation

submitted in partial fulfillment of the

requirements for the degree of

Doctor of Philosophy

University of Washington

2023

Reading Committee:

Dwayne Arola, Chair

Ramulu Mamidala, Chair

Xu Chen

Program Authorized to Offer Degree:

Materials Science and Engineering

University of Washington

Abstract

Laser Powder Bed Fusion of Ti-6Al-4V: A Round Robin Analysis of Mechanical Property Variability

Reid Schur

Chair of the Supervisory Committee:
Dwayne Arola
Department of Materials Science and Engineering
Ramulu Mamidala
Department of Mechanical Engineering

Interest in Additive Manufacturing (AM) has quickly progressed from its application to prototypes to stress-critical components. One driving factor is the development of metal AM processes that enable the creation of parts with mechanical properties that rival those achieved by conventional wrought form metal, while enabling nearly unlimited freedom of design. But before widespread adoption of the technology can occur, robust approaches to machine and component qualification must be developed. This “missing link” will require a thorough understanding of the mechanical property variability that exists in the printing of components and its root causes.

Variability in the mechanical properties of components produced by metal AM can occur on three hierarchical levels, including intra-build, inter-build, and inter-machine. In this dissertation, each of these sources of variability is considered in Laser Powder Bed Fusion (LPBF) AM of Grade 5 Ti-6Al-4V. To achieve the necessary statistical power, the evaluation is performed through a round robin approach

involving six different organizations printing an identical set of six builds on the same make and model printer and with the same lot of gas atomized powder.

The intra-build analysis evaluated the spatial variability in microstructure and tensile mechanical properties of metal produced within each of the six printers. While most of the machines exhibited negligible spatial variability in porosity and mechanical properties, the metal from specific machines exhibited parabolic distributions in the porosity and tensile properties. In these machines, the least detrimental porosity (smallest pores overall and fewest number of large pores) was at the center of the build plate. In some machines this trend was oriented along the y-axis (parallel to the gas flow), while in one machine it was radially symmetric in the x-y plane. The shape and spatial position of these distributions suggest that gas flow and laser incidence angle are the most likely root causes to variability.

The inter-build variability was evaluated in terms of the porosity and tensile properties with respect to powder reuse and changes in machine health. A careful analysis of the powder chemistry and particle size distribution showed that the powder quality did not degrade significantly with reuse over the six builds. Furthermore, there were no trends in porosity or tensile properties due to powder reuse. However, the strength of metal produced from one machine in the round robin did undergo degradation related to machine health. Although a definitive root cause was not identified, a change to the laser spot size occurred, which could have caused the decrease in tensile properties.

Finally, the inter-machine variability was also evaluated through the metal porosity and mechanical properties. There were significant differences in porosity and tensile properties between many of the machines. While the porosity distributions were statistically similar for five of the six machines, lack of fusion (LOF) pores were found in metal of the sixth machine, with as many as 0.3 pores/mm^3 and diameter $\geq$ 0.125 mm. The largest variability in tensile properties resulted from differences in the post-processing heat treatments. For the machines with identically heat treated metal, the properties exhibited coefficients of variation (CoV) in strength that rivaled that of wrought form titanium (1-2%). The largest CoV was exhibited in the strain at failure, with values as large as 12.6%.

Results from this round robin investigation are the first to quantify the variability in mechanical properties within and across multiple identical machines operated in different organizations. As such, the results and complimentary analyses make a unique contribution to the literature and establish a foundation of understanding that supports industrialization of LPBF. This work will support efforts aimed at machine qualification and the certification of components. However, further research on the root causes of process variability and its effect on fatigue properties will be a critical next step to the widespread adoption of the technology for aerospace applications.

Table of Contents

List of Figures

List of Tables

Acknowledgements

The six years I spent working on my M.S. and Ph.D. at the University of Washington would not have been possible without the support of many individuals.

My biggest thanks go to my family and friends, who provided endless support from start to finish. Without your push, I may not have started this journey, and your encouragement certainly saw me through it.

To my advisors, Dr. Arola and Dr. Mamidala, you have my gratitude for providing an environment that enabled me to grow as a scientist and as an individual. I am deeply appreciative of the opportunities you provided, and the lessons you have both taught me will not be forgotten.

Thanks to all of the students who contributed to this body of work, and those who are continuing to progress its objectives. This work and the greater AM investigations at UW would not be possible without your collaboration and insight.

Boeing has also been a steadfast proponent of this study, not just through funding, but through the input of their engineers. In particular, Stacey Huang and Cory Cunningham provided endless support that was critical to the success of this project.

Finally, the staff of the UW were always happy to assist, especially Bill Kuykendall, Eamon McQuaide, and John Young. Their positive attitudes and depth of knowledge made execution of the research smoother and more enjoyable.

Chapter 1. Introduction

1.1. Metal Additive Manufacturing

Like all forms of additive manufacturing (AM), metal AM is a manufacturing technology that fabricates parts through a layer-wise approach. A variety of types of AM exist for producing parts from metals. However, broadly speaking, metal AM can be divided into two main categories including Directed Energy Deposition (DED) and Power Bed Fusion (PBF). Although additional techniques do exist, they are of less prominence today [1].

Both DED and PBF techniques offer unique advantages and disadvantages, and both are beginning to be deployed in industrial settings. Traditionally reserved for prototyping, metal AM's advance into service components is a relatively recent occurrence. Certain industries are farther along in its adoption, such as the biomedical sectors where you can find PBF parts in biomedical implants [2,3], and the space industry, with both PBF and DED [4,5] components having already traveled outside the atmosphere. However, industries with especially stringent safety demands, such as commercial aerospace, are taking a conservative approach in its implementation.

The disparity in timeline of adoption lies primarily in certification and qualification. Although the biomedical industry does face regulatory processes, they are not typically as rigorous as those associated with commercial aerospace. Stringent demands on quality placed by the Federal Aviation Administration (FAA) and other regulatory bodies require a demonstrated and thorough understanding of the AM process. Traditionally, this knowledge would be generated through rigorous experimentation and data generation [6]. Large sample sizes yield statistical descriptions of property distributions for a given process, including the design

allowables, which can then be used by engineers for designing parts. The MMPDS is one example of this approach, with tabulated properties for thousands of processes and materials [7]. Process qualification by data generation, however, is an incredibly time and resource intensive process. Furthermore, any minute alterations in process, material, or, for AM specifically, part geometry, may necessitate a re-certification of the property data [6].

Another, more contemporary thought to certification is Integrated Computational Materials Engineering (ICME). ICME still relies on the generation of experimental data, but pairs it with computational modeling. A wide range of data is collected, often including but not limited to mechanical properties, porosity, and microstructure of the material under scrutiny. By varying processing conditions, models can be generated with predictive capabilities. If the predictive power is strong enough, it would ideally enable small changes to be made to a process or part without triggering a full re-certification [6].

Whichever process of certification is ultimately used, it must be able to describe the metal property distributions with strong statistical or predictive capabilities. Without this, the outlook for applications of metal AM is bleak. Stress critical components may need to rely on high rates of non-destructive evaluation (NDE) or destructive testing on sacrificial parts, both of which can be cost prohibitive and have their own limitations [8]. The industry could instead turn to producing low criticality parts; however, this may not utilize AM to its full capabilities. It is therefore paramount to develop robust descriptions of the material properties of metal AM components to realize its full potential.

Various organizations, including researchers, government agencies, and standards organizations, have developed roadmaps to identify key roadblocks in the metal AM certification process and focus the AM community's efforts on these areas [2,9–11]. These documents cover a

variety of topics, including powder certification, process qualification, and post-processing, as well as describe how to evaluate them using conventional qualification and ICME. America Makes' Standardization Roadmap for Additive Manufacturing nicely lays out nearly 100 identified knowledge gaps [2]. Among these are many that discuss property variability, a topic spanning the entire printing process from start to finish. Variability is frequently cited as a major hurdle in metal AM, owing to the many potential sources and their varying effects [2,12]. Property variability can be separated into three categories: inter-machine, inter-build, and intra-build variability. These concepts are illustrated in Fig. 1.1. This study will fill many of the knowledge gaps regarding process variability from these three categories and help to further the implementation of metal AM in the aerospace industry and beyond.

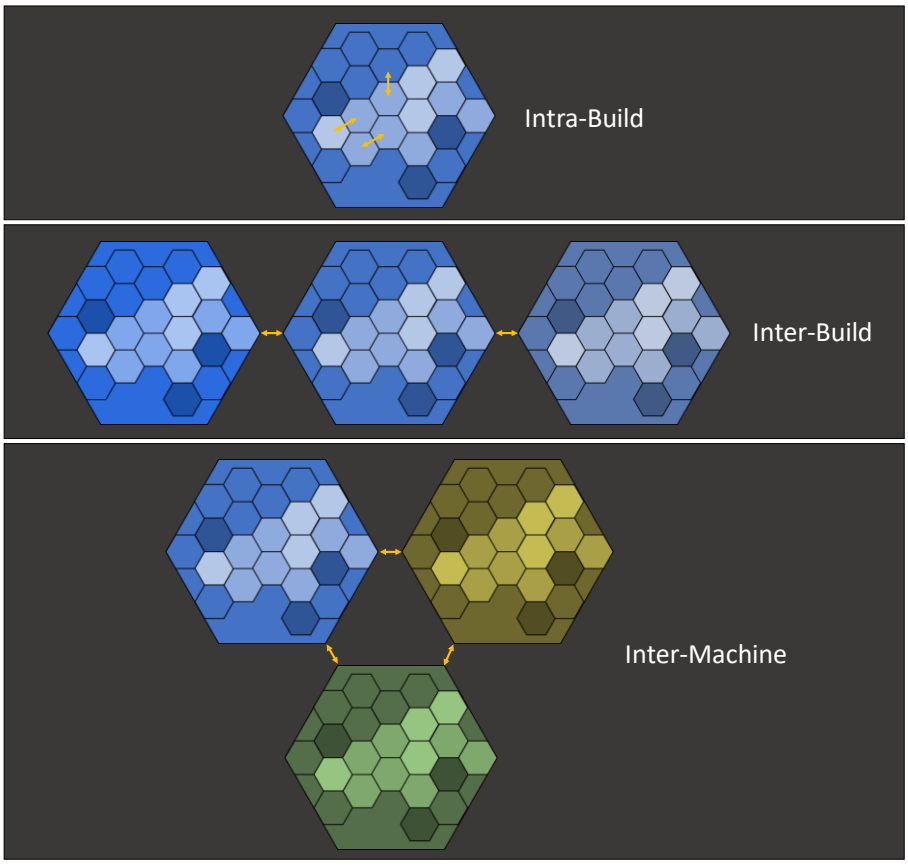

Fig. 1.1: Conceptual representation of the three levels of variability applicable to mechanical properties.

1.2. Objective and Aims

The roadmaps published to-date make it clear that a significant amount of work must be performed before widespread certification of AM parts for the aerospace community can take place. Of the many knowledge gaps outlined in the roadmaps, one of the most frequently highlighted is an understanding of process variability. To address this concern, this study will consider property variability in the manufacture of Ti-6Al-4V components printed with a fixed LPBF process. Ti-6Al-4V is a common aerospace alloy that is ideal for metal AM due to its good

printability and the challenges it faces with conventional manufacturing. Through the use of a fixed process without changes in operating procedures or process parameters, the intrinsic variability within and between printers can be characterized. Specifically, this study will pursue the following aims in printing Ti-6Al-4V on a LPBF printer with a fixed process:

Aim 1: Characterize the magnitude and sources of intra-build variability in tensile properties for multiple identical make/model machines using the same fixed process.

Aim 2: Characterize the magnitude and sources of inter-build variability in tensile properties for multiple identical make/model machines using the same fixed process.

Aim 3: Characterize the magnitude and sources of inter-machine variability in tensile properties between multiple identical make/model machines using the same fixed process.

Chapter 2. Literature Review

Laser powder bed fusion holds tremendous potential for the future of aerospace. But for that potential to be fully realized, an understanding of process variability and its contribution to mechanical property variability is needed to support the manufacture of components with high reliability. Although inter-machine, inter-build and intra-build variability are frequently cited as on-going concerns, research has been performed in these areas. In this chapter, a description of these categories of variability is presented along with a review of selected relevant publications on these topics.

2.1. Inter-Machine Variability

Arguably, machine-to-machine, or inter-machine variability has one of the most substantial contributions to the variation in part properties produced by LPBF. Different machine manufacturers inevitably approach metal AM differently, and those differences can manifest in variations of the part quality [13–16]. Even considering identical make and model machines, there is evidence suggesting there can be differences in the LPBF products [2,17]. Machine health, sensor and component calibration, environmental conditions, feedstock material, process parameters and human factors could all play vital roles in the extent and sources of inter-machine variability [2,18,19].

For LPBF specifically [1,2,9,10], there are reported efforts that cover a range of materials, including SS 316L [20], 15-5PH [14], Inconel 625 [21], and 4340 steel [13] . The breadth of materials represented in discussions of variability highlights the spread of research in this area. Unsurprisingly, the aforementioned studies have reported that there are differences in

metal quality and its mechanical properties between machines of different make/model. For instance, Obeidi et al. investigated four LPBF machines, including models from Aconity, 3D Phenix Systems, EOS, and Concept Laser [20]. Eight different parameter sets were utilized on each of the four machines, yielding 24 total tensile coupons. Clear differences were observed between the machines in terms of the mechanical properties and porosity of the metal. The Aconity, 3D Phenix Systems, and Concept Laser machines all showed strong dependence on the parameter set used. Taking the Concept Laser M1 as an example, strain to failure values ranged from 4% (190 W, 1200 mm/s, 60 μm layer thickness) to 39% (190 W, 800 mm/s, 30 μm layer thickness). Even more remarkable, is the response of the EOS M280, which showed much less dependency on process parameters; the strain to failure of metal from the EOS M290 varied between 34% and 44%. Apart from the intrinsic value of this effort, root causes of the variability or process sensitivity were not determined. It should also be noted that the parameter sets were not necessarily optimized for each of the machines in the aforementioned study, which raises an important question, i.e., how should a study be designed to best compare the properties of metal that is from multiple machines? There are other studies that have adopted an alternative approach, which involves freedom of parameter selection instead of homogenizing it across machines. For example, Ahuja et al. allowed each of their six participants to design their own parameter set, resulting in very large differences in properties [14]. The yield strength and Ultimate Tensile Strength (UTS) of the metal reported in the aforementioned study each span over 1000 MPa, while the elongation at failure ranges between 0% and 35%. With differences this large, it becomes difficult to determine if they are attributed to machine characteristics or parameter set choices.

Studies that included multiple machines of the same make and/or model in their fleet did not focus on the results of similar machines, but instead concentrated on the greater cross-machine comparisons. One such study from Jelis et al. included both an EOS M270 and EOS M280. However, the only tangible comparison of the products from each machine was to state that the number of failed prints varied between them [13]. Other studies that included multiple machines, such as that by Ahuja et al., did not identify which properties came from which machines, or even which machines were duplicates in their study [14]. The closest effort to the present body of work presented is described in a white paper published by EOS that analyzed the variability in metal across multiple M290s [17]. In that study, three EOS M290s printed identical jobs with Grade 23 Ti-6Al-4V. The printed tensile coupons were tested, and an Analysis of Variance (ANOVA) of the properties revealed minor but statistically significant differences between machines. Average yield strength and UTS for the three machines ranged from 987-1000 MPa and 1041-1056 MPA, respectively. The strain at failure also had low variability, with the means spanning from 15.2 to 16.3%. These properties were still found to be statistically different despite the small difference in magnitude, due to the small standard deviations within each machine.

Although the study by EOS is an important contribution to the field of LPBF, there are some limitations to consider. For example, all three M290s were owned and operated by EOS and details surrounding their history were not included in the paper. It would be beneficial to include machines from multiple locations with varied use histories, so the influence of machine health and condition could be interrogated or at least reflected in the results. In addition, although the study involved coupons from multiple prints on each machine, only 32 specimens appeared to be built on each machine; increasing the sample size could increase statistical

confidence in the results. Furthermore, it is unclear from their report if all printed coupons were utilized.

2.2. Inter-Build Variability

Inter-build variability is defined here as the difference in part quality from one print to another that were produced on the same machine. Taking PBF as an example, this topic could include powder reuse, changes in machine health, and intrinsic process variability from print to print. Each of these topics is discussed in the following paragraphs.

Most literature in the public domain focuses on the topic of variability associated with powder reuse. Unfused powder from the build undergoes a sieving process to remove large, sintered powder agglomerates [22]. Two general reuse strategies exist, distinguished by the decision to replace or not to replace depleted powder with virgin (unused) powder. Significant research has been conducted on the topic of powder reuse, spanning Electron Beam Powder Bed Fusion (EPBF) [23–27] and Laser Powder Bed Fusion (LPBF) [27–33], and for a variety of materials. The effects of reuse vary according to the specific combination of process and material. However, changes in the powder and resulting quality and/or mechanical properties of printed parts are rather common with powder reuse [24–26,28,30–32,34–42]. Regarding the reuse of Ti-6Al-4V specifically, EPBF typically causes larger changes in powder characteristics with reuse, including increasing oxygen content [26,34,38,41], decreasing fines content (small powder, sometimes defined as < 15 μm in diameter) and other particle size distribution (PSD) changes [26,34]. There is also reported degradation of the powder morphology with reuse [26,34,38]. These effects are seen to lesser and varying extents in LPBF of Ti-6Al-4V. In

general, the reported studies have mixed findings regarding the effects of powder reuse and are summarized in Table 2.1.

Comparing results between the various studies is difficult due to inconsistencies in several variables, including feedstock grade, machine, powder reuse strategy and sieving. The study by Thejane et al. found that different machines appear to have different results in oxygen uptake from powder reuse [42]. Other differences between studies, such as the sieve size used after each build, can have a large influence on the PSD. Although 63 μm sieves are commonly used for LPBF, studies also specified the use of 50 and 80 μm sieves. Despite these differences, the results of the studies commonly indicate an increase in oxygen uptake and in the particle size with reuse that is reflected in the PSD; the increase is attributed to either a decrease in fines or powder sintering.

Oxygen content has significant implications for Ti-6Al-4V. As an interstitial element in the alloy, oxygen has a strong effect on its mechanical properties. Increasing oxygen weight percent by fractions of a percent can lead to substantial decreases in ductility and large increases in strength [43]. Oxygen is also an alpha phase stabilizer, which is the more brittle of the alpha and beta phases found in the dual phase alloy Ti-6Al-4V, potentially altering the microstructure [44]. Studies have also shown that oxygen content can have a large influence on melt pool viscosity and melt track stability within the AM process [31].

Table 2.1: Summary of Ti-6Al-4V powder reuse studies in LPBF.

AUTHOR	MATERIAL	MACHINE	REUSE STRATEGY	NOTEABLE RESULTS
LEARY ET AL. [35]	Grade 23 Ti-6Al-4V	Unknown	Single Batch, 5 reuse cycles	Decrease in fines, PSD D10, D50 and D90 increased, no trend in powder O or N content
QUINTANA ET AL. [45]	Grade 23 Ti-6Al-4V	Unknown	Single batch, 31 reuse cycles	PSD D85 decreased, O content increased (0.09 to 0.13 wt%), improved flowability, strength increased slightly
CARRION ET AL. [36]	Gas Atomized Grade 23 Ti-6Al-4V	EOS M290	Single batch, 15 reuse cycles	Decrease in fines, PSD narrowed, O content increased (0.08 to 0.12 wt%), no change in tensile or fatigue properties
THEJANE ET AL. [42]	Grade 23 Ti-6Al-4V	Concept Laser and another unknown machine	Concept Laser: single batch, 10 reuse cycles Unknown machine: single batch for 10 reuse cycles, top-up from 11-25	O content increased in the unknown model machine, but remained constant in the Concept Laser printer
HARKIN ET AL. [30]	Plasma Atomized Grade 23 Ti-6Al-4V	MLab Cusing R	Top-up, 9 reuse cycles	No change in PSD, O content increased (0.095 to 0.125 wt%), improved flowability
CORDOVA ET AL. [28]	Gas Atomized Grade 5 Ti-6Al-4V	SLM Solutions 280	Single batch, 11 reuse cycles	Slight shift upward in PSD, no change in O content, improved flowability
MEIER ET AL. [31]	Grade 5 Ti-6Al-4V	EOS M280	Single batch, 12 reuse cycles	Decrease in fines, small increase in O content, decrease in elongation at failure
SEYDA ET AL. [40]	Gas Atomized Ti-6Al-4V	Unknown	Single batch, 12 reuse cycles	PSD shifts upward

Inter-build variability may also result from random process deviations or machine degradation. Degradation of critical components can cause substantial changes to the properties of printed parts. In a LPBF machine, this may include the optics that focus the laser, the recoater blade condition, or surface coatings in the machine that undergo degradation and flaking to name a few. One study reported by Bean et al. investigated the effect of the laser focal position on roughness, microstructure and tensile properties [46]. By changing the focal position of the laser to 5 mm above and below the processing plane, they showed that all three changed noticeably compared with the "optimal" focal length i.e. focused on the powder bed. A schematic showing the focal position of the laser with respect to the processing plane is shown in Fig. 2.1. Roughness of the print was the largest affected by focal offsets, ranging from approximately 7.5 to 15 µm under standard argon processing gas. The roughness was stable around 7.5 µm from +2 to -2 mm about the processing plane and worsened rapidly outside these boundaries. Tensile properties were also affected, with the ultimate tensile strength (UTS) and reduction in area showing the most sensitivity. For +3, 0, and -3 mm focal point offset about the processing plane, the corresponding UTS were 1403, 1423, and 1400 MPa with a maximum standard deviation (STD) of 4.1 MPa. The reduction in area showed similar variability, with values of 27.9, 30.2, and 26.8% for +3, 0 and -3, respectively, and a maximum STD of 1.3. By characterizing the microstructure, the authors showed that there was a difference in melt penetration depth with focal offset and attributed the changes in tensile properties to the changes in microstructure. Results from this study indicate that noticeable changes in microstructure and corresponding tensile properties of the metal can result from changes to the optics. Focal changes such as those shown in Bean et al. [46], may result from degradation of the optical components, either directly or through thermal lensing. Since the focal point of an EOS M290 is manually adjusted using a

visual verification, there could be differences in the focal setpoint between machines as well, making this relevant to both inter-machine and inter-build variability.

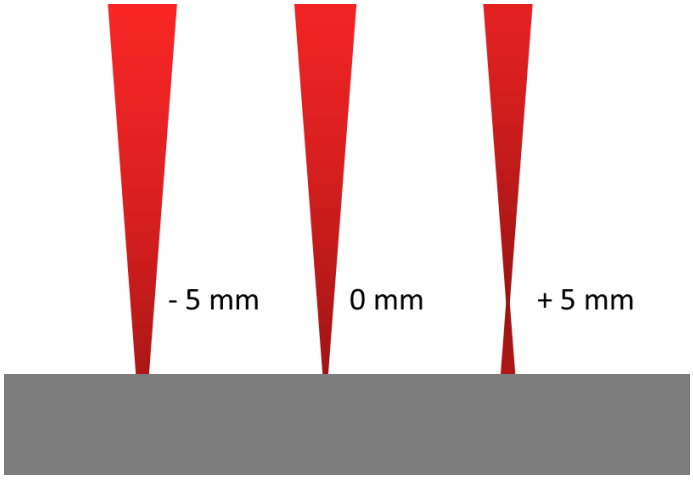

Fig. 2.1: Schematic representation of the laser focal position with respect to the processing plane.

Regarding stochastic inter-build variability, one can envision electrical power fluctuations affecting the laser power, environmental conditions changing the humidity and thereby powder flowability [18], or vibrations from local activity in the manufacturing space impacting the powder bed. These events are undoubtedly much harder to identify as root causes of variability, owing to the wide range of possible events and contributions, as well as unknown frequencies of occurrence. To the author's knowledge, no literature exists that has investigated the stochastic variability present in repeated prints by PBF processes or the effects of machine health that could lead to degradation of properties.

2.3. Intra-Build Variability

Variability can also occur from part-to-part within a single print, which is termed intra-build variability. Spatial variations in the AM process can result in property differences across the build space. This type of variability is thought to be a direct result of the process physics, and

as such will be unique across the metal AM processes. Spatial variability in the process physics could also be unique to different make and model machines of the same technology. Considering LPBF, there are three main sources of spatial variability, namely gas flow, laser incidence angle, and recoater movement. Each of these factors has been explored to varying degrees.

While the gas delivery systems differ between machine makes and models, the intentions are the same: (1) to provide an inert atmosphere that reduces contamination of the hot metal and the likelihood of hazardous combustion, and (2) to sweep away by-products of the melting process [47,48]. LPBF is a relatively dirty process, with smoke, condensate, and spatter constantly being generated around the melt pool [48,49]. Smoke can attenuate the laser, while condensate (vaporized and re-solidified metal) can redeposit on the powder bed and create regions of abnormal chemistry, due to the altered composition of condensate [22,48,49]. In the case of printing Ti-6Al-4V, Keaveney et al. confirmed theories that the vaporization of powder in LPBF forms condensate [48]; the condensate produced in printing of Ti-6Al-4V contains high levels of carbon (51 wt%), aluminum (3.5 wt%), and oxygen (6.5 wt%,), and only 8.7 wt% titanium content. Given that small changes in oxygen content of molten metal can significantly affect its viscosity, this could have important implications for the mechanical properties in LPBF if condensate is redeposited [50,51].

Although the inert gas flow is intended to remove both smoke and condensate, its efficacy has been questioned in various studies. Insufficient gas flow can have large effects on porosity, as reported by Reijonen et al., where a strong correlation was found between insufficient gas flow and porosity [47]. Volumetric porosity content varied from approximately 0.005% to nearly 10%, varying as function of both gas velocity and build plate location. The gas velocity appeared to have the greatest effect on porosity, characterized by a logarithmic

relationship. While the lowest gas velocity clearly increased the porosity, the differences in porosity from 2-4 m/s gas velocity were much smaller, spanning from 0.005% to 0.2%. Furthermore, the spread of data for each gas velocity was large, with a typical range of approximately 0.07% for the velocities above 1 m/s, showing that location within the build space is important, regardless of the overall gas velocity.

Other investigators have reported that common LPBF machines do not have uniform gas flow within the build space [49,52], which can cause spatial variation in metal quality and its mechanical properties [52]. For instance, Ladewig et al. characterized the gas flow inside an EOS M280 and discovered the gas velocity decreased from the back to the front of the machine, shown schematically in Fig. 2.2, thereby altering the degree of laser scattering that occurred from accumulating smoke [49]. Ferrar et al. found similar results in an MTT ReaLizer 250, indicating that the concerns associated with gas flow consistency are potentially machine agnostic [52]. The disruptions in gas flow uniformity over the build envelope can cause regional differences in part porosity [47,52,53]. Ferrar et al. quantified this in the MTT ReaLizer 250 by printing lattice structures, with porosity ranging from approximately 57% to 65% across the build chamber [52]. Although the magnitude of these values seems extremely high, the authors do not differentiate between porosity and empty space between the lattice struts. Emphasis here is placed on the range in porosity that is observed.

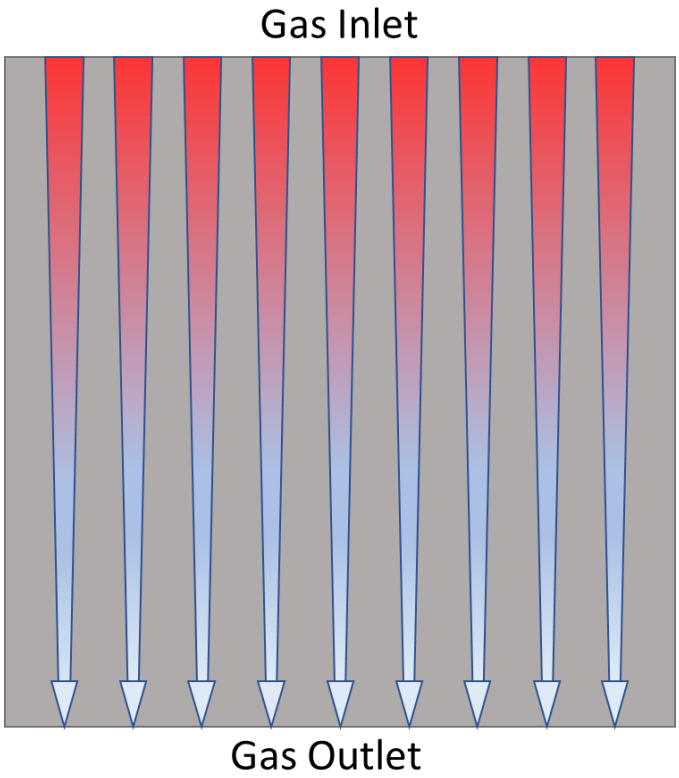

Fig. 2.2: Schematic representing the gradient in inert gas flow velocity from the gas inlet to outlet.

A second source of spatial variability in LBPF is the laser incidence angle. In single laser machines, the laser is positioned directly above the center of the build plate. As a result, the farther the laser strikes from the center, the greater its incidence angle becomes, thereby distorting the beam's profile to an ellipse. Distortion of the laser profile increases the cross-section of the incident beam and decreases its energy density [54,55]. Studies by Chen et al. and Fathi-Hafshejani et al. were able to correlate this effect to changes in surface roughness and porosity [56,57]. Fathi-Hafshejani et al. found that both the surface roughness and volumetric porosity content increased with radial distance and attributed these relationships to the lower energy density [56]. The average roughness increased from 25 µm to 37 µm as the angle of incidence increased from 0 to 18 degrees. The range of angles used in this machine is expected to

be similar to those used in other AM machines of similar build volume size, including the EOS M290, due to simple geometric relationships. Machines with larger build volumes may require a wider range of angles of incidence, however, possibly exacerbating this issue further.

Lastly, there is additional complexity to process variability in the printing process that is added by the recoater blade. In most LPBF and EPBF systems, a recoater blade sweeps a thin layer of powder across the build plate. Several studies have found that powder is distributed unevenly, forming a gradient in particle size along the recoater path [57,58]. Models created by Phua et al. agree with Chen's experimental results that a typical recoater blade introduces powder segregation [58]. Chen et al. hypothesizes further that this effect might cause gradients in melt pool temperature throughout the build space that vary as a function of the local PSD [57]; this hypothesis is based on work from Niu et al. suggesting that a higher surface area to volume ratio associated with smaller particles could increase laser absorption [59]. Phua et al. went on to design a toothed recoater blade that could decrease powder size segregation [58].

It is apparent from these studies that each factor (gas flow, laser interactions, and recoater movement) can influence part quality individually, but also that synergistic relationships likely exist between them. While these studies that concentrate on individual factors are extremely useful in understanding their contributions, they do not necessarily capture interactions with other sources of variability. Additionally, these interactions could be present in studies attempting to investigate single factors and cause a convolution of the results. Regardless, studies that assess the overall variability are essential to advance the understanding of metal AM processes, since variability will not necessarily be the sum of individual factors. The following investigations focus on both microstructure and mechanical property variability in LPBF to advance the current level of understanding and address an important concern for the aerospace

industry. The findings are expected to contribute to the development of confidence in this technology and its application for the manufacturing of components for commercial aircraft.

Chapter 3. Experimental Design, Methods and Materials

The inter-machine, inter-build and intra-build variability assessments in this work are based on a round robin assessment of LPBF process variability. Chapters 4-7 each discuss one of the three levels of variability. Although each chapter has a unique focus of analysis, they are derived from the same body of experimental work. The experimental design, methods and procedures governing the round robin are presented here.

3.1. Experimental Design

Assessing the process variability as defined by the objectives in Chapter 1 requires a meticulously/carefully designed experimental plan. As there are a multitude of factors that can affect the outcome of this study, it is paramount to minimize these effects by establishing a standard operating procedure. The approach used to assess all three levels of variability is discussed here in detail.

3.1.1. Build Design

To capture intra-build variability, a build design was needed that could encompass the impacts of the laser incidence angle, recoater, and gas flow. Each of these factors operates on a different axis or combination of axes in the machine: the laser spot shape changes with radial distance, the recoater moves along the y-axis, and the gas flow moves along the x-axis, although the velocity may vary as a function of both x and y. In this study, the build space was discretized as shown in Fig. 3.1. The 250 x 250 mm build plate was divided into five zones: the center and the remaining four corners. X, y, and radial distance can thus be captured. Additionally, this division was repeated at a second height, located 67 mm above the first level, to assess the

influence of z-height in the chamber. Zones were labelled as A0-A4 and B0-B4, with A and B corresponding to the bottom and top levels, respectively, matching the visualization below.

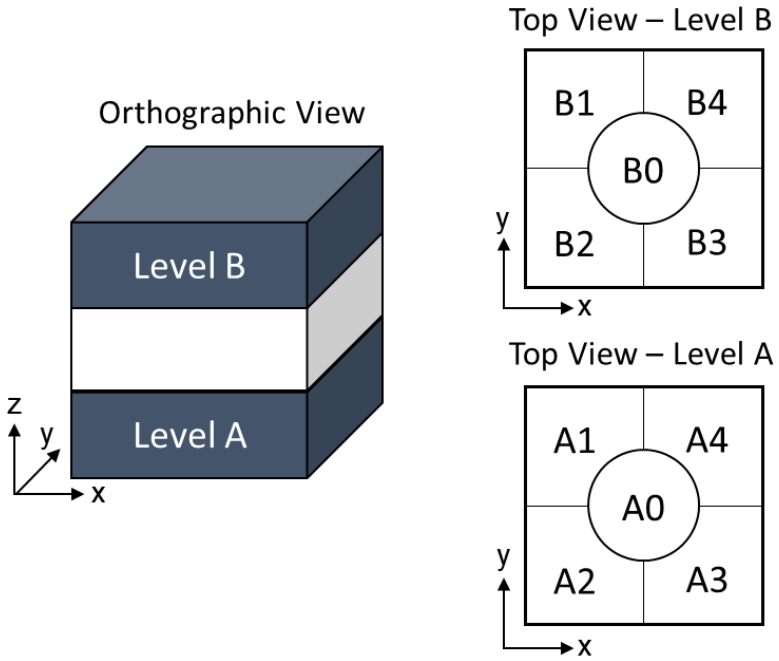

Fig. 3.1: Visualization of the division of the build space, consisting of five zones at two height levels.

Each zone was populated with tensile coupons. Vertically and horizontally oriented coupons were printed to capture the microstructural anisotropy that can occur [60]. Ten vertical and nine horizontal coupons were positioned in each zone, for a total of 190 coupons in the build. A digital rendering of the design is shown in Fig. 3.3 alongside magnifications of the coupons illustrating the serialization used. A photograph of a completed print is included in Fig. 3.2.

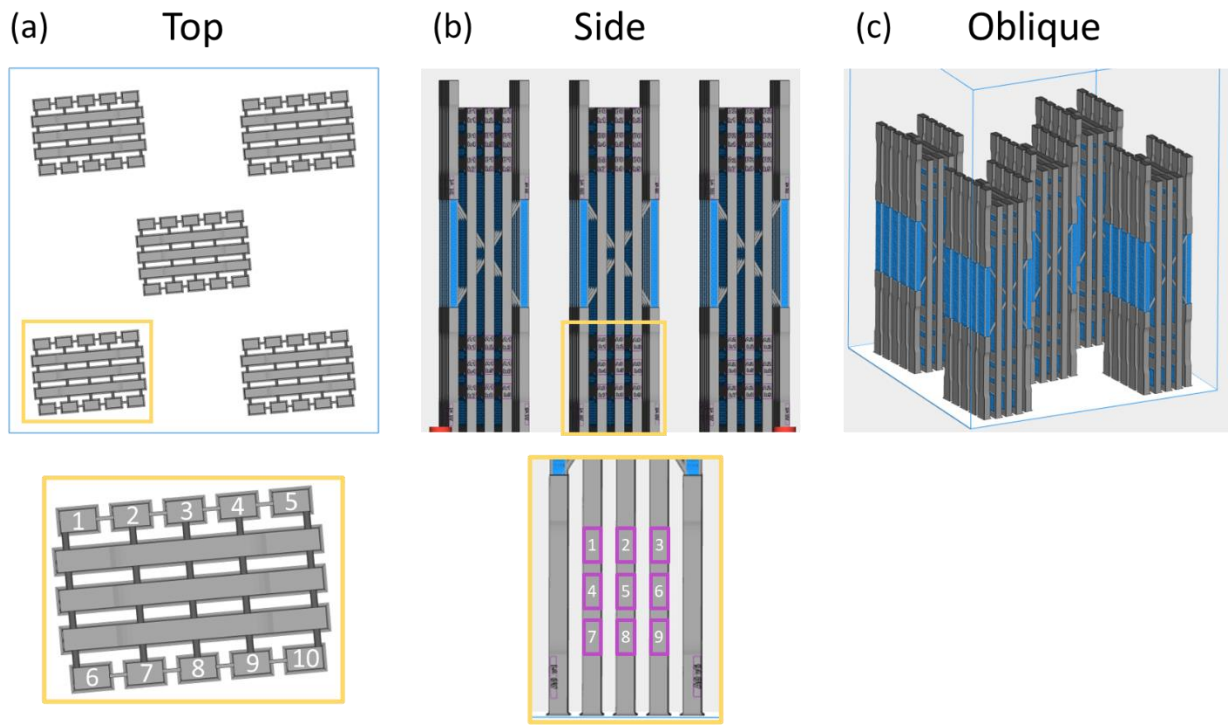

Fig. 3.3: A rendering of the build design from the (a) top, (b) side and (c) oblique views. Expanded views of each show the numbering scheme used to identify individual coupons.

Fig. 3.2: A photograph of a completed print still attached to the build plate.

3.1.2. Print Sequence

Inter-build variation is assessed by analyzing identical builds that have been printed on the same machine. The more repetitions, the more easily trends will be observed resulting from powder reuse or machine health. However, increasing the number of prints will also increase the cost to the study's participants as powder consumption rises and machine time is taken away from production jobs. It was crucial to approach this study with budget in mind. A compromise was reached to balance these two competing factors; six prints would be built with an effort made to decrease powder consumption. The first and last print in this study contain the full complement of 190 coupons, as shown in Fig. 3.3, while the four intermediate prints are composed of 76 coupons to reduce powder consumption. Coupons are positioned identically as in the full design, but the number of zones is reduced from ten to four. Each of the four intermediate prints contains the center zone (Zone 0) and one of the four corners at both A and B heights. The corner represented changes from Build 2 to Build 5, such that all corners are printed in one of the builds. A visual representation of this sequence is shown in Fig. 3.4. Each aspect of these design choices supports the goals of intra- and inter-build analysis, while having enough coupons for the data to be statistically significant. By rotating through the four corners in the intermediate builds, coupons are printed in each of the zones at least three times, creating a sufficient sample size for intra-build analysis. Simultaneously including Zone 0 in all prints provides a consistent reference point to evaluate inter-build variability.

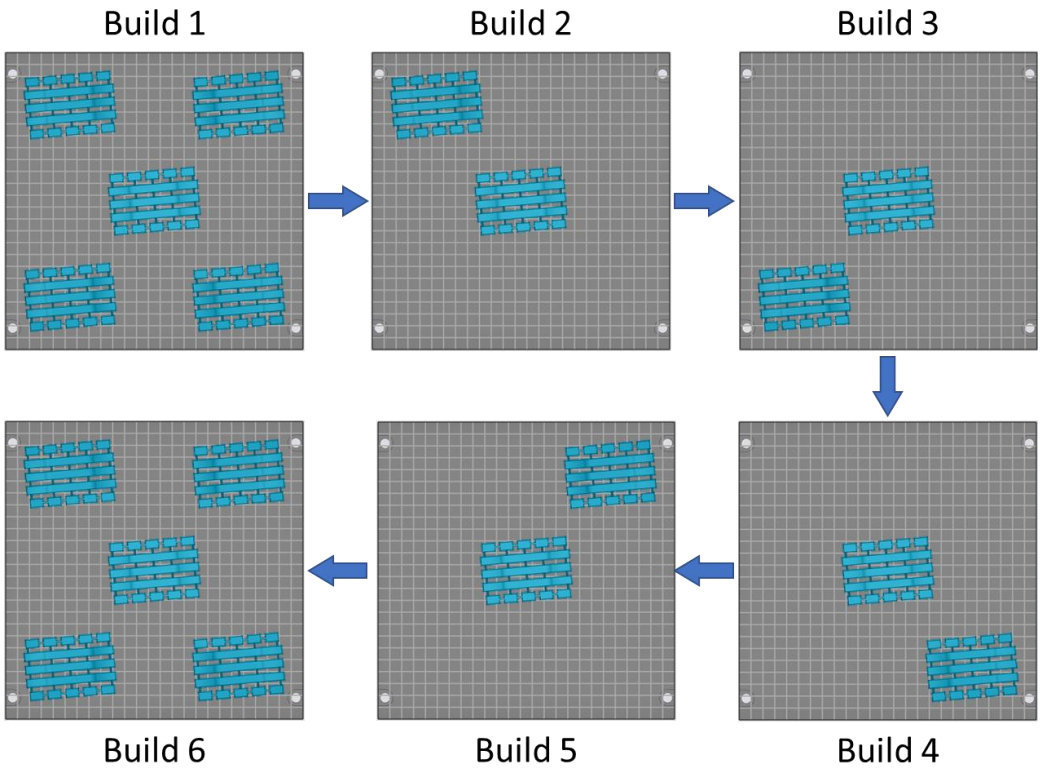

Fig. 3.4: The sequence of six builds printed by each study participant, shown from a top view.

3.1.3. Round Robin Experimental Design

The broadest level of the evaluation covers inter-machine variability, requiring the assessment of multiple machines. A common approach to this type of experiment is a round robin, in which multiple contributors with similar or identical equipment each manufacture parts for comparison. A few examples exist in the literature for LPBF, including the previously mentioned study by Jelis et al. [13]. One of the most important takeaways from their work was the importance of standardizing the manufacturing process across all machines, including limiting the study to a single machine make and model.

As a common LPBF printer, the use of the EOS M290 in this study allowed for the selection of five organizations with "identical" machines to the M290 at the University of Washington to partake in the round robin, for a total of six participants. All five are industry organizations, including leaders in aerospace, printing bureaus, and original equipment manufacturers (OEM). Specifically, this includes The Boeing Company, Lockheed Martin, Toray Precision Company, EOS, and 3D Logics. From this point in the dissertation and onwards the identities are blinded, and each is identified by their randomly assigned ID, P1-P6. Each participant was vetted to ensure their machine could be operated in a way that conformed to the needs of the study. More information about the vetting process can be found later in this chapter.

Each of the six participants printed the six-build sequence on their M290 for a total of 36 builds, allowing for the assessment of intra-build, inter-build, and inter-machine variability.

3.2. Materials and Methods

3.2.1. Feedstock Material

This study focuses on LPBF with Grade 5 Ti-6Al-4V, an aerospace grade structural alloy prized for its high strength to weight ratio. LPBF printers use fine powder as the raw material. This investigation used a plasma atomized, pre-alloyed Grade 5 Ti-6Al-4V powder provided by the machine manufacturer, EOS. A single manufactured lot of 900 kg was secured and divided between the six participants. At the onset of the study, each company acquired 100 kg from that lot, with the remainder kept in reserve. A certificate of analysis provided by EOS showed that the powder met composition requirements dictated by ASTM F2924 for Grade 5 Ti-6Al-4V [61]. Particle size analysis by laser diffraction found the PSD d10, d50 and d90 to be 30, 41, and 57 µm, respectively. Other analyses, including water content, powder density, and printed part

quality were all found to be within specifications. The full certificate of analysis can be found in Appendix A.

3.2.2. Manufacturing Equipment

The M290 of EOS was selected for this study. The M290 is a single laser printer with a 250 x 250 mm print bed and a 325 mm build height. A schematic of the machine is shown in Fig. 3.5. There are three elevators in the machine that control the powder volume and its distribution, including the powder dispenser, build plate, and overflow bin. Powder from the powder dispenser on the right side of the machine is swept across the build plate by the steel or silicone recoater blade before any excess powder is pushed into the overflow bin. Regions of the powder bed are then melted using the laser to form a slice of the printed part. After the layer is complete, the dispenser elevator is raised and the build plate and overflow bin elevators are lowered, creating space for another layer of powder. In this way, the thickness of the deposited powder layer can be controlled by the movement of the elevators: the farther the build plate elevator drops in an increment of building, the thicker the layer. The standard layer thicknesses for Ti-6Al-4V using the M290 ranges from 30-60 μm. Details of the parameters used in this study will be discussed below. After the elevators move, a new layer of powder is swept across the build plate by the recoater, and the process repeats until the full height of the build is reached.

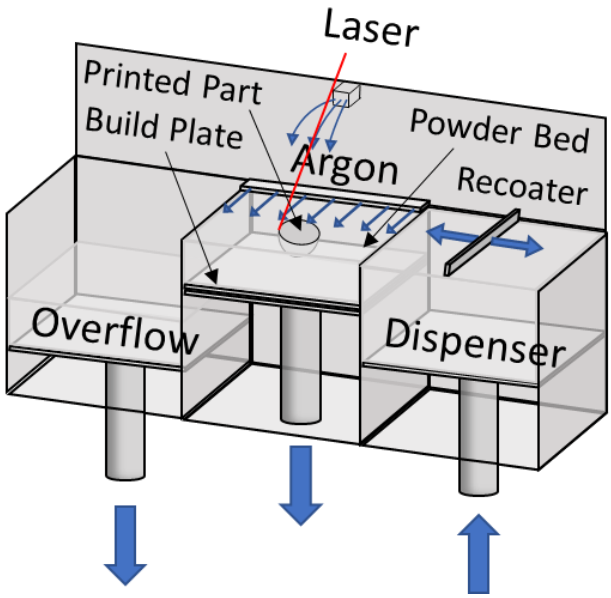

Fig. 3.5: A schematic of the interior of the EOS M290 LPBF system.

An inert gas is circulated through the printer throughout the printing process. As described in Chapter 2, this creates a non-reactive environment and removes some of the process-byproducts (primarily smoke and condensate). The gas enters the chamber from two locations, both at the back of the machine: (1) at a height level with the powder bed, and (2) above the processing plane. A baffle assembly at the back of the printer directs gas through a nozzle to produce a "laminar" layer of gas flow just above the powder surface, which is intended to blow the smoke and condensate to the front of the machine, where an outlet carries the contaminated gas away to a filtration system. This study used the EOS grid nozzle instead of the standard nozzle, a decision based on a recommendation from one of the study's participants, who provided evidence of its improved performance. Gas entering from the top of the chamber cascades down onto the build plate, suppressing smoke that might rise towards the laser optics.

Before the laser reaches the build plate, it passes through a series of optical components that refine and control the beam. After the infrared beam is created by the Yb-fiber laser, it first

passes through a collimator, which ensures the photons are travelling in parallel. The beam is then reflected off two mirrors controlled by galvanometers. Each mirror controls the motion of the laser along one of the x- or y-axes of the machine. Until this point, the laser diameter is still too large. To rectify this, the laser passes through a series of lenses, called the F-theta lens assembly. These glass lenses focus and refine the beam, such that the beam diameter is reduced to a maximum of 100 μm at the powder bed. The exact diameter will vary from M290-to-M290 due to individual calibrations. F-theta lenses are unique from other types of optical lenses. Classical spherical lenses create a spherical focal surface which is unsuitable for LPBF. F-theta lenses flatten that surface into a plane, resulting in similar spot sizes across the entire powder bed. After passing through the F-theta lens assembly, the beam passes through a cover glass that protects the bottommost F-theta lens from damage, before traveling to the powder-coated build plate.

3.2.3. Build File Preparation

Before printing could begin, build files had to be generated. Computer-Aided Design (CAD) software was used to generate designs for the tensile coupons. The geometries were loaded into Materialise Magics [Materialise NV, Belgium], a build preparation software. Scenes specific to the EOS M290 were used to position the coupons in the desired locations and create perforated support structures in the necessary locations. The completed scene was exported as a collection of Standard Triangle Language (STL) files for use in the EOSPRINT software.

EOSPRINT is an EOS specific build preparation software for controlling process parameters and exporting the finished file. A standard EOS parameter set for printing of Ti-6Al-4V (Ti64_PerformanceM291 1.10) was used with minor modifications for the duration of this study. Critical Key Process Variables (KPV) for the infill are shown in Table 3.1. Two

modifications were made to this parameter set to increase the build speed. First, support structures were melted every other layer, i.e. a layer thickness of 120 µm. Second, contours were turned off for all parts. Scan paths consist of two primary regions: infill and contours. The former, as its name implies, melts the interior of the part. The latter outlines the part, which consequently decreases the surface roughness but increases the residual stresses of the part [62] Since all coupons are machined before testing, contours were deemed unnecessary, and turned off to decrease the laser scanning time and residual stresses. With the processing parameters set, the build files were exported for printing.

Table 3.1: Key process variables used for the LPBF process.

Key Process Variables	
Laser Power	270 W
Hatch Rotation	67 °
Hatch Spacing	120 µm
Layer Height	60 µm

3.2.4. Machine Operating Procedures

Upon uploading the build file to the M290, the machine was prepared for the build. First, a thorough cleaning of the machine was performed. Typically, this includes vacuuming all interior surfaces to remove Foreign Object Debris (FOD) and loose powder, as well as inspecting and cleaning the optics cover glass if needed. Although more thorough procedures are outlined by EOS if a material change takes place, however this was not necessary during the present study because material changes did not occur between the six prints for any participant. An inspection of the steel recoater also takes place during the setup; the recoater is replaced if any damage is

found on the blade. Next, a 250 x 250 mm titanium build plate is installed in the M290 and manually leveled. The build plates are at least 19 mm thick to avoid warping and have a machined or ground finish. The leveling procedure uses a feeler gauge to level the y-axis (front and back) of the machine, followed by leveling the x-axis (right and left) with a depth gauge attached to the recoater blade. The recoater blade serves as the reference for height in these procedures. Finally, the build plate is raised until there is negligible gap between it and the recoater blade.

An optional step in the setup is a laser power measurement test. Study participants equipped with a Primes PocketMonitor can measure the output power of their laser at a nominal 280W and compare the measured and expected values. Only two participants in the study provided this data.

Next, the designated powder is loaded into the powder dispenser. For the first build, the powder was in the unused condition and regarded as virgin powder; subsequent builds were comprised of a blend of used and virgin powder to minimize total powder consumption. Filling the powder dispenser begins by loading 20 kg of powder into the dispenser. 75 g of powder is scraped off the top surface of the dispenser using a stainless-steel spatula and is reserved in a vial for future powder analysis. The deposited powder is compacted using a flat stainless-steel spatula, wherein the spatula is repeatedly inserted into the powder and twisted. This motion allows the powder to settle, allowing more powder to be placed in the dispenser and creating a denser layer after the recoating process. The process of loading, sampling, and compacting powder is repeated three more times until the dispenser is filled. In total, approximately 74 kg of powder is placed into the M290 for each build and 300 g are sampled across four heights in the dispenser, complying with powder sampling standard ASTM B215 [63].

With the dispenser filled, powder is swept across the build plate using the steel recoater blade. Doing so allows for a visual verification that the build plate is level and the first layer will have sufficient coverage. The M290 is then closed and backfilled with argon of at least 99.996% purity. The build can then be started by the operator. A generalized process for the machine setup is outlined in Fig. 3.6.

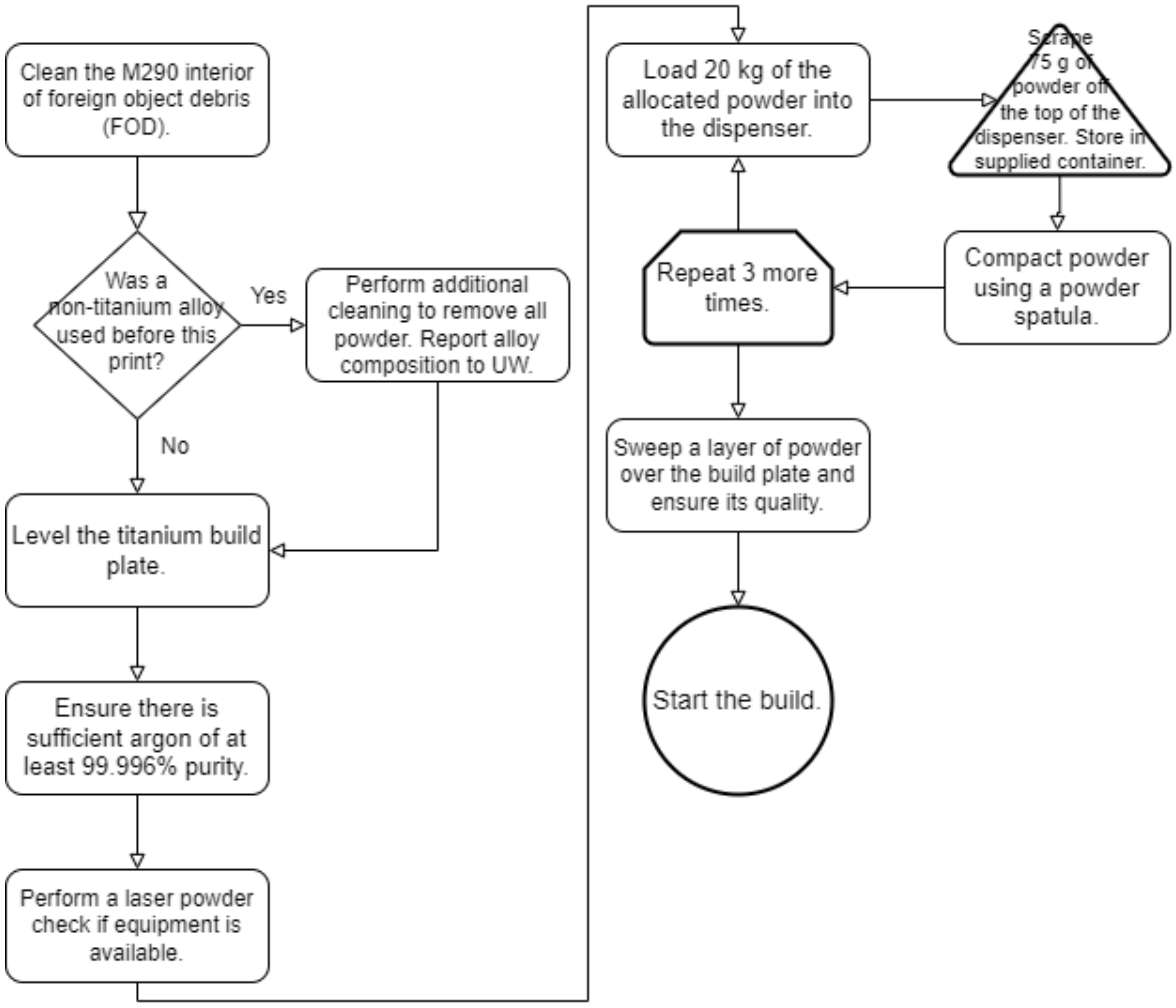

Fig. 3.6: Process diagram illustrating critical steps in the LPBF machine setup.

After a print reaches completion, the unfused powder from the chamber is removed manually or by clean vacuum. Powder is then passed through a 63 μm sieve to remove aggregates and sintered powder. The remaining powder is weighed and powder consumed/lost is replaced with virgin powder from the allocated powder lot, such that 80 kg of mixed reused/virgin powder was achieved. A manual mixing process is then performed, wherein the combined reused and virgin powder is agitated inside a sealed metal drum by inverting it 30 times. The powder lifecycle after a print is outlined in the flowchart presented in Fig. 3.7.

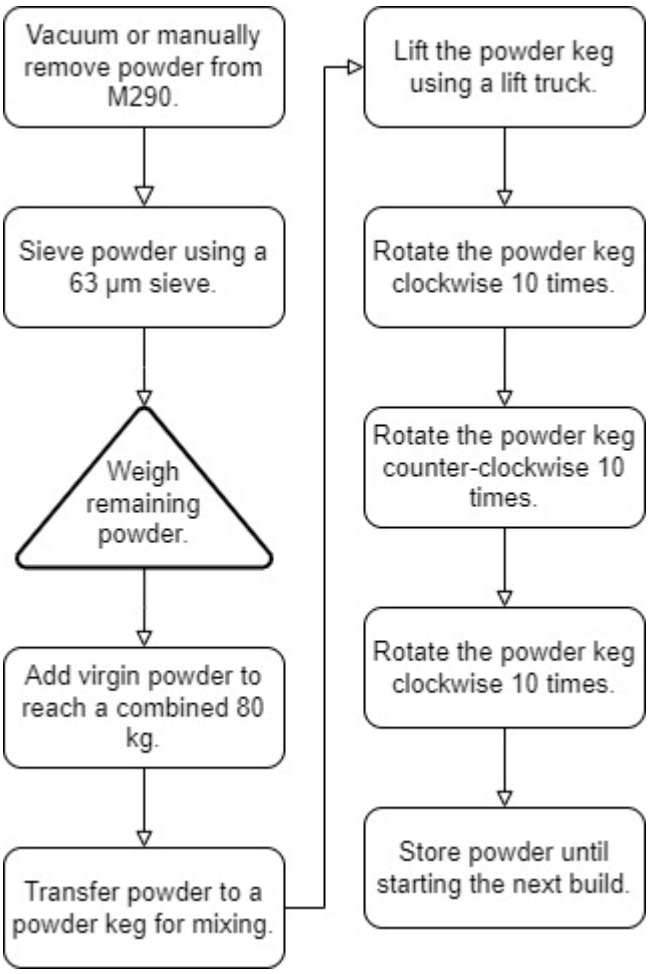

Fig. 3.7: Process flowchart describing the powder recycling process.

3.2.5. Post-Processing

In its printed state, the coupons contain very high residual stresses and an undesirable martensitic microstructure [60,64]. A heat treatment within the annealing temperature range was performed on the printed metal, either while still attached to the build plate or after separation. This heat treatment consisted of a one-hour ramp to 745 °C, holding at that temperature for two hours, followed by furnace cooling to room temperature. A rapid air cool was allowed after the temperature dropped below 500 °C, below which no microstructural changes are expected. In an investigation of various heat treatments, Frkan et al. found that a similar heat treatment resulted in a mixture of α' (martensitic Hexagonal Close Packed (HCP)) and α (non-martensitic HCP) that is more ductile than the as-built fully α' structure [65]. Additionally, this treatment will relieve the residual stresses to minimal levels [66].

Metal from four of the participants was heat treated at the University of Washington in an argon atmosphere furnace [LH 120, Nabertherm, Germany], while P1 and P3 heat treated their metal in-house in vacuum furnaces. Vacuum and argon environments are intended to prevent oxidation of the metal, however some contamination still occurred in some of the metal. This was deemed acceptable due to the removal of compromised material during the machining process. A minimum of 0.5 mm of material was removed from all surfaces of the coupon gauge sections, exceeding the minimum 0.08 mm required by AMS2801B for a similar heat treatment in an unprotected environment [67]. Additionally, small differences were found in the heat treatment cycles between the three furnaces. The effects of this will be explored in later chapters.

Machining the coupons took place over several steps. Since adjacent coupons were connected by support structure, preliminary bandsaw and abrasive waterjet steps were used to separate them. Coupons could then be milled using a Computer Numerical Control (CNC)

process. Dry milling consisted of a single, full depth of cut pass with the parameters and end mill described in Table 3.2. Final gauge section dimensions were 6 x 4.5 mm with a typical roughness of R_a = 0.45 µm, complying with ASTM E08M for subsize coupons [68]. For reference, the as-built coupons had roughness values approximately 30 times larger than its machined counterparts.

Table 3.2: KPVs of the coupon milling process.

Cutting Parameters	
Feed Rate	5 in/min
Spindle Speed	500 RPM
End Mill Specifications	
Composition	TiAlN coated carbide
Flutes	4
Diameter	0.5 in
Corner Radius	0.03 in

3.2.6. Powder and Bulk Metal Chemical Analysis

A powder sample was acquired by each of the six suppliers during the setup for each build as detailed in Section 3.2.4. The acquired powder samples underwent inert gas fusion (IGF) by a qualified service provider [Fort Wayne Metals, IN, USA] to measure the O, H, and N content per ASTM E1409 and E1447 [69,70]. Additionally, select printed metal from three of the suppliers was analyzed by the same test methods for O, H and N content.

3.2.7. Tensile Testing

To determine the static property distributions, a subset of the total number of built coupons were evaluated by tensile testing. Specifically, four horizontal and four vertical coupons were

chosen pseudo-randomly from every zone of each of the 36 builds, culminating in 864 vertical and horizontal coupons, or 1728 total. Specifically, for each build, two vertical coupons were randomly selected from the back row (1-5) and front row (6-10) of each zone. Likewise, one horizontal coupon was randomly selected from the three coupons in each row of the 3 x 3 array of horizontal coupons, and the fourth coupon was randomly selected from a random row. Thus, Builds 1-6 each had a different selection of coupons that were tested. To standardize the results across machines, the same coupons were tested of the metal from each participant. In other words, the same, pseudo-randomly selected coupons in Build 1, 2…6, were tested of the metal from each participant, but the particular coupons were re-randomized for each build number. A portion of the sampling scheme used in Build 1 is shown in Fig. 3.8 as an example. Although the majority of tensile tests were successful, it should be noted that failed tests did occur, typically due to fracture outside the instrumented section of the gauge section. This reduced the number of successful tests to 1652 coupons.

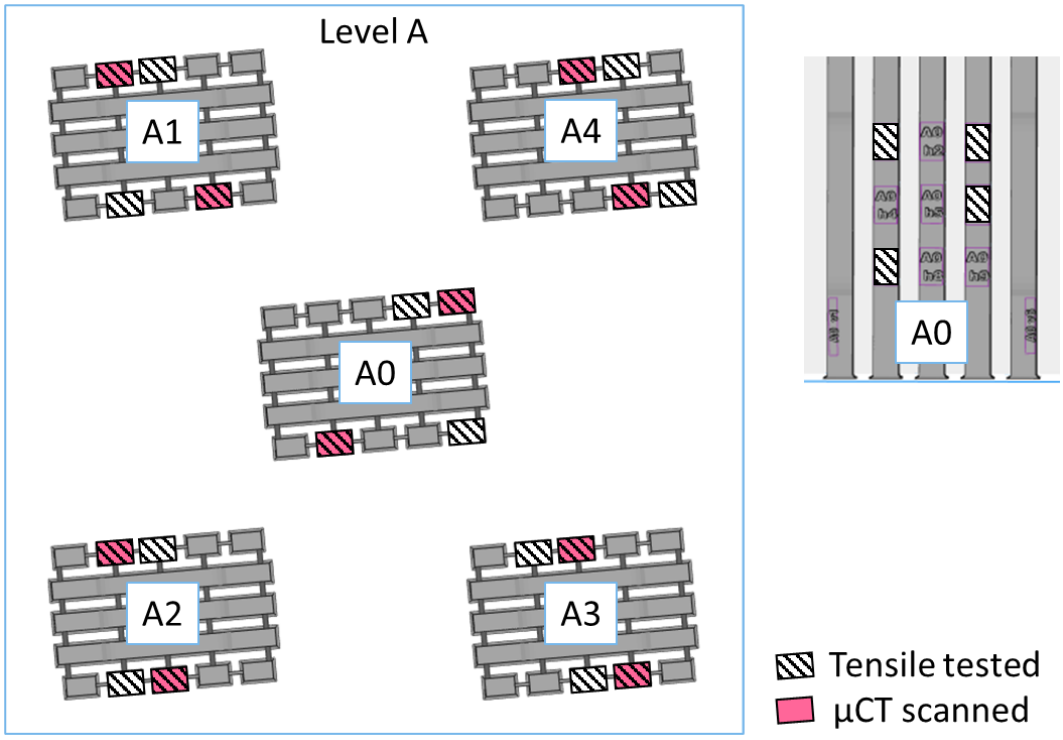

Fig. 3.8: Example coupon selection scheme from Build 1. All level A vertical coupons selected for µCT and tensile testing are shown on the left and the horizontal tensile tested coupons in level A Zone 0 are shown on the right.

The remaining coupons were reserved for future investigations. Additionally, every time of the load frame was used, a wrought annealed Ti-6Al-4V coupon was tested first, for a total of 33 coupons across the study. These coupons were waterjet from one sheet of wrought form Ti-6Al-4V to minimize their variability. Testing wrought coupons in this way provides an assurance that the load frame is working properly and consistently between uses. Furthermore, the variability observed for the wrought coupons can be used as a comparison for the AM material.

Tensile testing was performed on an Instron load frame [Instron, MA, USA] at 1.27 mm/min for a 25 mm gauge section length [68]. Displacement was measured with a clip-on

extensometer. Tensile properties, including elastic modulus (E), yield strength (YS), ultimate tensile strength (UTS), and strain at failure (%el), were calculated using custom Python scripts.

3.2.8. Micro Computed Tomography

Micro x-ray computed tomography (μCT) is a useful technique for visualizing the interior of structures. X-rays are generated from a source and oriented to pass through the object being scanned. A detector on the other side of the object detects the transmitted x-rays. Thicker regions of material scatter or absorb more of the x-rays, which the detector represents as a gray-scale two-dimensional (2D) projection of the object. By rotating the object and taking an image at each position, a three-dimensional (3D) reconstruction can be generated. These models can be detailed enough to map interior voids and highly complex structures that exist within the part. Due to the concerns with porosity in metal components printed using LPBF, μCT is an invaluable tool for this investigation.

The μCT scans were performed on a commercial scanner [North Star Imaging (NSI) Model X5000, MN, USA]. A helical scan was used to capture the entire gauge section of each evaluated coupon, with scan parameters kept constant across all scans. The scans were conducted with 5760 projections at 204 kV and 44 μA, with 2 frames per second (fps) collection, yielding a voxel size of approximately 8 μm. After reconstructing the scans, the volumes were analyzed in VGSTUDIO [Volume Graphics, Germany] and pores with a minimum of 27 voxels were identified based on their gray scale. A variety of metrics were calculated for each pore, including size, sphericity and location. Size can be defined a number of ways, including the effective diameter (diameter of a sphere enclosing the defect), surface area of the defect, cross-sectional area along a particular plane, and volume. Sphericity is defined as the ratio between the surface area of a sphere with the same volume as the defect and the surface area of the defect, therefore ranging between 0 and 1.

To have the best chance at correlating porosity data and mechanical properties, μCT was performed on vertical tensile coupons prior to mechanical testing. Approximately half of the vertical coupons selected for testing were scanned in the machined condition. The coupons were selected in a similar pseudo-random fashion as the coupons for tensile testing; one vertical coupon was randomly chosen from the two coupons selected for tensile testing from each front and back row of every zone. For consistency, these selections were again kept identical across participants but randomized for each build in the six-build sequence. Fig. 3.8 provides an example of how coupons were selected. Vertical coupons were exclusively scanned to better establish a correlation between lack of fusion (LOF) porosity and mechanical performance [71]. Large LOF defects form along the layer interfaces due to insufficient laser energy, resulting in flat, high aspect ratio defects. Applying a load parallel to the build z-direction results in mode I loading of the pores, creating a more severe stress concentration effect than if loading was applied to horizontally (x- or y-) printed coupons. Therefore, scanning the vertical coupons provides the best chance of identifying any influence of pores on the mechanical performance.

3.3. Controlling Undesired Variability: Process Control Document

Additional sources of variability can confound the assessment of process variability. Hence, it is paramount that they are mitigated. AMS7003 is a standard specifically dealing with how to create a fixed and repeatable LPBF process for aerospace applications [72]. Many of the requirements outlined in this standard were codified into a governing Process Control Document (PCD) for this round robin, which was followed by all study participants. The full PCD

(with some content redacted for privacy) can be found in Appendix B. The remainder of this chapter is devoted to explaining key aspects of the PCD.

3.3.1. Machine Condition and Configuration

Although some participants in the study operate multiple M290s, they were only permitted to use one for the duration of the study. The use of multiple machines would confound the analysis of inter-machine variability. Each machine was also vetted before use. Participants were surveyed to identify software versions, environmental conditions, machine maintenance histories, and material histories. Preferences were placed on machines that had only used titanium alloys and specific software versions. However, some exceptions were allowed if properly documented. For example, while five of the six machines in the study were new enough that EOSPRINT 2 build files could be used, one machine (P6) was running an old software version, requiring build files be prepared separately with EOSPRINT 1.

Adequate maintenance was required throughout the study in accordance with the PCD. At a minimum, participants had to perform maintenance meeting the recommended frequency of the manufacturer, i.e., at 6-month intervals. These service visits included annual laser focus checks, seal replacements, and more.

The M290s used in the round robin were almost entirely “stock” machines without modifications. A minor modification to the machine design was the use of the EOS grid nozzle attachment. As per the recommendation by one of the industry partners, this nozzle was mandated for use by all partners across the study. Another hardware requirement was the use of a high-speed steel recoater blade. EOS offers several material choices, including soft recoater blades; these blades were prohibited for this study.

3.3.2. Feedstock Powder

The Ti-6Al-4V powder used in LPBF can vary significantly in its PSD and morphology and, to a lesser extent, its chemistry. Different methods of manufacturing the powder, such as plasma atomization or gas atomization, can result in different powder morphology and entrapped gas content [73]. Even for a single manufacturing method, differences in PSD can be achieved by altering the processing parameters. To minimize these differences, a single 900 kg batch of plasma atomized Grade 5 Ti-6Al-4V powder was allocated for this study, with each participant receiving a 100 kg portion. This step ensured that all participants began the study with powder exhibiting the same PSD, chemistry, and morphology. Any additional powder needed during the study had to come from the remaining 300 kg of the original powder batch.

The manufacturer of the M290 dictates that the equipment must be operated under particular environmental conditions. Specific combinations of temperature and humidity ranges are allowed, and these were adopted by the PCD for machine operation and powder storage. It is well known that high humidity can decrease powder flowability, while too low humidity can increase the chances of static discharge that may ignite the powder during handling [18]. Adhering to the recommended ranges minimizes these risks.

3.3.3. Powder Extraction and Reuse

After the print is completed, excess powder is removed from the three elevators for reuse. Five of six participants used a clean vacuum, whereas the final participant (P5) manually scooped the powder out from the build chamber. Participants were instructed to then sieve the powder with a 63 µm sieve. After sieving, the lost or consumed powder was replaced with virgin powder from the allocated powder lot and mixed with a manual process detailed in the methods section of this chapter. One participant (P3) was allowed to blend the powder with a v-blender.

3.3.4. Post-Processing

Before evaluation of the tensile coupons can begin, they must undergo heat treatment and machining. The specifics of these processes are detailed in the methods section, however the steps taken to reduce variability are relevant here.

After the printing process, a significant amount of residual stress can remain in the coupons due to the extremely high cooling rates [64]. It is advised to stress relieve the coupons on the build plate to avoid residual stress-induced distortion caused by the separation [64]. Performing stress-relief on the build plate was not feasible for the round robin given the difficulties of shipping build plates back-and-forth across the world. Instead, the support structures were specifically designed to resist the high residual stresses even after separation from the build plate. Participants were instructed to separate coupons from the build plate before shipping them to the University of Washington for heat treatment. No stress-induced distortion was observed in the specimens.

Two of the participants (P1 and P3) were permitted to heat treat the coupons in their own vacuum furnaces, allowing them to do so on the build plate. Both furnaces met the requirements outlined in the PCD regarding temperature variations (± 10°C at 745°C) and thermocouple use. The coupons from the four remaining participants were heat treated in one argon atmosphere furnace at the University of Washington.

Following heat treatment, the coupons were machined to final dimensions. Machining was performed at the University of Washington with a CNC milling process to minimize variability between coupons.

3.3.5. Material Characterization

Operator induced error is a common occurrence. Whether it is for material testing or equipment operation, differences in technique can lead to variability in the end product. Wherever possible, material characterization was performed by a single operator, including the vast majority of the μCT scans and reconstructions, and tensile testing. Although the same operator could not operate the M290s across the six participants, each individual company was asked to have their six builds be set up by the same technician if possible.

3.4. Conclusion

The round robin investigation presented in this chapter was designed to support characterization three aspects of variability in LPBF, including inter-machine, inter-build, and intra-build variability. A discretization of the build space into five regions at two height levels provides a method for performing regional intra-build analysis that encompasses the main known contributors to process variability, namely recoater movement, laser incidence angle, and argon gas flow. Six repeated builds printed by each of the six participants provides the inter-build and inter-machine aspects of variability. A robust PCD was developed and adhered to by each participant in the study to minimize any unwanted sources of variability.

Chapter 4. Intra-Build Variability

Variation in the mechanical properties of metal in LPBF may occur spatially within the build space in response to the effects of recoater movement (x-axis), inhomogeneous gas flow (y-axis), and laser incidence angle (radially). This category of variability is referred to here as intra-build variability. Understanding the spatial variability in build quality and metal produced is not only important to improving additive technology but to design for additive manufacturing (DFAM) and, in aerospace, understanding factors that can contribute to metal quality and the certification process. Since it is most economical to fill the entire build space, either with many small parts or fewer large parts, it is critical to know if the properties will vary from part-to-part or within individual larger parts. The intra-build variability of the porosity distributions and corresponding tensile properties of metal from each participant will be explored in this chapter. The null hypothesis to be tested is there is no variability in metal quality or mechanical properties of metal produced within the build chamber. The general experimental design, methods and materials adhere to the Round Robin study and its PCD. Details of these topics can be found in Chapter 3.

4.1. Results

4.1.1. μCT

Although the objective of this chapter is to identify variability within the build space, it is important to first establish the distribution of pores within individual coupons. One coupon from each of the six participants was randomly selected from Build 1, and the kernel density estimates of pore diameters from those coupons are shown in Fig. 4.1. The shape of the distributions for

P1-P5 is similar, consisting of a sharp peak with skew towards smaller pore sizes. Small secondary peaks are present in the distributions of P2 and P4. The distribution for the coupon from P6 is significantly wider and has a high frequency of large pores. Nevertheless, the diameter corresponding to the highest frequency (annotated on each plot) is similar across all six machines, ranging from 0.53 to 0.6 µm.

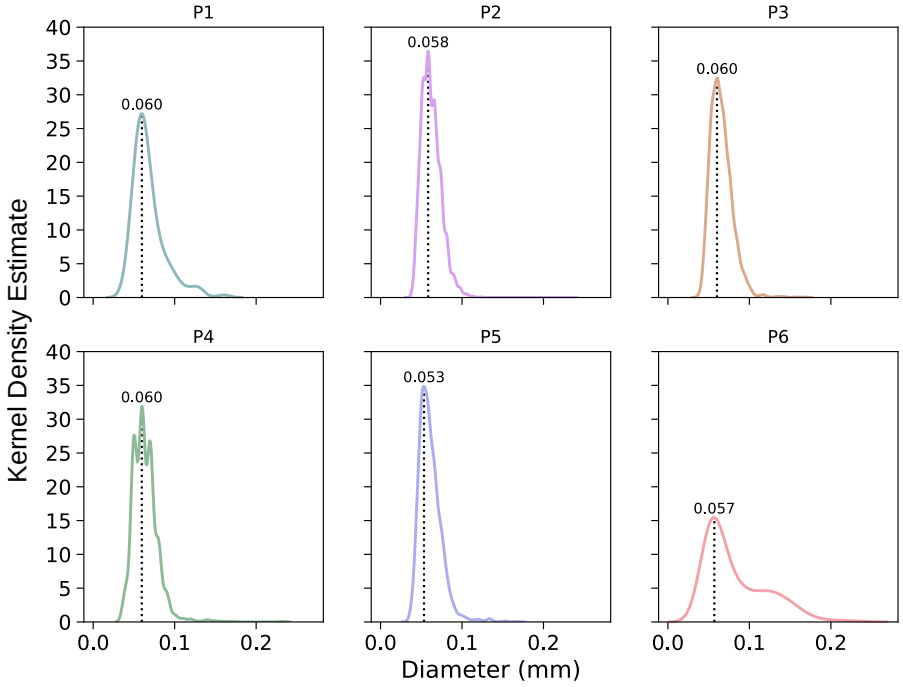

Fig. 4.1: Kernel density estimates showing the frequency of pore sizes present in a representative coupon from each participant. The diameter at the primary peak is annotated on each plot.

It is also important to identify if the pores are homogeneously distributed throughout the coupons. The locations of pores are plotted in Fig. 4.2 based on their z height within the coupon and their edge distance, which measures the distance from the pore to the nearest free surface. Based on this figure, it is evident that the pores are approximately evenly distributed throughout the coupons. The one exception is P5, which has a higher frequency of pores towards the top of

the scanned volume. However, there is variability from sample to sample and this is not representative of all coupons from P5. Thus, no consistent trends were observed in pore location within individual coupons.

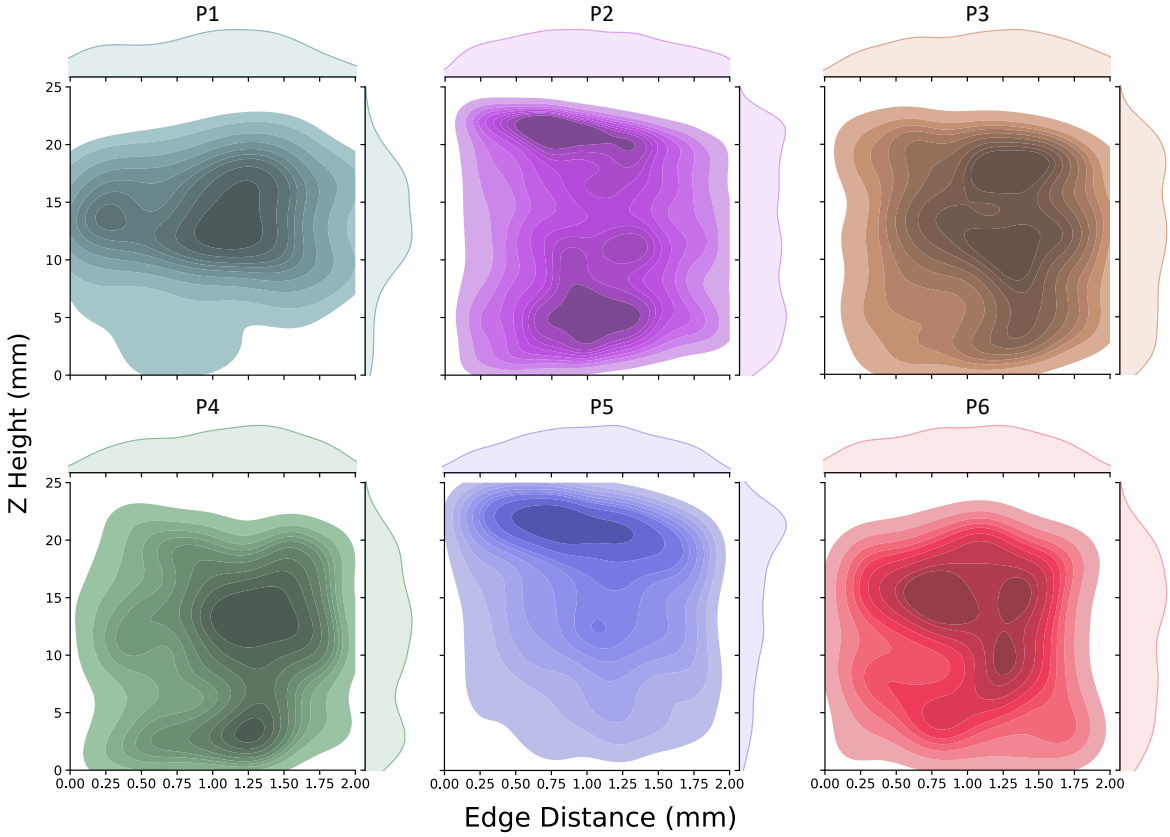

Fig. 4.2: The frequency of pores within a single coupon from each participant.

To compare porosity between multiple coupons across the build space, the distributions of each coupon are represented by its average pore diameter, average pore sphericity, and the number of pores with effective diameter larger than 0.125 mm. Reducing the porosity distributions of each coupon to three scalar values facilitates the evaluation of differences between coupons as a function of the build space.

As described in Chapter 3, the build space was discretized into five zones (0 to 4) at two height levels (A and B) as previously shown in Figure 3.1. The distributions of average pore sizes are plotted as kernel density estimates for each participant and separated by the A and B levels in Fig. 4.3. For most machines, there is strong overlap between the distributions of the two height levels. However, for P6 there is a higher frequency of coupons with larger average diameter in the A level than the B level.

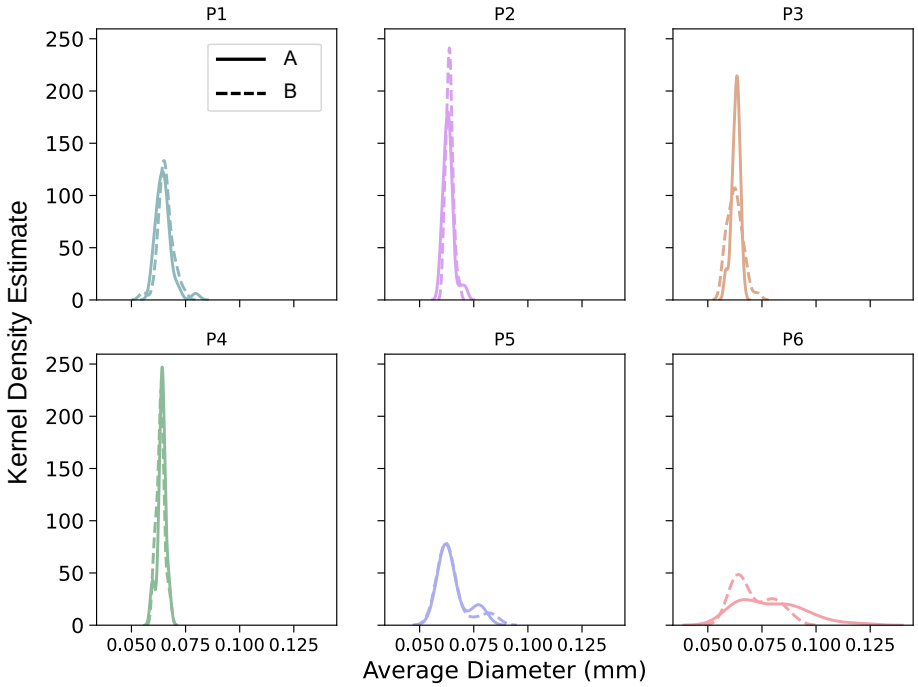

Fig. 4.3: Kernel density estimates showing the frequency of pore sizes present at the A and B height levels for each participant.

To explore this further, the average diameter, average sphericity, and count of large pores are plotted in Fig. 4.4 as a function of the build height for each participant. The annotated labels indicate significantly different pairs identified by one-way ANOVA tests with probability $p < 0.05$. As evident from the distributions, the metal of P6 exhibited significant differences in pore characteristics between the A and B levels. This was true for the average pore size and number of

large pores, whereas the average sphericity was statistically similar between levels. Thus, in general, variation in porosity with build height can largely be ignored, as five of the six machines had no significant differences in the porosity. The cause for the differences in porosity with height of P6 requires further scrutiny.

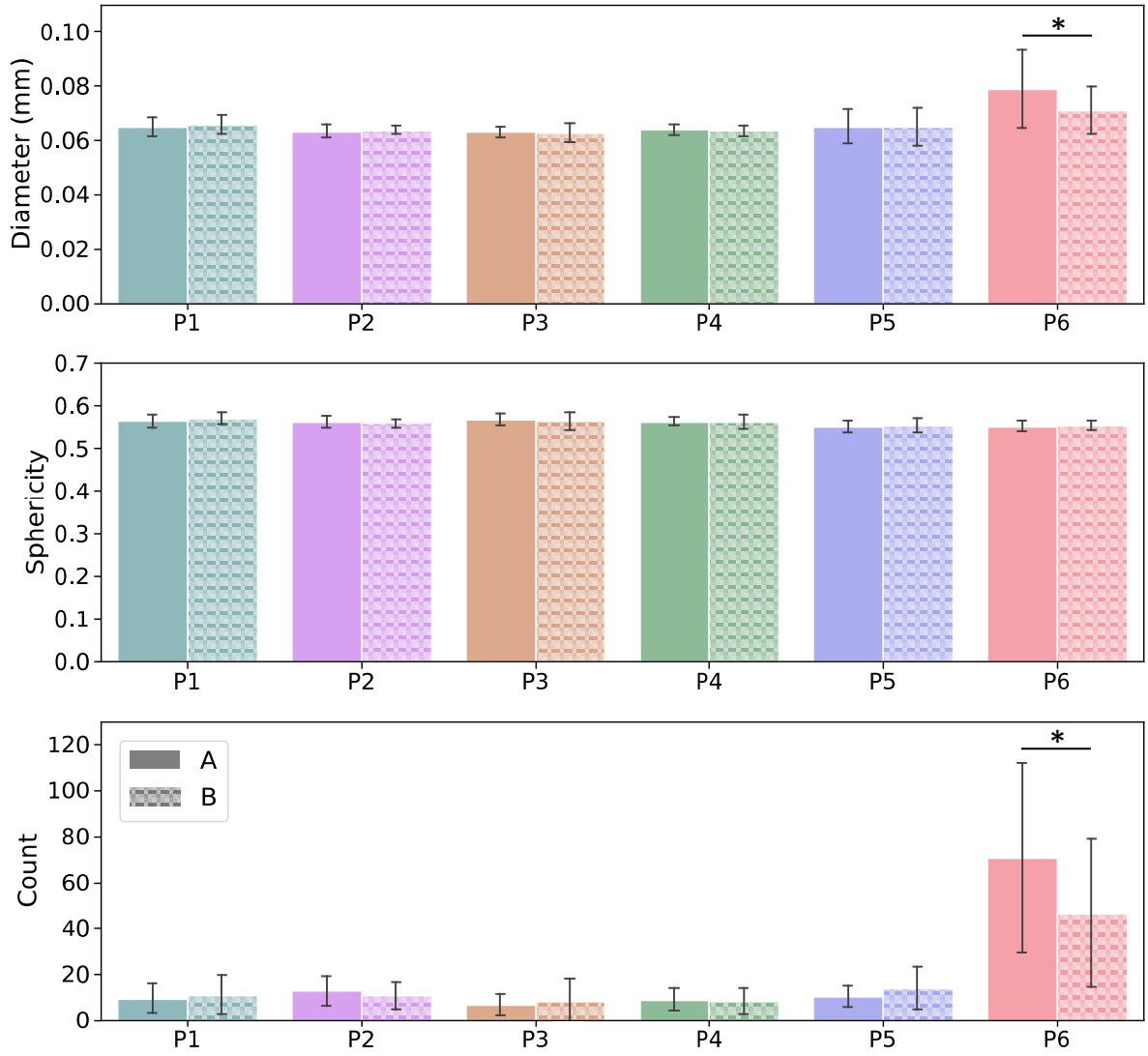

Fig. 4.4: Average diameter, average sphericity, and number of large pores as a function of the build height for each participant.

Spatial variability across the x- and y-axes is considered first by performing a zonal analysis. Due to the low sample size present in each zone for a given participant (i.e., 12 coupons), the data will not be presented as continuous distributions. Instead, the average values of the pore characteristics from each zone are plotted for each participant in Fig. 4.5. For P1-P5, results for the A and B height levels are grouped together for the analysis. Since the pore characteristics were identified to be statistically different for P6 across the two levels, each level is plotted separately for their machine and labelled as P6A and P6B. According to a one-way ANOVA, the metal of P1 and P3 have significant differences between zones for the average pore diameter. Furthermore, P2 and P6B have significant differences between zones for the pore sphericity, and P2, P3, P5 and P6A have differences in the number of large pores ($d \geq 0.125$ mm) per coupon between zones.

Ad-hoc Tukey tests were performed and reveal which zones are statistically different from the others and are annotated in Fig. 4.5. Zone 4 is frequently identified as an outlier, which is due to significantly larger pores than other zones for P1 and P3, and highest and lowest sphericity for P2 and P6B, respectively. The results are more sporadic for the number of large pores; Zones 1-4 contain the greatest number of large pores, but there is no apparent consistency among results for the different machines. However, Zone 0 never contains the highest frequency of large pores. Furthermore, the trends seen in the data of P6 are similar for both the A and B levels. Based on this consistency, the data from the two levels will be combined for the remainder of this chapter to increase the sample size.

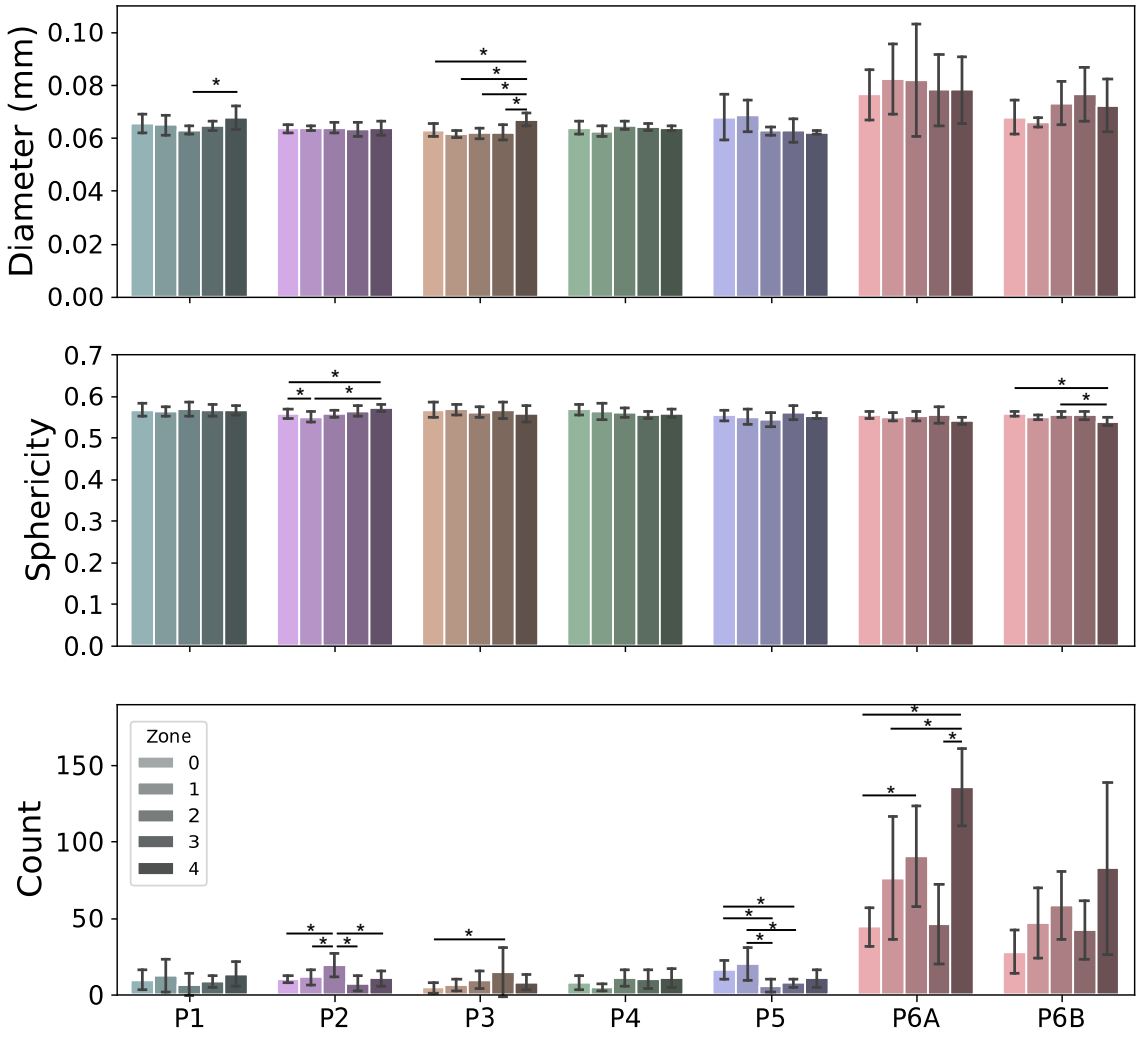

Fig. 4.5: Average pore diameter, sphericity, and number of large pores for each participant as a function of the zone.

It is prudent to perform an analysis of the x- and y-position dependency on a more granular level to discern the nature of the zonal differences. To investigate the potential spatial variation in pore distribution in terms of the x- and y-location further, the porosity metrics are plotted as a function of each coupon's positional coordinates according to the coordinate references in Fig. 4.6. These properties are plotted against the x-axis location of the coupons in

Fig. 4.7 for each participant. Shown are the pore diameter, sphericity and the number of large pores. A second-degree polynomial regression was performed on the data. For most machines, there is no trend in any of the porosity metrics as a function of position on the x-axis. However, the porosity of metal from P6 does show a strong parabolic relationship. The smallest average pore diameter and lowest number of large pores exists in the center of the x-axis for their machine, which corresponds to the center of the build plate; the largest diameter porosity is found at the edges of the build plate (Fig. 4.6) with the smallest and largest coordinate in x. Interestingly, the inverse relationship is seen for the sphericity, with the highest sphericity of pores identified in metal from the center of the build plate.

A similar representation of the data is shown in Fig. 4.8 for the porosity as a function of position along the y-axis. Akin to its distribution with x, the metal of P6 exhibits a strong parabolic relationship between porosity and position along the y-axis. The lowest porosity metal comes from the center of the build plate, and gradually worsens towards the edges. P3 and P4 appear to show a similar, but weaker trend in the sphericity.

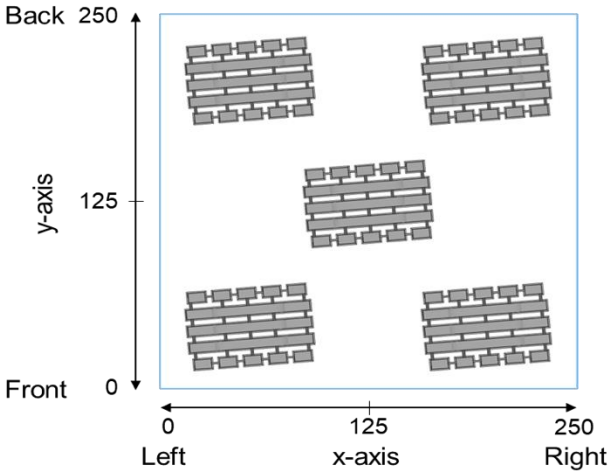

Fig. 4.6: Schematic showing the alignment of the x- and y-axes with build space.

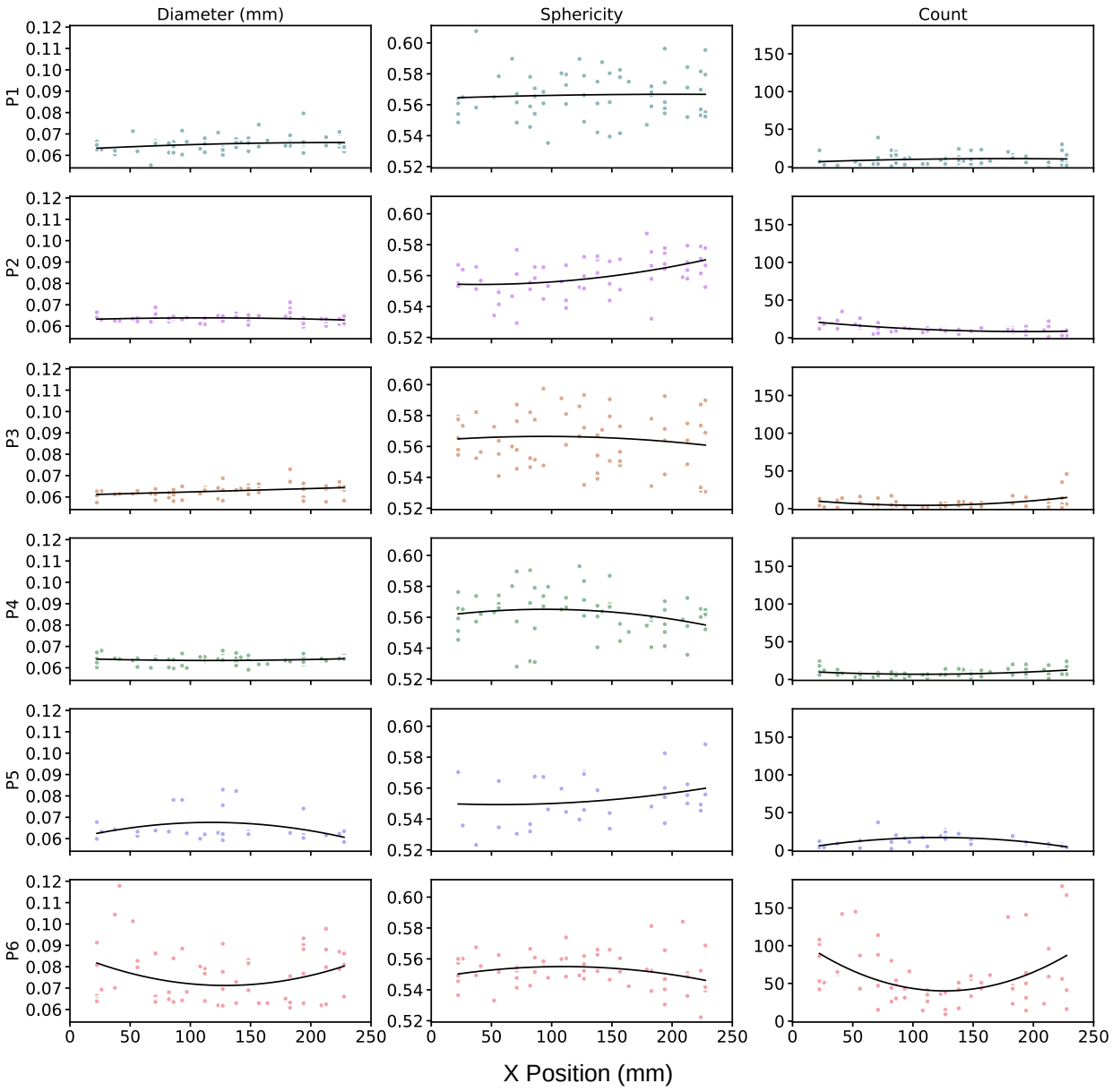

Fig. 4.7: Average diameter, average sphericity, and count of large pores per coupon ($d \geq 0.125$ mm) as a function of the x-axis position of each coupon. Each row contains the data for one participant. Polynomial regression was applied, and the best fit lines are shown.

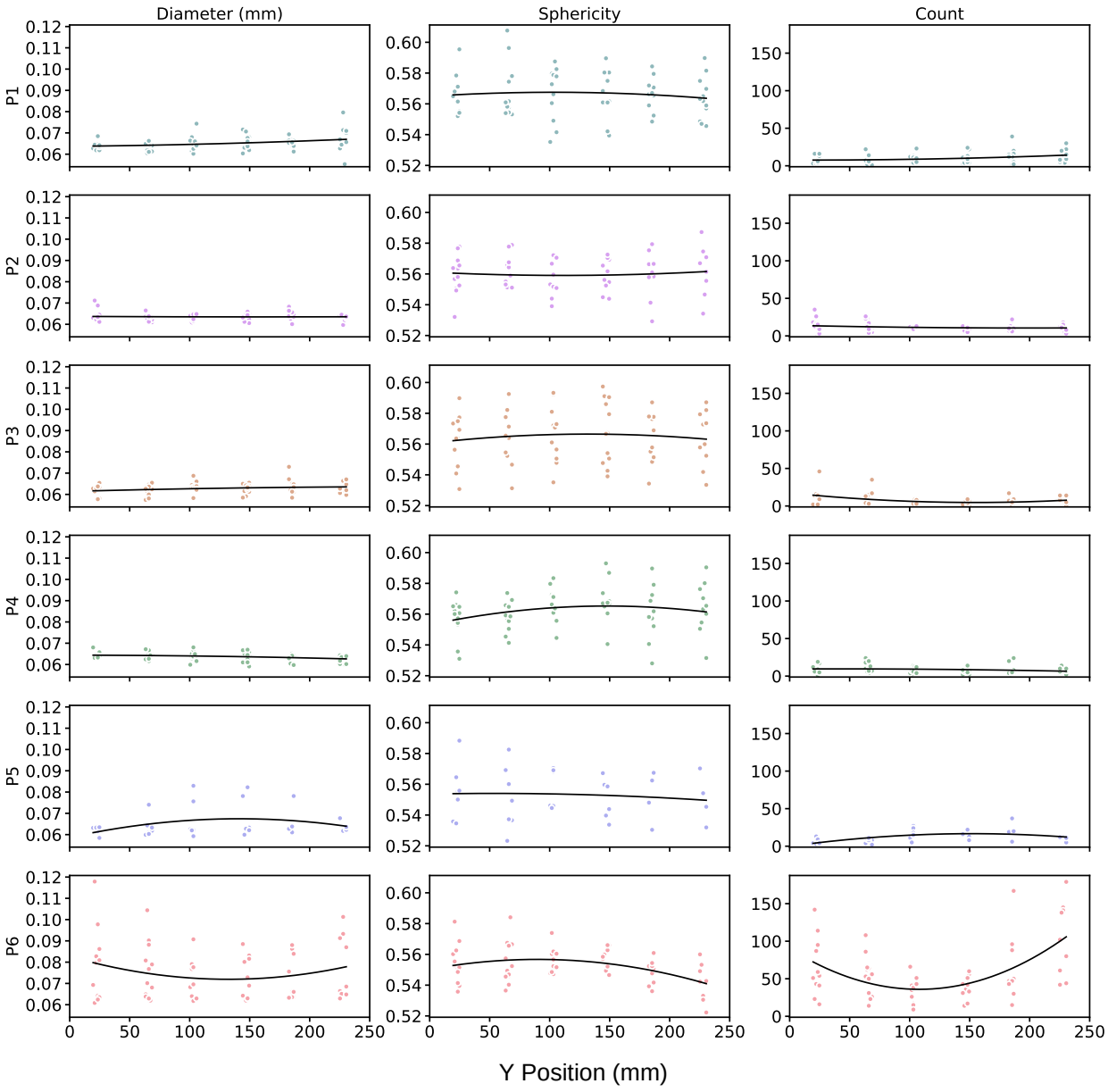

Fig. 4.8: Average diameter, average sphericity, and count of large pores per coupon ($d \geq 0.125$ mm) as a function of the y-axis position of each coupon. Each row contains the data for one participant. A second order polynomial regression was applied, and the best fit lines are shown.

During development of the µCT method, 40 vertical coupons from P1 were scanned in the unmachined condition. These coupons provide a higher degree of x/y spatial granularity than

that presented in Fig. 4.7 and Fig. 4.8 since they include scans of all vertical coupons from Zones 1 and 2 and within both the A and B height levels. In reference to the distribution of these coupons with respect to the machine, the two rows of vertical coupons are referred to as the front and back sets of each zone, as illustrated in Fig. 4.9. An analysis of these coupons revealed that there are some zonal differences in porosity content. When considering just the 100 largest pores per coupon (Fig. 4.10), the distribution for level A of Zone 2 is bimodal, whereas the other zones have distributions that are closer to gaussian. It is noteworthy that this representation reveals that coupons from the front row of Zone 2 often have larger pores than the back row. Performing the same analysis for the sphericity shows that level A of Zone 2 has a concurrent decrease in pore sphericity from the back to the front regions. It is notable that the results of this analysis were dependent on the porosity metric used for the evaluation. The use of average diameter or sphericity including all pores for each coupon (rather than the largest 100) did not show the same distinction between the front and back rows of coupons.

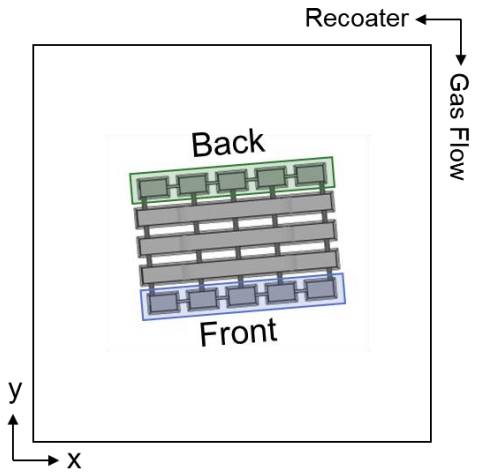

Fig. 4.9: Schematic depicting the front and back notation of the two rows of vertical coupons within each zone. The x- and y-axes are shown with the gas flow and recoater directions for reference.

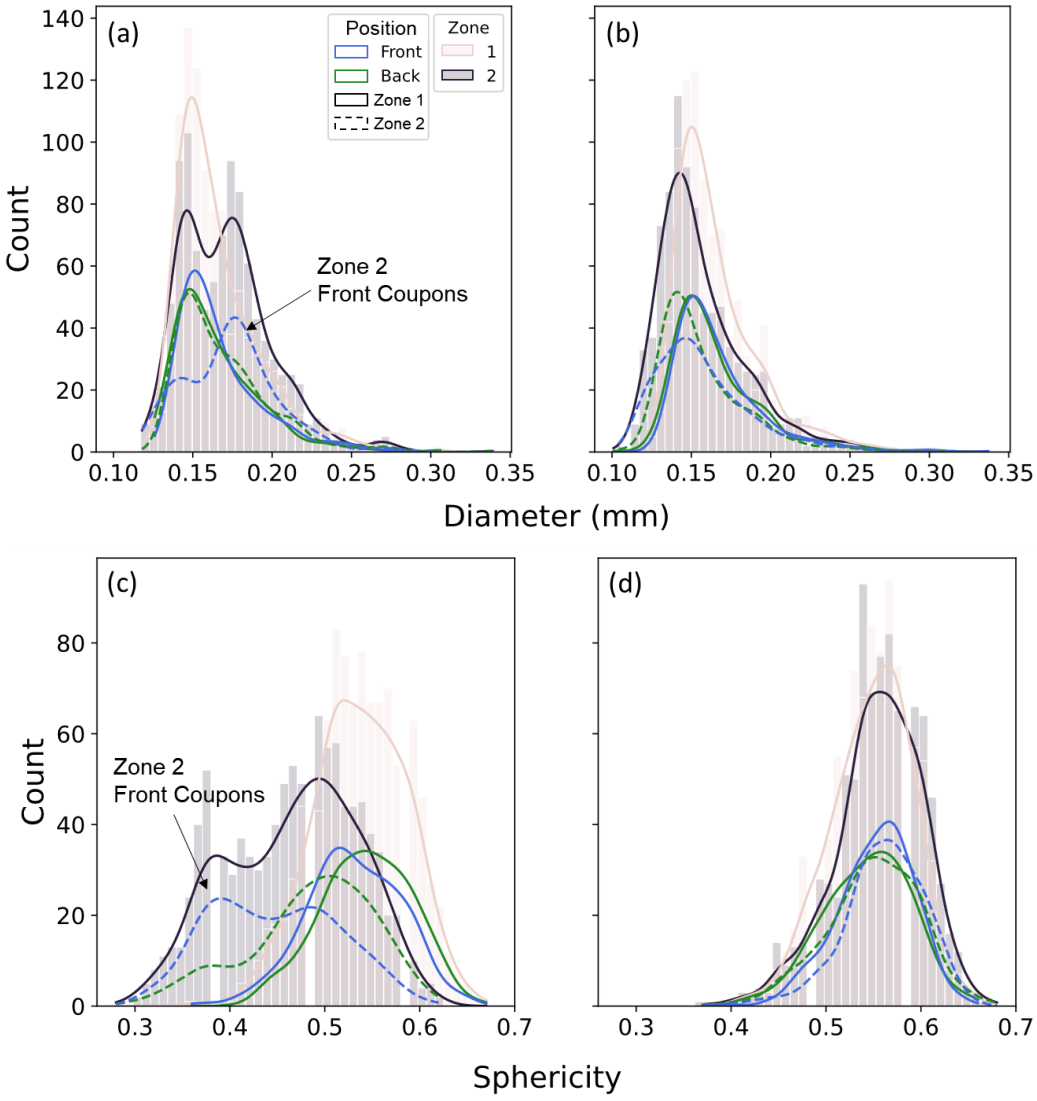

Fig. 4.10: Histograms showing the diameter of the 100 largest pores from each coupon from Zones 1 and 2 for the A (a) and B (b) levels. Each plot contains smooth curves fitted to the overall size distribution from each zone. Fitted curves are also shown for a further subdivision of the data corresponding to the position of coupons within the front or back row of each zone. Similar results are shown for the sphericity in (c) and (d). Results are for metal from P1.

Previous work has shown that pores can form preferentially near the surface of PBF parts [74]. To determine if this trend applies to results of this study, and if it could be the cause of the phenomena observed in Fig. 4.10, the distribution of pores was examined in a representative

coupon across the volume and as a function of distance from the surface. These results are shown in Fig. 4.11 (a) and (b) for before and after machining, respectively. Edge distances of 0 correspond to pores at the surface of the coupon, whereas higher values correspond to pores located closer to the center. The unmachined coupon in Fig. 4.11 has a high concentration of pores near the surface that are absent after machining. Excluding contributions of the near surface pores, the larger number of detected pores in the as-built coupon could be due to x-ray beam scattering that result from the rough surface of the coupon and cause increased false readings.

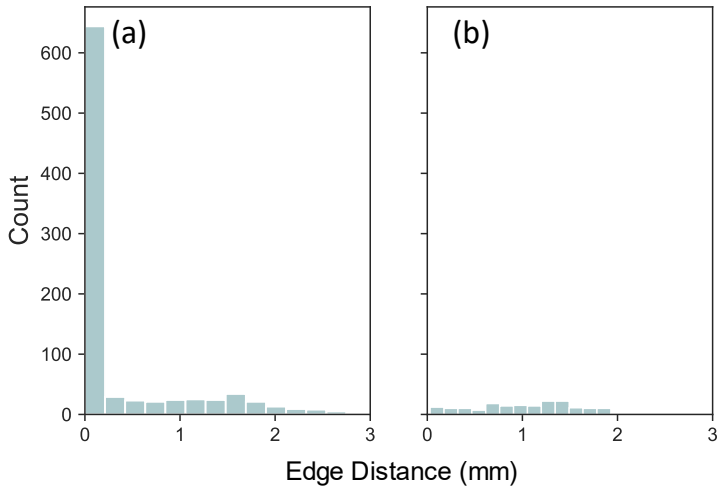

Fig. 4.11: Frequency of pores as a function of their distance to the nearest free surface for a coupon before (a) and after (b) machining.

Given the large number of near surface pores that are removed by machining, the results of Fig. 4.10 were further analyzed to determine if those pores were responsible for the trend in Zone 2. The porosity distribution from each coupon was modified to exclude pores located within 0.5 mm of the surface to mimic the machining process and then replotted. These results are shown in Fig. 4.12 and exhibit the same bimodality as seen for Level A of Zone 2.

Furthermore, while less prominent, the back row of Level A of Zone 2 also shows a secondary peak of larger porosity and lower sphericity.

The aforementioned analysis was repeated for the machined metal of each participant. Due to the significantly smaller sample size in each zone (two versus ten coupons), the data was grouped across the two heights and all six builds. The average pore diameter and sphericity for the largest 100 pores per coupon were found and grouped according to their zone and whether they were in the front or back position. One-way ANOVAs were performed for each participant, and no significant differences were found within any of the zones. The data was also separated by level based on the results of Fig. 4.10, and no statistical differences were observed. Bar plots presenting results of this analysis can be found in Appendix B.

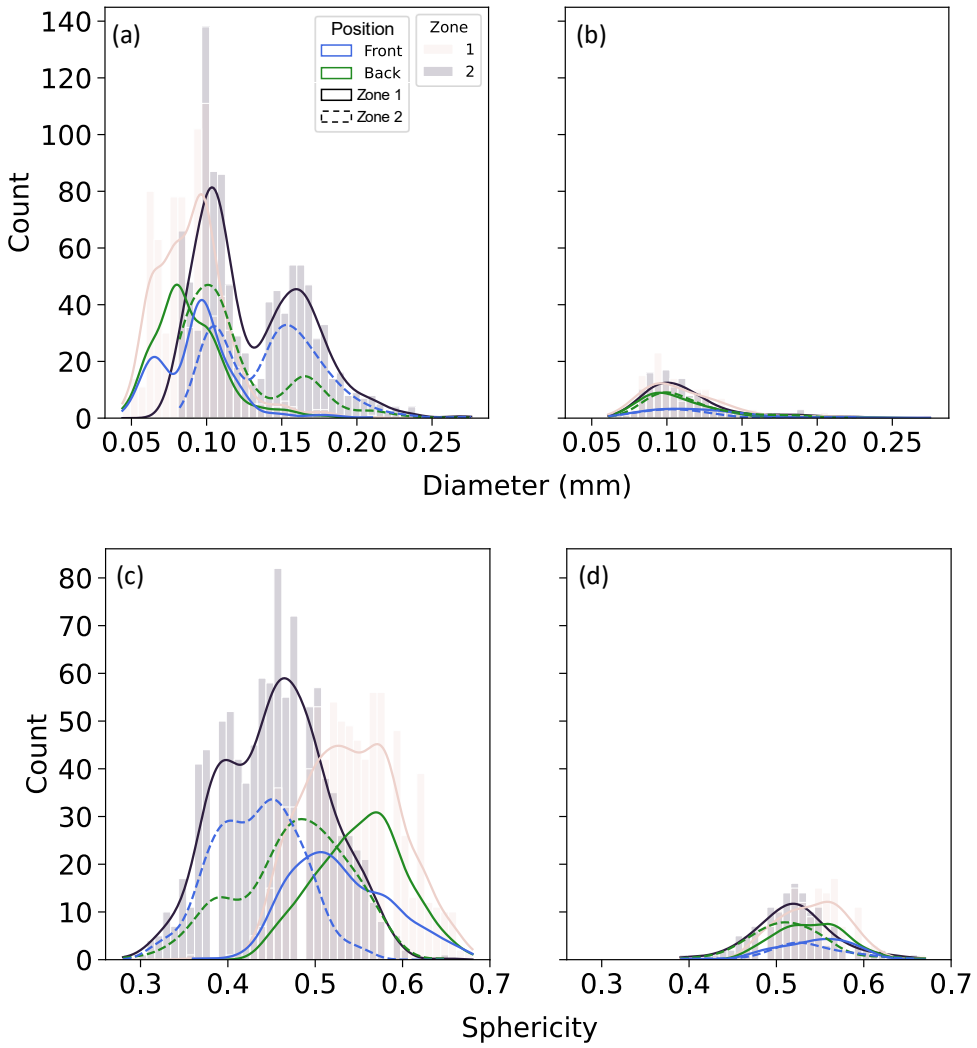

Fig. 4.12: Histograms showing a sampling of the diameter of the 100 largest pores at least 0.5 mm from the surface from each coupon from Zones 1 and 2 for the (a) A and (b) B levels. Each plot contains smooth curves fitted to the overall distribution from each zone. Fitted curves are also shown for a further subdivision of the data corresponding to the position of coupons within the front or back row of each zone. Similar results are shown for the sphericity in (c) and (d).

To summarize, the variability in pore characteristics and porosity were analyzed as a function of the build space. Although the metal from most participants was similar across the z-axis of the build space, one consistent trend was the higher quality metal produced in Zone 0. The center of the build plate generally had the smallest average pore size of the five zones for

most machines. However, the metal of P6 was unique from that of the other machines. In addition to the larger pore sizes, which will be explored further in Chapter 6, their machine also exhibits the greatest spatial variability, with strong parabolic relationships observed across the width and depth of the build envelope. Metal in the center of the build plate had the smallest and most spherical pores, as well as the lowest average pore size, while the edges had larger and less spherical pores. Simultaneously, their porosity showed a z-height dependency, with larger pores located in coupons of the A level. Thus, although some spatial variability in porosity distributions was observed in most M290s, it was most pronounced for P6.

4.1.2. Tensile Testing

Similar analyses to those performed with the porosity were performed to understand the spatial variability in the mechanical properties of the metal. To understand how the tensile properties are distributed (i.e. normally, skewed, etc.), the complete property distributions are plotted as kernel density estimates for the vertical and horizontal coupons of each participant. The YS, UTS, and strain at failure are shown in Fig. 4.13, Fig. 4.14, and Fig. 4.15, respectively, as a function of the build height. From these plots it is observed that the property distributions of most machines are approximately gaussian in shape. However, many of the distributions display some level of skewness. Regarding strength, the distributions are frequently positively skewed. The metal of P3 exhibits prominent skewness in strength as evident in Fig. 4.13 and Fig. 4.14. The strain at failure of the vertical coupons, on the other hand, is negatively skewed for many of the machines. With regard to the effect of height level, most machines do not show a large difference in the shape of distributions between the A and B levels. The largest differences are observed in the strength of P2 and the strain at failure of P6.

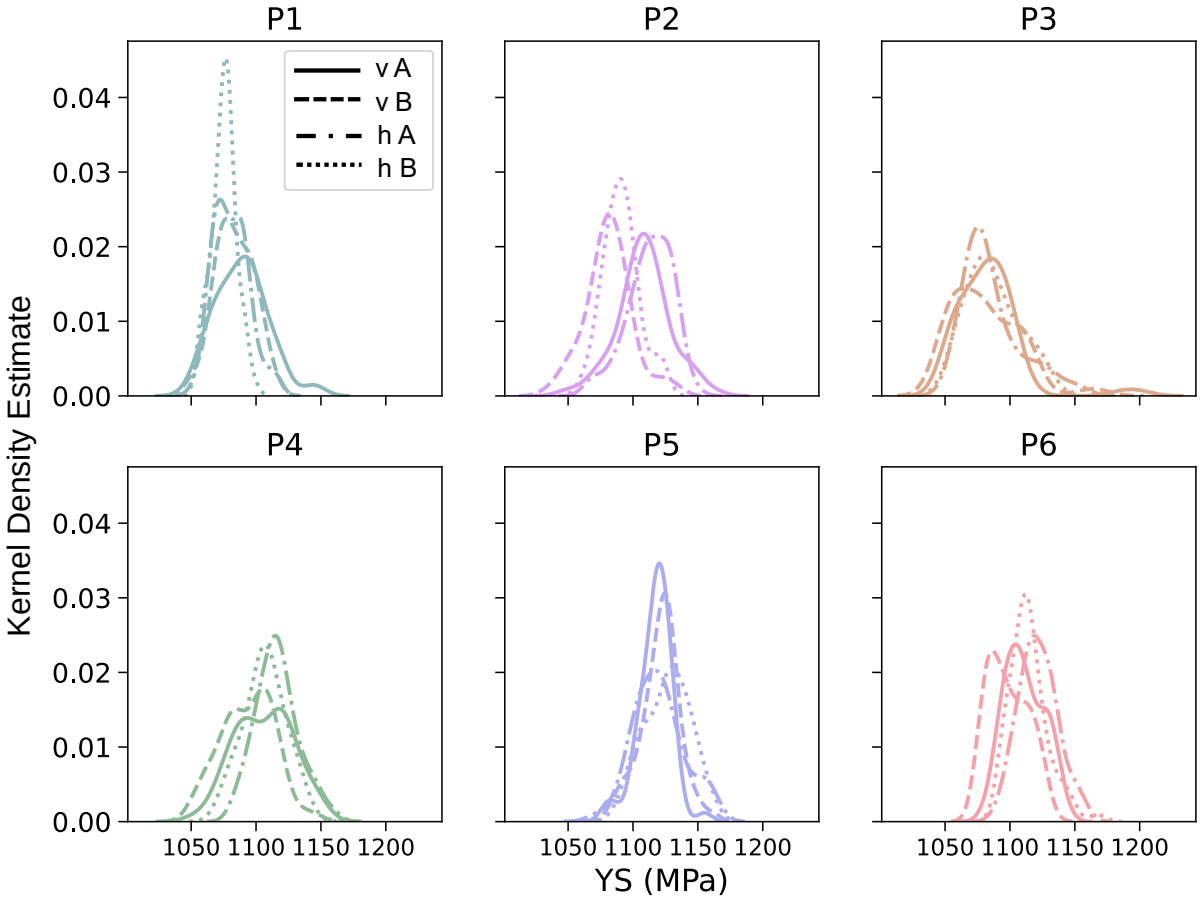

Fig. 4.13: YS distributions for the horizontal and vertical coupons of each participant, separated by height level.

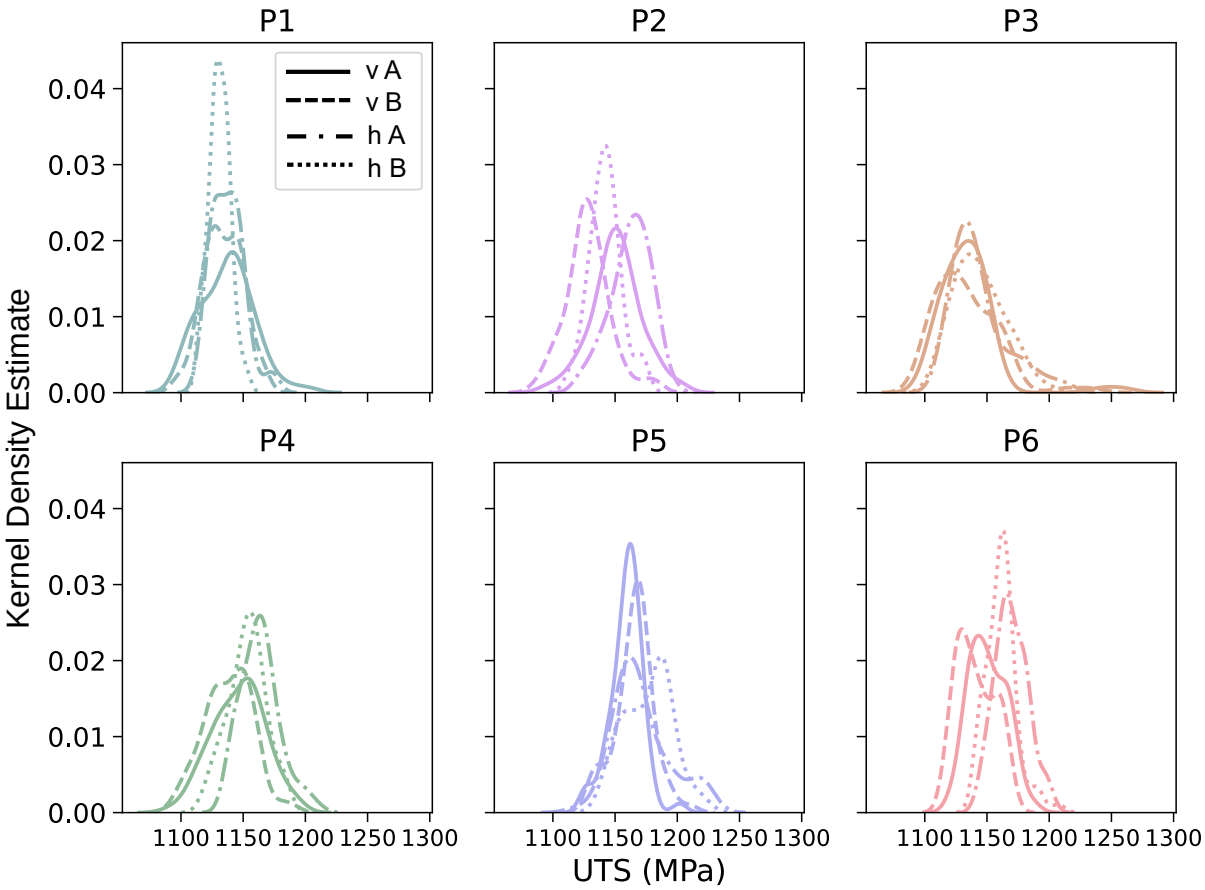

Fig. 4.14: UTS distributions for the horizontal and vertical coupons of each participant, separated by height level.

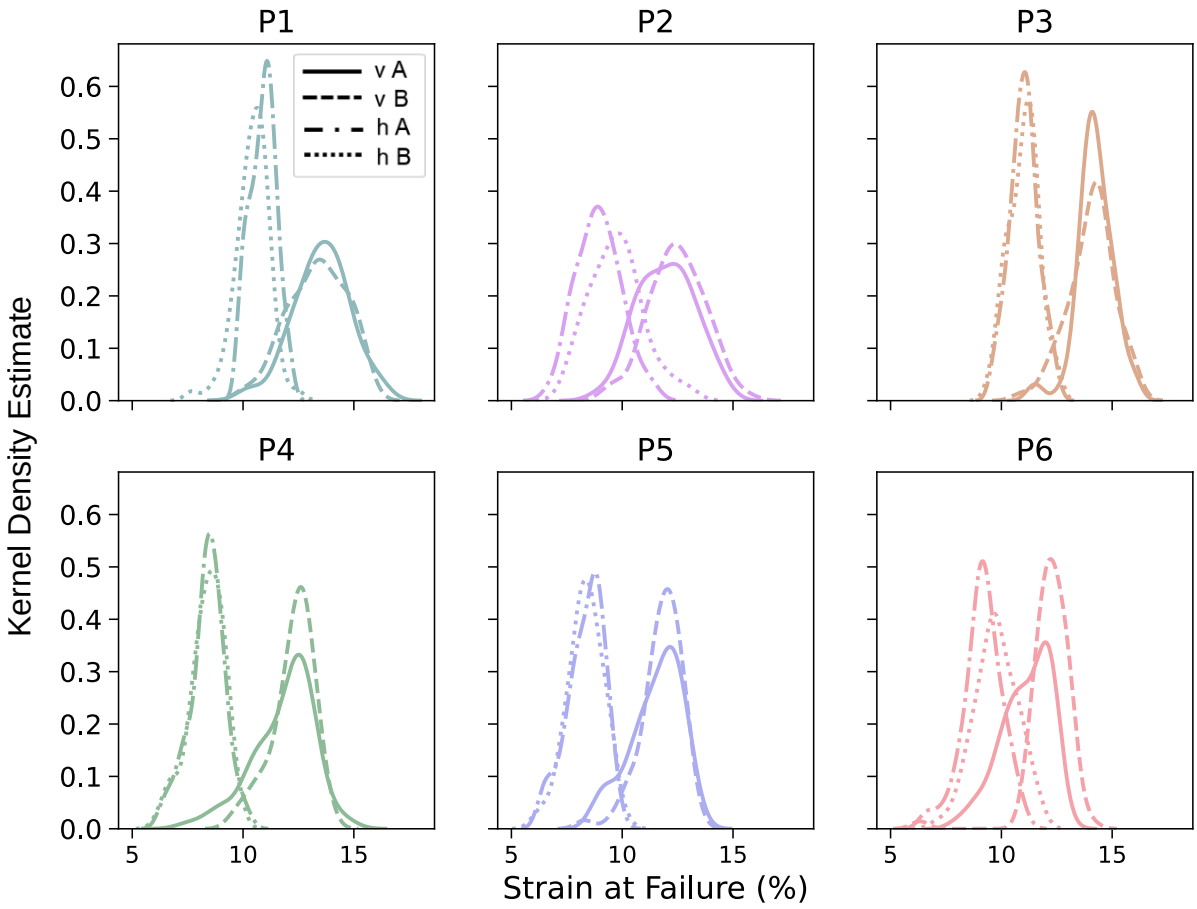

Fig. 4.15: Strain at failure distributions for the horizontal and vertical coupons of each participant, separated by height level.

A comparison between the mean values of YS, UTS and strain at failure of metal from the A and B levels is shown in Fig. 4.16 and Fig. 4.17 for the vertical and horizontal coupons, respectively. One-way ANOVA results are annotated on each figure. Overall, the mechanical properties of the vertical coupons are very consistent. Although there are significant differences in the YS and UTS between the A and B levels for some machines, the difference is very small, with differences of approximately 12 and 10 MPa, respectively. Furthermore, significant differences in the strain at failure between the levels are only present for the metal of P4 and P6.

For those two machines, the difference in strain at failure is approximately 1%. The YS and UTS of the horizontal coupons from the A and B levels are significantly different for most participants. However, as with the vertical coupons, the magnitude of the difference is very small, with averages of approximately 9 and 8 MPa, respectively. There are fewer significant differences for the strain at failure of the horizontal coupons than the strength, with half of the participants showing no statistical difference between the A and B levels.

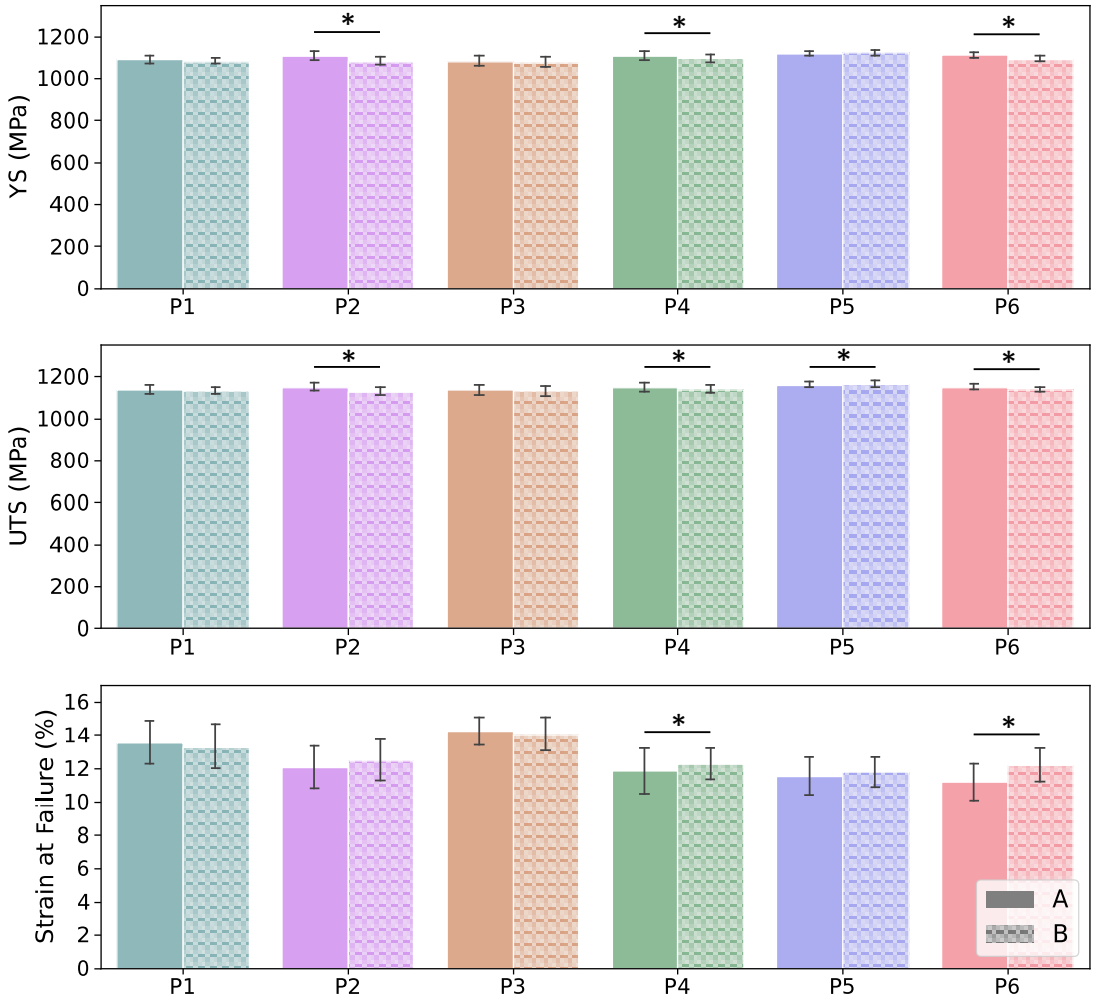

Fig. 4.16: YS, UTS, and strain at failure of the vertical coupons as a function of the build height for each participant.

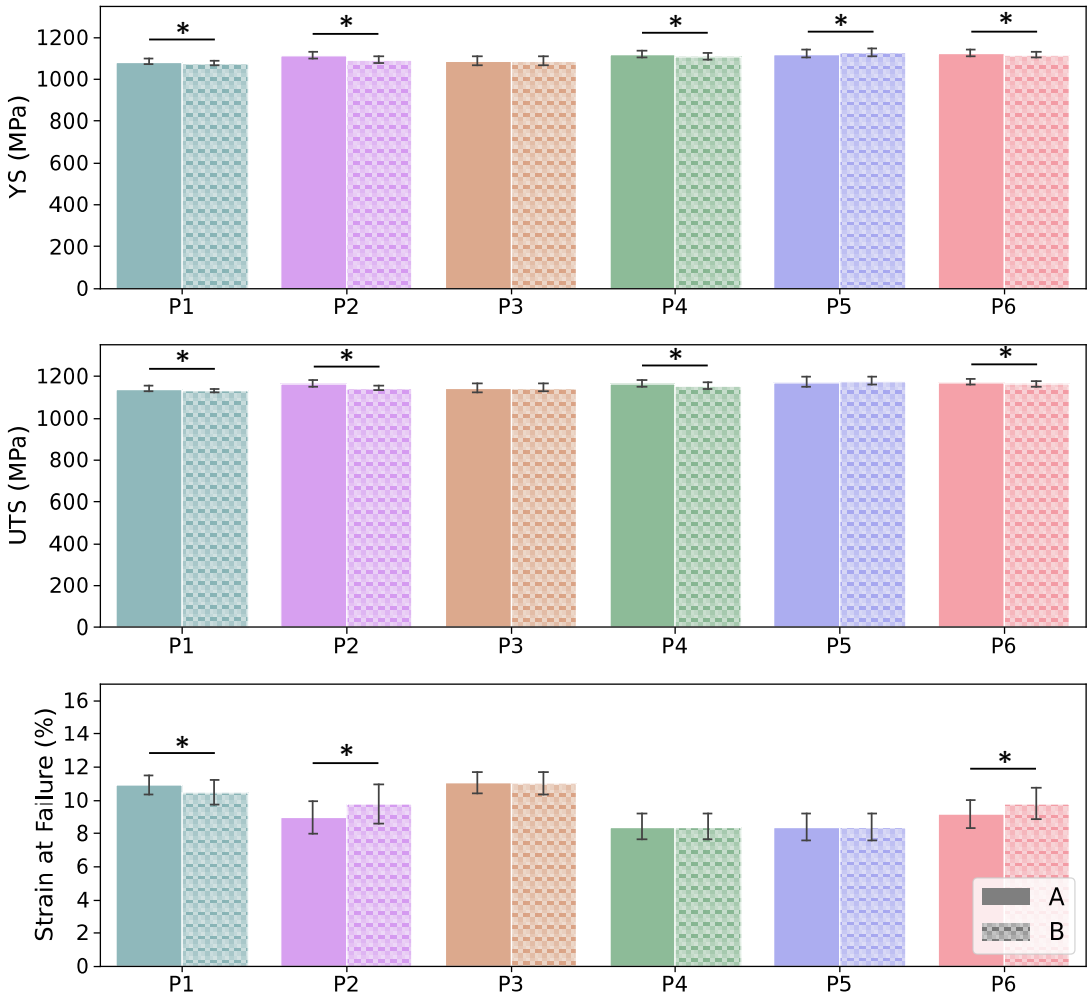

Fig. 4.17: YS, UTS, and strain at failure of the horizontal coupons as a function of the build height for each participant.

The zonal variations in mechanical properties of the metal are shown in Fig. 4.18, Fig. 4.19, Fig. 4.20, and Fig. 4.21. Due to the small differences in magnitude between the A and B levels for the YS and UTS, the heights are pooled to create a larger sample size for the vertical and horizontal coupons in Fig. 4.18 and Fig. 4.20, respectively. However, the strain at failure had larger differences between the heights for several machines. Therefore, the statistical analysis is performed independently for the A and B levels, with the vertical and horizontal coupons

represented in Fig. 4.19 and Fig. 4.21, respectively. For the vertical orientation, results from one-way ANOVAs reveal that there were significant differences in the YS and UTS of the metal across zones from P1 and P3. However, there were no significant differences in the strain at failure across zones for any participant at either height level. For the horizontal coupons, significant differences in the YS were observed across zones for the metal of P1, P3, P5 and P6. For the UTS there were significant differences across zones for P3 and P5, and in the strain at failure for P2 in the A level and P6 in the B level.

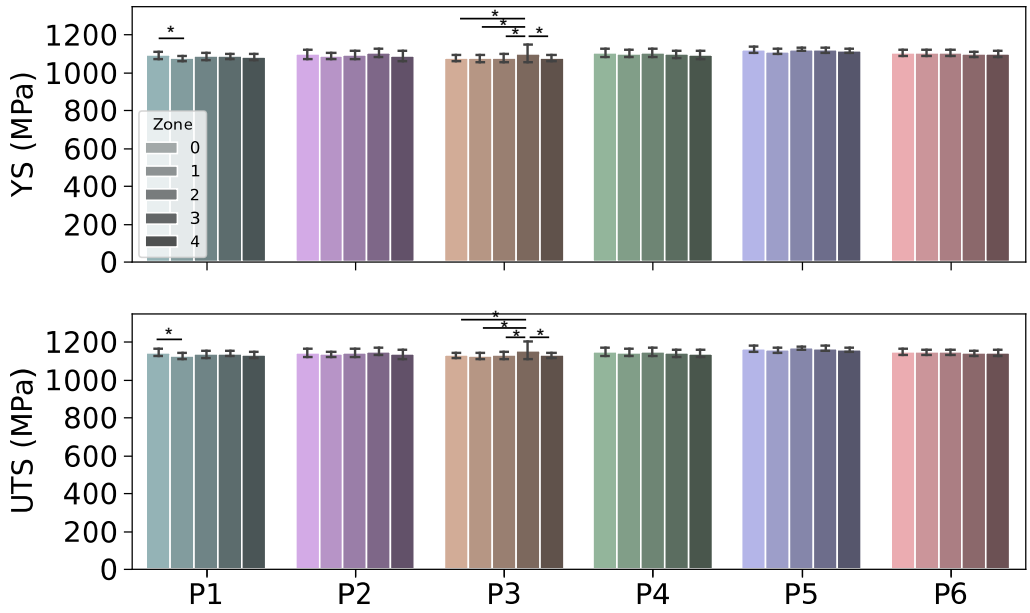

Fig. 4.18: YS and UTS of the vertical coupons for each participant as a function of the zone.

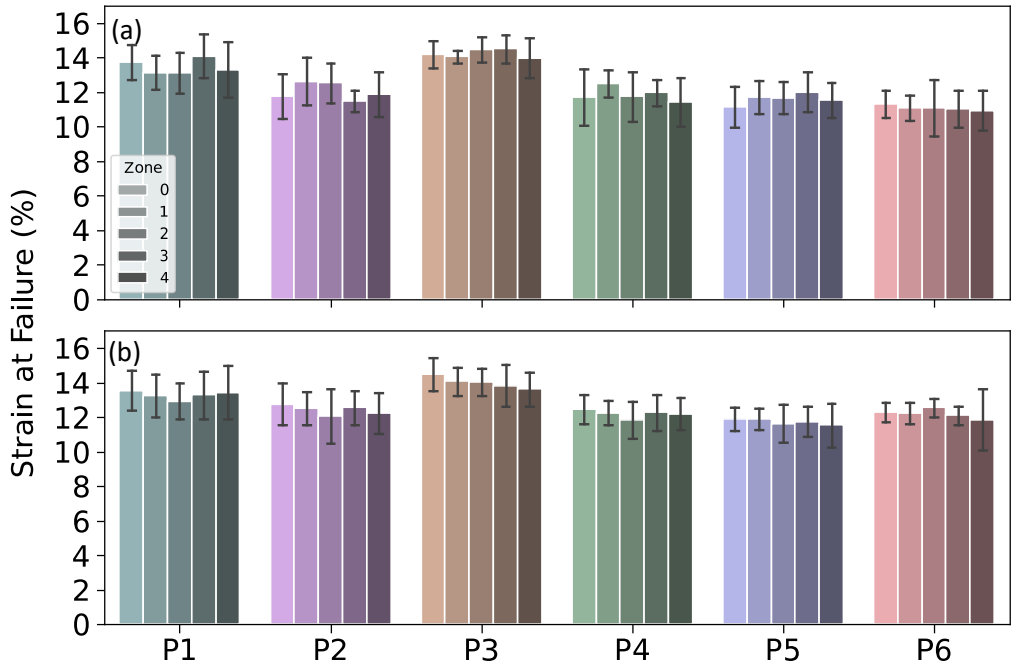

Fig. 4.19: Strain at failure of the vertical coupons for each participant as a function of the zone for the (a) A and (b) B height levels.

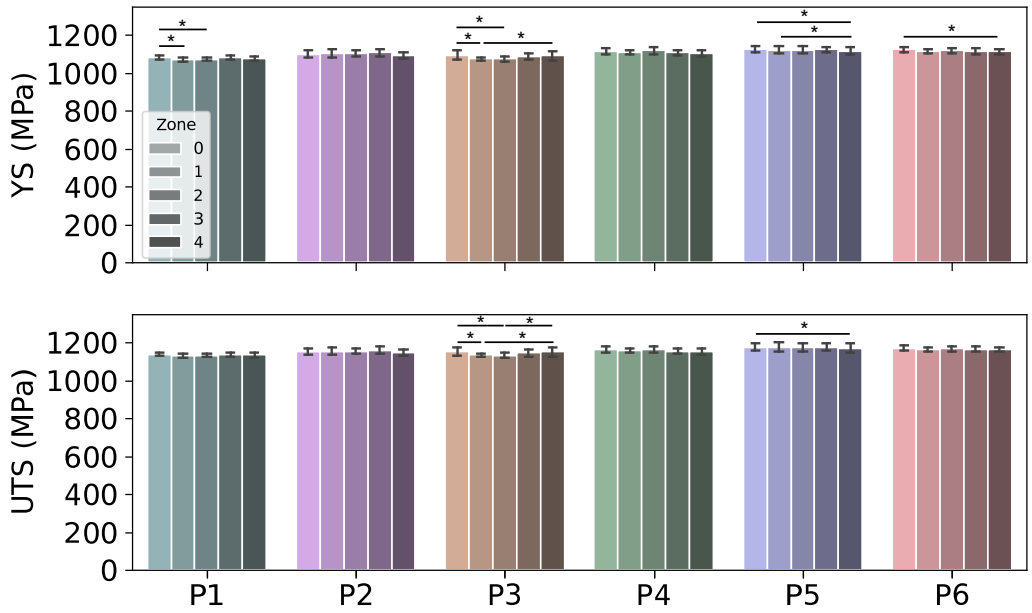

Fig. 4.20: YS and UTS of the horizontal coupons for each participant as a function of the zone.

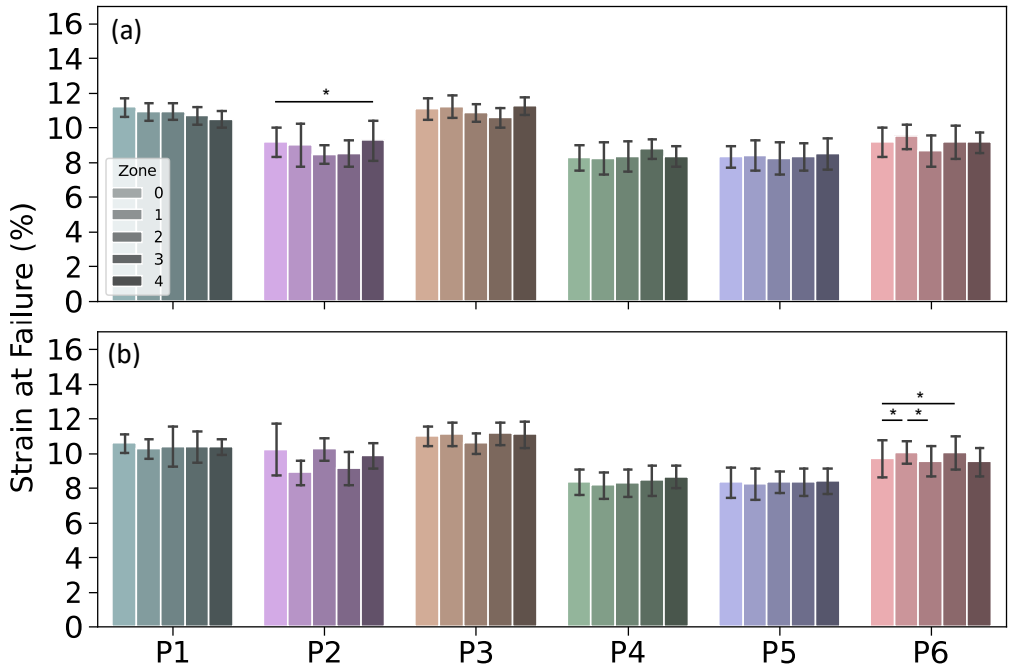

Fig. 4.21: Strain at failure of the horizontal coupons for each participant as a function of the zone for the (a) A and (b) B height levels.

The spatial variability in mechanical properties was characterized with more refined positional resolution using results from the vertical coupons. The horizontal specimens could not be evaluated with the same resolution for two reasons. First, because the horizontal coupons are stacked in the z-direction in a 3 x 3 array, the number of discrete x,y coordinates they occupy is only three per zone, in comparison to ten for the vertical coupons. Consequently, the number of positions sampled on the build plate is limited. Second, the horizontal coupons were located in the center of each build zone (an oversight in the build design), resulting in tight clusters of their x,y positions. As a result, the zonal analysis captures most of their spatial variability. For completeness, he horizontal coupon responses are included in Appendix B for reference.

Mechanical property distributions for the vertical coupons are plotted as functions of the x- and y-axes in Fig. 4.22 and Fig. 4.23, respectively, with polynomial fits applied. The mechanical properties of metal from most participants does not show strong correlations with the x-axis. The strongest relationships were found in the YS, UTS and strain at failure of metal from P1, the YS and UTS of metal from P4, as well as the strain at failure of P6. In all three cases, there is a weak parabolic relationship between the properties and the x-location. Consistently observed in the metal of these three participants, the highest properties are found in the center of the build plate, while the lowest properties are found on the outskirts. However, the metal from P3 follows a different trend, with the right side of their build plate containing several outliers with high strength. Despite these outliers, there is no overall trend in their data.

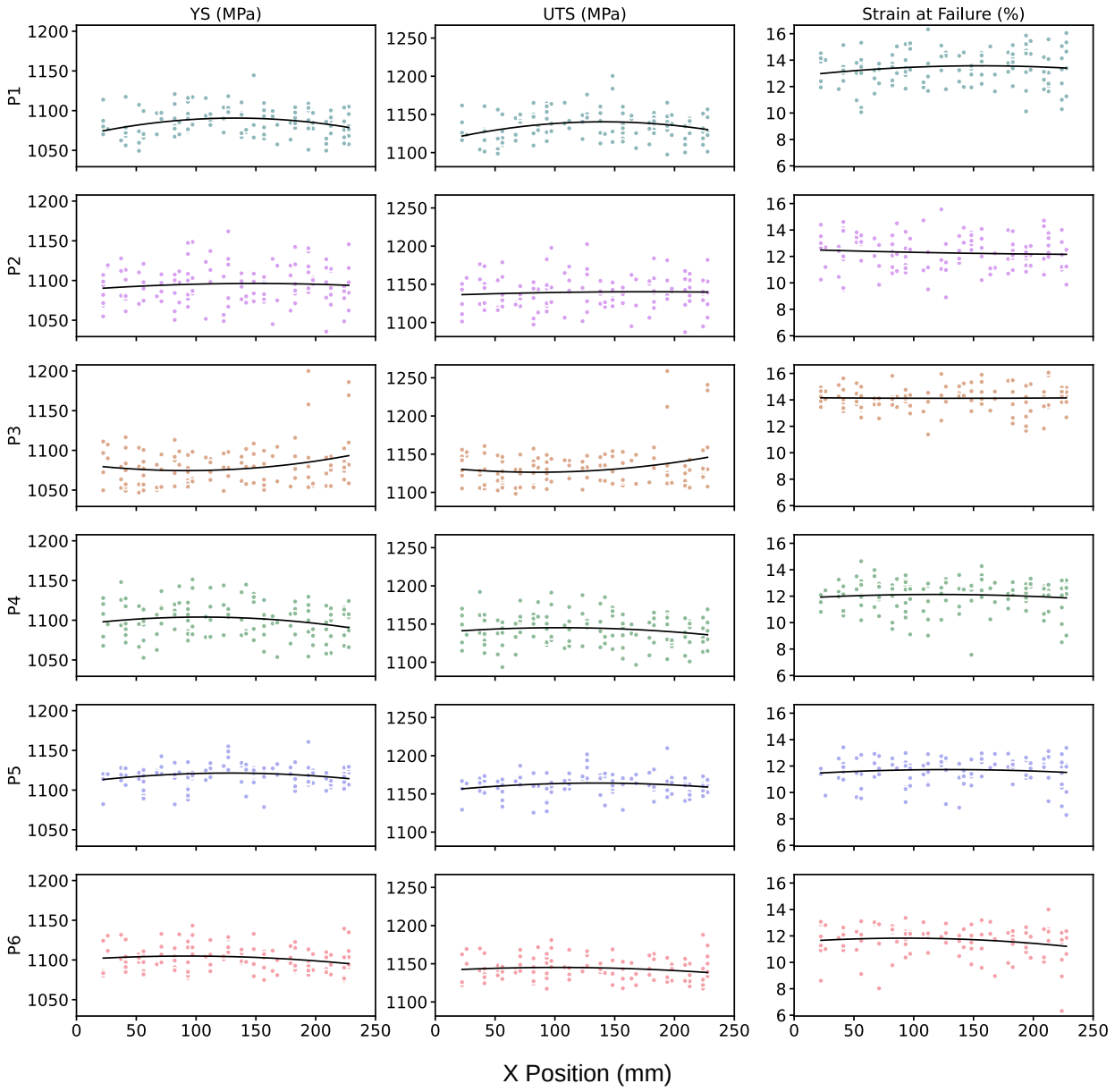

Fig. 4.22: The YS, UTS, and strain at failure distributions of metal with vertical orientation as a function of the x-axis position of each coupon. Each row contains the data for one participant. Polynomial regression was applied, and the best fit lines are shown.

Regarding the property distributions with respect to the y-axis, the trends are similar, with metal from P1 and P6 having the strongest parabolic relationship between location and performance. As noted in the property trends for the x-axis, coupons from the center of the y-axis appear to have the highest strength and ductility.

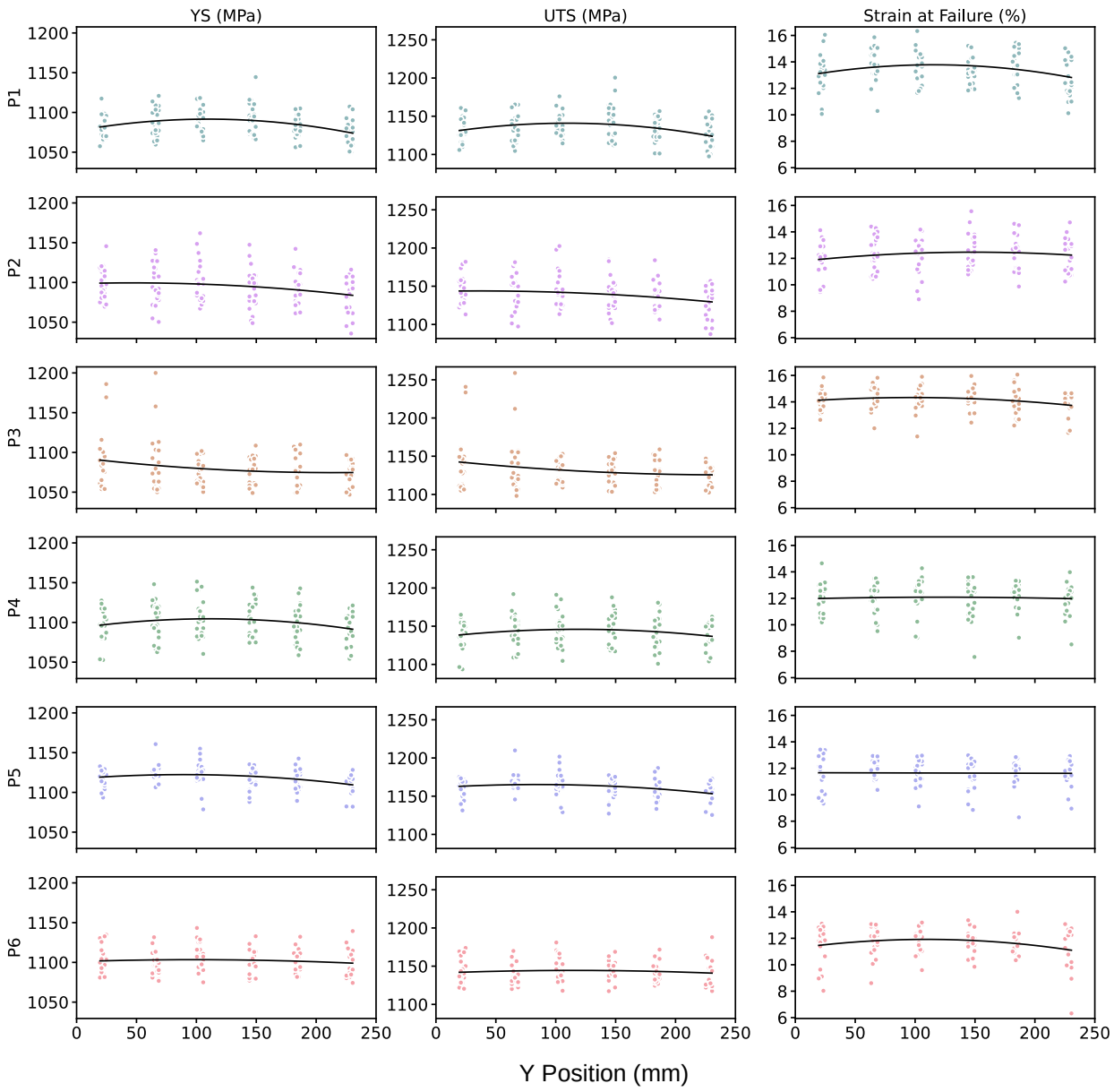

Fig. 4.23: The YS, UTS, and strain at failure distributions of metal with vertical orientation as a function of the y-axis position of each coupon. Each row contains the data for one participant. Polynomial regression was applied, and the best fit lines are shown.

Akin to the treatment of the porosity characteristics within individual zones (Fig. 4.10), a similar intra-zonal analysis was applied to the tensile properties. The mechanical property data of vertical coupons was separated according to their location within each zone, either in the front

row or back row. One-way ANOVA tests revealed only one case of significant differences between the front and back: P1's strain at failure in Zone 1. For brevity, the strain at failure of metal from P1 is shown in Fig. 4.24, while the YS, UTS and strain at failure for all remaining participants is found in Appendix B.

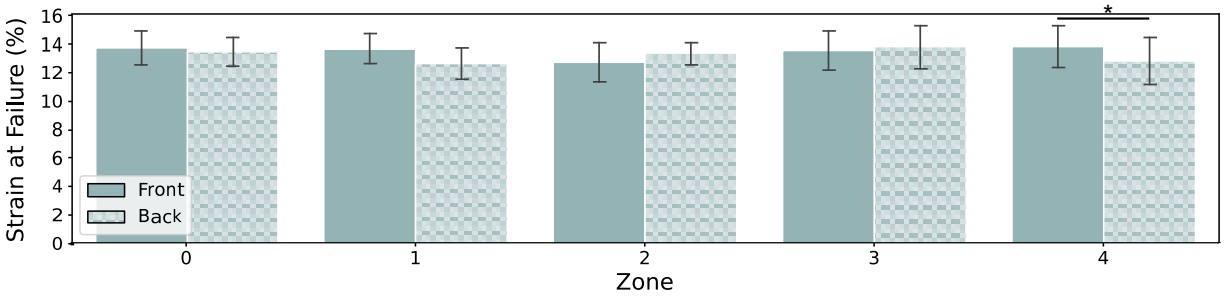

Fig. 4.24: The strain at failure of metal from vertical coupons of each zone for P1, separated by the front and back rows of coupons.

4.2. Discussion

The primary objectives of this chapter were to quantify the intra-build variability in metal quality and mechanical properties. The porosity distribution within individual coupons was considered first. It is essential as it is the first presentation of porosity data in this body of work, and it is important to the understanding the mechanical property distributions overall. The distribution of pore diameters for six representative coupons (i.e., one from each machine) shown in Fig. 4.1 reveal that most machines have an approximately gaussian distribution, albeit with a skew towards smaller pore diameters. However, the coupon from P6 has a non-gaussian distribution, containing a primary peak and a secondary region of large diameter pores. The presence of this second peak indicates there are two families of pores, which may have different formation mechanisms, an idea that will be explored later in this dissertation.

The location of pores within individual coupons is also significant. Pores located near the surface of a coupon can have a larger impact on crack initiation than pores located deeper beneath the surface. The location of pores within the same coupons shown in Fig. 4.1 were plotted in Fig. 4.2, which shows the frequency of pores along the z height of the gauge section as well as their distance from the nearest free surface. Most coupons have pores that are approximately evenly distributed throughout the coupon volumes. Although the coupon shown for P5 has an increase in pore frequency with z height, this is not representative of all coupons. Hence, overall, the pores in metal from all partners appear to be randomly distributed within the coupons.

With the distribution of pores within individual coupons established, the variability in porosity within the build space is considered. The variability was first evaluated as a function of the build height in Fig. 4.3 and Fig. 4.4. For most participants, the average diameter, average sphericity, and number of large pores (≥ 0.125 mm diameter) are similar between the A and B levels. A one-way ANOVA confirmed that the metal of P6 was the only one to exhibit a significant difference. Metal of the A level exhibited an average diameter 8 μm higher than the B level, and an average of 24 more large pores per coupon (+0.04 pores/mm^3), an increase of 52%.

With regards to the height dependency in P6's metal, there are two potential contributions of relevance, including heat accumulation and thermal lensing. The build plate serves as a heat sink for the deposited layers of molten metal. As the build height increases, the molten metal of each deposited layer is farther away from the build plate. As a consequence, heat from the laser must transfer through the previous layers of printed metal beneath it and the surrounding powder bed, which has lower thermal conductivity than bulk metal [75]. As the layers accumulate this may result in a gradual buildup of heat that could cause an increase in laser penetration depth due

to the higher intrinsic heat; it increases the potential for the development of pores through key-hole mode melting. However, this explanation seems unlikely as it would apply across the machines of all participants in the study.

Another potential cause is thermal lensing of the laser optics. Thermal lensing is a phenomenon in which the glass optics heat up during use [76]. The increased temperature results in physical deformation of the lens and a change of its refractive index; the combined effects act to decrease the focal length of the laser. Bean et al. observed that changes of the focal length by a few millimeters can have large effects on the porosity [46]. Even in the Hot Isostatic Pressed (HIP) condition, a heat treatment that can close most pores, porosity increased from 0.05 vol% to 0.43 vol% as the focal point was adjusted to three-millimeter out-of-focus.

If thermal lensing gradually accumulated with progression of the printing process, it could have caused a small change in the focal point or even an out-of-focus beam by the B level, thereby increasing the porosity. Damaged optics or dust accumulated on the optics can absorb energy from the laser faster than the glass will on its own [76]. That may explain why P6's metal appeared to exhibit porosity at an elevated level compared with other participants. The greater age of their machine could have resulted in more degradation of the protective coatings on the lenses, which caused a greater degree of thermal lensing. Computational modeling on thermal lensing by Bonhoff et al. suggests that the optics reach thermal lensing equilibrium, i.e., the maximum temperature increase for a given processing condition, after approximately 10-20 layers [76]. That is very small compared to the 3666 layers of the builds in this study. Admittedly, the aforementioned study lacks experimental validation of their simulations. Therefore, thermal lensing could be a contribution to the height dependency in tensile properties of the metal for P6, but this is largely speculative without further evidence or examination.

Next, the spatial variation in porosity of the metal was considered in terms of the build zones in Fig. 4.5. Due to the difference in porosity distributions in the metal of P6 between the A and B levels, their data was separated according to the z-height of coupons for this analysis, whereas the data obtained from both levels of all other machines was pooled. For most participants, the metal of Zone 0 possessed the lowest average pore size and the lowest number of large pores, whereas metal within the four corners zones (1 to 4) contained the largest size and number of pores. This trend is also observed for P6, in addition to the overall difference in average pore size between the A and B levels for the metal of P6.

To explore this further, the porosity of individual coupons was plotted with respect to their x- and y-axis coordinates in Fig. 4.7 and Fig. 4.8, respectively. Considering the x-position, the metal of P6 shows the strongest relationship. The average diameter, average sphericity, and count of large pores all have parabolic relationships; the largest and least spherical pores reside at the extreme positions of the x-axis (Fig. 4.7). Conversely, the lowest porosity and pore size are located in the center of the x-axis, i.e. the center of the build plate. A similar relationship was identified for the pore data of P6 metal along the y-axis as well (Fig. 4.8). The superposition of these parabolic trends along these two axes can be imagined as a paraboloid. Since these trends are roughly axisymmetric and therefore radial in nature, it suggests that the laser incidence angle is a primary contributor to the spatial variability exhibited. As discussed in Chapter 2, the shape of the laser spot on the powder bed elongates with radial distance from the center of the build plate [54,56]. This distortion in spot shape not only changes the geometry of the weld tracks, but its energy density as well, possibly in excess of 5% [56]. Gas flow or recoater movement act primarily along a single axis, making it unlikely they are the main cause of the trends in porosity for P6.

While the diameter of pores increased with radial distance on the build plate, the sphericity decreased. The different contributing mechanisms of pore formation in LPBF can result in unique shapes and sizes. LOF pores are characterized by their low sphericity and typically large effective diameter and form due to insufficient laser incident energy. Key-hole pores are smaller (~50 μm diameter), more spherical and form due to too excessive energy [77]. Therefore, the lower sphericity of metal from P6, especially at the radial extremes, suggests an increase in LOF pores, corresponding to insufficient laser incident energy. This further supports the theory that increasing laser incidence angle decreases the laser energy density at the peripheries of the build chamber and causes the formation of LOF voids. Comparing these results to the other machines in the study, only the sphericity of P4 is suggestive of a similar parabolic shape, although the scatter is too substantial to confidently make this conclusive.

The porosity of metal from P6 had a strong correlation with radial position from the build plate center (i.e. x- and y-axes). However, this trend was not exhibited by other machines, which suggests that the influence of laser incidence angle overall is typically low. Nevertheless, it is likely that the lower energy density caused by high incidence angle exacerbates other problems with the laser-optics system of the EOS M290 of P6, contributing to their unique property distribution. Degradation of the optics or software versions of the control systems and build file preparation are possible culprits, as will be discussed further in Chapter 6.

There were trends in the porosity of metal along a single axis for some of the other machines. For instance, the pore sphericity of P2 and P4 has a weak linear trend, with an increase in sphericity from the left to the right of the build chamber. The x-axis coincides with the recoater direction. One potential contributing effect is sorting of the powder particle size as observed by Chen et al. [57]; larger powder particles tended to be carried farther by the recoater

blade than the small particles, resulting in a gradient of particle size along the x-axis. They postulated that this could result in differences in melt pool temperature, since smaller particle sizes absorb more laser energy than larger ones. But even if trends in particle size along the recoater path changed the local temperature, there is insufficient evidence to suggest that the local "altered" process conditions contributed to the apparent gradient in porosity within the build space. Instead, the trend is more likely associated with gas flow.

Although the argon travels along the y-axis of the M290, some studies have shown that there can be components of variability in gas flow along the secondary (x) axis [52]. Any disruptions in the laminarity of the gas flow could interrupt its ability to remove the smoke and condensate generated by interactions between the laser and powder bed/melt pool, both of which can be detrimental to the metal quality. Smoke can rise above the powder bed and attenuate the laser, whereas condensate can redeposit on the powder bed. Due to its higher oxygen content, condensate can interact differently with the laser and cause the formation of defects [48,49,78]. If the gas flow disruption is sufficient, these byproducts may remain, attenuate the laser incident energy and result in increased level of LOF voids. Ferrar et al. showed that there were large differences in gas velocity along the secondary axis of an EOS M280, a predecessor of the M290, which correlated with porosity variability [52]. Although this is a possible cause, it is unclear why only the porosity for P2 and P4 exhibited this trend. Further experiments investigating the gas flow conditions of each machine would be beneficial to understanding the root cause of this variability.

With regards to the y-axis, the metal of several machines exhibited trends in porosity. For instance, the average diameter of pores in the metal of P5 exhibited a parabolic shape that was inverted in comparison to the trend for P6, with the largest average pore size in the center of the

build plate. It should be noted, however, that P5 had half the number of scanned coupons as other machines due to μCT equipment failures, and this trend could be an artefact of the decreased sample size. The sphericity of pores in metal of P3, P4 and P6 share a weak parabolic trend, with greatest sphericity in the center. Some participants did not have clear trends in the porosity of their metal but did show increased variability at the extremes of the y-axis. Based on the lower sphericity in the front of the machine for P4, and the greater scatter at the extremes for metal of the other participants, there may be degradation in the gas flow across the build plate that is most impaired at the front (minimum y). This region of the EOS M290 is where the argon is evacuated from the chamber by a baffle system. An experimental study by Ladewig et al. reported that this area of the EOS M280, had greater beam scattering and lower gas velocity [49]. They concluded that the lower gas velocity increased the smoke content, causing attenuation of the laser and redeposition of spatter and condensate. The porosity distributions in the metal from several participants support these conclusions. Indeed, beam attenuation could have increased the local LOF content and decreased the average pore sphericity. For some participants, metal from the back of the machine (with high y-axis values) also contained low sphericity pores or greater scatter, suggesting there may be another phenomenon contributing to porosity and that is related to the gas flow. Although porosity was not observed to be worse near the gas inlet in the study by Ferrar et al. [52], a computational fluid dynamics (CFD) model produced by Moran et al. of an M290 indicated this region had larger turbulence that correlated with an experimentally verified higher porosity content [53]. Those findings could explain the higher level of porosity at the back of the machine and greater variability for several participants in this study. Overall, the distribution in porosity suggests that the argon gas flow distribution is a primary factor, but that

there are other “machine-dependent” contributing factors to the porosity that obscure a universal tend.

There is a quality of the RR build design that is a limitation to this analysis. Specifically, the x- and y-positions of the coupons are not completely independent. Due to the placement of zones in an ‘X’ shape on the build plate, the x- and y-positions of coupons are coupled. As a result, when the property distributions are plotted as functions of the x- or y-position, there is a simultaneous shift in position of the other axis that could contribute to results of the analysis performed.

Finally, the location of coupons within the zones was considered in Fig. 4.10. An initial evaluation of all coupons from Build 1 of P1 from four regions (Zones 1 and 2 from Levels A and B) revealed an interesting phenomenon. When considering just the largest 100 pores from each coupon, the distributions were nearly identical for most coupons. However, a portion of coupons in the front row from Level A of Zone 2 contained noticeably larger pores. One plausible explanation for this occurrence is insufficient gas flow. Oxygen-rich spatter and condensate produced during the melting process should be carried by the argon gas away from the molten metal [49]. The distance these byproducts travel will be a function of the gas velocity and direction. If there is insufficient gas flow, condensate and spatter may fail to travel outside the zone and redeposit downstream onto the powder bed. Hence, spatter and condensate that are generated in printing of horizontal coupons and vertical coupons in the back row could be deposited on the front row of coupons if the gas velocity is insufficient. That contamination has the capacity to cause the nucleation of pores [48].

Repeating the aforementioned analysis for the metal in the machined condition from all participants did not yield similar results. Specifically, the porosity of metal from the front and

back rows of vertical coupons were statistically similar in every zone for all participants, including the metal from Level A and Zone 2 for P1. The surface condition of the machined and as-built surfaces was different between these datasets and the distribution of pores within individual coupons of these two conditions was significantly different. A ring of large pores was found in the as-built coupons near the exterior faces of the gauge section. That peripheral ring was removed by machining. The as-built dataset was therefore modified by excluding pores within 0.5 mm from the free surfaces, to evaluate if that was the cause of the trend. However, it did not have a significant effect on the intra-zonal distribution of pores. It is possible that the sample size of machined coupons is too low to provide an adequate assessment of intra-zonal variability in the porosity. Since only two coupons were μCT scanned from each zone in the machined condition (due to cost and time restrictions), one from the front row and one from the back row, the data had to be grouped across builds and levels. Pooling the data in this manner introduced sources of variability that could obscure potential intra-zonal variability that exists. Despite this limitation, there were important findings concerning the spatial variability in porosity on a less discrete scale.

In summary, most machines exhibited weak or nonexistent trends with respect to porosity and the x, y, or z position. A few machines had trends along the x- or y-axes that were suggestive of inconsistencies in the gas flow. The metal of P6 had the greatest variability, and exhibited radial and height dependencies in porosity that were parabolic in nature. Based on the information obtained, the root causes for this porosity distribution are the combined effects of laser incidence angle, machine age, and potentially thermal lensing.

Following analysis of the porosity distributions, the variability in mechanical properties was evaluated. First, the normality of the YS, UTS, and strain at failure distributions were

considered for the A and B height levels in Fig. 4.13, Fig. 4.14, and Fig. 4.15. Although the general shapes of the distributions were normal, they were often skewed. The distributions for the strength were positive (or right) skewed, indicating there are outliers that have higher strength than most of the coupons. The reverse was observed for the strain at failure, with negative (or left) skewed distributions indicating low ductility of some coupons. In most cases, these outliers were not dependent on the height level, as they were found within both the A and B levels. Their presence will be discussed in a later chapter. Notably, the property distributions of the A and B coupons were shifted for the strength of metal from P2 and the strain at failure of P6.

To investigate this further and understand the magnitude and statistical importance of the height as a build design factor, the mean property distributions were presented separately for the vertical and horizontal coupons (Fig. 4.16 and Fig. 4.17). Although significant differences were observed between properties of metal from the A and B levels for many machines, the overall magnitude was small. For example, the average difference between the means of YS and UTS for the vertical coupons between the A and B levels was only12 and 10 MPa, respectively. Slightly lower differences in the means were observed for the horizontal coupons, with 9 and 8 MPa for the YS and UTS, respectively. During tensile testing of the AM metal, wrought Ti-6Al-4V coupons were prepared from a single sheet of material (N=33) to perform a validation of the equipment and methods, and obtain a measure of variability. The standard deviation in the YS and UTS for the wrought material of 18 and 19 MPa, respectively, was almost twice the degree of variability observed between the A and B levels. Therefore, differences in strength from the A and B levels can be considered negligible for applications of the metal and for this investigation. However, the differences in ductility between the A and B levels are greater than for the strength.

The largest difference was observed in the metal of P6, with strain at failure of 11.2% and 12.2% in the A and B levels, respectively.

One participant (P2) had larger differences between mean properties of the A and B levels, with values for the YS and UTS of the horizontal coupons of 22 MPa and 20 MPa, respectively. The strength of metal from the A level was higher than that of the B level. The strain at failure for that machine also varied between the levels, with coupons from level B having higher ductility than A. This tradeoff between strength and ductility is a common occurrence in metallic materials and is often indicative of microstructural or compositional differences. Since the feedstock material was identical between the A and B levels, the difference may stem from the accumulation of heat with build height or thermal lensing effects, both of which could affect the microstructure. As the second oldest machine in the study, critical systems such as the laser may have undergone more degradation than the other machines. As with the proposed explanation of thermal lensing for P6, degradation of the optical components may have increased the amount of thermal lensing seen in their M290 and produced this discrepancy between the A and B levels.

A lower laser energy caused by laser beam focal errors or angle of incidence could result in a lower temperature melt pool [79]. That would cause both increased frequency of LOF voids and finer microstructural features resulting from the faster cooling rate, which would decrease the ductility (P6) and increase the strength (P2) of the metal. As the optics heat up due to thermal lensing, the focal position shifts, causing a change in melt pool temperature as the build progresses. The ductility of metal from other participants also varied between the two levels. The metal of P2 and P4 had similar trends to that of P6, with lower strain at failure in the A level. However, the metal of P1 and P3 showed the opposite relationship. Despite this difference in

ductility rank between the A and B levels across the machines, thermal lensing could still be responsible. During thermal lensing, the focal distance will decrease [76]. The result of this will be dependent on the initial setpoint for the focal point of the laser. If the setpoint is located below the powder bed, the laser would shift more in focus as thermal lensing occurs, thereby making the melt pool smaller but hotter. On the other hand, if the focal point is positioned on the powder bed or above it, the laser will become more out of focus with build progression as thermal lensing continues, and potentially resulted in lower temperatures with this defocus. As such, an in-depth assessment of the laser optics system of each machine would be beneficial to assessing the z-height property dependencies.

Significant differences in the YS, UTS and strain at failure were also observed across the build plate. Results presented in Fig. 4.18 and Fig. 4.19 showed the mechanical properties of metal from vertical coupons as a function of zonal location. Significant differences in strength were only identified for P1 and P3, while there were no significant differences identified for the strain at failure. The pair-wise comparisons between zones for these two machines revealed that each has unique relationships between zones. For the horizontal coupons, more machines were identified as having significant differences between zones for all three properties. As with the vertical coupons, the zones identified as statistically different varied from machine to machine.

To investigate this further, the mechanical properties for the vertical coupons were plotted as functions of the x- and y-positions in Fig. 4.22 and Fig. 4.23, respectively. Similar plots for the horizontal coupons are found in Appendix B, as those results were limited by the number of unique locations due to clustering of the horizontal coupons in the center of each zone. While the strength of most participants is similar across the x-axis, metal from P1 and P4 have outliers with low strength on the edges of the build plate, however the trends are weak. The

strain at failure of P6 also appears to decrease at the edges of the build plate along the x-axis, which may be related to the effect of incidence angle in that machine.

With respect to the property distribution along the y-axis, the strongest relationship occurs for the metal of P1; parabolic trends are evident in the YS, UTS and strain at failure. All three properties exhibit maxima near the center of the build plate for the vertical coupons. Since the gas flow moves along the y-axis, this trend could result from impaired gas flow at the front and back of the machine, in comparison to the middle. The strain at failure of metal from P6 also shows a parabolic trend, with the lowest ductility in the corners of the build plate. This trend coincides with porosity results, where the average pore size increased radially outward from the center of the build plate. As with the x-axis correlation between porosity and strain at failure, the trend is expected to result from failures that initiate from pores or a root cause that involves both the porosity and the microstructure of the metal that are associated with the aforementioned factors.

Finally, the intra-zonal position of coupons was considered where the front and back rows of coupons from each zone were compared (Fig. 4.9) in terms of the YS, UTS and strain at failure. Results from one-way ANOVAs identified only one significant difference, namely in the strain at failure for Zone 1 of P1 (Fig. 4.24). The front row of coupons had a higher strain at failure than the back row. Although Zone 4 exhibited the same relationship, it is not statistically significant. This trend is consistent with the y-axis distribution, where strain at failure followed a parabolic relationship along the y-axis. The same explanation of turbulent gas flow at the back of the machine is the most plausible hypothesis for the root cause of this difference in Zone 1.

Based on the statistical comparisons, the null hypothesis must be rejected. Statistical differences were identified in both the porosity and tensile properties across the build space.

With regards to the tensile properties, the magnitude of spatial differences in strength across the build space were small and were only significant due to the low standard deviations. The variation in strain at failure was more widely distributed and showed trends with position for some participants. Notably, the strain at failure of metal from P1 had a parabolic relationship with position, possibly due to gas flow inhomogeneities. In addition, the metal of P6 also had a strong correlation between radial position and strain at failure, which matches the trends seen in their porosity, potentially indicating a causal relationship.

4.3. Conclusion

The porosity and tensile properties of metal printed with six different EOS M290s were evaluated for spatial variability. Investigation of the x, y, and z position of coupons revealed unique property distributions for different machines. The metal produced in half of the machines in this study exhibited strong property dependence along one or more axes. This includes machines with 20 MPa differences in strength between the A and B heights, 20 MPa zonal differences, and radial porosity dependency. The variability observed in porosity and tensile properties is problematic from a DFAM perspective since the property distributions are unique to each machine. Potential solutions to overcoming the variability include limiting the usable build space to the center of the chamber and utilizing knock-down factors to account for the lowest possible properties. However, these approaches will limit the utility of AM.

Results also showed that the largest degree of variability in metal quality and properties is limited to a subset of the six machines. Specifically, only one machine exhibited significant variability in metal properties along all three axes (x, y and z). Evidence suggests that laser optics condition, machine age, and gas flow may have been root causes or contributors to the

observed variability in these machines. To establish machine equivalency and avoid the need for individual DFAM for every machine, machine health and the contributions of individual subsystems (laser-optics system, gas flow, recoater blade) must be considered.

Chapter 5. Inter-Build Variability

Inter-build variability refers to the variation in metal quality and/or mechanical properties that occurs between repeated builds from any single machine. As previously discussed, this may include trends resulting from powder reuse, degrading machine health, and stochastic variability. This topic is important in any industry setting where quality of metal must be consistent from one print to the next, and particularly when powder reuse is part of the standard operating procedure. Understanding the effects of powder reuse in LPBF is important to ensure that metal quality can be controlled, while also minimizing material costs and waste. In this chapter, the evaluations include powder quality, μCT results, and tensile properties of metal compared across the six builds to evaluate the null hypothesis, i.e., there is no significant variability from build-to-build over the six builds performed by each participant. Details about the methods, materials, and experimental design were presented within Chapter 3.

5.1. Results

5.1.1. Powder Characteristics

The light element content (wt%) of powder samples that were obtained from each participant and build were evaluated using IGF. As described in Chapter 3, these samples were collected before each print, such that the powder sample from Build 1 was in the virgin state, and subsequent builds contained a mixture of virgin and sieved reused powder. Results for the oxygen, hydrogen, nitrogen, and, for some participants, carbon content are presented in Table 5.1. In addition, the limits in these elements as defined by ASTM F2924 for Grade 5 Ti-6Al-4V are listed for reference. The weight percent of each element stayed within the accepted limits for

all participants [61]. These elements are of particular importance to ensure the alloy meets the composition requirements stipulated in the standard [61], as well as their impact on mechanical performance. The O, H, N and C atoms tend to fill interstitial sites in the crystal structure, thereby causing simultaneous strengthening and embrittlement [43].

For most participants, the analysis was performed on a single powder sample from Builds 1, 3 and 6, however in a few cases Build 5 was included as well. Testing one powder sample every other build reduced the expenditure associated with testing while still providing enough information to identify trends. An additional five samples from Build 1 of P1 were tested to understand measurement variability, and the standard deviations for each element will be used as an estimate of measurement and sample error. The results of the single measurements from each participant are plotted in Fig. 5.1 as a function of build number. The O content of powder from a few partners (e.g., P1 and P3) shows the highest R^2 with build number, although the sample size is admittedly limited. Although the linear regressions in O content for P1 and P3 exhibit higher R^2 values, neither case is clearly a trend across all three measurements. For example, the O content of Builds 1 and 3 for P1 are similar, and within the standard deviation of the repeated measures test (0.007 wt% O). Even the lower O content seen in Build 6 for P1 is within the standard deviation of the repeated measures of the other builds. The same can be said for P3, where all of the measurements are within the standard deviation of the repeated measures test. Thus, although there is scatter in the O content from build-to-build, and more generally the C, H

and N content, there are no significant changes in the powder chemistry as a function of build number.

Table 5.1: Tabulated light element composition for each build of each participant. The maximum allowable values dictated by ASTM F2924 are included for reference, as are the standard deviations of the repeated measures test.

	Build Number	Carbon	Hydrogen	Nitrogen	Oxygen
ASTM	-	0.08	0.015	0.05	0.2
P1	1	0.0152	0.003	0.0198	0.1694
	3	0.0151	0.0031	0.0161	0.168
	6	0.0151	0.0029	0.017	0.163
P2	1	0.015	0.0023	0.0152	0.164
	3	0.0148	0.0024	0.0135	0.155
	6	0.0154	0.003	0.0178	0.173
P3	1	NA	0.0016	0.0145	0.161
	3	NA	0.00205	0.01495	0.1625
	5	NA	0.0017	0.0135	0.165
	6	NA	0.0019	0.0131	0.164
P4	1	0.0151	0.0027	0.0156	0.163
	3	0.0182	0.0027	0.0163	0.169
	6	0.016	0.0027	0.0153	0.167
P5	1	NA	0.0022	0.0154	0.162
	3	NA	0.002	0.0154	0.148
	5	NA	0.002	0.0163	0.15
P6	1	0.0157	0.0016	0.0123	0.155
	3	0.017	0.0022	0.0162	0.166
	6	0.0164	0.0018	0.0145	0.158
Repeated Measures Standard Deviation (P1)	1	0.0011	0.0003	0.0006	0.0065

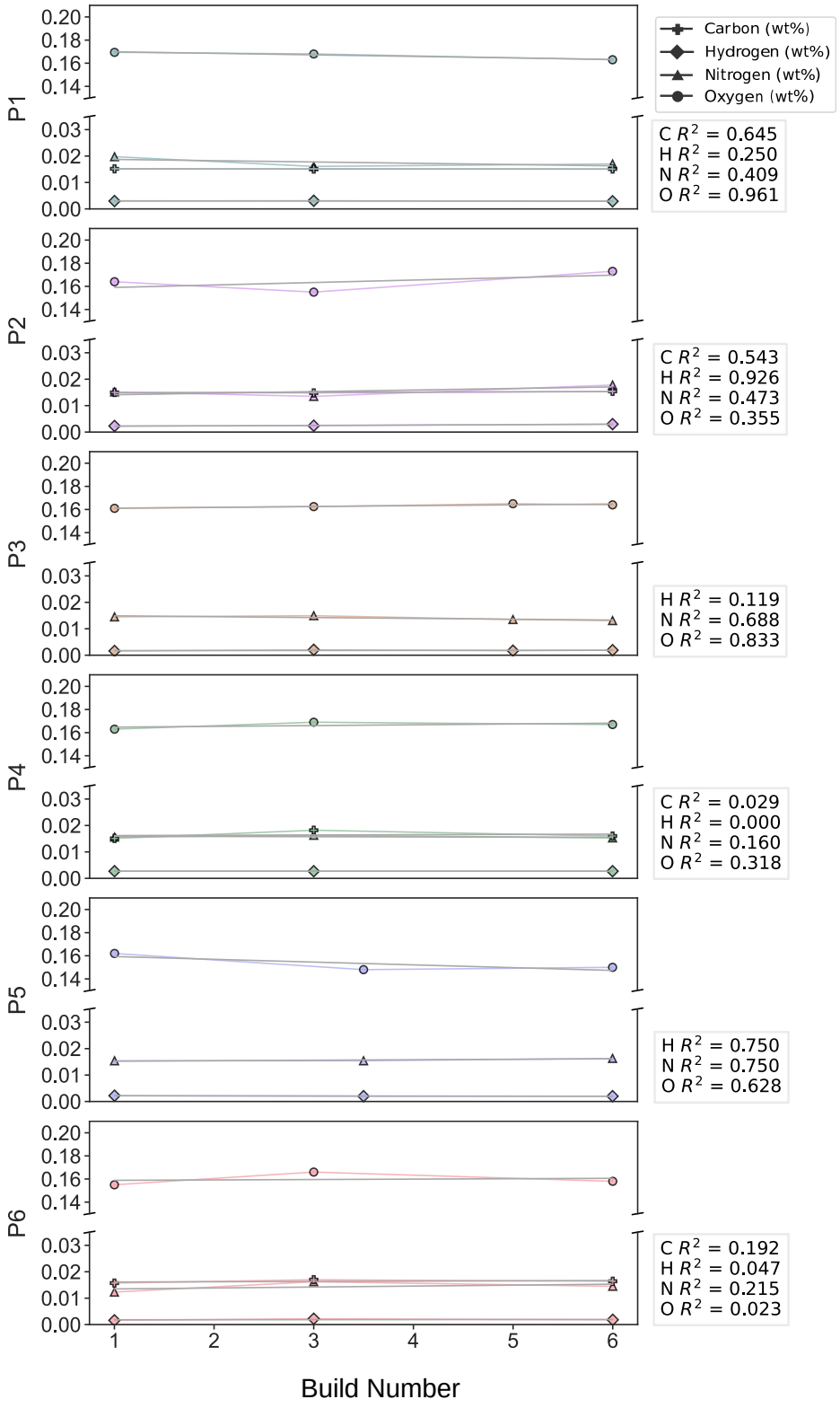

Fig. 5.1: Evolution of powder chemistry measured by IGF as a function of build number for each participant.

The PSD of the collected powder samples was evaluated using LSPA as outlined in Chapter 3. Five to ten samples were evaluated from each build and for each participant to increase the confidence in the findings. The d10, d50, and d90 measures of particle diameters were extracted from the powder size distributions and are plotted as a function of the build number for each participant in Fig. 5.2. While there are no clear trends in the d10 particle size, the d50 and d90 of P6 increased with build number. Specifically, the d50 increased by 17% (from 34.5 to 40.5 µm) and the d90 increased by 23% (from 46.5 to 57.3 µm). Although the d90 of P3 also increased by 10 µm (from 49.6 to 59.6 µm) the difference appears to be due to scatter in the data, not following a consistent trend with build number. In addition, while the R^2 values for the powder of P5 are high and suggest a possible trend, the slope is small at -0.5 µm/build. The overall change was small compared to the standard deviations, which was also true for the remaining participants excluding P6, where the change in particle size usually changed by no more than one or two microns over the six builds.

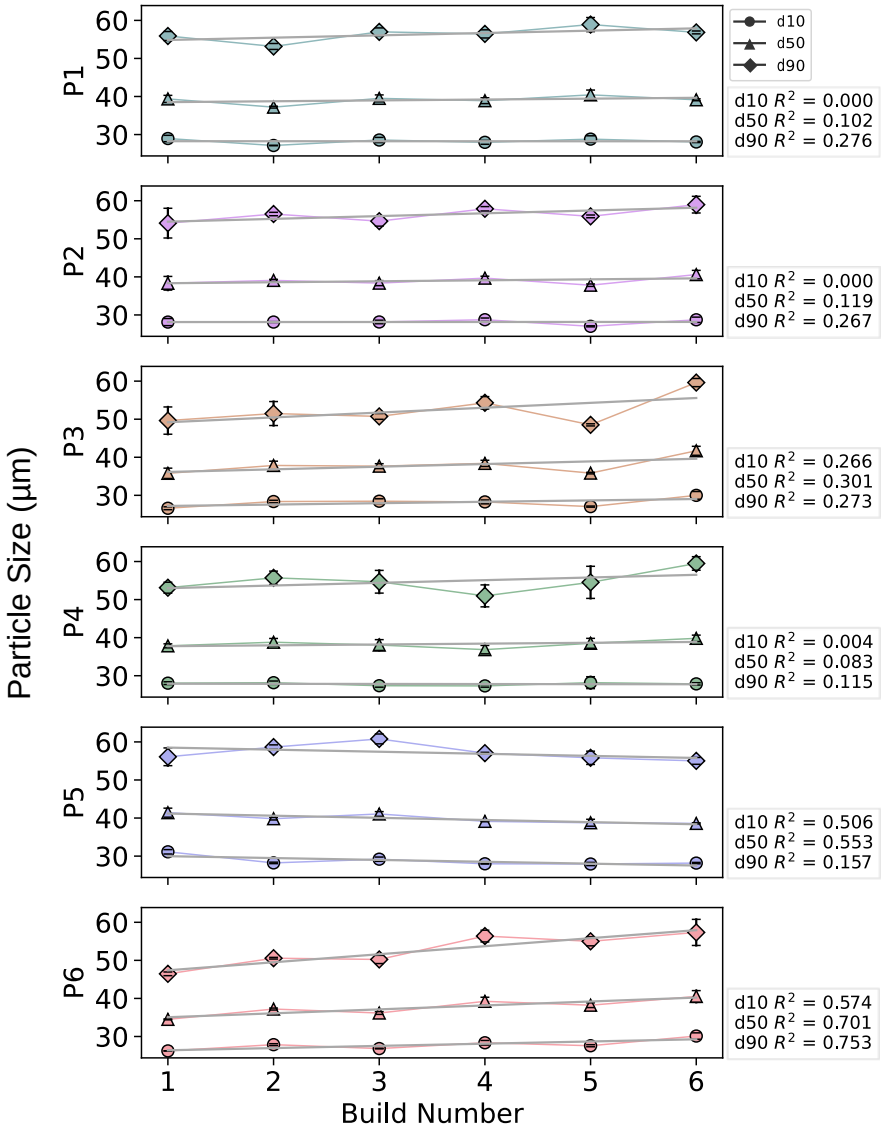

Fig. 5.2: The measures of d10, d50 and d90 particle sizes for each machine as a function of the build number. Linear regression is applied to each percentile and R^2 values are noted to the right of each subplot.

5.1.2. µCT

The porosity was evaluated using the average pore diameter and sphericity for each of the scanned vertical coupons. While the peripheral zones printed in each build from Build 2 to Build 5 are different, Zone 0 is present in all prints of the six-build sequence. It provides a consistent

reference without introducing potential intra-build variability. The average pore size and sphericity for each participant is plotted as a function of build number for Zone 0 in Fig. 5.3. Although there is scatter in the data, both between builds and in some cases within builds, there are some trends evident in the data.

The most notable trend in the pore diameter is observed for the metal of P5 where the average diameter appears to increase with build number. However, P5 had approximately half the number of scanned coupons as the other participants due to µCT equipment failures, and which only originated from Builds 2-4. Build-to-build variability in the pore diameter of metal from P6 covers a similar range of values as Builds 2-4 of P5, but no trend was observed overall. Without a larger sample size, it is difficult to conclude whether the variability in porosity from P5 is stochastic or reflects a significant trend.

The metal of P4 and P2 had the second and third strongest trends in the pore characteristics, respectively. Both trends occurred for the pore sphericity, whereas there was no trend in the pore size. In the case of P4, the sphericity decreases with build number. However, this apparent trend and higher R^2 value come from the high and low sphericity of Builds 2 and 6, respectively, not necessarily due to a consistent trend across all the builds. For the metal of P2 the inverse trend takes place, with an increase in sphericity with build number. This apparent trend is consistent and linear for Builds 1-4 and then stabilizes by Build 6. Unfortunately, no coupons were scanned from Build 5 due to µCT equipment failures. The trend in sphericity for P2 is more reliable as a trend than that of P4 because of the consistent changes from Builds 1-4 and the lower scatter between builds. Nevertheless, the sphericity only increases by approximately 6% over the four builds, i.e., from 0.54 to 0.57 on a scale of 0 to 1. That change is unlikely to be relevant to the mechanical behavior.

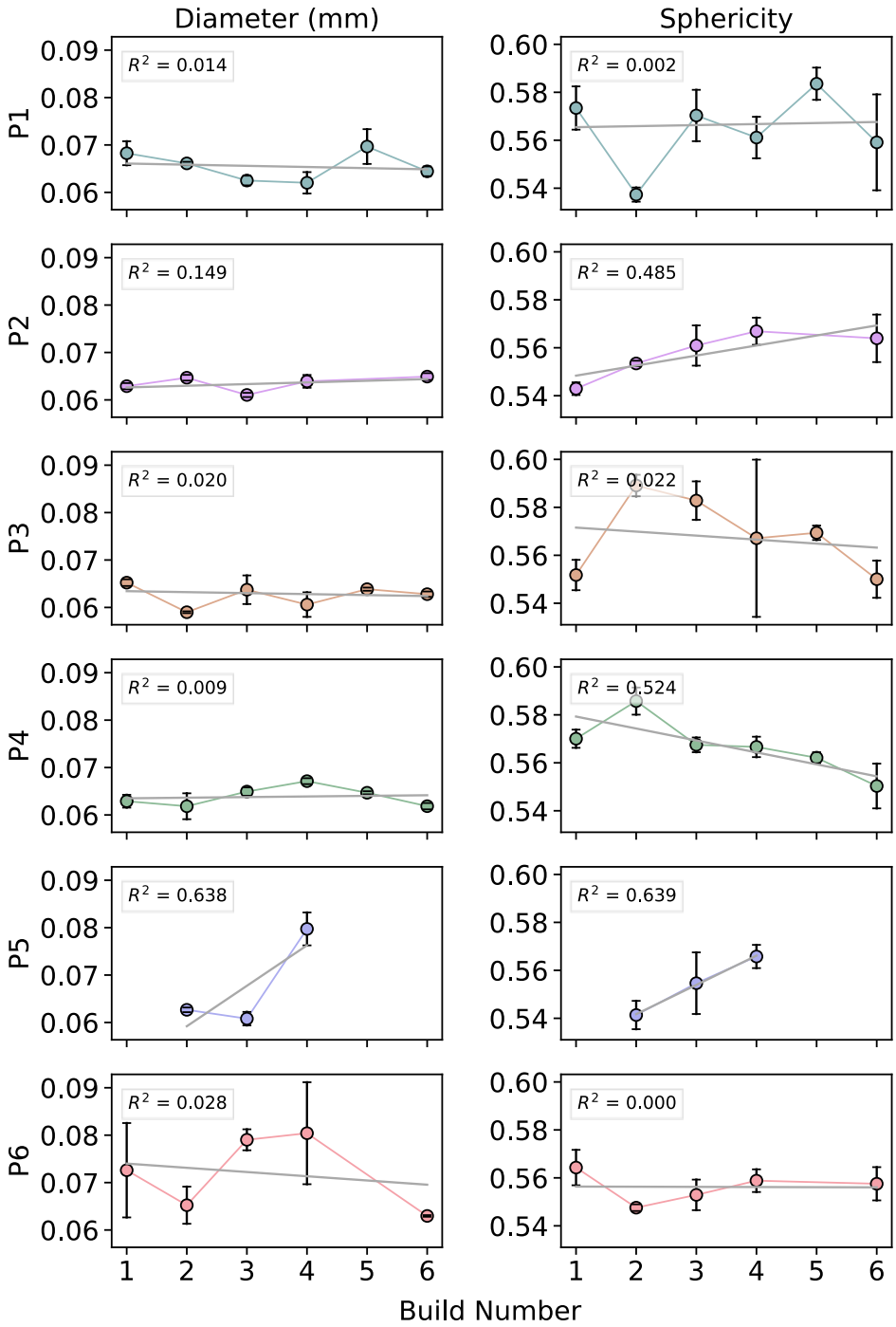

Fig. 5.3: Average diameter (left) and sphericity (right) of pores from the vertical coupons for each participant as a function of build number. Linear regression fits are shown with R^2 values annotated.

Variability in the porosity and pore characteristics was also observed from build-to-build. This random, or stochastic, variability is captured using the Coefficients of Variation (CoV), defined as the standard deviation divided by the mean. The CoVs are presented in Table 5.2 for the pore diameters and sphericity across the six builds for each participant. While the values for most machines are low, i.e., below 5% CoV, the diameters of pores from P5 and P6 show much larger stochastic variability, at 15.4% and 10.9%, respectively. In the case of P5, this variability seems to originate from large pore diameters that occurred in Build 4, however in the absence of data from Builds 1, 5, and 6 due to μCT failures, it is impossible to know if this was an isolated incident. For P6, however, the high stochastic variability is not isolated to an outlier build. Instead, several of the builds contain large average pore sizes, while the rest have lower average diameters.

Table 5.2: Coefficients of variation for the pore diameters and sphericity across the six builds for each participant. Note the large CoV values in the pore diameter for metal from P5 and P6.

Participant	CoV of Diameter (%)	CoV of Sphericity (%)
P1	4.7	2.8
P2	2.5	1.7
P3	3.7	2.8
P4	3.3	2
P5	15.4	2.2
P6	10.9	1.1

5.1.3. Tensile Testing

To examine the effects of inter-build variability on mechanical properties, only the tensile properties of metal from Zone 0 are considered for each participant since the metal from that zone was available in all builds and from all partners. Fig. 5.4 shows the property distributions representing the average properties as a function of build number, and fits the data with a simple

linear regression model. Each of the six rows corresponds to one of the six participants, while the columns represent the YS, UTS and strain at failure. The R^2 values for the regressions are annotated on each plot for reference. It is important to note that most of the R^2 values in Fig. 5.4 are low, and are typically below 0.1. The highest R^2 reported is 0.46, which corresponds to the UTS of the coupons with vertical orientation of P3. Furthermore, the slope of the fit lines is also typically small. Together, these characteristics suggest that there are no strong trends in the quasi-static tensile properties with build number.

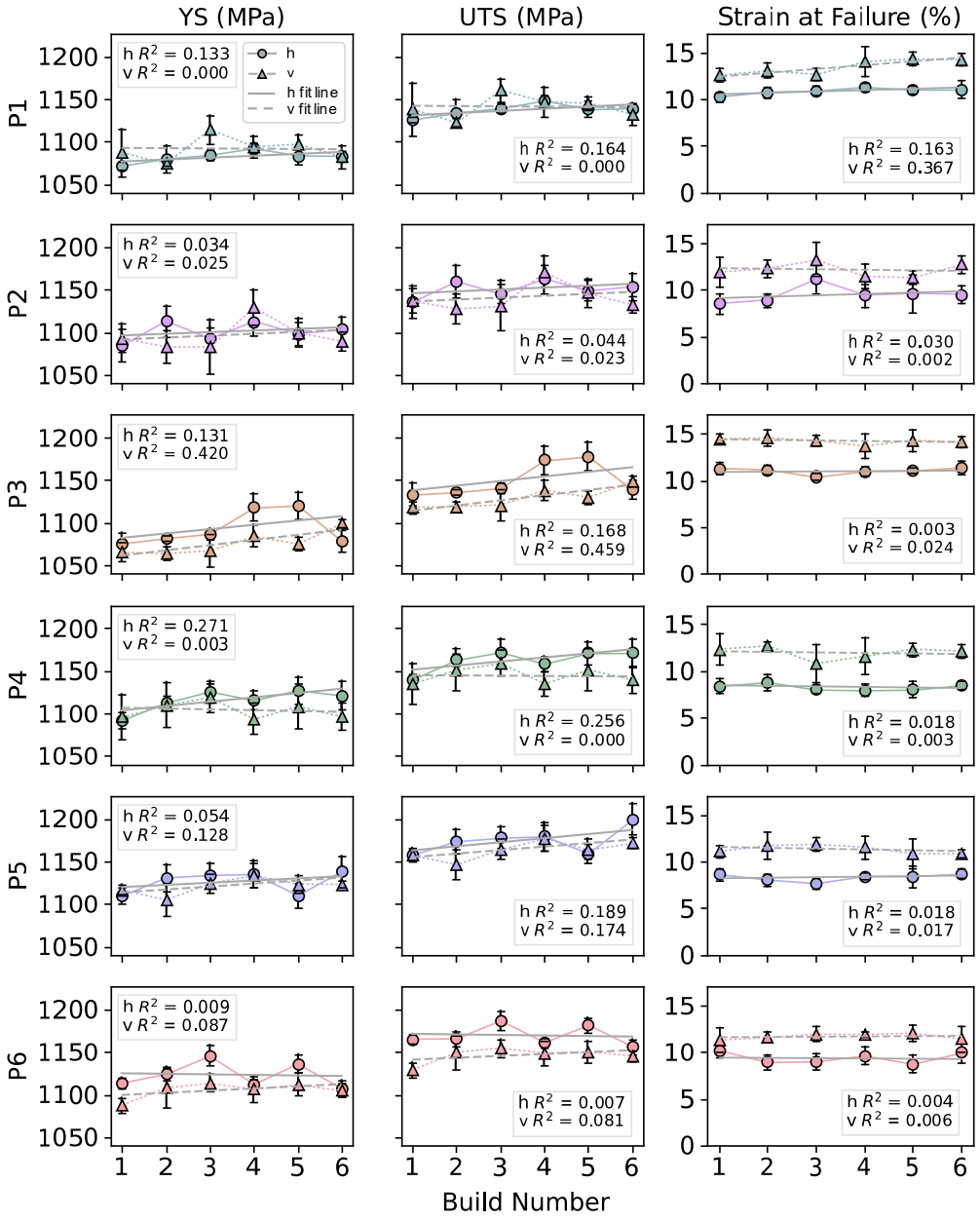

Fig. 5.4: The YS (left), UTS (middle) and strain at failure (right) of horizontal (*h*) and vertical (*v*) coupons for each participant as a function of build number. Linear regression fits are shown with R^2 values annotated.

The strongest trend evident in the mechanical properties with subsequent builds was the increase in YS and UTS of vertical coupons from P3. Inspecting the results of metal from P3

closer, the YS and UTS of both the horizontal and vertical coupons undergo an increase in strength with build number for Builds 1-5. The slopes in strength for the horizontal and vertical coupons are approximately 5 and 6 MPa/build, respectively. While the strength of the vertical coupons continue to increase in Build 6, the average YS and UTS of the horizontal coupons decreases to a level consistent with Builds 1-3. If this final build is excluded from the horizontal data, the R^2 values of the horizontal coupons would increase to 0.633 and 0.606 for the YS and UTS, respectively. The horizontal coupons appear to follow a general increase in strength with build number, however there are some noticeable variations in the response after Builds 3 and 5. Based on further communication with the points of contact for P3 about the processing of their metal, the groupings of Builds 1-3, 4-5, and 6 correspond to which prints were heat treated together in the vacuum furnace of P3. That additional understanding suggests that there was a possible variability in those three heat treatments.

Due to the grouping of properties according to builds, the temperature records from the heat treatments peformed by P3 were acquired and are presented in Fig. 5.5. Examining the thermocouple logs of the first two heat treatments (corresponding to Builds 1-3 and 4-5, respectively) indicates there is a small difference in the time-temperature control. The first heat treatment took longer to reach 745°C, resulting in 10 minutes longer at temperatures above the annealing threshold than the second heat treatment. This resulted in 277 minutes in the annealing range for Builds 1-3, compared with 267 minutes for Builds 4-5. The importance of this difference in heat treatment cycle will be discussed in the next section.

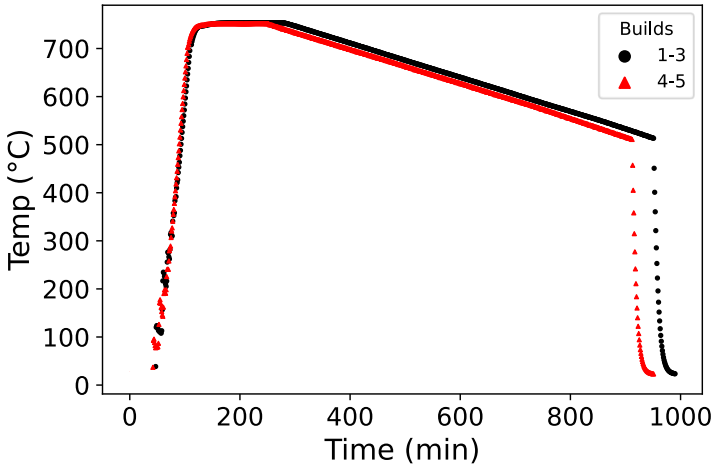

Fig. 5.5: Thermocouple logs for the first and second heat treatment cycles performed by P3. The cycles are labelled in the legend according to the Build numbers that were heat treated in each lot.

Although the YS, UTS and strain at failure of most machines did not follow trends resulting from powder reuse or machine health, stochastic variability resulted in property differences from build-to-build. The stochastic variability is captured by the CoV values presented in Table 5.3. All of the CoV values for the YS and UTS are below 2%, while most are approximately 1%. These values are all lower than the CoV values of the wrought form titanium that was tested. Admittedly, the strain at failure has higher CoV values (up to 9.9%) than the strength parameters, but most are significantly lower than the variability exhibited by the wrought titanium.

Table 5.3: Coefficients of variation for the YS, UTS, and strain at failure across the six builds for each participant.

	Participant	CoV of YS (%)	CoV of UTS (%)	CoV of Strain at Failure (%)
Vertical	P1	1	0.9	5.6
	P2	1.7	1.5	6.1
	P3	0.6	0.7	2.3
	P4	0.9	0.9	5.9
	P5	0.9	1	3.5
	P6	1.1	1	2.1
Horizontal	P1	0.7	0.7	3.5
	P2	1.1	0.9	9.9
	P3	1.9	1.9	2.9
	P4	1.3	1.1	4.1
	P5	1.2	0.9	4.5
	P6	1.3	1	6.3
	Wrought	1.8	1.8	8.3

5.2. Discussion

The analysis of powder samples collected before each build by IGF (Fig. 5.1) showed that the light element composition (oxygen, nitrogen, hydrogen, and carbon) stayed within the limits of Grade 5 Ti-6Al-4V as dictated by ASTM F2924 [61]. That finding indicates that the powder could continue to be reused beyond the limits of this study and that it is acceptable for a second phase of the round robin program, which will focus on the stress-life fatigue behavior. Furthermore, there were no trends in oxygen, hydrogen, nitrogen or carbon content with build number. While there was some correlation between the light elements and build number based on the regression models, they correspond to slopes that are negligible. For example, the R^2 value for hydrogen content in the powder of P2 is 0.926, but only relates to a 0.00014 wt%/build increase in H.

Regarding the oxygen content of the powder, there was a substantial amount of scatter in the results, across builds for specific machines and between some of the machines as well. Specifically, the in the oxygen in powder of P2, P4 and P6 have R^2 values for linear regression below 0.4, whereas the values for P1, P3, and P5 range from roughly 0.6 to as high as 0.96 for P1. Considering the slope of the trend line for powder of P3, the oxygen content increased by 0.0007 wt%/build. At that rate, it would take 71 builds for the oxygen content to rise from its initial value (0.15 wt%) to the ASTM standard limit of 0.2 wt%. By comparison, the slopes of P1 and P5 were both negative, with values of -0.0013 and -0.003 wt%/build, respectively. A negative trend in oxygen content with powder reuse is not expected since there is no mechanism for removal of oxygen from the powder in the handling process. Of note here, the repeated measures testing of powder from P1 had a standard deviation of 0.007 wt% O, which serves as an approximate measure of the testing and sampling errors. The differences between O content of the builds from P1 all fall within 0.007 wt% of each other. Hence, the variation in oxygen content noted for this machine appears to be within the error of the IGF testing.

Despite the small degree of changes to light element chemistry overall, the positive and negative trends in oxygen content for P1, P3, and P5 should be considered critically. As there was only one measurement made for each powder sample due to the cost of IGF. Only the repeated measures test can be used to evaluate the variability of the measurements, but this may not be an adequate measure of the sampling error because the variability in sample error may change with powder reuse. There is an expected rise in oxygen contaminated material in the reused powder that may not be captured from a single measurement due to the small sample size. Conversely, it is possible that a small sample could oversample oxygen rich material. Thus, a

portion of the build-to-build variability may exist due to changes in the sampling error with powder reuse.

The limited variations in powder chemistry as represented by the distribution in light elements is consistent with some of the published powder reuse studies. An assortment of studies on powder reuse in LPBF were reviewed in Chapter 2, and the changes in oxygen content with reuse varied [28,30,31,35,36,42,45]. While some studies reported no change in oxygen content [28,35,42], others showed varying levels of increasing oxygen content [30,31,36,45]. One limitation in this literature is that most of these studies used Grade 23 Ti-6Al-4V, a lower oxygen content version of the alloy. The two studies that used Grade 5 Ti-6Al-4V recorded little to no change in oxygen content of the powder [28,31] over 11 and 12 builds. The difference in results for the Grade 5 and Grade 23 could indicate a decrease in the diffusion constant of oxygen in the Grade 5 alloy due to the higher initial oxygen content. However, that comment is speculative.

There is another factor to consider in the reuse protocol. For the present investigation, the introduction of virgin powder after every build to replace consumed powder would also have a diluting effect that reduces the detectability of oxygen introduced during the printing process. Specifically, of the 74 kg of powder placed in the dispenser before every build, the participants recorded consumption of up to 9.67 kg. This consumed mass includes powder that is consolidated into coupons, support structures, and powder lost due to condensate formation and sieving of the powder to remove agglomerates. The powder lost by consumption accounts for up to 13% of the total powder mass in the dispenser and is replaced by virgin material. Hence, not all powder in the dispenser has undergone six builds of reuse by the sixth build, which would cause some dilution and offset the overall increase in oxygen content of some powder particles that results from use.

Another commonly observed effect in powder of the published studies on reuse was a change in the PSD. In general, a decrease in the content of ultra-fine particles (termed fines) occurs [31,35,36], and an increase in overall particle size [28,35,40,45]. Some alternative observations have been reported as well, such as a constant PSD, but less frequently [30,36]. The fine particles are expected to disappear preferentially with powder reuse by sintering to other particles or becoming airborne during powder handling. Although the shift towards larger particle sizes may be partially explained by the loss of fines, another potential contribution is the sintering of powder together. Powder near the melt pool experiences high temperatures, and can undergo sintering by solid state diffusion, resulting in larger powder particles. Together these processes can cause an increase in the particle sizes, which is reflected by the PSD.

As evident in Fig. 5.2, the metal of P6 was the only one to exhibit trends with build number. The absence of trends in P1-P5 could be explained by the top-up powder reuse strategy used in this study. Replacement of lost/used powder with virgin powder may be overshadowing changes to the PSD that may otherwise have occurred. Most studies that have reported changes in the PSD with reuse used a single batch of powder for the duration of their investigations [28,31,35,36,40,45]. In other words, the volume decreased as a result of consumption and without replacement with virgin powder. In fact, only one of the reported reuse studies used a "top-up" strategy similar to the one used in this round robin investigation, and they also recorded no change in the PSD [30]. Therefore, the results presented here agree with published results when the powder reuse strategy is taken into account.

The PSD of P6 was an exception to the results from the other participants in this study. Their d50 and d90 measures appeared to increase linearly with build number (Fig. 5.2), as confirmed by the higher R^2 values. The greatest change and highest R^2 were recorded for the

d90, with an increase in size of 2.1 μm/build and an R^2 value of 0.75. From inspection of the results from individual builds, the PSD of Build 1 differs most significantly from the other machines. The d90 and d50 were lower than the powder from other machines, in particular. Since the powder from Build 1 was un-sieved virgin powder from the same lot used by P1-P5, this difference in PSD is unexpected. And while this difference may have been caused by measurement errors, another possibility is a failure to follow the PCD. The PCD dictated that Build 1 use un-sieved virgin powder. If P6 mistakenly sieved their powder before Build 1, it would have resulted in the decrease in D50 and D90 particle sizes observed compared to the other machines.

Although the powder elemental composition and PSD did not show definitive or significant trends with powder reuse, small changes in chemistry can affect the melt pool stability and the porosity [50]. To explore this further, the average pore size and sphericity were plotted versus the build number in Fig. 5.3. For most participants, there was no definitive trend with powder reuse. There are apparent trends in the porosity parameters for the metal of P4 and P5, but these are in questionable. In the case of P4, the apparent decrease in sphericity with powder reuse arises from the unusually high and low sphericity of Builds 2 and 6, respectively; the sphericity of the other builds is approximately constant. Regarding the porosity of metal from P5, there is an apparent trend where the sphericity and diameter of pores increase with build number. However, only coupons from Builds 2-4 were scanned from their metal due to μCT equipment failure. Hence, although the porosity in the metal of P4 and P5 may not exhibit trends, they do exhibit stochastic variability from build-to-build, which will explored later.

The strongest trend was observed in the pore sphericity of metal from P2 where there is a linear increase from Build 1-4, after which point the sphericity appears to plateau. Excluding

Build 6, the R^2 value increases to 0.78. It is important to highlight that the increase in sphericity from Build 1-4 is small, only 0.02. The root cause does not appear to be the powder chemistry or PSD alone, since no trends were observed in those factors. Highly oxidized spatter or condensate [48] that went undetected by IGF due to the small sample volume could increase the frequency of LOF defects [50]. But LOF defects have low sphericity, whereas the trend observed was an increase in sphericity with powder reuse. Further investigation into the sphericity of pores in metal from P2 is needed to identify the potential root causes of the apparent trend in pores. Regardless of the changes identified, the magnitude of the change was small, which would seem to be insignificant from an industrial perspective. Further evaluation of the porosity and powder characteristics with further reuse will be beneficial to provide additional data with increasing build number and supplement the current understanding.

As previously noted, there was a substantial degree of stochastic variability present for some machines. The CoV values presented in Table 5.2 reveal that P5 and P6 had large random variability in pore diameter, with 15.4% and 10.9%, respectively, while the remaining machines had CoVs an order of magnitude smaller. For the sphericity, metal from all participants exhibited low stochastic variability (~2%). Stochastic variability could come from a variety of sources, including humidity levels that affect powder flowability, electrical fluctuations that modulate the laser power, sporadic machine health issues, or vibrations in the manufacturing environment. The machine of P5 was located in a less controlled environment than many of the other participants, which could have resulted in greater variability in these sources of stochastic variability. However, identifying the specific causes of stochastic variability is outside the scope of this work. It is noted, however, that the stochastic variability is machine dependent.

Considering the tensile properties in Fig. 5.4, there were no strong trends with powder reuse. All of the R^2 values fall below 0.5. Trends are not expected if machine health is maintained and the feedstock material does not change. Since the powder PSD and chemistry did not exhibit definitive trends with reuse, the tensile properties are expected to show stochastic variability akin to those observed in the porosity. In most cases, the CoV between builds for the strength was low, as shown in Table 5.3. For the YS, the maximum CoV between builds for a participant was 1.9%, while most values were approximately 1%, regardless of the coupon orientation. Nearly identical values were observed for the UTS. These CoV compare very favorably with the variability observed in the wrought material tested alongside the AM Ti-6Al-4V, which had CoV of 1.8% for the YS and UTS. However, the strain at failure exhibited higher variability, with a maximum CoV of 10.4% for the horizontal coupons of P2. This exceptionally high stochastic variability is an outlier amongst the six participants. The metal from the other five machines had an average CoV for the strain at failure of 4.5%. Compared with the wrought material, which had a CoV of 8.3% for the strain at failure, the AM metal performed exceedingly well. Even the relatively high variability of P2 is not significantly larger than the variability observed in the wrought metal. As with the stochastic variability in porosity, there are a number of possible sources previously listed that may account for the observed differences from build-to-build. An identification of the particular sources at fault is outside the scope of this work but will be a worthwhile effort.

Although the metal of most participants exhibited purely stochastic variability between builds, it is necessary to elaborate further on the YS and UTS of metal from P3. For the vertical coupons, the strengths increased from Build 1-6, whereas they increased from Build 1-5 for the horizontal coupons, and then decreased substantially in Build 6. Removing Build 6 from the

linear regression of the horizontal coupons, the R^2 values for the YS and UTS increase to 0.63 and 0.61, respectively, which warrants a closer inspection.

There are two root causes that could account for the distribution in YS and UTS for the metal of P3. The first involves the contribution of heat treatment. P3 performed their heat treatments with a vacuum furnace in their facility and in three separate batches which correspond to Builds 1-3, 4-5, and 6. Referring to Fig. 5.4, there is an increase in the YS and UTS of the horizontal coupons after Build 3, and then a decrease in Build 6, which correlates with the heat treatment lots. The heat treatment temperature logs for the first two lots were shown in Fig. 5.5; there is a small but clear difference in heating rate between them. As a result, the metal in the first heat treatment (Builds 1 – 3) spent ten minutes longer within the annealing temperature range than the second. Ten minutes is relatively small compared to the total annealing time of 277 min. However, a study by Tsai et al. found that increasing the soak time from four to eight hours at 600°C resulted in a YS increase of approximately 40 MPa [80]. The average YS of Builds 1-3 was 1073 MPa, compared to 1101 MPa for Builds 4-5. While a direct comparison cannot be made in these two heat treatment cycles, the different heat treatment temperatures (600°C versus 745°C) would result in different rates of microstructural coarsening and more coarsening expected at the higher temperature. Yet, a ten-minute difference would not explain the nearly 30 MPa difference between the two heat treatment lots.

A second possible root cause is related to the maintenance schedule of the M290 operated by P3. Routine maintenance was performed several months before the first build, and then again after Build 5. Although the maintenance records do not indicate all the calibrations made to the M290, there is a record that the diameter of the laser changed between the two maintenance checks. Specifically, the diameter of the laser fired at 200 W increased from 80.1 to 85.6 μm.

This amounts to a decrease in energy density of the laser of 12.5%. A decrease in energy density could result in a cooler melt pool and a faster cooling rate of the metal, which would manifest as a finer microstructure and higher strength metal. Bean et al. showed that adjusting the focal position of the laser by ±3 mm resulted in up to 23 MPa difference in strength [46], similar to the magnitude of strength change observed between Builds 1-3 and Builds 4-5. A change to the microstructure due to differences in laser energy density could decrease the strain at failure as well. However, this was not observed in the present investigation.

The service records from P3 do not indicate that the laser diameter was adjusted during maintenance. Nevertheless, any change to the laser or its focal position could have resulted in the abrupt shift of strength in Build 6 (Fig. 5.4) back to the levels seen in the first few builds. These results highlight the importance of keeping thorough maintenance records and documenting any/all changes made to machine configuration. If possible, more robust research should be performed to assess the influence of hardware configuration changes, such as laser spot size on metal quality and properties.

While the results of this chapter generally indicate that there are limited changes in the metal porosity and its mechanical properties with reuse, which is at least partly attributed to the top-up powder reuse strategy, stochastic variability and trends due to machine degradation were observed. Therefore, the null hypothesis that negligible variability occurs from build-to-build must be rejected. To reiterate, the stochastic variability of tensile properties between builds typically had CoV values less than that of wrought material. This degree of variability can easily be accounted for in DFAM. However, the stochastic variability of porosity might be more difficult to overcome where fatigue is concerned.

5.3. Conclusion

Inter-build variability resulting from LPBF was evaluated in terms of the metal porosity and tensile properties. Relevant to the progression of changes between builds, the feedstock condition was also assessed in terms of the powder chemistry and PSD. In general, the composition and particle size distribution of the powder did not change progressively with build number (i.e., powder reuse) for any of the six participants. Similarly, there was no systematic change in the porosity characteristics with powder reuse for most machines. The strongest trend noted in the increasing sphericity of the metal from P2 was minimal in magnitude. However, there was a large degree of random variability for all machines that was evident in the average pore size from build-to-build.

Finally, the mechanical properties of the metal were characterized in uniaxial tension. In general, there was no trend in the mechanical properties with increasing build number except for that of P3, where the strength increased with build number. The changes in metal properties for that partner were diagnosed to result from the heat treatment or machine health degradation. Both were found to be possible root causes and responsible for the changes in metal properties trends. Although a change in beam diameter was observed in the laser for P3, the maintenance records did not indicate if or how it was addressed. As such, maintaining machine health and documenting changes made to machine configurations on metal properties are critically important. The effects of this contribution could be more severe to the fatigue properties of the metal. Further work must be performed by the research community to evaluate the influence of machine health on porosity and mechanical performance. Finally, stochastic variability was observed from build-to-build for all machines. Typically, the magnitude of the stochastic

variability was low, with CoV for the strength and ductility similar to or lower than the CoV of the tested wrought coupons.

Chapter 6. Inter-Machine Variability

Chapter 3 introduced the three categories or primary sources of metal variability in LPBF, namely intra-build, inter-build and inter-machine variability. Intra-build and inter-build variability were presented in Chapters 4 and 5. The broadest level of variability is that resulting across metal from multiple machines, or specifically, multiple EOS M290s. Inter-machine variability is one of the least explored types of variability in the research community. It is of substantial importance to the comparison of results between publications as well as the industrial qualification of metal components where multiple machines are utilized. In the round robin program, inter-machine variability was assessed by a comparison of property distributions between the metal of the six participants, and a statistical analysis was performed to identify differences in the metal produced by each machine. Furthermore, an effort has been made to isolate potential root causes of the most significant differences.

6.1. Materials and Methods

Investigation of the metal from machine-to-machine primarily involves the use of results from μCT and tensile testing of the printed coupons. However, the metal microstructure and fractography of the fractured samples are also used to support the results. Table 6.1 contains the number of coupons that were tested by μCT and static loading for each participant. As described previously, the coupons were heat treated and machined prior to μCT scanning and tensile testing. Details of those processes, material characterization, and experimental design and operation can be found in Chapter 3.

Table 6.1: The number of tensile coupons evaluated by μCT scanning and tensile testing for each participant.

	μCT Scanned	Tensile Tested
P1	66	279
P2	59	281
P3	65	268
P4	68	277
P5	34	265
P6	62	282

The evaluation of microstructure in this chapter was performed using Electron Back Scatter Diffraction (EBSD). The system at the UW that supports this technique uses a special detector [Oxford Instruments, UK] inside an Apreo SEM [ThermoFisher Scientific, MA, USA] to capture diffraction patterns from backscattered electrons. These signals can be used to calculate crystallographic information about the microstructure from reference crystallographic data for Ti-6Al-4V (α and β phases), including the orientations of individual grains. An exploratory EBSD assessment was performed on three coupons, including two from P3 and one from P4. This investigation was performed after tensile testing to investigate microstructure as a cause of variance between the metal of the participants. The microstructure was evaluated from the grip section of the coupons to avoid plastic deformation that occurred in the gauge section during tensile testing.

6.2. Results

6.2.1. Microstructure

The microstructure of selected vertical coupons from the builds of P3 and P4 was evaluated by EBSD. Typical phase maps from vertical coupons of both participants are shown in Fig. 6.1. These images show the microstructure of the grip section perpendicular to the loading direction (i.e. perpendicular to the print direction). The grains are colored according to their crystallographic orientation based on an Euler map coloring scheme. Under visual inspection the microstructure is similar between the two participants, warranting qualitative assessment.

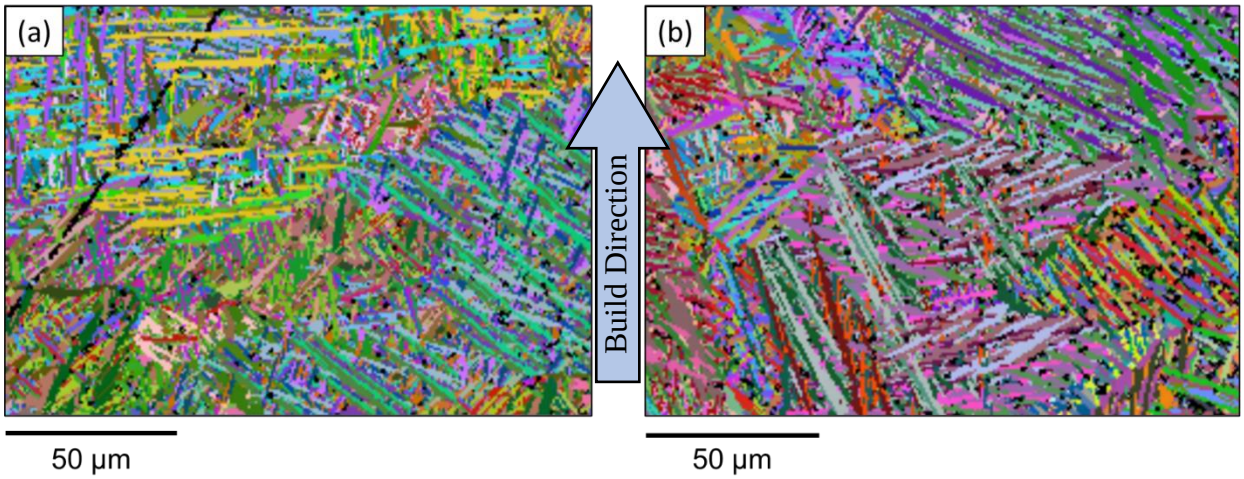

Fig. 6.1: Crystallographic orientation maps of coupons from P3 (a) and P4 (b).

Although EBSD is useful for understanding crystallographic texture, it also supports an easy identification of individual grains, as it is used here. Metrics of each individual grain from all coupons measured by EBSD were analyzed to determine any differences in their size. The mean breadth (width), length and area of grains from both participants are shown in Table 6.2. While the values for P3 are slightly higher than P4, the standard deviations in size are large and prevent a robust statistical analysis. Additionally, the grain size distributions are not gaussian due

to the minimum detection size set to 25 pixels to avoid erroneous grain measurements, making the standard deviations an inaccurate measure of the true variability. Plotting the grain size distributions as cumulative density plots in Fig. 6.2 reveals that the slightly higher average grain size of metal from P3 is due to a higher frequency of large grains (longer and wider). The frequency of small grains appears to be similar between the machines. Based on this preliminary investigation of the microstructure, there appear to be some small differences in grain size between the metal of P3 and P4. A more thorough comparison of the grain structure is warranted and is currently underway.

Table 6.2: Average grain size ± the standard deviation for P3 and P4.

	Length (µm)	Breadth (µm)	Area (µm²)
P3	13.95 ± 9.12	3.97 ± 1.77	26.81 ± 25.51
P4	13.6 ± 7.49	3.83 ± 1.61	24.21 ± 18.92

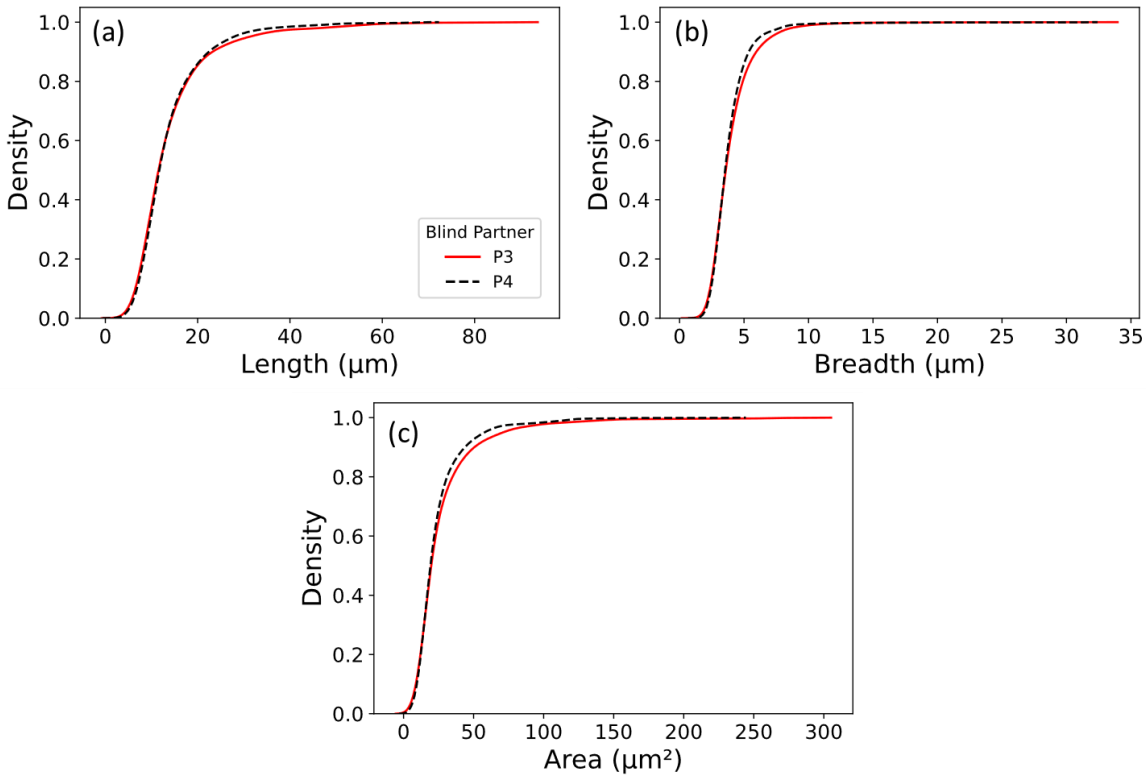

Fig. 6.2: Cumulative density plots for the grain length (a), breadth (b), and area (c) for P3 and P4.

6.2.2. μCT

Porosity of the metal produced by each of the participants was evaluated by μCT and used to characterize the inter-machine variability. Coupons were selected from all six prints of each participant according to the scheme described in Chapter 3. The porosity distributions of metal from these coupons were developed and are presented in Fig. 6.3 as kernel density estimates. Specifically, the average diameter and sphericity of pores were calculated for each coupon and are shown in Fig. 6.3 (a) and (b), respectively. The pore diameter distribution has a strong positive (i.e., right) skew towards large pores. From comparison of the individual distributions for the metal of each machine, the distributions of P1-P5 are all similar in shape and peak location. However, the distribution of P6 is much wider, corresponding to a high frequency of large pores. In comparison, the sphericity is more normally distributed. Both the overall distribution and the underlying distributions of many machines are approximately gaussian, however there are shifts in the peaks between the different machines. Most notable, the distribution of P6 is shifted towards lower sphericity than the other machines.

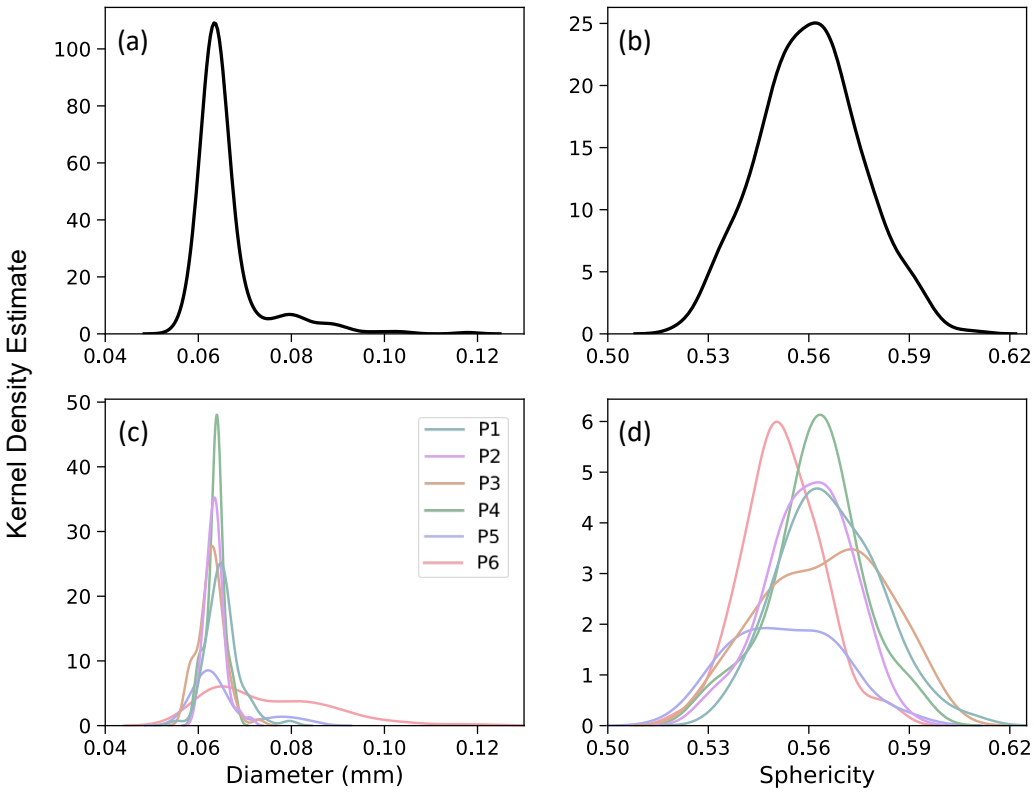

Fig. 6.3: Pore diameter and sphericity of the overall distribution ((a) and (b)) and for each participant ((c) and (d)).

To explore the differences observed in Fig. 6.3 further, the distributions were evaluated statistically. The pore diameters and pore sphericity are shown in Fig. 6.4 (a) and (b), respectively. The box plots in these figures represent the medians and upper and lower interquartile ranges (IQR). The outliers of each distribution are indicated by the individual data points. As evident in Fig. 6.4 (a), the metal of P6 contains substantially larger pores than the remaining participants. Interestingly, the average sphericity was also lower for P6 than all other machines except for P5. A one-way ANOVA was performed on this data, and the resulting p-values are shown in each figure. Both sets of data have p-values below 0.05, indicating that there are significant differences in porosity of metal between the machines. Furthermore, pair-wise

Tukey tests were performed, and the results are shown in Fig. 6.4 (a) and (b). Bars between two participants that are annotated with a '*' indicate they are significantly different. As evident in Fig. 6.4 (a), the mean pore diameter of metal for P6 is significantly larger from all other machines, whereas the pore diameter of metal from all other participants is statistically similar. The pore sphericity exhibited more distinct variation. Although the pore sphericity for the metal of P5 and P6 is statistically similar, it is significantly different from the sphericity of pores in the metal from P1, P3, and P4; no other statistical differences were observed.

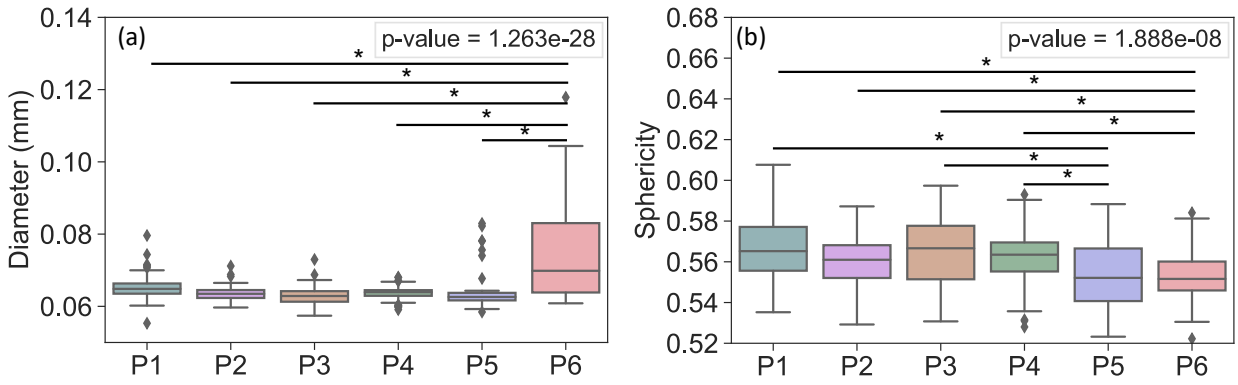

Fig. 6.4: Box plots for the average pore diameter (a) and sphericity (b) for each participant. Note that p-values from the ANOVA are annotated in each plot ($p \leq 0.05$ is significant). Significantly different pairs identified by an ad-hoc Tukey test are identified by bars labelled '*'.

To further understand the differences in the porosity of metal produced by P6, cumulative density plots for the pore diameter distribution are plotted in Fig. 6.5 (a). The entire distribution of pores for the metal of all six participants (i.e., including all pores in all coupons evaluated) shows that there are minimal differences between the majority of participants (P1-P5). However, the metal from one machine (P6) shows a higher frequency of large pores. Further analysis was performed by counting the number of large pores (greater than 0.125 mm diameter) per scanned coupon as shown in Fig. 6.5 (b). The metal from P1-P5 contains a similar number of large pores

per coupon with averages of 7-12 (i.e. 0.012-0.02 per mm^3), whereas P6 shows a mean of 59 pores per coupon (0.098 per mm^3), which exceeds even the outliers of the other five suppliers. Note that the outliers in the distribution for P6 indicated that as many as 179 large pores were present per coupon (0.298 per mm^3).

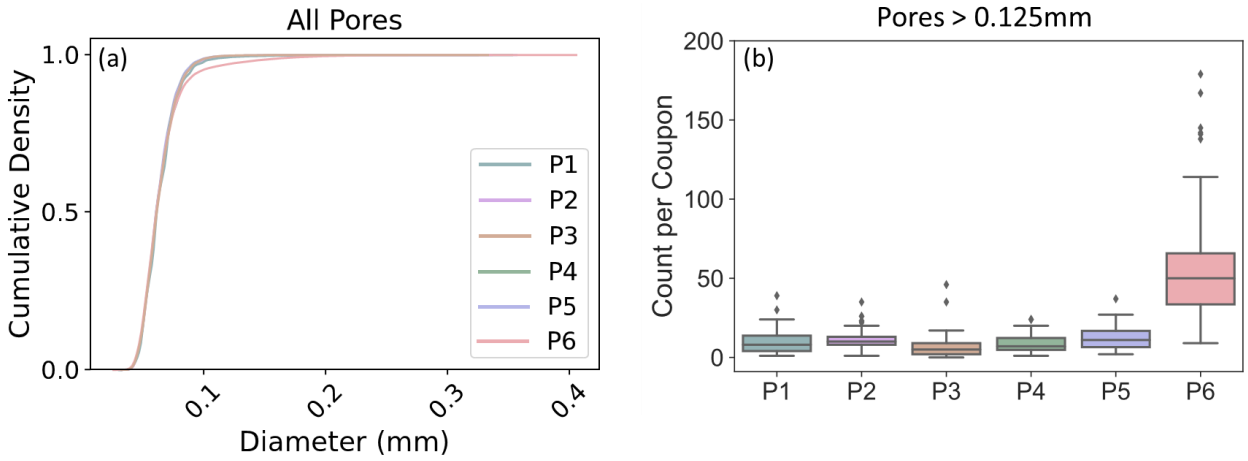

Fig. 6.5: A cumulative distribution plot (a) depicting the frequency of pore sizes found in the metal of each participant. Box plots for each participant showing the frequency of large pores are presented in (b), where the distribution depicted by each box is comprised of the number of pores larger than 0.125 mm per coupon.

Selected µCT slices from a vertical coupon produced by P6 are shown in Fig. 6.6. Each image represents a slice within the x-y plane of a coupon, which is in-plane with the printed metal layers. It is important to note that all three slices show a distinct linear arrangement of large pores, which are visible as dark gray entities amidst the light gray background. The lines of pores are outlined in yellow to aid in identification. While this feature was common in the metal of P6, it was not identified in the metal of the other participants. An additional feature was observed in a scanned coupon from P6 as shown in Fig. 6.7. This coupon contained two

intersecting lines of pores, with an interior offset angle of approximately 67° between the two lines. The significance of that alignment will be discussed later in this chapter.

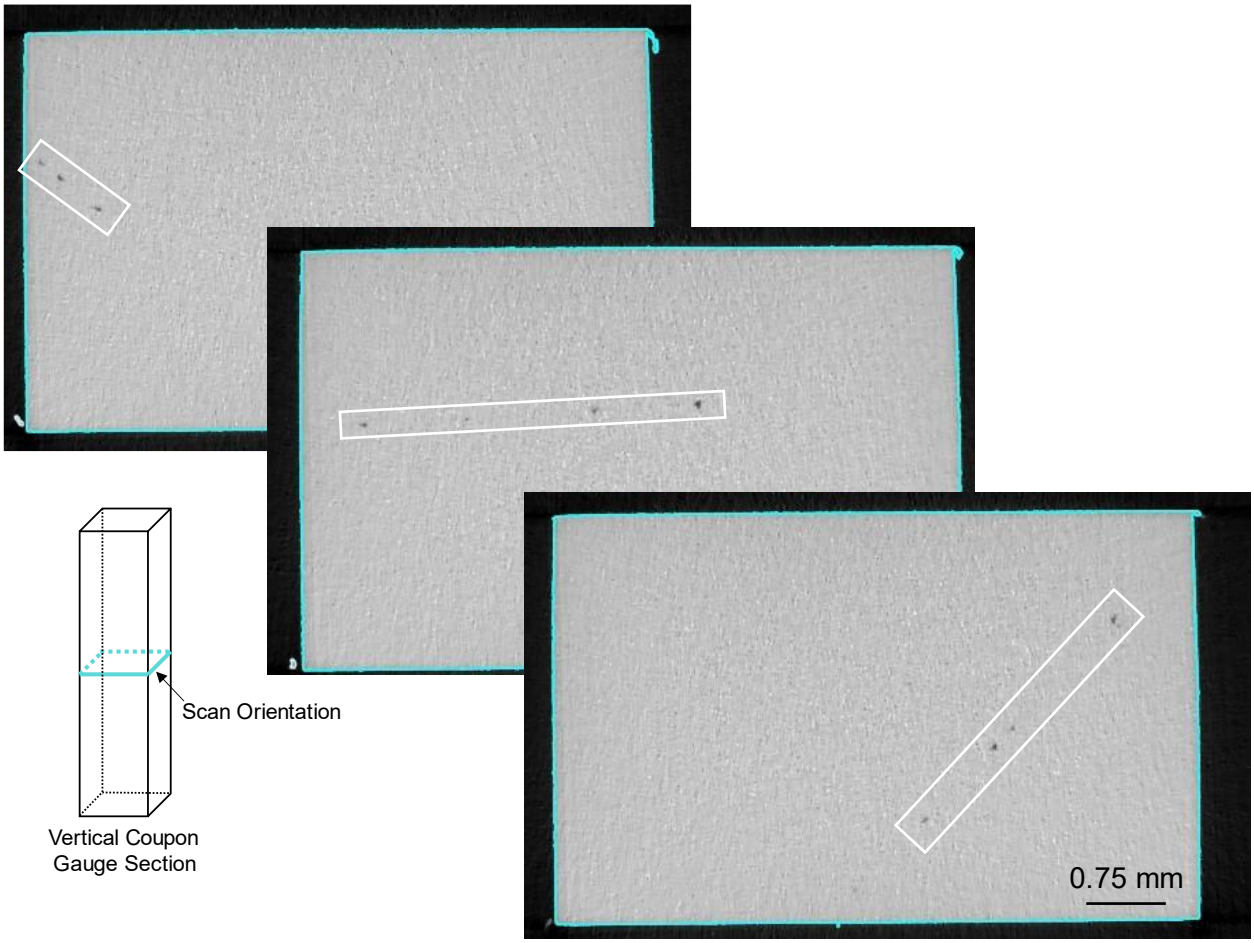

Fig. 6.6: µCT slices of a vertical coupon from P6 showing the build plane, perpendicular to the loading direction. The scans reveal straight lines of large pores that are outlined in white. A schematic indicates the orientation of the images.

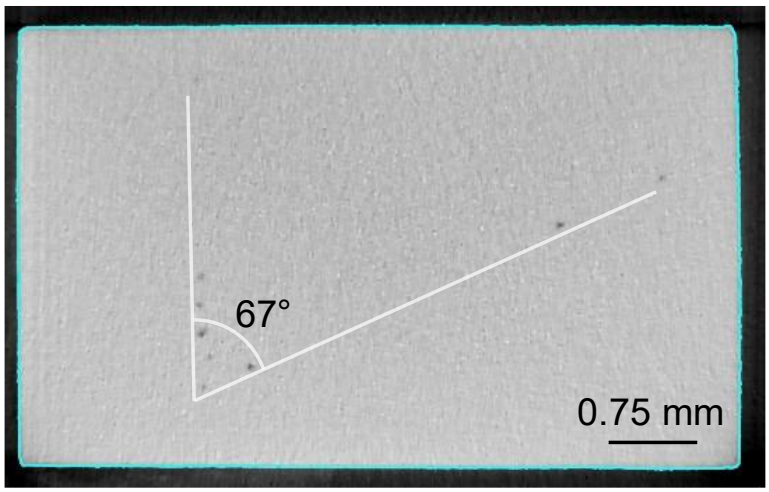

Fig. 6.7: Micro CT slice of a vertical coupon from P6 containing two intersecting lines of large pores, and with an intersection angle of 67°.

In summary, the porosity distributions of metal from P1-P5 showed similar characteristics. The average pore size was statistically similar between the participants, except for the significantly larger pores in the metal of P6. Overall, there was a larger degree of variability in the sphericity of pores from the participants than the pore diameter. In addition, the porosity characteristics of the metal from P5 and P6 were significantly different from the rest. The metal of P6 contained a high frequency of large pores with lower sphericity which were distributed in lines, which is a feature that is unique to their metal.

6.2.3. Tensile Testing

Distributions of the YS, UTS, and strain at failure of metal for each participant are presented in Fig. 6.8. The distributions in YS and UTS reveal that the overall distributions, i.e., representing coupons from all participants, are approximately gaussian. The individual distributions for the metal of each participant are plotted beneath the overall distribution. Evident from these individual contributions, it is apparent that there is a shift in the distributions between

the metal of different machines. In particular, the horizontal coupons of P1 and P3 have lower strength than the other participants, leading to the bimodality present in the overall distribution of the YS of the horizontal coupons. In contrast to the overall strength distributions, the overall strain at failure distributions are bimodal. The distributions of both the vertical and horizontal coupons exhibit secondary peaks or shoulders at high strain at failure values, which is more pronounced for the horizontal coupons. In examination of the distributions for each participant, there is a separation between P1 and P3 with respect to the remaining machines. The metal of both P1 and P3 has higher strain at failure compared to the other participants, which causes the bimodality of the overall distributions.

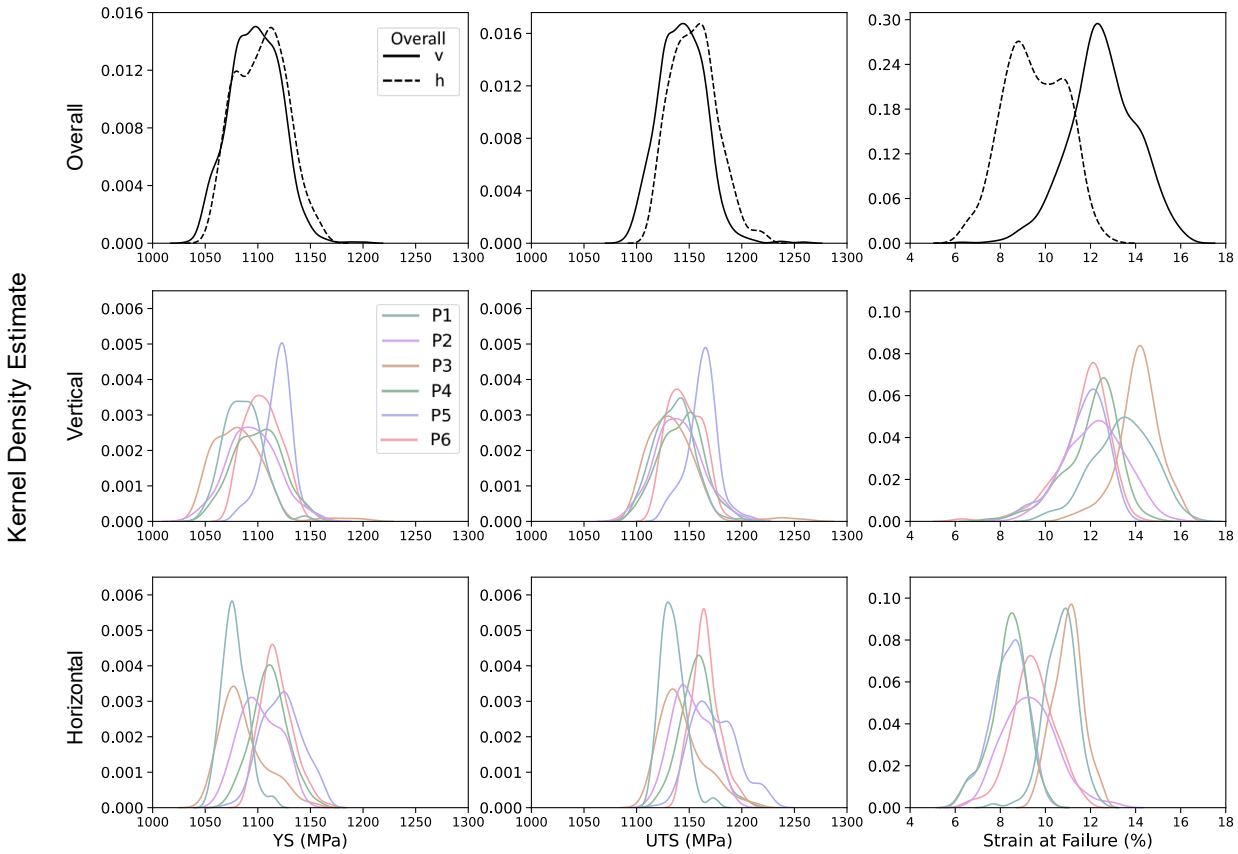

Fig. 6.8: Tensile property distributions for the vertical (middle row) and horizontal (bottom row) coupons of each participant and the overall distributions (top row) of all coupons.

Table 6.3 presents a summary of the mechanical properties, including the elastic modulus (E), YS, UTS, and strain at failure (%el). The overall mean property values were obtained by combining the data from all six participants and are compared to the minimum values specified by ASTM F2924 for annealed PBF Ti-6Al-4V [61]. Note that nearly all the mean values exceed the minimum requirements. The mechanical properties of metal from the individual machines were also compared to the standard specifications. While most meet the tensile performance requirements defined by the standard, those obtained from a few machines do not. Specifically,

the strain at failure for the horizontal coupons of P2, P4, P5, and P6 do not meet the minimum value of 10%. It is important to note that the metal from P1 and P3 exhibits higher ductility and lower strength than the other participants.

Despite the potential concern with properties of the horizontal metal in Table 6.3, the results exhibit a high degree of consistency when comparing metal across machines, with only a few exceptions. The Coefficients of Variation (CoV) were calculated for the properties of each participant and coupon orientation and are listed in Table 6.4. Interestingly, the CoV for the YS and UTS were very low, with maxima of only 2.2% and 2.4%, respectively. Variability in the strain at failure was greater, with a maximum CoV of 12.6%.

Table 6.3: The average tensile properties for each participant alongside the average across all machines (overall). The minimum values required by ASTM for Grade 5 Ti-6Al-4V are included for comparison. Properties failing to meet the ASTM requirements are colored in red.

		P1	P2	P3	P4	P5	P6	Overall	ASTM
E (GPa)	V	125	130	127	123	126	123	125	-
	H	116	125	127	111	125	115	120	
YS (MPa)	V	1086	1095	1082	1100	1119	1104	1098	825
	H	1078	1102	1086	1111	1123	1118	1103	
UTS (MPa)	V	1136	1140	1134	1142	1162	1146	1143	895
	H	1134	1152	1144	1158	1174	1166	1155	
el (%)	V	12.6	11.4	13.2	11.3	11.0	11.0	11.8	10
	H	10.7	9.3	11.0	8.4	8.3	8.4	9.1	

Table 6.4: The coefficient of variation of each property for each participant and print orientation.

		P1	P2	P3	P4	P5	P6	Overall
CoV of E (%)	V	7.1	5.1	4.6	6.0	5.1	4.9	5.9
	H	4.8	5.0	4.1	5.8	5.3	5.3	7.1
CoV of YS (%)	V	1.6	2.1	2.4	2.0	1.2	1.5	2.1
	H	1.1	1.7	2.0	1.5	1.7	1.3	2.2
CoV of UTS (%)	V	1.6	1.9	2.2	1.8	1.3	1.4	1.9
	H	1.0	1.5	1.9	1.4	1.8	1.1	1.9
CoV of %el (%)	V	9.6	10.5	6.6	9.9	8.9	9.9	11.8
	H	6.6	12.6	5.9	9.3	9.6	10.1	14.0

It is also apparent from Table 6.3 that there are some differences in the mechanical properties of the horizontal and vertical coupons. For every machine, the horizontal coupons exhibited lower strain at failure than the vertical coupons. Percent differences between the horizontal and vertical coupons ranged from 18-30%. The difference in strength between the two orientations was inconsistent and less significant, with a maximum percent difference of 2% for the UTS. To illustrate these differences, the overall average YS, UTS, and strain at failure of the metal from all machines are shown in Fig. 6.9 for both orientations.

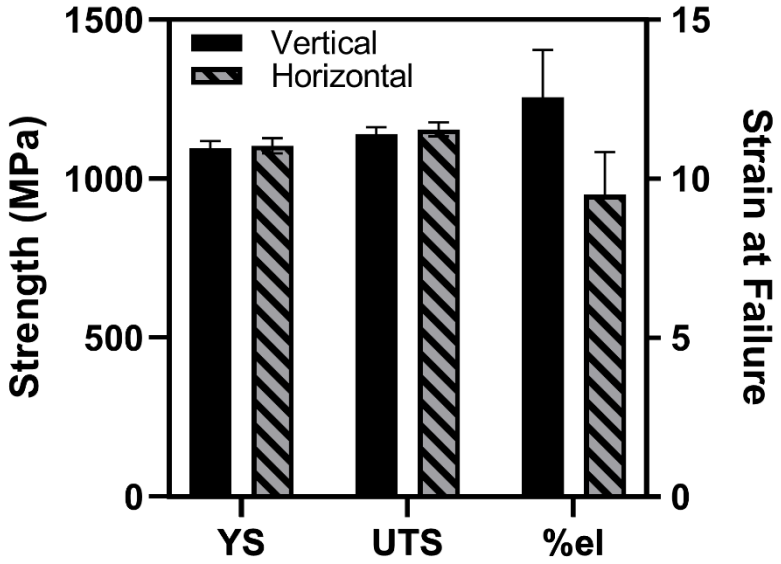

Fig. 6.9: Average mechanical properties of the metal from all participants, separated by orientation.

To understand the primary contribution to the difference in strain at failure of the vertical and horizontal coupons evident in Fig. 6.9, fracture surfaces from the two orientations were evaluated metallographically. Representative horizontal and vertical coupons from Build 1 of P4 exhibiting typical properties were selected and mounted in a hot press. The samples were ground

and polished to reveal the cross-section of the fracture surface and Kroll's etchant was used to reveal the underlying microstructure and detail the crack path. Composite images of the entire length of the fracture surface were taken with an optical microscope and are shown in Fig. 6.10.

The fracture paths for specimens with vertical and horizontal orientations are shown in Fig. 6.10 (a) and (b), respectively, and exhibit similar features. Both coupons have distinct shear lips that border (or bound) the interior flat region of fast fracture. The fast fracture regions of the two coupons are similar in size and texture, with both exhibiting a rough appearance. Magnified sections of the fast fracture regions of these fractographs are shown in Fig. 6.11 (a) and (b) for the vertical and horizontal coupons. An example of fracture along a grain boundary is annotated for the vertical coupon in Fig. 6.11 (a). No clear examples of this type of fracture were found in the path of fracture of the horizontal specimens, potentially indicating a difference in failure mode.

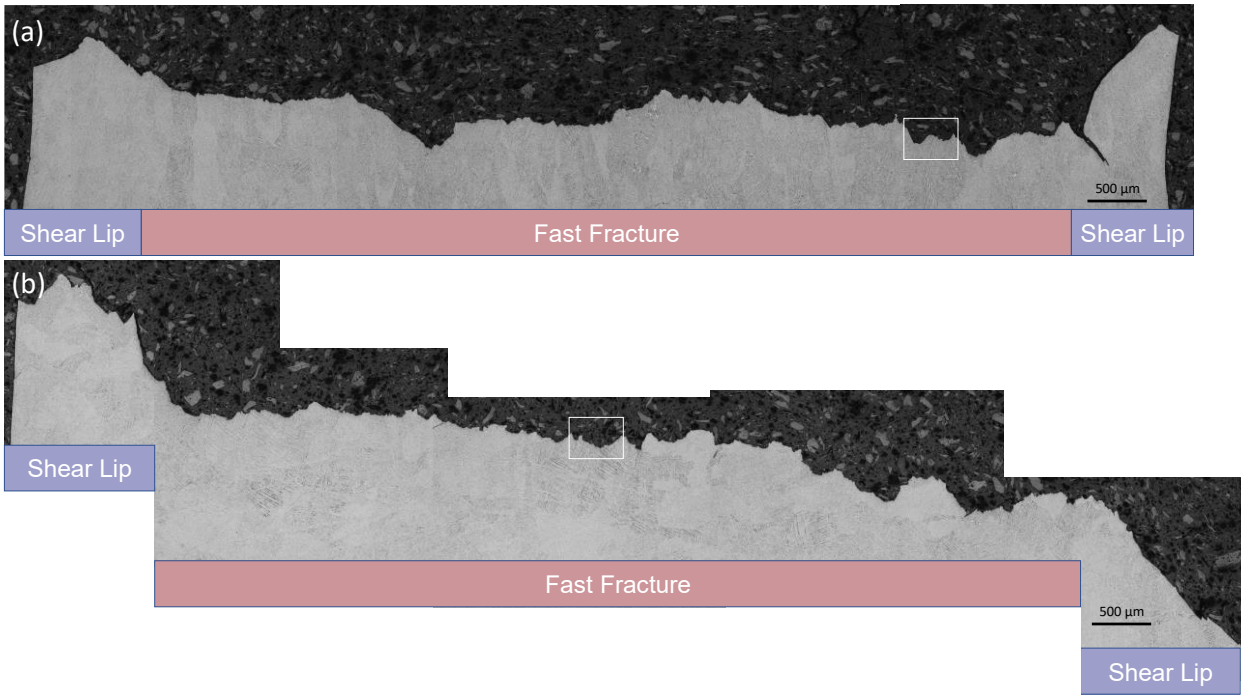

Fig. 6.10: Micrographs of representative (a) vertical and (b) horizontal fracture surface profiles. The vertical direction is the axis of uniaxial tension. Boxed regions are shown at higher magnification in Fig. 6.11.

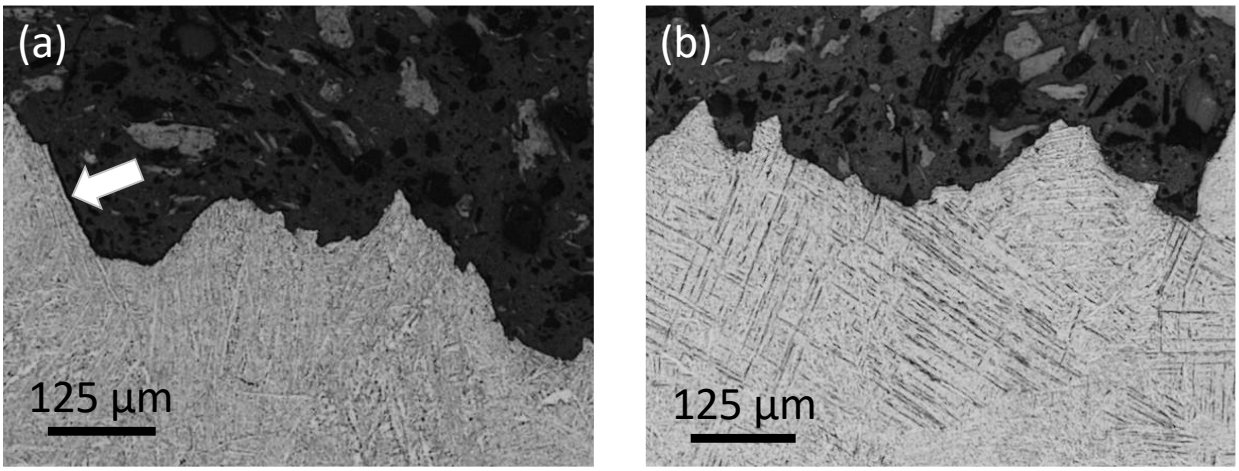

Fig. 6.11: Magnified regions of the flat fast fracture region of the fractographs shown in Fig. 6.10 for the (a) vertical and (b) horizontal coupons.

To investigate the inter-machine variability more thoroughly, the mechanical properties were further examined through the use of boxplots and statistical tests. Fig. 6.12 shows boxplots for the property distributions for each participant along with the p-values from a one-way ANOVA. It is important to note that despite the large degree of consistency in metal properties as inferred by the CoV values, there were significant differences in the properties between participants for both the vertical and horizontal orientations. Ad-hoc Tukey tests were applied to each property to identify the individual differences and the pairs of statistically similar participants are annotated on the figure.

Several important observations can be made from the Tukey test results Fig. 6.12. First, the horizontal coupons exhibit more statistically significant differences in the mechanical properties between machines than the vertical coupons. Secondly, for the vertical coupons, the strain at failure shows a clear grouping of P2, P4, P5, and P6. Although there are some statistical differences between them, they stand apart from results of the metal from P1 and P3. Finally, in

addition to the aforementioned high ductility and low strength of metal from P1 and P3 when compared to the other machines, the metal of P5 shows the opposite relationship, with significantly higher YS and UTS for the vertical coupons.

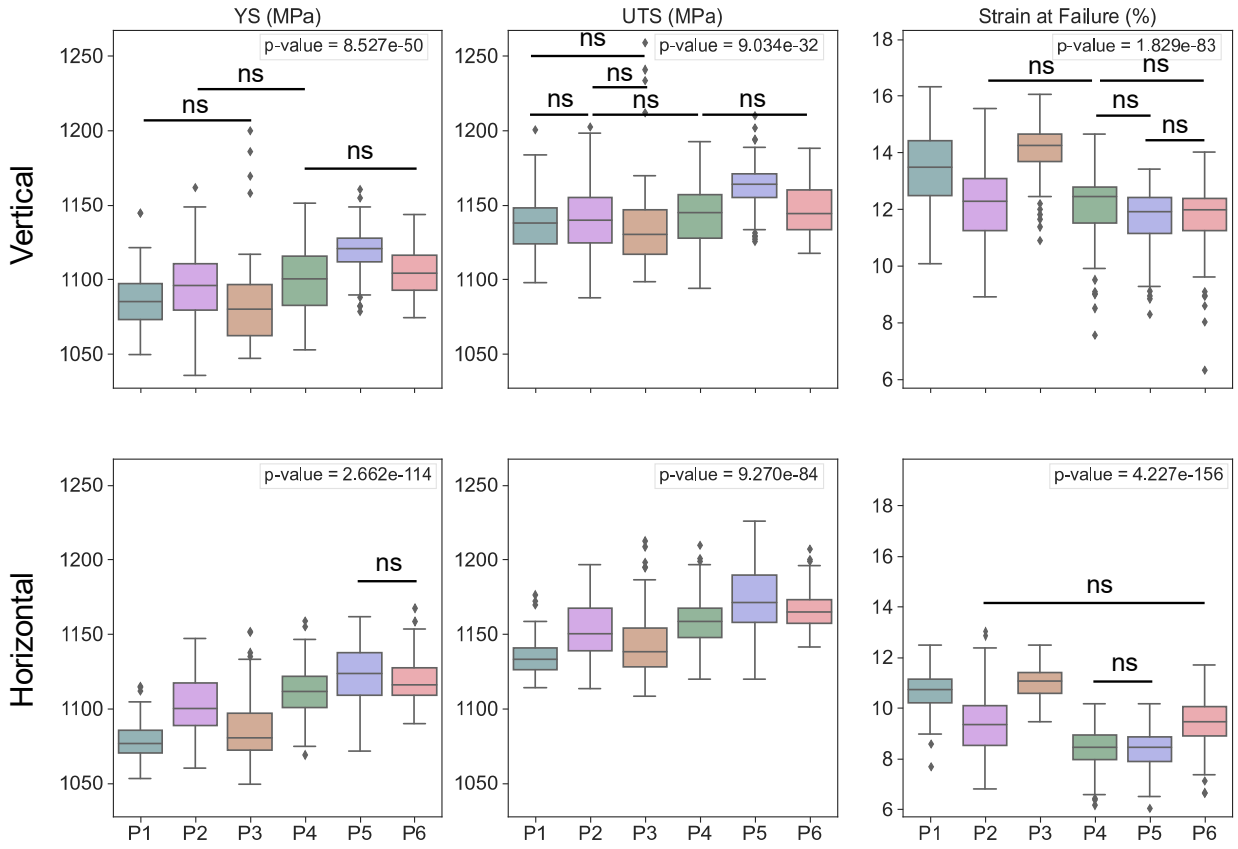

Fig. 6.12: The average tensile properties for the horizontal and vertical coupons of each participant including the YS, UTS and strain at failure. The p-value from a one-way ANOVA is noted in each subplot. Non-significant pairs identified by an ad-hoc Tukey test are identified by bars labelled 'ns'.

In addition to their value in comparing the means, boxplots are also useful for identifying outliers in the metal from each participant. The detrimental outliers are those with low mechanical properties, most of which occur for the strain at failure of the vertical coupons. The fracture surfaces of several of these outlier specimens from P4, P5, and P6, which had the worst

performing outliers, were chosen for fractographic analysis. The fracture surfaces from the specimens of each of these three participants, are shown in Fig. 6.13. The strains at failure for these coupons were 8.51%, 8.58%, and 6.32%, for P4, P5, and P6, respectively. For the coupons from P4 and P5, the fracture surfaces have a shear lip that extends around most of the circumference. A flat, fast fracture region in the center extends to the edge of the coupons, interrupting the shear lips. A closer examination of the coupon from P4 where the flat fracture extended to the edge did not reveal any features of interest. However, the same region on the coupon of P5 revealed large voids, as shown in the enlarged view. Further investigation of the machined surface of the gauge section of the coupon from P5 showed that large LOF voids were exposed by the machining process along the entire face of the coupon.

The fracture surface of the specimen for P6 in Fig. 6.13 is macroscopically unique from those of P4 and P5. The shear lip surrounds the entire fracture surface, with an enclosed flat region of fast fracture. Higher magnification of the fast fracture region reveals a large number of smooth regions distributed on this surface that are approximately 200 μm in diameter, as well as partially melted powder particles. These features are LOF voids that coincide with the fracture surface.

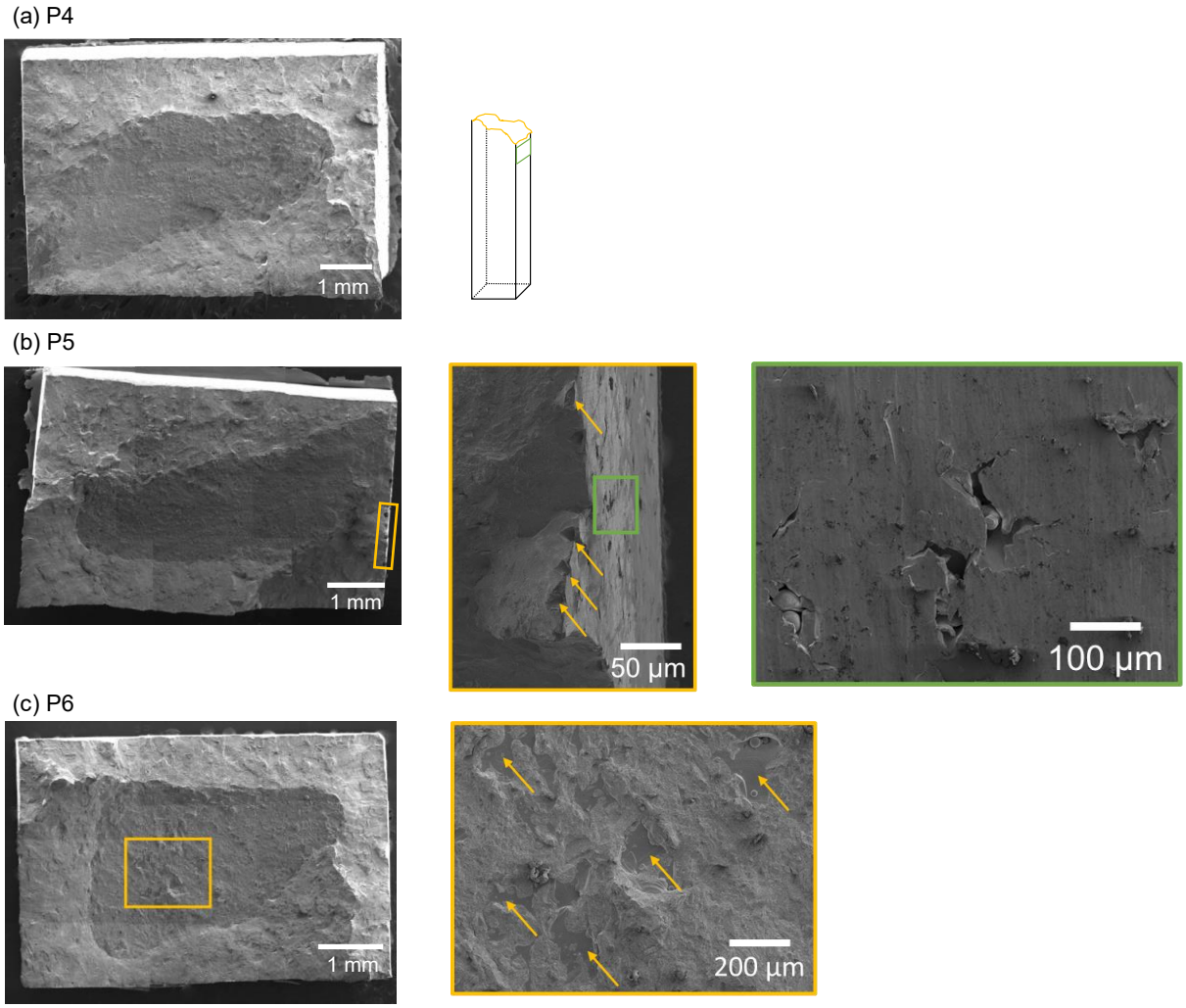

Fig. 6.13: Stitched SEM fractographs of vertical coupons with low strain at failure from P4 (a), P5 (b), and P6 (c). Regions of interest are shown with higher magnification alongside the entire fracture surface. A schematic alongside (a) indicates the locations where enlarged images were taken.

Weibull probability distributions are plotted for the YS, UTS, and strain at failure of each participant in Fig. 6.14, Fig. 6.15, and Fig. 6.16, respectively. Plotting the data according to the Weibull probability can indicate consistency of the mechanical properties and the reliability of the metal. A steeper slope, i.e. the Weibull Modulus (m), indicates greater consistency of the metal. In the cases of the YS and UTS, the distribution is not linear when plotted according to the

Weibull probability axes. The distributions in strength suggest that the 2-parameter Weibull distribution is not a good fit to the data. As such, power law fits were not applied to these plots and a three parameter Weibull model or other extreme value approach may be more appropriate for describing these distributions. Alternatively, the distributions are bimodal, but the distributions in Fig. 6.8 did not show strong bimodality.

The Weibull distribution of the strain at failure, however, follows a much more linear distribution, as evident in Fig. 6.16. Power law regression was applied to the horizontal and vertical coupon data for each participant, and the Weibull moduli are annotated on each plot. Overall, the slopes range from 11.5-18.7 for the vertical coupons and 9.8-21 for the horizontal coupons. For most participants (P1, P3, P4, P6), the Weibull modulus of the horizontal coupons is greater than that of the vertical coupons. However, the difference is only large for P1, with vertical and horizontal moduli of 12.9 and 18.5, respectively. In addition, some of the Weibull distributions have tails, i.e. a group of coupons with low strain at failure and a higher Weibull modulus. This is especially true for the horizontal coupons of P2, P3, P4 and P5. Furthermore, the distribution in strain at failure of the horizontal coupons of P2 is significantly less linear than the other distributions.

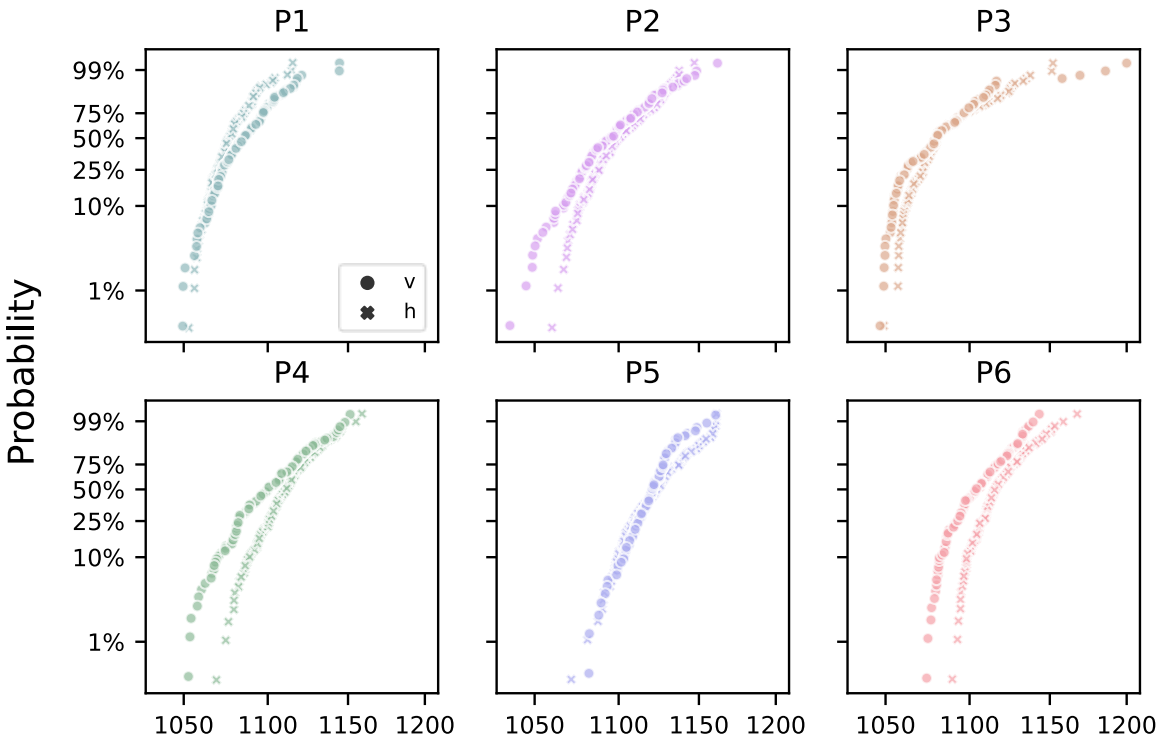

Fig. 6.14: Weibull probability distributions of the YS for the vertical and horizontal coupons of each participant.

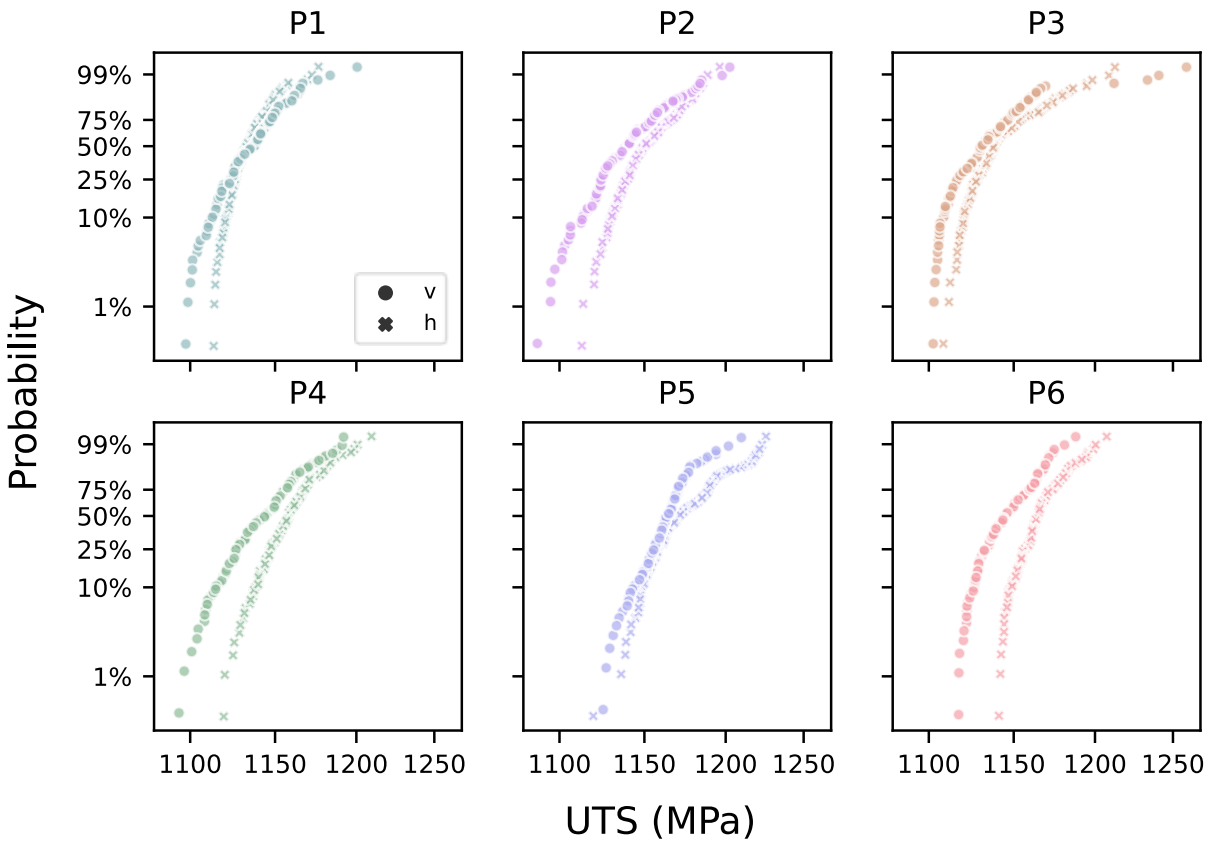

Fig. 6.15: Weibull probability distributions of the UTS for the vertical and horizontal coupons of each participant.

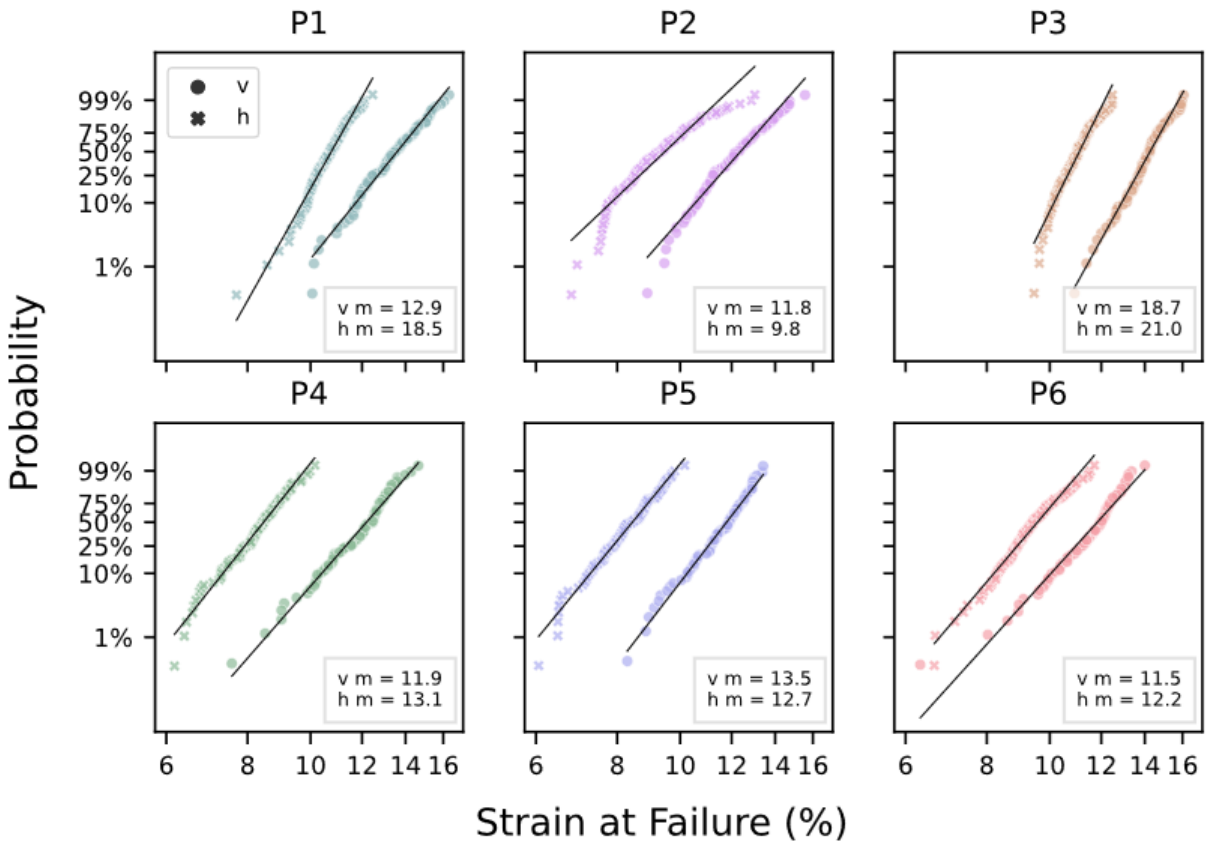

Fig. 6.16: Weibull probability distributions of the strain at failure for the vertical and horizontal coupons of each participant. Power law regressions are plotted for each coupon orientation and the slopes are annotated on each plot.

To understand the effects of porosity and its variability on the mechanical performance of the metal, an evaluation of the strain at failure of the metal was performed with respect to the porosity distributions. The porosity was characterized in five ways, including the: i) average pore diameter, ii) average pore sphericity, iii) maximum pore diameter, iv) number of pores with a diameter greater than 0.125 mm, and v) the 90th percentile pore diameter (d90). Fig. 6.17 plots the strain at failure versus these porosity metrics including the metal from all participants. Since µCT scanning was only performed on vertical coupons, this figure is restricted to that orientation. The porosity metrics (i-v) were calculated for the entire pore distribution for each

coupon, and the strain at failure of each coupon was plotted versus its porosity metrics in Fig. 6.17. As evident from the Pearson correlation coefficients (r), there is no apparent correlation between the strain at failure and any of the porosity metrics that were considered, although a few coupons with especially high levels of porosity do exhibit low ductility. The strongest correlation was identified for the count of large pores, with a correlation of -0.328. Although this correlation is not very strong, further analysis of these responses was conducted.

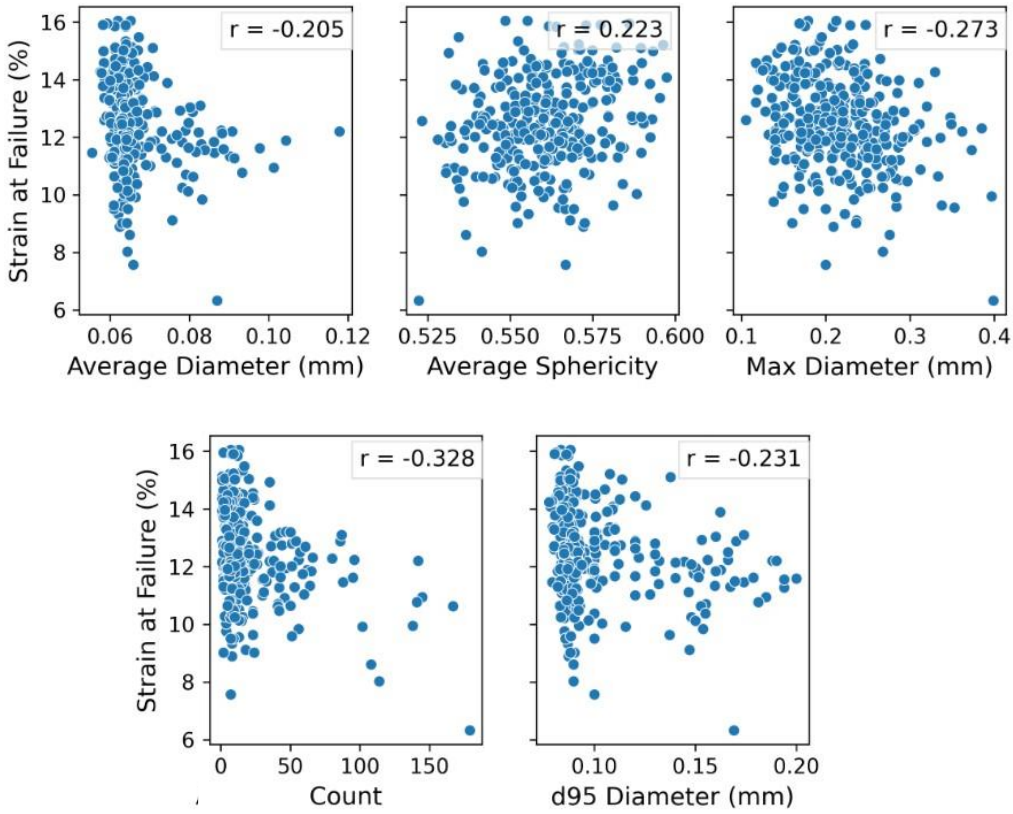

Fig. 6.17: An examination of the metal strain at failure with respect to the average pore diameter, average pore sphericity, maximum pore diameter, number of pores with diameter > 0.125 mm, and d90 pore diameter. The Pearson correlation coefficients (r) are annotated on each plot.

To further explore the relationship between the porosity and strain at failure of the vertical coupons, the average diameter and average sphericity of pores from each coupon were recalculated using a restricted portion of the entire porosity distribution. Since the greatest correlation in Fig. 6.17 was noted for the count of large pores, the average diameter and sphericity of the pores greater than 0.125 mm diameter were calculated for each coupon, and the results are plotted in Fig. 6.18 (a). Surprisingly, the correlation between strain at failure and diameter or sphericity of this subset of pores decreased with respect to the original correlation. Finally, the pore distributions within each coupon were restricted to pores greater than its d90 diameter, and the average pore diameters and sphericity were evaluated again. These new assessments are shown in Fig. 6.18 (b). There is a substantial increase in the correlation between strain at failure and porosity, however the strengths of the correlations are still limited, with values of -0.281 and 0.394, respectively.

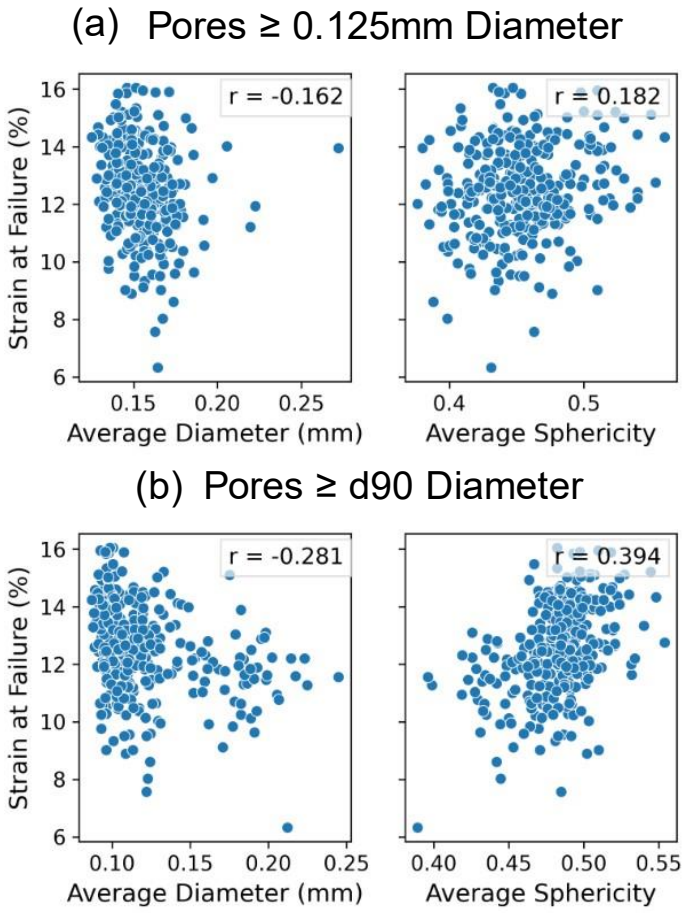

Fig. 6.18: An examination of the metal strain at failure with respect to the average pore diameter and average sphericity of pores greater than 0.125 mm (a) and of pores greater than the d90 diameter (b). Pearson correlation coefficients (r) are annotated on each plot.

The measures of porosity applied in Fig. 6.17 and Fig. 6.18 do not account for the spatial position of pores with respect to each other or their proximity to free surfaces. In addition, they do not account for multiple pore characteristics simultaneously. To capture the potential synergistic effect of multiple pore characteristics, the modified Void Descriptor Function (VDF) was used to estimate the pore severity and to evaluate the correlation with strain to failure as shown in Fig. 6.19. This function was created by Watring et al. and is based on the original work of Erickson et al. [81,82]. It incorporates the effects of pore clustering, sphericity, pore-pore

interactions, and distance to the nearest free surface using Laplacian mathematics. The general form of this equation is presented in Equation 6.1. Each of the four fractions in the exponential corresponds to one of the porosity characteristics, i.e., pore clustering, pore sphericity, pore-pore interactions, and distance to the nearest free surface. Further details of this equation can be found in the study by Watring et al [81].

$$VDF(v_{ref}, P) = \sum_{i=1}^{n} \frac{v_i e^{-\frac{S_i}{aL} - \frac{|c - r_i^*|}{\rho c} - \frac{a_i}{\gamma} - \frac{k_i}{\zeta}}}{V_{gauge}} \qquad \text{Eqn. 6.1 [81]}$$

Each of the four terms is weighted using Bayesian optimization to maximize the correlation coefficient between the strain at failure and the VDF value. Despite the expansion in void characteristics that are considered using this approach, there is no apparent improvement in the correlation with strain at failure, with overall correlation coefficient of only 0.036.

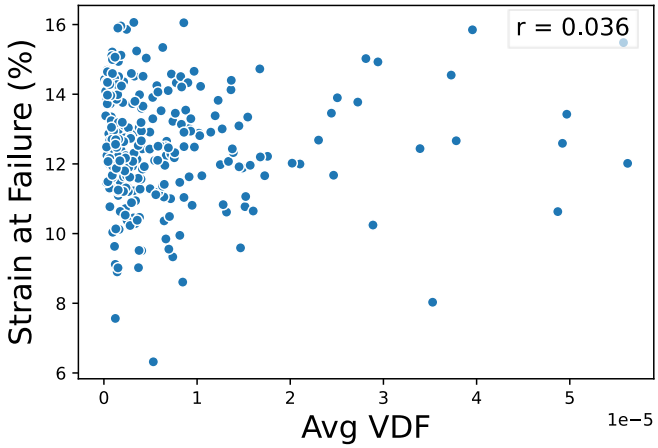

Fig. 6.19: Strain at failure plotted against the VDF of each coupon.

6.3. Discussion

The micrographs shown in Fig. 6.1 reveal that the microstructure of the printed and heat treated metal is a combination of HCP α and BCC β phases with some retained martensite, which is contained within the boundaries of prior β grains. In both EPBF and LPBF, thermal gradients form along the z-direction of the build chamber due to the layer-wise melting that occurs. This thermal gradient, combined with remelting of the previously melted metal, creates elongated grains with their primary axis oriented along the build direction [60,83]. For Ti-6Al-4V, Simonelli et al. thoroughly explored the phase transformations that occur in LPBF [60]. The most dominant feature of the microstructure is the elongated β phase grains, termed prior β grains, which are oriented approximately vertically from the build plate. As the newly solidified metal rapidly cools, it undergoes a phase transition, with the β almost completely transforming into α', a martensitic HCP phase that possesses higher strength and lower ductility than the parent β phase [84]. One consequence of the transformation is that the prior β grain boundaries remain, resulting in small α' grains contained within the confines of the original prior β grain boundaries. During the annealing heat treatment that was performed, the martensite within the prior β grains largely decomposes into a mixture of α and β, where α is the dominant phase. This is expected to result in a high strength alloy that is more ductile than the original martensitic structure. Results from a visual analysis of the microstructure via SEM and using EBSD showed that there was significant variability in the grain size and grain morphology within individual coupons.

To assess if there is variability in the microstructure of metal between participants, representative tensile coupons were chosen from P3 and P4 for further analysis. The sample size was small due to the long preparation time needed for the EBSD sample preparation. An

evaluation of the average grain sizes (Table 6.2) showed that the metal of P3 exhibited a slightly larger grain length and breadth than those parameters for the metal of P4. However, these differences were small in comparison to the large standard deviations in grain dimensions. In addition, the grain size distributions were heavily skewed to smaller grains. As a consequence, the standard deviation is not the most accurate representation of the variance in the data.

To pursue a better understanding of the differences in grain size of metal between P3 and P4, cumulative density plots were generated (Fig. 6.2). This approach to presenting the data shows that there is a clear difference in the distributions for the metal of P3 and P4. The microstructure of metal from P3 consists of a higher frequency of large grains (length, breadth and area) than P4. However, the composition of small grains is similar for the two participants. The influence of the differences in microstructure and its origin will be addressed later.

Analysis of the μCT data revealed that the pore size distributions of metal built by the machines of P1-P5 were not statistically different, whereas the metal of P6 was substantially different from all other participants. The average effective diameter of pores within coupons from P6 was 0.08 mm, compared with 0.07, 0.06, 0.06, 0.06, and 0.07 mm for P1-P5, respectively (Fig. 6.4 (a)). Although the quantity of small pores (effective diameter less than ~75 μm) was similar across all machines as shown in Fig. 6.5 (a), the number of large pores was not. Specifically, the metal of P6 contained a larger maximum pore size, as well as a greater number of large pores with effective diameter greater than 0.125 mm, as shown in Fig. 6.5 (a) and (b), respectively. The metal produced by P6 contained an average of 59 pores per coupon (0.098 per mm^3) with an effective diameter greater than 0.125 mm, which surpassed even the outliers of metal analyzed from the other participants. Another unique observation regarding the metal of P6

is that the large pores were typically distributed in lines like those shown in Fig. 6.6. Similar porosity patterns were not observed in the metal of other participants.

Based on the unique porosity and pore distribution in the metal produced by P6, further evaluation of the printing process was conducted. The machine used by P6 was vetted before the round robin began and complied with the hardware setup and maintenance history requirements of the study. In addition, the process parameters and operating procedures used in the builds of P6 were verified to be in accordance with the PCD. That suggests that the most likely cause of the high frequency of large voids is related to software or hardware factors, such as rake defects, optics or laser inconsistencies, or issues with gas flow. But issues attributed to powder raking were ruled out due to the unique pore alignment visible in Fig. 6.7. The two intersecting lines of pores in this μCT slice are likely formed in adjacent layers. The laser melts through multiple layers of powder in each pass, which can cause the generation of pores within a previously deposited and consolidated layer of powder [85]. This reasoning is reinforced by the approximate 67° angle between the two lines of pores, which is consistent with the angular rotation of the laser hatching pattern in consecutive layers. Defects related to raking of the powder, such as recoater damage or material adhered to the blade, would form troughs through the powder bed along its direction of travel. The alignment of pores would not change direction from layer-to-layer [86]. Hence, it is very unlikely that the porosity was recoater induced.

Another potential contributing factor to the porosity in metal of P6 is the age of the machine, which could be relevant to the optics, laser, or gas flow. Clocking in 3987 hours of laser use during its lifetime by the end of the study, the M290 of P6 is the most heavily used machine of the six, surpassing all but P2 by thousands of hours. The machine operated by P2 is nearly as old, however, with 3838 hours of use. Both P2 and P6 have a history of compliance

with the suggested maintenance procedures outlined by EOS. However, this does not necessarily rule out the degradation of the optics, laser, or argon gas flow systems as potential causes [47,56]. One distinct difference between the M290 system used by P6 and all other participants, including P2, is the software version. The M290 of P6 is operated with the previous generation of build preparation and control software with respect to the other machines, which could cause issues with build file preparation or process control. Although machine age is a likely factor, further investigation is needed to identify the specific root cause, i.e., gas flow, optics, or software.

Following comparison of the porosity distributions of metal from each machine, the tensile properties of metal from each machine were evaluated. The distributions of YS, UTS, and strain at failure were first plotted to examine the overall distribution of properties for the metal from all partners, as well as for each individual participant; these results were presented in Fig. 6.8. Although the overall distributions were approximately gaussian, secondary peaks were present in the YS of the horizontal coupons and the strain at failure of both coupon orientations. Assessing the underlying distributions from each participant revealed that the secondary peaks are due to the unique distributions of individual machines. The greatest shifts in the strain at failure were exhibited by the metal of P1 and P3, both of which have higher strain at failure and lower strength than the other machines. The root causes of these differences will be explored in detail later. The distributions of strain at failure for individual participants are also left skewed, indicating there are outliers with low strain at failure, which will also be explored further.

Overall, the metal printed by all participants achieved mechanical performance in the machined and annealed conditions that met or exceeded expectations. The overall average properties consistently met the minimum requirements for Grade 5 Ti-6Al-4V designated by

ASTM F2924 [61], except for the strain at failure. The horizontal coupons from partners P2, P4, P5, and P6 did not meet the required minimum strain at failure of 10%. For these machines, the ductility was lower than the required minimum, with the largest deficit of 1.7%. A modification of the heat treatment, including an increase of the soak time or temperature, are possible ways to increase the metal ductility and meet the standard [84]. Nevertheless, that is not the focus of this study.

With regards to variability in the mechanical properties, there is a clear difference in the metal between the vertical and horizontal orientations. The horizontal coupons exhibited lower ductility than those with vertical orientation for every participant, with minimum and maximum percent differences across all partners of 18% and 30%, respectively. The higher ductility of vertical coupons has been observed in the literature [87–89]. A previous investigation of the mechanical properties of Ti-6Al-4V produced by EPBF showed similar anisotropy in ductility that was attributed to microstructural texture [87]. As suggested by Simonelli et al., the long prior β grain boundaries in LPBF may act as weak interfaces that are predisposed to fracture, thereby facilitating intergranular fracture mode in tension applied perpendicular to the build direction [60]. Wilson-Heid et al. noticed that the anisotropy in ductility was only present in LPBF Ti-6Al-4V if there was microstructural anisotropy [89]. Consequently, metallographic investigation of the fracture surfaces was performed to investigate if this caused the orientation-dependent property differences observed.

The fracture surfaces of representative vertical and horizontal coupons were evaluated using optical microscopy to assess if there were orientation-dependent differences in the apparent mechanisms of failure (Fig. 6.10). Overall, the two surfaces showed very similar characteristics. Fracture of the coupons begins in the interior-most “flat” fast fracture region before propagating

to the boundaries of the cross-section and generating shear lips adjacent to the surfaces. An inspection of the fast fracture regions at higher magnification (e.g., Fig. 6.11) did not provide clear evidence of failure along the prior β grain boundaries in the horizontal coupons that would support previous claims in literature [60]. Only the vertical coupon contained a clear case of intergranular failure as shown in Fig. 6.11 (a), which is likely a prior β grain boundary due to its long length. Although these results do not support the hypothesis that intergranular failure is contributing to the orientation dependence of the strain at failure, further evaluation is needed. The microstructural fractographic evaluation provided here was limited to three coupons. It should be strengthened by further evaluation that includes multiple positions on the fracture surface and a greater number of specimens to provide stronger confidence in the data.

Another plausible cause of the difference in ductility between the horizontal and vertical coupons was presented by Voisin et al. in a synchrotron analysis of Ti-6Al-4V produced by LPBF [88]. That investigation observed that the porosity present in horizontal coupons expanded and coalesced during tensile testing in a unique manner from the behavior of the vertical coupons. Their reasoning was that the average distance between adjacent pores in cross-sections orientated perpendicular to the loading direction was smaller for the horizontal coupons, owing to the formation of pores at the ends of scan vectors. Within a layer of the print, these pores are spaced apart by the hatch distance (120 μm). Pores within each layer are separated from each adjacent layer by the layer thickness (60 μm). Thus, if we consider a plane perpendicular to the loading direction for a vertical coupon, the pores are approximately 120 μm apart from each other. On the other hand, for a horizontal coupon, the pores on a plane perpendicular to the loading direction are only 60 μm apart. According to the authors, this smaller spacing facilitates the coalescence of voids and results in premature fracture. The greater ductility of the vertical

coupons in this study matches results reported in the literature [88]. In the absence of clear crack propagation along prior β grain boundaries in the horizontal coupons, the results suggest that the orientation specific ductility are more likely attributed to porosity differences than microstructural texture.

One surprising finding from tensile testing was that the strength of printed metal was very consistent across all machines, as evident in Table 6.3. In fact, the CoVs listed in Table 6.4 for the yield strength of the individual machines ranged from 1.3-2.4% for the vertical coupons and 1.1-2.0% for the horizontal coupons. The CoVs for the UTS were nearly identical in magnitude, with ranges from 1.3-2.2% and 1-1.9% for the vertical and horizontal orientations, respectively. Considering that the CoVs from the Grade 5 Ti-6Al-4V wrought form coupons tested for YS and UTS are both 1.8%, these variations within machines are surprisingly low, and in many cases are lower than the wrought form metal. This is a unique finding that was only possible from results of the round robin and as a consequence of the robust PCD. Despite the low degree of variation in strength within machines, the statistical comparisons in Fig. 6.12 showed that there were significant differences in strength between some of the machines in the round robin. Due to its importance to the industrialization of LPBF, a more detailed assessment of contributing factors is necessary.

Regarding the strain at failure of the vertical coupons, there is one group of machines with statistically insignificant differences (P2, P4-P6), whereas the results for metal from P1 and P3 stand apart from the rest. These groups are differentiated according to the furnace used for heat treatment. Specifically, the metal of P2, P4, P5, and P6 was heat treated in the same argon atmosphere furnace and in many cases did not exhibit significant differences in ductility. In turn, the metal of P1 and P3 were statistically different from all other machines and were heat treated

in their own vacuum furnaces. Thermocouple logs from all three furnaces were analyzed to identify potential differences of importance. Representative heat treatment temperature cycles from each furnace are shown in Fig. 6.20. Interestingly, each of the heat treatments has a unique temperature-time response. In the case of P3, the cooldown period was significantly longer than the other two furnaces. The longer cooldown resulted from a controlled ramp in cooling rate instead of shutting off the furnace, as was performed for the other two furnaces. As a consequence, the metal of P3 remained above the annealing threshold temperature (705°C) [90] for 4.62 hours, compared to the 2.3 hours for the vacuum furnace used by P1, and 2.27 hours for the argon furnace used for P2, P4, P5 and P6. As a result of the extended period of annealing, the microstructure of the metal from P3 underwent coarsening (Fig. 6.2), an increase in ductility (Fig. 6.12), and a reduction in strength compared to the metal of P2, P4, P5 and P6.

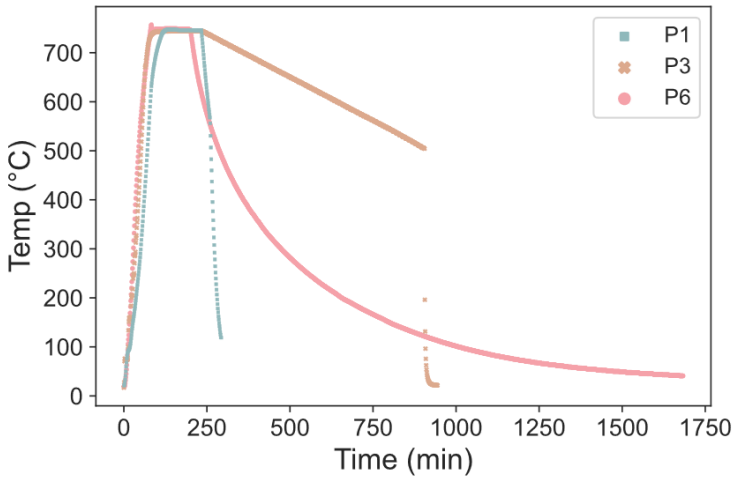

Fig. 6.20: Typical thermocouple logs for each of the three furnaces used for heat treatment in the round robin. The logs of P6 were used to represent the metal of P2, P4, P5 and P6.

There was also a large difference in the cooling rate of the argon furnace and the vacuum furnace used by P1. The divergence in cooling temperature history takes place around 500°C; the

furnace of P1 continues to cool rapidly, whereas the cooling rate of the argon furnace decreases with time more slowly and asymptotically approaches room temperature. Both responses were permitted by the PCD, which specifies that the furnace may be rapidly air-cooled below 500°C. This flexibility in cooling was allowed because the microstructure was not expected to change significantly below the 500 °C temperature. In fact, if the microstructure had been able to coarsen below 500°C, then the metal of P2, P4, P5, and P6 should have had wider alpha laths than P1 and exhibited great ductility. Yet, results from the experimental evaluations showed the reverse in terms of ductility. Of note, a contradictory study by Ter Haar et al. on Ti-6Al-4V found that extended periods at low elevated temperatures (480-560 °C) resulted in an increase in strength [66]. This behavior was attributed to the formation of ultra-fine β particles. That study performed a low-temperature heat treatment on metal in an initial martensitic state. The extended period of treatment at low temperature in the present study occurred after an anneal transformed the structure to an α + β state. It is unclear if the ultra-fine β particles would still form in this situation. Clearly, a more refined microstructural evaluation is needed to determine if this caused the lower ductility and higher strength of metal from P2, P4, P5, and P6.

Another potential contribution for the higher ductility of metal from P1 and P3 was the influence of argon versus vacuum atmospheres in the furnaces. Although both types of furnaces are accepted by most standards [90], it is possible there is a difference in the oxygen content present. The higher strength and lower ductility of metal treated in the argon furnace could potentially be explained by a higher partial pressure of oxygen [43,91]. As such, inert gas fusion (IGF) was performed on metal from multiple coupons of each of P1, P3 and P4 to compare the levels of O, N, and H in the metal from each furnace. These results are tabulated in Table 6.5 and

indicate there is no significant difference in O, N, or H content resulting from the furnace atmospheres. Even if there had been differences in O content within the furnace that resulted in diffusion into the metal, these "contaminated" regions would be removed by machining. A minimum of 0.5 mm was removed from each face of the gauge section, far exceeding the minimum 0.08 mm required by AMS2801B for similar heat treatment in an unprotected environment [67]. Therefore, the high ductility and low strength of metal from P1 is likely due to inter-machine variability or heat treatment cooling rate differences, not the furnace atmosphere.

Table 6.5: Light element chemistry for tensile coupons from P1, P3 and P4.

	O wt%	N wt%	H wt%
P1-1	0.157	0.022	0.002
P1-2	0.154	0.025	0.002
P3-1	0.155	0.017	0.001
P3-2	0.154	0.019	0.001
P4-1	0.154	0.025	0.003
P4-2	0.156	0.025	0.004

To exclude the possible effects of heat treatment differences, the properties of metal from P2, P4, P5, and P6 can be considered. The property variability between these four machines is very low, with mean property values including both orientations of 1095-1123 MPa for the YS, 1139-1174 MPa for the UTS, and 8.3-12.4% for the strain at failure. Comparing these values to the three M290s evaluated in the EOS whitepaper [17], the variability in the present study is higher. [17] The mean YS and UTS of the M290s in the white paper varied by 13 and 15 MPa, respectively, compared to the 28 MPa and 35 MPa in this round robin. However, it should be noted that the EOS paper only included vertical coupons. Given the wide range of operating

environments and use histories of the printers in the present study, the slightly greater variability is not surprising. However, the variability observed in the strain at failure was much greater.

In the EOS whitepaper, the difference between the machine strain at failure means was only 1.1%, compared with the 4.1% seen in this study. Notably, much of that variation comes from the difference between horizontal and vertical coupons. The white paper only evaluated vertical coupons, however. Separating results for the strain at failure of horizontal and vertical coupons from the present study results in ranges of 1.2% and 0.7%, respectively, which are consistent with the whitepaper. Hence, when the variability induced by heat treatment is excluded (by considering only the metal treated within a single furnace, i.e., P2, P4, P5 and P6), the degree of inter-machine variability in this study is consistent with that reported by EOS [17].

To further understand the overall reliability of the metal from each participant, the mechanical properties were plotted as Weibull probability distributions in Fig. 6.14, Fig. 6.15, and Fig. 6.16. Weibull distributions are commonly used to assess the reliability of strength in brittle and quasi-brittle materials. Applying the Weibull distribution to the YS and UTS did not result in linear distributions in strength as might be expected. The curved distributions suggest that a 2-parameter Weibull distribution is not appropriate for this data. This response may be due to size effects. The Weibull model functions best with a homogeneous material [92]. When the material is heterogeneous, non-uniform stress states can develop and result in a poor fit to the Weibull model [92]. AM metal is inherently heterogeneous at multiple length scales; the grain structure contains elongated prior β grains, the size of the α grains inside the prior β grains can vary, and the size and orientation of voids varies significantly as well. These inhomogeneities could decrease the applicability of the 2-parameter model. The distributions may be better described by the 3-parameter model or other extreme value statistics.

The Weibull distribution did fit the strain at failure distributions more adequately. Most of the distributions for the horizontal and vertical coupons are approximately linear on the Weibull probability axes, with the exception of the horizontal coupons of P2. For most machines, the Weibull moduli of the horizontal coupons is slightly higher than that of the vertical coupons, indicating they have less variability in strain at failure. Porosity may explain the greater variability of the vertical coupons with respect to those with horizontal orientation. Indeed, the LOF pores are most detrimental to the performance of the vertical coupons. Their contribution to failure depends on their location within the coupon and with respect to each other, which leads to increased variability from coupon-to-coupon.

Across the six machines, there is significant variability in the Weibull moduli describing the strain at failure distributions. In particular, the horizontal coupons of P1, and both coupon orientations of P3, have larger Weibull moduli compared to the other machines. This trend matches the discrepancy in heat treatments, where the metal of P1 and P3 were heat treated differently than the metal of the other machines. The Weibull moduli of P3 are the greatest of all six machines, with values of 18.7 and 21 for the vertical and horizontal coupons, respectively. It is conceivable that the longer heat treatment time for P3 homogenized the microstructure, and desensitized the failure process to internal pores, thereby decreasing the variability in strain at failure. Additionally, it was observed in Fig. 6.3 that metal from P3 had slightly lower average pore size and higher sphericity than metal from other machines, which could have also contributed to the increased consistency in the strain at failure responses.

In addition to the lower Weibull moduli of metal from P2, P4, P5, and P6, the metal from these partners also exhibited the most outliers with low ductility, which were most frequently of vertical orientation. Fractography can help to understand these outliers. Fracture surfaces from a

selected outlier coupon from P4, P5, and P6 were shown in Fig. 6.13. Each of these coupons failed with low strain at failure. Results of fractography showed that the cause of the low strain at failure was different for each. The lowest strain at failure of the three coupons was seen for P6, at 6.32%. An assessment of the fracture surface revealed large LOF pores were distributed across the fracture surface. These pores appeared to be larger and more frequent than in other coupons and facilitated early fracture. As previously identified, the metal of P6 contained an unusually high frequency of large pores (Fig. 6.5). Their presence on the fracture surface confirms that they can have a significant effect on the tensile properties when they are clustered together.

In contrast, the coupon from P5 showed evidence that fracture originated from the surface. The region of flat, fast fracture intersected with the surface of the coupon, indicating a likely origin of failure. Higher magnification investigation of this region revealed large LOF pores at the surface that were not found throughout the bulk metal. Furthermore, these pores were found to be present along the entire length of the machined gauge section. These pores would not have been identified by μCT scanning since they are not encapsulated within the coupon. It was identified in Chapter 4 that there is a high concentration of pores located near the surface of the as-built coupons that should be removed by machining. The presence of large numbers of LOF pores on the surface of this machined coupon could indicate two possibilities. First, insufficient machining may have occurred. However, the coupon dimensions were found to be within the tolerances of the CNC process, making this unlikely. Second, the coupon may have had pores located farther from the free surface than expected, preventing them from being removed during machining. This would be a concern from a design for additive manufacturing (DFAM) perspective, as outliers in performance can dictate the use of larger safety factors.

Finally, the fracture surface of a coupon from P4 was analyzed. Similar to the coupon from P5, the fast fracture region extended to the surface of the coupon, indicating a surface failure origin. Unlike the coupon from P5, however, there were no clear defects located on or near the surface. In the absence of defects, fracture may have originated from microstructural differences or local variation in chemistry, such as high oxygen content. This coupon is from the front row of Zone 4 (front right of the machine), indicating that it may have been influenced by the slower gas flow in this region [49]. Slow gas flow could enable redeposition of condensate with high oxygen content or attenuate the laser causing microstructural changes due to laser energy loss. However, these comments are speculative, as the fracture surface did not display any obvious defects in this region.

Although there were LOF defects evident on the fracture surfaces of some outlier specimens that were categorized according to their ductility, there was not a strong correlation between µCT and ductility overall (Fig. 6.17); considering the entire pore distribution of each coupon, the largest Pearson correlation was only -0.328, which was observed for the count of large pores. This is considered a weak negative correlation. Pearson correlation coefficients range from -1 to 1, which correspond to perfect negative and positive correlation, while a value of 0 would indicate no correlation. Restricting the distribution of each coupon to only include pores with diameter greater than its d90 diameter (Fig. 6.18 (b)) increased the correlation between strain at failure and pore diameter and sphericity, however the correlation was still weak.

The low correlation between porosity and the ductility of metal can be explained by several factors. First, in the absence of large defects for P1-P5, the small porosity content is not expected to contribute to the strain at failure [88]. Gong et al. found that small pores amounting

to 1 vol% or less, like most of the porosity seen in this study, were not detrimental to tensile properties [93]. Therefore, coupons with the most extreme pore content, like some from P6, could influence ductility and lead to variability between the machines. Second, pores exposed to the surface of the coupon, like those seen in the coupon from P5 in Fig. 6.13, would not be identified by µCT. This weakness of µCT may further lower the observed correlation between porosity and strain at failure. Finally, the porosity metrics considered do not individually capture the full severity of porosity. Pore size, shape, and location are all important, and may not correlate strongly on their own.

To address this last consideration, the modified VDF developed by Watring et al. and Erickson et al. [81,82] was adopted, and the results are shown in Fig. 6.19. This equation was developed to predict the location of failure within the gauge section of a coupon, thus its application here to predict tensile properties is beyond its intended application. Nonetheless, the equation captures many of the key characteristics of porosity distributions within a coupon simultaneously. The weights of each porosity characteristic were determined using Bayesian optimization, where the correlation between strain at failure and VDF of the entire dataset was maximized. Unfortunately, the resulting correlation was weak. Although the porosity did not correlate with tensile properties, it is important to highlight that the porosity distributions are expected to correlate strongly with fatigue life, which will be explored in the next phase of the round robin.

In summary, inter-machine variability was evaluated between the metal printed with six different M290s. Significant differences in porosity and tensile properties were found. While the porosity distributions of most participants was statistically similar, the metal produced by P6 contained a high frequency of large LOF voids. These pores appeared to contribute to the lower

ductility of the metal from P6, as LOF voids were identified on the fracture surface of specimens from that participant. However, there were no strong correlations between the pore metrics and the tensile properties of the metal that considered the metal of all participants. The largest contributor to variability in the tensile properties between the participants originated from differences in heat treatment furnace used. The metal of P1 and P3 was treated with different furnaces than the other partners and exhibited both higher ductility and lower strength than that of the other participants. Metal from the four participants heat treated in the same furnace exhibited greater consistency with an extent of variability that is similar to that reported by EOS in a white paper [17]. However, statistical differences in the mechanical properties still remained. This observation is of substantial importance to industrial practices involving metal AM as it establishes that parts manufactured on one machine may exhibit different properties than parts from another machine even though the parts are built with the same make and model system, using the same feedstock and the exact same process parameters.

6.4. Conclusion

With growing interest in the adoption and application of metal AM in aerospace, understanding the inter-machine variability is critical. Not only is this necessary for quality control and in the pursuit of certification, both the targets of industrial practice, it is also an important factor to consider for studies within the research community. To assess these effects, a round robin investigation of inter-machine variability between six EOS M290s was performed in terms of the porosity distributions and tensile properties of the metal. Results showed that the porosity distributions between five of the participants were statistically similar, but that the metal of P6 metal contained a high frequency of large pores and was significantly different. Linear

arrangements of pores within build layers that corresponded to the laser raster direction helped to identify several possible root causes, including software version and degradation of critical components caused by aging of the machine.

The tensile properties of metal from all six participants met or nearly met the standard requirements for Grade 5 Ti-6Al-4V produced by LPBF. Small adjustments in heat treatment could have been performed to meet the requirement as only the strain at failure of some horizontal coupons was out of compliance. There was a significant difference in the ductility of the vertical and horizontal coupons of all participants, with highest ductility exhibited by the vertical coupons. Greater ductility in vertical orientation metal is expected due to microstructural texture or porosity, which creates more tortuous intergranular fracture paths for the vertical coupons than those with horizontal orientation. Statistically significant differences in tensile properties were identified between many of the machines, but the magnitude is generally small and potentially of limited industrial relevance. One exception to the more random variability is the mechanical properties of metal produced by P1 and P3, which showed higher ductility and lower strength relative to the other four participants. For both participants, differences in the heat treatment, involving time schedule and environment, appear to be the root cause.

Overall, results from this investigation indicate that in the absence of post-processing differences related to heat treatment, similar porosity and tensile properties can be achieved across machines of the same make and model. However, small differences in machine configuration and machine health could have a substantial influence on the metal quality, which was identified in the strain at failure in the present investigation. It is therefore paramount that these factors are considered when reporting property data in the research community, and that

consistent machine maintenance is performed by all parties trying to produce high pedigree metal.

Chapter 7. Conclusions and Future Work

7.1. Conclusions

The objective of this dissertation was to characterize the variability in metal quality and mechanical properties of Grade 5 Ti-6Al-4V resulting from LPBF with a fixed process. Three components of variability were considered, including intra-build, inter-build, and inter-machine. Property variability and contributions of the three primary components are of particular importance to the qualification of metal AM components, especially where the highest pedigree of metal is required (i.e., aerospace applications). The mechanical properties in tension and porosity distributions were evaluated across all three levels of variability using a carefully designed and executed round robin study. Six different organizations, including The University of Washington as lead, and five industry participants contributed metal from six sequential builds according to an experimental design that followed a strict process control document. The findings presented here, including the properties, assessment of variability and its root causes, provide substantial new understanding of the AM process. Furthermore, this study highlights topics of critical importance for future investigation.

7.1.1. Intra-Build Variability

Intra-build variability is the spatial variation in metal quality within the build volume of the printer and can result from problems stemming from the machine subsystems (e.g., laser, gas flow, and recoater effects). Intra-build variability was assessed by printing tensile coupons in five distinct zones of the build space at two different height levels. By designing the builds in this manner, the mechanical properties and porosity could be evaluated statistically and according to the location of each discrete coupon in the build space.

The porosity and mechanical properties of the metal were grouped according to the zone in which they were built, which enabled a statistical comparison of properties from each zone. According to this approach, most of the six printers behaved similarly; the variation between the two height levels and within the x-y build space was small and typically not statistically significant. When statistical differences were identified the magnitude of the variability was generally small and of limited importance to industrial applications. For instance, the coefficients of variation (CoV) between zones ranged from 0.4-0.9% for the YS and UTS and 0.7-4.1% for the strain at failure, regardless of the coupon orientation. These values are similar to, or even lower than, the CoV in properties for wrought coupons tested in this study. In comparison, the CoVs of wrought metal were 1.8% and 8.3% for the for the strength and strain at failure, respectively, highlighting that the degree of intra-build variability was rather limited.

The intra-build analysis showed that not all machines performed identically. One of the printers (P6) exhibited unique trends in metal properties within the build space and had significant differences within both the x-y plane and z-direction. Evaluating the porosity and mechanical properties according to the coordinates of each individual coupon revealed that the center of the build plate produced the highest quality of metal for P6 and helped to identify root causes of the variability. The trend was symmetric about the x- and y-axes, pointing to the laser incidence angle as a root cause. Other machines exhibited similar parabolic property distributions along only the y-axis but behaved differently overall, suggesting inconsistent argon gas flow as a likely source of the variability. The results established that each machine may exhibit different property distributions, and that it must be accounted for when positioning parts within the AM machines. Furthermore, identification of the root causes of variability is critically important to understanding and improving AM technology.

7.1.2. Inter-Build Variability

Inter-build variability reflects the changes in metal quality that occur over repeated builds, which could originate from changes to the feedstock powder quality and/or changes in machine health. This component of variability is important when repeated batches of components must meet the same property requirements, as well as any time powder reuse is utilized to reduce operating costs and material waste.

To understand changes in properties with powder reuse, samples of powder were collected from each participant before each of the six repeated builds and analyzed to identify changes in light element chemistry and/or the particle size distribution. Minimal changes in the powder characteristics were observed for all participants, which could partially be due to the top-up powder reuse strategy, in which consumed powder was replaced with virgin powder.

Evaluation of the porosity distributions and tensile properties of metal from each of the six participants revealed minimal changes with powder reuse. However, a trend was observed in the metal for one machine in the study, and the root cause was traced back to a probable degradation of the machine health. Although the exact cause is unknown, the laser spot size was found to increase over the duration of the study, and likely affected the metal quality. Hence, machine health is critically important to the generation of reliable and reproducible data within the research community, as well as the production of high-pedigree metal in an industry setting. Although changes to the laser (e.g., focal point, diameter, power output) or gas flow systems (e.g., nozzle design, baffle design, differential pressure) are expected to have the largest effects, other aspects have received less attention from the research community, such as sensor calibration, and are worthy of future investigation.

Despite the overall absence of trends in metal quality and mechanical properties with powder reuse, there was stochastic variability from build-to-build. The CoVs for each machine were calculated across the six builds. Including both orientations of coupons from Zone 0, the CoVs ranged from 0.6-1.9%, 0.7-1.9%, and 2.2-10.4% for the YS, UTS, and strain at failure, respectively. As noted with the intra-build variability, these values of CoV compare favorably with those of the wrought Ti-6Al-4V. Thus, while there is stochastic variability present, it is comparable to (or does not exceed) the variability exhibited in a single sheet of wrought material. However, that statement is based on the conditions of printing in this study, which were highly controlled.

7.1.3. Inter-Machine Variability

Inter-machine variability is the broadest of the three types of variability evaluated in this round robin study. Machine configuration and health were expected to be the greatest contributors to the variability between multiple machines of the same make and model. In the present investigation, this was found to be true for the porosity distributions of the machines. The metal from one machine (P6) contained a high frequency of large LOF pores compared to the other five participants. While a definitive root cause was not identified, the machine health and age are the strongest candidates. As the oldest machine in the study, it used previous generations of build preparation and control software compared to the other five machines. These factors likely resulted in differences in the build file or control of the laser that increased the development of porosity that was present in their metal.

Regarding the tensile properties of the six participants, large variation was observed in the strength and ductility of the metal across machines. However, the greatest contribution to property variability resulted from the post-processing heat treatments performed. Excluding the

metal from two machines with different heat treatment, the tensile property variability for the remaining four machines was very consistent. Although statistical differences were still observed between metal with similar heat treatments, the differences were minor. For the vertical coupons, the CoV between the metal from the four machines with similar heat treatments for the YS, UTS, and strain at failure were 0.9%, 0.9%, and 2.4%. For the horizontal coupons, the values were 0.8%, 0.8%, and 6.8%, respectively. These low CoVs are a remarkable achievement for metal AM by LPBF and indicates that consistent and high-quality metal can be produced across multiple machines.

The round robin study presented in this body of work has revealed that there are intra-build, inter-build, and inter-machine contributions to variability in the quality and properties of metal produced by LPBF. Although the tensile properties and porosity distributions were often statistically similar between machines, differences still existed. Most notably, if post-processing variability is excluded, machine health and software configuration had the greatest influence on property variability at all three levels. Hence, machine maintenance and documentation of changes that occur during maintenance were identified to be crucially important to managing the quality of components produced on any single machine. Without proper maintenance and an understanding of its effects on part properties, machine equivalency cannot be achieved, and DFAM may require adjustments for each individual machine. While these results are novel and impactful, further research on the influence of machine health on metal quality is paramount to the successful development of metal AM technology and its implementation for mission critical applications.

7.2. Recommended Future Work

The analyses presented in Chapters 4-6 explored the variability present in LPBF of Ti-6Al-4V and proposed root causes responsible for the observed variability. In some cases, the root causes could not be concluded, but further work could be performed to confirm the root causes and identify their independent contributions. Several avenues of further investigation of the tensile round robin are identified below, as well as additional studies that can branch off from this work.

7.2.1. Machine Maintenance

During the analysis of inter-build variability in Chapter 5, only one machine (P3) produced metal that exhibited a trend for the tensile properties. The increasing strength with build number, followed by a sudden drop occurring after a machine maintenance, suggests that a change to the machine configuration was the likely root cause. While the maintenance logs do not indicate what changes were made to the machine that may have resulted in the decrease in strength, an increase in the laser diameter between the start and end of the study was noted. Changes to the laser focal position, for example, can be made during a maintenance visit and could change the laser diameter at the powder bed. Investigations should be performed to better understand the effects of a change of this type on the metal quality. Furthermore, efforts should be made to document and evaluate the effects of all tasks performed during routine machine maintenance.

7.2.2. Microstructural Evaluation

In Chapter 6, the largest source of machine-to-machine variability was identified as differences in the heat treatments performed. Three variations in the cooling rate of the heat treatment were observed, including (1) controlled ramp, (2) furnace cool, and (3) furnace cool to

500°C followed by rapid air cool. The tensile properties of each of these groups were found to be statistically different from the others. A preliminary microstructural evaluation of groups (1) and (2) revealed some differences in the microstructure that could explain the differences in tensile properties that were observed. However, a larger sample size that includes multiple coupons from across the build space would increase the statistical confidence in this finding. Furthermore, inclusion of group (3) in the microstructural analysis could verify that heat treatment differences were the cause of the statistically different mechanical properties resulting from heat treatment. Although studies exist comparing the effects of different heat treatments on Ti-6Al-4V, most focus on larger differences in procedures, such as larger differences in soak time or temperature. As such, further analysis of the microstructure could shed light on the variability seen in this investigation, but also help to refine the understanding of heat-treating AM metal.

7.2.3. In-Situ Process Monitoring

In addition to the large tensile property and μCT datasets, in-situ process monitoring signals were also collected from three of the six machines in the form of layer-wise images, optical thermography, and melt pool thermography. This data can be mined to identify if there are correlations between the porosity and in-situ signals. If correlations can be identified between the datasets, likely using machine learning, it can enable in-situ quality inspection and even in-situ corrective action to heal detected defects. Clearly, this capability has the potential to reduce qualification times and reduce the need for performing LPBF according to a fixed process.

7.2.4. Round Robin: Fatigue Variability

The body of work presented here on tensile property variability is an important step in the widespread qualification of AM components. However, tensile properties do not capture an

important aspect of the mechanical behavior that is critically important for the qualification of aerospace grade components. Aerospace parts are often subjected to cyclic loading, necessitating evaluation of the fatigue and damage tolerance responses of the metal. The round robin investigation performed here should be extended to cover these mechanical properties.

Using high-cycle fatigue as an example, the same build design style used in this study can be used to evaluate fatigue properties. By replacing the tensile coupons with fatigue coupons, a series of builds can be printed on multiple machines of the same make and model, thus providing an assessment of the intra-build, inter-build, and inter-machine contributions to variability. To reduce the number of fatigue samples being tested and simultaneously maximize the statistical power of the data, the majority of the coupons should be tested at an identical stress level to evaluate the variability in cycles to failure at the selected stress. Simultaneously, a small subset of the coupons could be tested at different stress levels to generate a stress-life diagram for each machine. While an investigation of this size is time consuming, which is only exacerbated by the longer test times associated with fatigue, these investigations are critical to our understanding of process variability in metal AM and its implementation in industry.

Chapter 8. References

[1] ISO/ASTM-International, Spanish standard UNE-EN ISO / ASTM 52900 Additive manufacturing General principles Fundamentals and vocabulary, (2022).

[2] America Makes, AMSC, Standardization Roadmap for Additive Manufacturing - Version 2.0, America Makes & ANSI Additive Manufacturing Standardization Collaborative (AMSC). 2 (2018) 1–269.

[3] B.M. Colosimo, Q. Huang, T. Dasgupta, F. Tsung, Opportunities and challenges of quality engineering for additive manufacturing, Journal of Quality Technology. 50 (2018) 233–252. https://doi.org/10.1080/00224065.2018.1487726.

[4] A. Thryft, SpaceX Reveals 3D-Printed Rocket Engine Parts, DesignNews. (2014). https://www.designnews.com/design-hardware-software/spacex-reveals-3d-printed-rocket-engine-parts (accessed December 18, 2022).

[5] J. Wattles, Relativity is 3D printing rockets and raising billions. Will its technology work?, CNN. (2022). https://www.cnn.com/2022/02/05/tech/relativity-rocket-space-feature-factory-scn/index.html (accessed December 18, 2022).

[6] M. Seifi, A. Salem, J. Beuth, O. Harrysson, J.J. Lewandowski, Overview of Materials Qualification Needs for Metal Additive Manufacturing, JOM. 68 (2016) 747–764. https://doi.org/10.1007/s11837-015-1810-0.

[7] Metallic Materials Properties Development and Standardization (MMPDS), 2011.

[8] A. Reardon, ed., Metallurgy for the Non-Metallurgist, 2nd ed., Materials Park, 2011.

[9] D.W. Gibbons, J.P.L. Serfontein, A.F. van der Merwe, Mapping the path to certification of metal laser powder bed fusion for aerospace applications, Rapid Prototyp J. (2020). https://doi.org/10.1108/RPJ-07-2020-0154.

[10] J. Fielding, A. Davis, B. Bouffard, M. Kinsella, T. Delgado, J. Wilczynski, K. Marchese, I. Wing, Department of Defense Additive Manufacturing Roadmap, 2016.

[11] D.L. Bourell, D.W. Rosen, M.C. Leu, The roadmap for additive manufacturing and its impact, 3D Print Addit Manuf. 1 (2014). https://doi.org/10.1089/3dp.2013.0002.

[12] M. Seifi, M. Gorelik, J. Waller, N. Hrabe, N. Shamsaei, S. Daniewicz, J.J. Lewandowski, Progress Towards Metal Additive Manufacturing Standardization to Support Qualification and Certification, JOM. 69 (2017) 439–455. https://doi.org/10.1007/s11837-017-2265-2.

[13] E. Jelis, M. Clemente, M. Hespos, S. Groeschler, E. Golden, R. Carpenter, Round Robin Study Evaluating Consistency of 4340 Steel Specimens Manufactured by Different Laser Powder Bed Fusion Machines, J Mater Eng Perform. 30 (2021) 6832–6843. https://doi.org/10.1007/s11665-021-06020-8.

[14] B. Ahuja, A. Schaub, D. Junker, M. Karg, F. Tenner, R. Plettke, M. Merklein, M. Schmidt, A round robin study for laser beam melting in a metal powder bed, South African Journal of Industrial Engineering. 27 (2016) 30–42. https://doi.org/10.7166/27-2-1201.

[15] H.K. Rafi, N. v. Karthik, H. Gong, T.L. Starr, B.E. Stucker, Microstructures and mechanical properties of Ti6Al4V parts fabricated by selective laser melting and electron beam melting, Journal of Materials Engineering and Performance2. 22 (2013) 3872–3883.

[16] Y. Zhai, H. Galarraga, D.A. Lados, Microstructure, static properties, and fatigue crack growth mechanisms in Ti-6Al-4V fabricated by additive manufacturing: LENS and EBM, Eng Fail Anal. 69 (2016) 3–14. https://doi.org/10.1016/J.ENGFAILANAL.2016.05.036.

[17] F. Endraß, A. Yağmur, Multi-Machine Capability Study, EOS Whitepaper. (2021) 1–7.

[18] C. Schadauer, G.R. Martetschalger, A.L. Ilie, A. Angerbauer, C. Lanzerstorfer, Casting powders: influence of the humidity on the flowability, Ironmaking & Steelmaking. 47 (2020) 460–463.

[19] M. Iebba, A. Astarita, D. Mistretta, I. Colonna, M. Liberini, F. Scherillo, C. Pirozzi, R. Borrelli, S. Franchitti, A. Squillace, Influence of Powder Characteristics on Formation of Porosity in Additive Manufacturing of Ti-6Al-4V Components, J Mater Eng Perform. 26 (2017) 4138–4147. https://doi.org/10.1007/s11665-017-2796-2.

[20] M. Ahmed Obeidi, S.M. Uí Mhurchadha, R. Raghavendra, A. Conway, C. Souto, D. Tormey, I.U. Ahad, D. Brabazon, Comparison of the porosity and mechanical performance of 316L stainless steel manufactured on different laser powder bed fusion metal additive manufacturing machines, Journal of Materials Research and Technology. 13 (2021) 2361–2374. https://doi.org/10.1016/j.jmrt.2021.06.027.

[21] C.U. Brown, G. Jacob, M. Stoudt, S. Moylan, J. Slotwinski, A. Donmez, Interlaboratory Study for Nickel Alloy 625 Made by Laser Powder Bed Fusion to Quantify Mechanical Property Variability, J Mater Eng Perform. 25 (2016) 3390–3397. https://doi.org/10.1007/s11665-016-2169-2.

[22] M. Lutter-Günther, M. Bröker, T. Mayer, S. Lizak, C. Seidel, G. Reinhart, Spatter formation during laser beam melting of AlSi10Mg and effects on powder quality, Procedia CIRP. 74 (2018) 33–38. https://doi.org/10.1016/j.procir.2018.08.008.

[23] G. Shanbhag, M. Vlasea, The effect of reuse cycles on Ti-6Al-4V powder properties processed by electron beam powder bed fusion, Manuf Lett. 25 (2020) 60–63. https://doi.org/10.1016/j.mfglet.2020.07.007.

[24] R. Schur, S. Ghods, C. Wisdom, R. Pahuja, A. Montelione, D. Arola, M. Ramulu, Mechanical anisotropy and its evolution with powder reuse in Electron Beam Melting AM of Ti6Al4V, Mater Des. 200 (2021) 109450. https://doi.org/10.1016/j.matdes.2021.109450.

[25] P. Nandwana, W.H. Peter, R.R. Dehoff, L.E. Lowe, M.M. Kirka, F. Medina, S.S. Babu, Recyclability Study on Inconel 718 and Ti-6Al-4V Powders for Use in Electron Beam Melting, Metallurgical and Materials Transactions B. 47B (2016) 754–762. https://doi.org/10.1007/s11663-015-0477-9.

[26] H.P. Tang, M. Qian, N. Liu, X.Z. Zhang, G.Y. Yang, J. Wang, Effect of Powder Reuse Times on Additive Manufacturing of Ti-6Al-4V by Selective Electron Beam Melting, JOM. 67 (2015) 555–563. https://doi.org/10.1007/s11837-015-1300-4.

[27] Y. Sung, M. Li, D. Luo, Y. Li, S. Biring, Y. Huang, C. Wang, S. Liu, K. Wong, Metal Powders in Additive Manufacturing: A Review on Reusability and Recyclability of Common Titanium, Nickel and Aluminum Alloys, Addit Manuf. (2021) 105565. https://doi.org/10.1016/j.addma.2021.102017.

[28] L. Cordova, M. Campos, T. Tinga, Revealing the Effects of Powder Reuse for Selective Laser Melting by Powder Characterization, JOM. 71 (2019) 1062–1072. https://doi.org/10.1007/s11837-018-3305-2.

[29] E. Santecchia, S. Spigarelli, M. Cabibbo, Material reuse in laser powder bed fusion: Side effects of the laser—metal powder interaction, Metals (Basel). 10 (2020) 1–21. https://doi.org/10.3390/met10030341.

[30] R. Harkin, H. Wu, S. Nikam, J. Quinn, S. McFadden, Reuse of grade 23 ti6al4v powder during the laser-based powder bed fusion process, Metals (Basel). 10 (2020) 1–14. https://doi.org/10.3390/met10121700.

[31] B. Meier, M. Skalon, F. Warchomicka, C. Belei, M. Görtler, R. Kaindl, C. Sommitsch, Effect of the reuse of powder on material properties of Ti6Al4V processed by SLM, in: AIP Conf Proc, 2019. https://doi.org/10.1063/1.5112682.

[32] L.C. Ardila, F. Garciandia, J.B. González-Díaz, P. Álvarez, A. Echeverria, M.M. Petite, R. Deffley, J. Ochoa, Effect of IN718 recycled powder reuse on properties of parts manufactured by means of Selective Laser Melting, Phys Procedia. 56 (2014) 99–107. https://doi.org/10.1016/j.phpro.2014.08.152.

[33] H. Asgari, C. Baxter, K. Hosseinkhani, M. Mohammadi, On microstructure and mechanical properties of additively manufactured AlSi10Mg _ 200C using recycled powder, Materials Science & Engineering A. 707 (2017) 148–158. https://doi.org/10.1016/j.msea.2017.09.041.

[34] S. Ghods, E. Schultz, C. Wisdom, R. Schur, R. Pahuja, A. Montelione, D. Arola, M. Ramulu, Electron Beam Additive Manufacturing of Ti6Al4V: Evolution of Powder Morphology and Part Microstructure with Powder Reuse, Materialia (Oxf). 9 (2020) 100631. https://doi.org/10.1016/j.mtla.2020.100631.

[35] R.O. Leary, R. Setchi, P. Prickett, G. Hankins, N. Jones, An Investigation into the Recycling of Ti-6Al-4V Powder Used Within SLM to Improve Sustainability, in:

SDM’2015: 2nd International Conference on Sustainable Design and Manufacturing, 2015: pp. 1–12.

[36] P.E. Carrion, A. Soltani-Tehrani, N. Phan, N. Shamsaei, Powder Recycling Effects on the Tensile and Fatigue Behavior of Additively Manufactured Ti-6Al-4V Parts, JOM. 71 (2019) 963–973. https://doi.org/10.1007/s11837-018-3248-7.

[37] Y. Sun, M. Aindow, R.J. Hebert, The effect of recycling on the oxygen distribution in Ti-6Al-4V powder for additive manufacturing, Materials at High Temperatures. 35 (2018) 217–224. https://doi.org/10.1080/09603409.2017.1389133.

[38] V. v. Popov, A. Katz-Demyanetz, A. Garkun, M. Bamberger, The effect of powder recycling on the mechanical properties and microstructure of electron beam melted Ti-6Al-4 V specimens, Addit Manuf. 22 (2018) 834–843. https://doi.org/10.1016/J.ADDMA.2018.06.003.

[39] V. Petrovic, R. Ninerola, Powder recyclability in electron beam melting for aeronautical use, Aircraft Engineering and Aerospace Technology: An International Journal. 87 (2015) 147–155.

[40] V. Seyda, N. Kaufmann, C. Emmelmann, Investigation of aging processes of Ti-6Al-4V powder material in laser melting, Phys Procedia. 39 (2012) 425–431. https://doi.org/10.1016/j.phpro.2012.10.057.

[41] C. Wei, X. Ma, X. Yang, M. Zhou, C. Wang, Y. Zheng, W. Zhang, Z. Li, Microstructural and property evolution of Ti6Al4V powders with the number of usage in additive manufacturing by electron beam melting, Mater Lett. 221 (2018) 111–114. https://doi.org/10.1016/J.MATLET.2018.03.124.

[42] K. Thejane, S. Chikosha, W.B. du Preez, Characterisation and Monitoring of Ti6Al4V (ELI) Powder Used in Different Selective Laser Melting Systems, South African Journal of Industrial Engineering. 28 (2017) 161–171.

[43] H. Conrad, Effect of interstitial solutes on the strength and ductility of titanium, Prog Mater Sci. 26 (1981) 123–403. https://doi.org/10.1016/0079-6425(81)90001-3.

[44] F.H. Froes, ed., Titanium Physical Metallurgy Processing and Applications, ASM International, 2019.

[45] O.A. Quintana, J. Alvarez, R. Mcmillan, W. Tong, C. Tomonto, Effects of Reusing Ti-6Al-4V Powder in a Selective Laser Melting Additive System Operated in an Industrial Setting, JOM. 70 (2018) 1863–1869. https://doi.org/10.1007/s11837-018-3011-0.

[46] G.E. Bean, D.B. Witkin, T.D. McLouth, R.J. Zaldivar, Process gas influence on microstructure and mechanical behavior of Inconel 718 fabricated via selective laser melting, Progress in Additive Manufacturing. 5 (2020) 405–417. https://doi.org/10.1007/s40964-020-00133-7.

[47] J. Reijonen, A. Revuelta, T. Riipinen, K. Ruusuvuori, P. Puukko, On the effect of shielding gas flow on porosity and melt pool geometry in laser powder bed fusion additive manufacturing, Addit Manuf. 32 (2020) 101030. https://doi.org/10.1016/j.addma.2019.101030.

[48] S. Keaveney, A. Shmeliov, V. Nicolosi, D.P. Dowling, Investigation of process by-products during the Selective Laser Melting of Ti6AL4V powder, Addit Manuf. 36 (2020) 1–9. https://doi.org/10.1016/j.addma.2020.101514.

[49] A. Ladewig, G. Schlick, M. Fisser, V. Schulze, U. Glatzel, Influence of the shielding gas flow on the removal of process by-products in the selective laser melting process, Addit Manuf. 10 (2016) 1–9. https://doi.org/10.1016/j.addma.2016.01.004.

[50] M. Skalon, B. Meier, T. Leitner, S. Arneitz, S.T. Amancio-Filho, C. Sommitsch, Reuse of Ti6Al4V powder and its impact on surface tension, melt pool behavior and mechanical properties of additively manufactured components, Materials. 14 (2021) 1–22. https://doi.org/10.3390/ma14051251.

[51] B.J. Keene, Review of Data for the Surface Tension of Iron and its Binary Alloys, International Materials Reviews. 33 (1988) 1–37.

[52] B. Ferrar, L. Mullen, E. Jones, R. Stamp, C.J. Sutcliffe, Gas flow effects on selective laser melting (SLM) manufacturing performance, J Mater Process Technol. 212 (2012) 355–364. https://doi.org/10.1016/j.jmatprotec.2011.09.020.

[53] T.P. Moran, D.H. Warner, A. Soltani-Tehrani, N. Shamsaei, N. Phan, spatial inhomogeneity of build defects across the build plate in laser powder bed fusion, Addit Manuf. 47 (2021) 1–9.

[54] S. Sendino, S. Martinez, A. Lamikiz, F. Lartategui, M. Gardon, J.J. Gonzalez, Analytical study of the melt pool distortion in the Laser Powder Bed Fusion Process caused by the angle of incidence of the laser and its effect on the surface finish of the part, IOP Conf Ser Mater Sci Eng. 1193 (2021) 012010. https://doi.org/10.1088/1757-899X/1193/1/012010.

[55] S. Sendino, M. Gardon, F. Lartategui, S. Martinez, A. Lamikiz, The effect of the laser incidence angle in the surface of l-pbf processed parts, Coatings. 10 (2020) 1–12. https://doi.org/10.3390/coatings10111024.

[56] P. Fathi-Hafshejani, A. Soltani-Tehrani, N. Shamsaei, M. Mahjouri-Samani, Laser incidence angle influence on energy density variations, surface roughness, and porosity of additively manufactured parts, Addit Manuf. 50 (2022) 1–9. https://doi.org/10.1016/j.addma.2021.102572.

[57] Z. Chen, C.H.J. Davies, Surface roughness of Selective Laser Melted Ti-6Al-4V alloy components, Addit Manuf. 21 (2018) 91–103. https://doi.org/10.1016/j.addma.2018.02.009.

[58] A. Phua, C. Doblin, P. Owen, C.H.J. Davies, G.W. Delaney, The effect of recoater geometry and speed on granular convection and size segregation in powder bed fusion, Powder Technol. 394 (2021) 632–644. https://doi.org/10.1016/j.powtec.2021.08.058.

[59] H.J. Niu, I.T.H. Chang, Instability of scan tracks of selective laser sintering of high speed steel powder, Scr Mater. 41 (1999) 1229–1234. https://doi.org/10.1016/S1359-6462(99)00276-6.

[60] M. Simonelli, Y.Y. Tse, C. Tuck, On the texture formation of selective laser melted Ti-6Al-4V, Metallurgical and Materials Transactions A. 45A (2014) 2863–2872. https://doi.org/10.1007/s11661-014-2218-0.

[61] ASTM-International, F2924-14: Standard Specification for Additive Manufacturing Titanium-6 Aluminum-4 Vanadium with Powder Bed Fusion, (2014) 1–9. https://doi.org/10.1520/F2924-14.2.

[62] K. Artzt, T. Mishurova, P.P. Bauer, J. Gussone, P. Barriobero-Vila, S. Evsevleev, G. Bruno, G. Requena, J. Haubrich, Pandora's Box-Influence of Contour Parameters on Roughness and Subsurface Residual Stresses in Laser Powder Bed Fusion of Ti-6Al-4V, Materials. 13 (2020) 1–24. https://doi.org/10.3390/ma13153348.

[63] ASTM-International, B215-15: Standard Practices for Sampling Metal Powders, (2015) 1–7. https://doi.org/10.1520/B0215-10.2.

[64] P. Mercelis, J.P. Kruth, Residual stresses in selective laser sintering and selective laser melting, Rapid Prototyp J. 12 (2006) 254–265. https://doi.org/10.1108/13552540610707013.

[65] M. Frkan, R. Konecna, G. Nicoletto, L. Kunz, Microstructure and fatigue performance of SLM-fabricated Ti6Al4V alloy after different stress-relief heat treatments, Transportation Research Procedia. 40 (2019) 24–29. https://doi.org/10.1016/j.trpro.2019.07.005.

[66] G.M. ter Haar, T.H. Becker, Low temperature stress relief and martensitic decomposition in selective laser melting produced Ti6Al4V, Material Design & Processing Communications. 3 (2021) 1–6. https://doi.org/10.1002/mdp2.138.

[67] SAE-International, AMS2801B: Heat Treatment of Titanium Alloy Parts, (2014) 1–15. http://usir.salford.ac.uk/7682/.

[68] ASTM-International, E8/E8M-16a: Standard Test Methods for Tension Testing of Metallic Materials, (2018) 1–30.

[69] ASTM-International, E1447−9: Standard Test Method for Determination of Hydrogen in Titanium and Titanium Alloys by the Inert Gas Fusion Thermal Conductivity Method, (2016) 1–4. https://doi.org/10.1520/E1447-09R16.2.

[70] ASTM-International, E1409-13: Standard Test Method for Determination of Oxygen and Nitrogen in Titanium and Titanium Alloys by Inert Gas Fusion, (2013) 1–7. https://doi.org/10.1520/E1409.

[71] S. Cao, Z. Chen, C.V.S. Lim, K. Yang, Q. Jia, T. Jarvis, D. Tomus, X. Wu, Defect, Microstructure, and Mechanical Property of Ti-6Al-4V Alloy Fabricated by High-Power

Selective Laser Melting, Jom. 69 (2017) 2684–2692. https://doi.org/10.1007/s11837-017-2581-6.

[72] SAE-International, AMS7003: Laser Powder Bed Fusion Process, (2018) 1–15.

[73] G. Chen, S.Y. Zhao, P. Tan, J. Wang, C.S. Xiang, H.P. Tang, A comparative study of Ti-6Al-4V powders for additive manufacturing by gas atomization, plasma rotating electrode process and plasma atomization, Powder Technol. 333 (2018) 38–46. https://doi.org/10.1016/j.powtec.2018.04.013.

[74] S. Ghods, R. Schur, E. Schultz, R. Pahuja, A. Montelione, C. Wisdom, D. Arola, M. Ramulu, Powder Reuse and its Contribution to Porosity in Additive Manufacturing of Ti6Al4V, Materialia (Oxf). 15 (2021) 1–10. https://doi.org/10.1016/j.mtla.2020.100992.

[75] L.C. Wei, L.E. Ehrlich, M.J. Powell-Palm, C. Montgomery, J. Beuth, J.A. Malen, Thermal conductivity of metal powders for powder bed additive manufacturing, Addit Manuf. 21 (2018) 201–208. https://doi.org/10.1016/j.addma.2018.02.002.

[76] T. Bonhoff, M. Poppe, J. Stollenwerk, J.H. Schleifenbaum, P. Loosen, Multi-physical analysis of thermo-optical effects for different Selective Laser Melting (SLM) scanning strategies, Procedia CIRP. 74 (2018) 97–101. https://doi.org/10.1016/j.procir.2018.08.048.

[77] T. DebRoy, H.L. Wei, J.S. Zuback, T. Mukherjee, J.W. Elmer, J.O. Milewski, A.M. Beese, A. Wilson-Heid, A. De, W. Zhang, Additive manufacturing of metallic components – Process, structure and properties, Prog Mater Sci. 92 (2018) 112–224. https://doi.org/10.1016/j.pmatsci.2017.10.001.

[78] C.L.A. Leung, S. Marussi, M. Towrie, R.C. Atwood, P.J. Withers, P.D. Lee, The effect of powder oxidation on defect formation in laser additive manufacturing, Acta Mater. 166 (2019) 294–305. https://doi.org/10.1016/j.actamat.2018.12.027.

[79] G. Bi, C.N. Sun, A. Gasser, Study on influential factors for process monitoring and control in laser aided additive manufacturing, J Mater Process Technol. 213 (2013) 463–468. https://doi.org/10.1016/j.jmatprotec.2012.10.006.

[80] M.T. Tsai, Y.W. Chen, C.Y. Chao, J.S.C. Jang, C.C. Tsai, Y.L. Su, C.N. Kuo, Heat-treatment effects on mechanical properties and microstructure evolution of Ti-6Al-4V alloy fabricated by laser powder bed fusion, J Alloys Compd. 816 (2020) 152615. https://doi.org/10.1016/j.jallcom.2019.152615.

[81] D.S. Watring, J.T. Benzing, O.L. Kafka, L.A. Liew, N.H. Moser, J. Erickson, N. Hrabe, A.D. Spear, Evaluation of a modified void descriptor function to uniquely characterize pore networks and predict fracture-related properties in additively manufactured metals, Acta Mater. 223 (2022) 117464. https://doi.org/10.1016/j.actamat.2021.117464.

[82] J.M. Erickson, A. Rahman, A.D. Spear, A void descriptor function to uniquely characterize pore networks and predict ductile-metal failure properties, Int J Fract. 225 (2020) 47–67. https://doi.org/10.1007/s10704-020-00463-1.

[83] X. Tan, Y. Kok, Y.J. Tan, M. Descoins, D. Mangelinck, S.B. Tor, K.F. Leong, C.K. Chua, Graded microstructure and mechanical properties of additive manufactured Ti–6Al–4V via electron beam melting, Acta Mater. 97 (2015) 1–16. https://doi.org/10.1016/J.ACTAMAT.2015.06.036.

[84] X. Yan, S. Yin, C. Chen, C. Huang, R. Bolot, R. Lupoi, M. Kuang, W. Ma, C. Coddet, H. Liao, M. Liu, Effect of heat treatment on the phase transformation and mechanical properties of Ti6Al4V fabricated by selective laser melting, J Alloys Compd. 764 (2018) 1056–1071. https://doi.org/10.1016/j.jallcom.2018.06.076.

[85] L. Sinclair, C.L.A. Leung, S. Marussi, S.J. Clark, Y. Chen, M.P. Olbinado, A. Rack, J. Gardy, G.J. Baxter, P.D. Lee, In situ radiographic and ex situ tomographic analysis of pore interactions during multilayer builds in laser powder bed fusion, Addit Manuf. 36 (2020) 1–14. https://doi.org/10.1016/j.addma.2020.101512.

[86] L. Scime, J. Beuth, Anomaly detection and classification in a laser powder bed additive manufacturing process using a trained computer vision algorithm, Addit Manuf. 19 (2018) 114–126. https://doi.org/10.1016/j.addma.2017.11.009.

[87] R. Schur, S. Ghods, E. Schultz, C. Wisdom, R. Pahuja, A. Montelione, D. Arola, M. Ramulu, A Fractographic Analysis of Additively Manufactured Ti6Al4V by Electron Beam Melting: Effects of Powder Reuse, Journal of Failure Analysis and Prevention. (2020). https://doi.org/DOI 10.1007/s11668-020-00875-0.

[88] T. Voisin, N.P. Calta, S.A. Khairallah, J.B. Forien, L. Balogh, R.W. Cunningham, A.D. Rollett, Y.M. Wang, Defects-dictated tensile properties of selective laser melted Ti-6Al-4V, Mater Des. 158 (2018) 113–126. https://doi.org/10.1016/j.matdes.2018.08.004.

[89] A.E. Wilson-Heid, Z. Wang, B. McCornac, A.M. Beese, Quantitative relationship between anisotropic strain to failure and grain morphology in additively manufactured Ti-6Al-4V, Materials Science and Engineering A. 706 (2017) 287–294. https://doi.org/10.1016/j.msea.2017.09.017.

[90] SAE-International, AMS-H-81200D: Heat Treatment of Titanium and Titanium Alloys, (2014) 1–24. http://usir.salford.ac.uk/7682/.

[91] M. Yan, W. Xu, M.S. Dargusch, H.P. Tang, M. Brandt, M. Qian, Review of effect of oxygen on room temperature ductility of titanium and titanium alloys, Powder Metallurgy. 57 (2014) 251–257. https://doi.org/10.1179/1743290114y.0000000108.

[92] J. Lamon, Brittle Fracture and Damage of Brittle Materials and Composites, 2016. https://doi.org/10.1016/C2015-0-01222-9.

[93] H. Gong, K. Rafi, H. Gu, G.D. Janaki Ram, T. Starr, B. Stucker, Influence of defects on mechanical properties of Ti–6Al–4 V components produced by selective laser melting and electron beam melting, Mater Des. 86 (2015) 545–554. https://doi.org/10.1016/J.MATDES.2015.07.147.

Appendix A: Process Control Document

University of Washington Round Robin (UWRR): Property Variability in AM of Ti6Al4V by SLM

Process Control Document

Prepared by:

Reid Schur, Sean Ghods, Alex Montelione, Rick Schleusener

Dwayne Arola*

Material Science and Engineering, UW

10/22/2020

Prepared for: Inner Core Participants

University of Washington (lead)

The Boeing Company

EOS

Lockheed Martin

Toray Precision Company

3D Logics

1. Overview

1.1. This document outlines the operating procedures and supporting details that will be followed throughout the first year of this round robin study. For convenience, we use the designation University of Washington Round Robin (UWRR) for this effort. The following procedures explain important aspects of the study and provide guidelines that we expect each study participant will adhere to. Overall, they conform to the guidelines for Laser Powder Bed Fusion (LPBF) processes outlined in AMS 7003 [1] for aerospace materials. The operating procedures described in this document are critical to achieving consistency in data between the participants of this study and in maximizing the utility of the data. If at any point a participant has questions regarding the program or operational issues, please contact:

1.2. **Contributing Members**: Points of Contact

1.3. Acquiring Powder

1.3.1. All participants shall print with powder from the same lot for this UWRR study. Each contributor shall acquire powder directly from EOS per the details in 1.3.1.1. Each participant shall acquire 100 kg[1] of powder to be used exclusively for this study. A total volume of 900 kg has been reserved for the UWRR. The powder certification is located in Appendix A.3.

1.3.1.1. POC for ordering powder from EOS:

1.3.2. Upon receipt from EOS, the powder should be placed in a controlled storage location and left sealed until preparing to perform the first build.

1.3.2.1. The storage location should be the same as where powder is normally stored for the partner (normal conditions) and documented. It is recommended that the powder be stored in a hazard free location, within a flammables/explosives cabinet.

[1] This is subject to change following finalization of the build file.

1.3.2.2. The environmental conditions should be 68-72F at less than 60% humidity, in accordance with EOS recommendations and UW operating procedures. Deviation from these conditions shall be reported to the UW for review.

1.3.2.3. Each participant shall provide a description of their powder storage condition, including temperature and humidity.

1.3.2.4. Participants should review Section 3.1.7 of AMS 7003 [1] concerning "Moisture and Contamination Control Plan". Any questions concerning this advisement should be discussed with the UW team.

1.3.2.5. Participants shall never mix the allocated powder batch with any other batches of powder.

2. Machine Pedigree

2.1. Participants shall use a single EOS M290 for the duration of the study.

2.2. Participants should use EOSPRINT operating software v.2.6. If partners are running a different version, this shall be documented.

2.3. Participants shall control ambient conditions around the machine to maintain a temperature of 68-72F and the relative humidity below 60%. Inability to maintain these settings must be reported to the University of Washington team for review of environmental conditions.

2.4. Participants shall monitor and document the machine operating environment, indicating the temperature and humidity. This should be recorded at the start and end of every build.

2.5. Participants shall document all powder chemistries that have been used in their machine prior to the UWRR, as well as what powder chemistries were used just prior to each build including all appropriate powder information, if applicable.

3. Qualified Process Parameter Sets

3.1. All participants shall use the Ti64_SpeedM291 1.10 parameter set. Gas flow rate will be adjusted to accommodate use of the grid nozzle. All necessary changes shall be included in the build file and shall not be changed. Details of this parameter set can be provided upon request.

4. Build Plate Material Specification, Preparation Requirements, and Re-Use Preparation Procedure

4.1. All participants shall build using a Ti-6Al-4V build plate. It is preferred that participants purchase a new Ti-6Al-4V build plate to be used exclusively for this study. The build plate shall be of EOS origin or match their plate geometry (see Appendix A.5). Plates with either 6 or 8mm bolt holes are acceptable. This includes a starting thickness of 25 mm. The plate shall be replaced if the thickness drops below 19 mm[2].

4.2. It is recommended that participants serialize their build plate and record the serial number prior to each build. This will ensure an incorrect build plate is not used.

4.3. Participants shall document the plate thickness before each build.

4.4. Participants shall document the plate surface roughness (average surface roughness, Ra) and ten-point height (Rz) and the method/process to achieve the surface finish (milling, grinding, etc). Ra and Rz should be approximately 1.4µm and 6.4µm, respectively, plus or minus 20%. The roughness parameters shall be measured by contact profilometer at 5 locations, 3 scans at each, on the build plate. Profiles shall be taken parallel to the recoating direction of the build plate. Approximate locations for the scans are shown in Appendix A.6. Sampling should be done with a cutoff length of 0.8 mm, low pass gaussian filter of 2.5 µm, and traverse length of 5.6 mm.

4.5. It is requested that the raw scan data be sent to the University of Washington as well as the calculated Ra and Rz.

4.6. If a participant is unable to document their plate's surface through profilometry as outlined, the University of Washington shall be contacted prior to the start of the study for an individualized approach.

5. Monitored Process Conditions

5.1. Contributors shall export and report the full Job Quality Report.

5.2. Contributors with EOSCONNECT shall also export and report the logs from the following sensors as recorded during the build:

5.2.1. EOS.Machine.Sensors.BuildingPlatform.Temperature

5.2.2. Machine.Sensors.Environment.HumidityRelative

5.2.3. EOS.Machine.Sensors.Environment.Temperature

[2] This guideline is subject to change, depending on the findings of the study.

5.2.4. EOS.Machine.Sensors.ExposureUnits.ExposureUnit1.Temperature (as well as units 2-4)

5.2.5. EOS.Machine.Sensors.Filter.O2Concentration

5.2.6. EOS.Machine.Sensors.Filter.Pressure

5.2.7. EOS.Machine.Sensors.ProcessChamber.O2Concentration.Bottom

5.2.8. EOS.Machine.Sensors.ProcessChamber.O2Concentration.Top

5.2.9. EOS.Machine.Sensors.ProcessChamber.Temperature

5.2.10. EOS.Machine.Sensors.Turbine.Pressure

5.3. Participants may be asked for additional logs if deemed necessary.

6. Build Chamber Purge Gas Type, Specification, Certificates, and Gas Traceability Plan

6.1. Participants shall use a minimum of 99.996% pure argon (argon 4.6) per EOS recommendations. Participants should document the specific purity of argon used in the machine.

6.2. Participants shall acquire and provide supplier certification of gas purity.

6.3. Contributors shall document their argon delivery system to the machine. This can be a simple drawing or explanation of how argon is stored and transferred to the machine.

7. L-PBF Machine Hardware or Software Modifications

7.1. A “grid nozzle ” (2200-5501) shall be used for all builds, and shall be documented.

7.2. A high-speed steel type recoater blade shall be used for all builds in the study. All contributors shall document the type of recoater blade installed on the machine used in the UWRR.

7.3. Any other software or hardware modifications made to the machine must be recorded and sent to the University of Washington team for review prior to the start of the study.

8. Standard Procedures and Work Instructions for General Machine Operation and Process Control

8.1. The machine operator shall clean the build chamber thoroughly to ensure there is no contaminating powder, in addition to the powder supply chamber. Other powder lots outside this study should be considered foreign material, even if the chemistry is similar, and as such the machine should be cleaned according to Section 6.8 of the EOS M290 Manual [2].

8.2. If participants use materials other than Ti-6Al-4V on their machine, they shall document their procedure used for cleaning the machine after switching materials and send to the UW for approval.

Note: If changing the type of metal, it is recommended to follow Section 6.8 of the

EOS M290 Manual [2] to avoid potentially hazardous situations and minimize

contamination.

8.3. Participants shall document any material swaps that take place during the course of the study and provide all relevant material specifications to the University of Washington.

8.4. Participants shall ensure enough argon is on hand to complete the build.

8.5. The “cartridge filter clogging %” and “laser emission on-time hours” shall be recorded prior to each build.

8.6. The powder shall be sampled prior to each build. Sampling shall take place during the dispenser filling procedure as outlined below.

8.7. The operator shall add approximately 20kg of powder to the dispenser. Using a stainless steel scoop, 75g of powder shall be scraped off the top of the freshly deposited powder from the center of the dispenser. The powder in the dispenser shall then be compacted using a powder spatula. This shall be repeated 3 more times or until the dispenser is full. 300g of powder should be collected in total and stored in the provided vial.

8.8. The 300 grams of powder from each build shall be provided to the University of Washington in the sealed container for evaluation and testing. Please ship samples attn. Reid Schur at the University of Washington, along with the fabricated parts of that build (section 8.21). Samples shall be placed in a desiccator at the University of Washington preceding testing. Testing by the University of Washington shall include the following:

8.8.1.1. The powder samples shall be tested at UW according to ASTM F3049-14 [4] to evaluate changes in powder feedstock quality over the duration of the study. Some tests may be outsourced by UW to a third party testing facility if the required testing equipment or protocol is not available.

8.8.1.2. Particle size analysis by light scattering shall be measured per ASTM B822 [5] or by image analysis per ASTM F3049-14 [4].

8.8.1.3. Light element chemistry shall be measured by inert gas fusion per ASTM E1447 [6] and ASTM E1409 [7].

8.8.1.4. Metallic chemistry shall be measured by x-ray fluorescence per ASTM E539 [8].

8.8.1.5. Flowability and apparent density shall be measured per ASTM B212 [9] and ASTM B213 [10].

8.8.1.6. Particle morphology and microstructure shall be evaluated by optical microscopy (OM) and scanning electron microscopy (SEM) methods.

8.9. The machine operator shall load the build file provided by the University of Washington for the build and complete the build setup using the Ti64_PerformanceM291 1.10 parameter set as defined in the build file. This parameter set contains modifications from the standard Ti64_PerformanceM291 1.10 parameter set, and shall not be modified in any way.

Note: All details concerning the printing conditions and part configurations shall be provided for each build by the UW team. Each build file shall have a unique name as follows: B1_final, B2_final, B3_final, B4_final, B5_final, B6_final.

A preview of builds 1 and 6 is provided in Appendix A.2.

8.10. The operator shall ensure that the dosing on the machine is set to automatic. The dosing settings in the build file shall not be altered.

8.11. The machine operator shall perform the printing preparations according to EOS SOPs as outlined in Section 6 of the EOS M290 Operating Manual [2]. Operator should also check the chiller is on and the monitoring suites are GREEN.

8.12. The operator shall use the layer camera to capture the 1st build layer from each build and provide this to the University of Washington.

8.13. Record the “laser emission on-time hours” after the build is complete.

8.14. After the build has completed, wait to open the chamber until the chamber has reached room temperature.

8.15. The operator shall remove the excess powder from the build chamber, dispenser and collector. It is recommended this be done using an IPCM Extra to conform to the University of Washington’s procedures. If this is not possible, powder extraction can be done according to standard practice at your organization. The method used by

each participant is expected to conform to EOS and should be documented. Additionally, the operator shall remove as much powder from the perforated supports as possible and combine with the rest of the recovered powder.

Note: Powder must be removed in such a way as to avoid contamination from the manufacturing environment or from other powder since this powder will be reused.

8.16. The used powder shall be sieved using a 63 µm mesh size.

8.17. The used powder shall be weighed. The weight shall be recorded and supplied to the University of Washington.

8.18. The operator shall mix the powder collected from the build chamber with an amount of reserved, virgin powder calculated as follows:

$$Added\ Virgin\ Powder\ (kg) = 80 - Sieved\ Powder\ Mass\ (section\ 8.16)$$

8.19. Powder shall only be added to replace powder consumed during the manufacturing process, as determined by the powder mass after sieving (8.18). Added powder shall come from the reserved powder from the allocated study powder lot.

8.20. The mixing procedure shall be performed as follows:

8.20.1. The operator shall add half of the used powder to a powder keg, then add half of the calculated quantity of virgin powder to the keg. The keg should then be closed. Using an EOS lift truck (or similar), the keg shall be lifted to allow it to freely rotate. The powder keg shall be carefully spun 10 times forwards (towards the operator), 10 times backwards, and 10 more times forwards. See Appendix A.7 for a schematic.

8.20.2. The previous method shall be applied to the other half of the used and virgin powder in an empty powder keg.

Note: This process should take place on an ESD mat or be grounded with a grounding wire to avoid potential hazards.

8.20.3. The UW shall be consulted on any deviations from this process prior to the start of the study.

8.21. Mixed powder shall be stored in airtight containers until the next build.

8.22. The operator shall separate the parts from the build plate. The method used for this process must be documented. Sectioning should be performed to separate the parts from the build plate. A schematic of the cut locations is shown in Appendix A.4, Figure A.4.1.

8.23. Participants with heat treatment capabilities may perform on-build plate stress relief. The furnace used shall meet the following conditions:

8.23.1. Utilize argon or vacuum environment to minimize oxidation.

8.23.2. Maintain temperature uniformity requirement of ±10 C within the work zone.

8.23.3. Thermocouples used shall adhere to AMS2750, including but not limited to the thermocouple type and calibration frequency.

8.24. Stress relief utilized shall adhere to the following procedure:

8.24.1. Two thermocouples should be placed within the furnace. If the heat treatment is performed on build plate, one thermocouple shall be in contact with the center of the build plate. The other thermocouple shall be in contact with a tensile coupon. If the specimens are separated from the build plate at the time of heat treatment, both thermocouples shall be in contact with tensile coupons.

8.24.2. Charge shall be placed in cold furnace and backfilled with argon or brought to vacuum level per participant organization's SOP.

8.24.3. Furnace temperature shall be raised to 745 ± 10C over approximately 60 minutes.

8.24.4. Soak at 745C for 120 minutes. The soak time shall begin when the lowest temperature thermocouple reaches 745C.

8.24.5. Furnace cool to 500C, then rapid cool. The furnace shall be under argon or vacuum for the duration of the cool.

8.25. No other work shall be performed on the parts. Participants should not attempt to remove additional support material or perform any surface finishing.

Note: All necessary post processing shall be performed at The University of

Washington, and include the following:

8.25.1. Separation of remaining support structures from samples.

8.25.2. Full stress relief on all samples if not performed by the participant, per 8.24.

8.25.3. Machining of the specimens to conform with ASTM E8 [12] dimensions and surface roughness.

8.26. Participants shall ship parts along with the vials of collected powder (section 8.6) to The University of Washington for testing and analysis. Parts and powder should be packaged with appropriate packing materials to prevent damage to the contents. Additionally, it is requested that the parts be wrapped in plastic to avoid powder escaping from the support structures. Contents shall be labelled with the following: Company-Build File Name-Build Number. It is advised they be shipped by standard ground shipping. Parts are individually labelled within the build files, and as such labelling of the parts is unnecessary.

Shipping address for all materials:

8.27. The build file for the subsequent build shall be supplied upon receival by the UW of printed parts, powder sample, and digital documentation.

9. Build Failures

9.1. Build failures shall be dealt with according to the build height in which failure occurs using the following guidelines.

9.1.1. If the failure occurs in the first layer of parts or earlier, the build shall be aborted. The powder on the build plate and in the collector shall be weighed and recorded. This powder must be sieved. The build layer in which failure occurred shall be communicated to the University of Washington. The UW will determine the appropriate amount of virgin powder that must be added to replace the consumed powder. The mixing procedure outlined in section 8 must be used to add this powder to the used powder. The build can then be restarted with the resurfaced plate.

9.1.2. If the failure occurs in the support structures between the A and B levels, the error shall be cleared and the build continued. The layer in which failure occurred shall be noted and reported to the University of Washington.

9.1.3. If the failure occurs in the second layer of parts, the build will not be continued or restarted. The powder remaining in the dispenser shall be weighed and reported to the University of Washington. The build shall be recovered as if it

was successful, and all parts shall be sent to the UW. The layer in which failure occurred shall be recorded and reported to the UW.

10. Ancillary In-Situ Monitoring Techniques Used During Deposition

    10.1. Participants shall provide details of whether they have melt pool monitoring or optical thermography. The UW team has both of these options and will capture that data during the builds. The team shall pursue documenting data acquired from the other participants with these capabilities.

    10.2. Participants shall provide in-situ powder layer pictures.

11. Check of Laser Prior to Each Build

    11.1. Contributors are requested to perform laser power measurements before builds. Readings shall be recorded and reported to the University of Washington. "Acceptable" readings shall be in accordance with the participant's standard practice.

12. Maintenance and Machine Calibration Data Plan

    12.1. Participants shall provide details regarding machine age and date of most recent maintenance/service. If the serial number is provided to the UW, that information can be made available from EOS with your consent.

    Note: It is expected that each participant will only use a single machine for this effort and that it remains the same throughout the duration of the investigation. It is also requested that every build in the series be performed by the same operator if possible. Participants will document if a different operator completes a build.

    12.2. All participants are requested to have service performed according to the recommended schedule and practice by EOS during the course of the evaluation.

    12.3. Participants shall provide a copy of the recent machine maintenance record including any anomalies, replacements or noted concerns.

    12.4. Participants shall provide details of the beam spot size, shape, beam quality, and the beam focal plane.

    12.5. Participants shall document routine maintenance performed by the machine operator.

Appendix A.1: Relevant Standards and Documents

[1] SAE-International, AMS7003: Laser Powder Bed Fusion Process, (2018) 1–15.

[2] EOS, M290 Operating Manual, Edition 2.19, (2019).

[3] ASTM-International, B215-15: Standard Practices for Sampling Metal Powders, (2015) 1–7. https://doi.org/10.1520/B0215-10.2.

[4] ASTM-International, F3049-14: Standard Guide for Characterizing Properties of Metal Powders Used for Additive Manufacturing Processes, (2014) 1–3. https://doi.org/10.1520/F3049-14.

[5] ASTM-International, B822-17: Standard Test Method for Particle Size Distribution of Metal Powders and Related Compounds by Light Scattering, (2017) 1–4. https://doi.org/10.1520/B0822-17.2.

[6] ASTM-International, E1447−9: Standard Test Method for Determination of Hydrogen in Titanium and Titanium Alloys by the Inert Gas Fusion Thermal Conductivity Method, (2016) 1–4. https://doi.org/10.1520/E1447-09R16.2.

[7] ASTM-International, E1409-13: Standard Test Method for Determination of Oxygen and Nitrogen in Titanium and Titanium Alloys by Inert Gas Fusion, (2013) 1–7. https://doi.org/10.1520/E1409.

[8] ASTM-International, E539-19: Standard Test Method for Analysis of Titanium Alloys by Wavelength Dispersive X-Ray Fluorescence Spectrometry, (2019) 1–10. https://doi.org/10.1520/E0539-11.2.

[9] ASTM-International, B212-17: Standard Test Method for Apparent Density of Free-Flowing Metal Powders Using the Hall Flowmeter Funnel, (2017) 1–4. https://doi.org/10.1520/B0212.

[10] ASTM-International, B213-20: Standard Test Methods for Flow Rate of Metal Powders Using the Hall Flowmeter Funnel, (2020) 1–4. https://doi.org/10.1520/B0213-13.2.

[11] SAE, AMS-H-81200D: Heat Treatment of Titanium and Titanium Alloys, (2014) 1–24.

[12] ASTM-International, E8/E8M-16a: Standard Test Methods for Tension Testing of Metallic Materials, (2018) 1–30.

Appendix A.2: Build Design

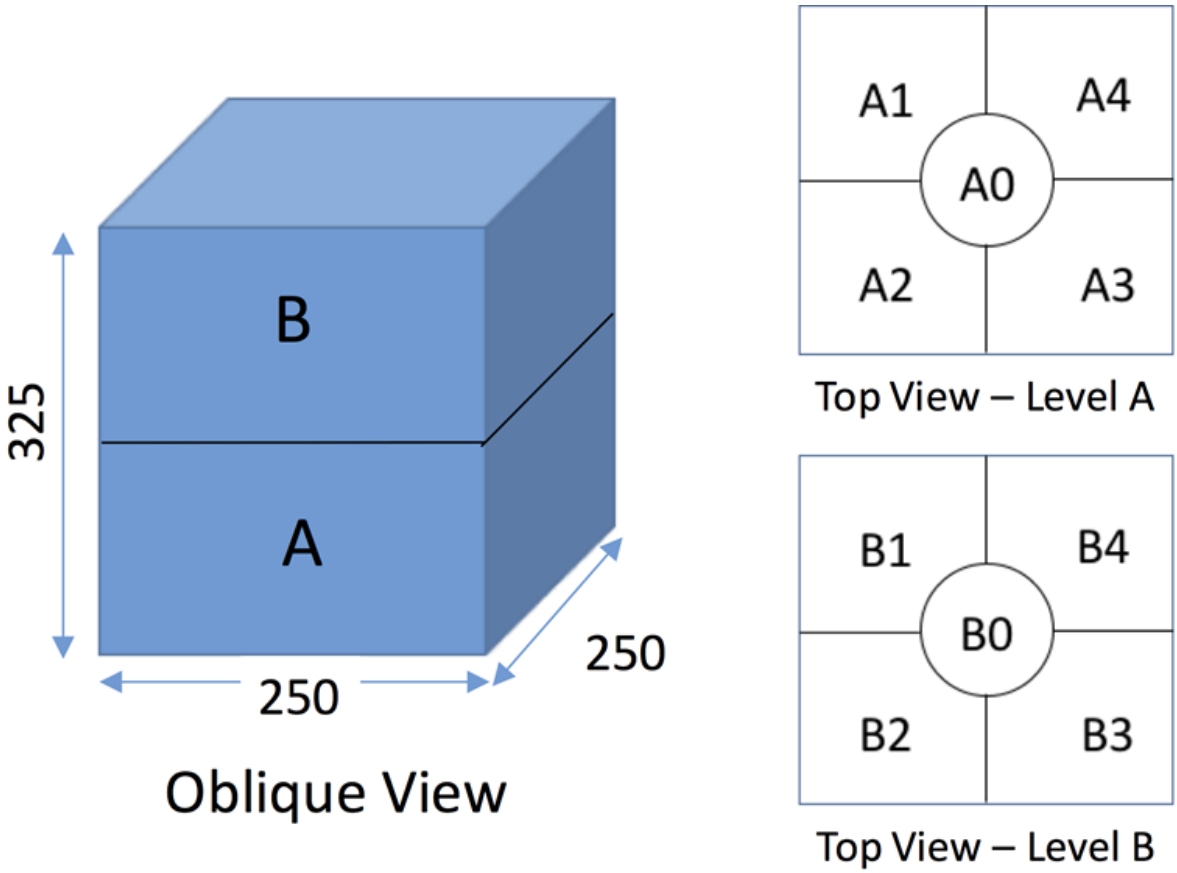

Fig. A.2.1: Oblique view of the EOS M290 build volume broken up into a A and B level. Top views of each level broken up into the 5 regions of interest. Region 0 for both levels is in the center and regions 1 through 4 are counterclockwise starting in the back-left corner of the build space.

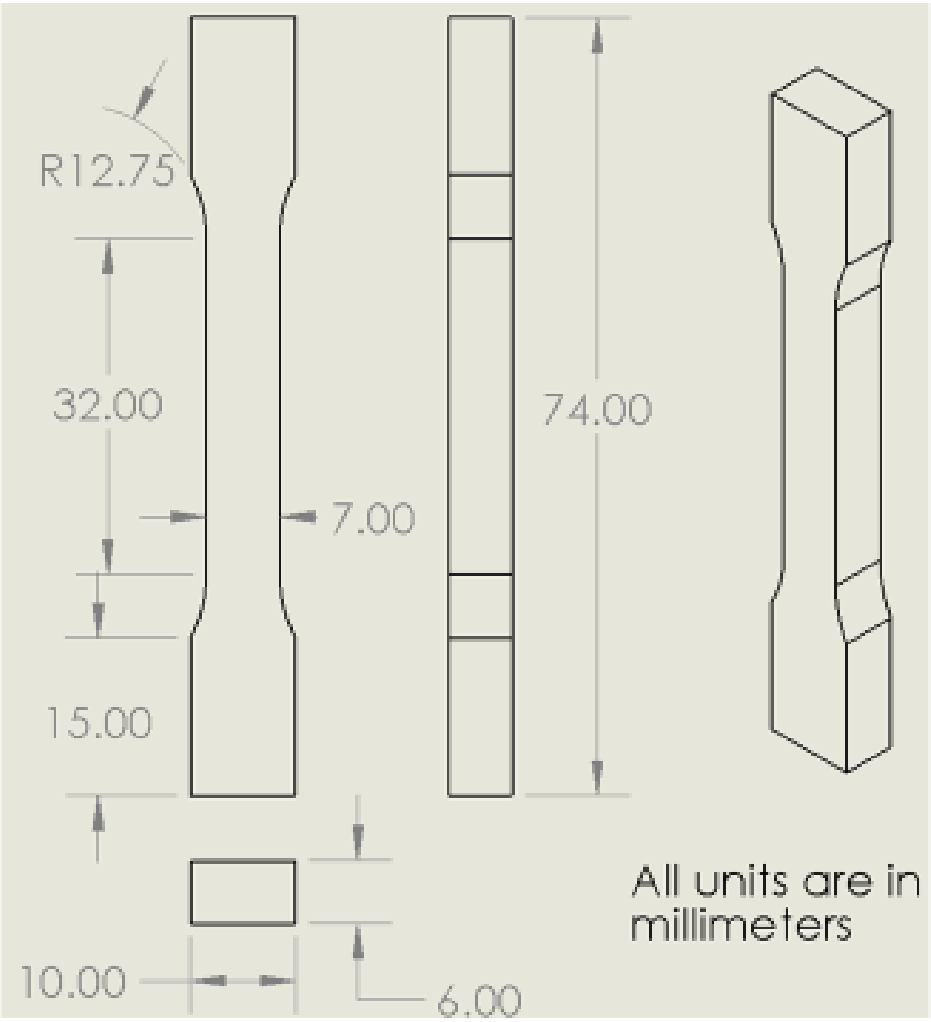

Fig. A.2.2**:** As-printed tension specimen dimensions. Specimen dimensions shall conform to ASTM E8 [12] subsize after machining.

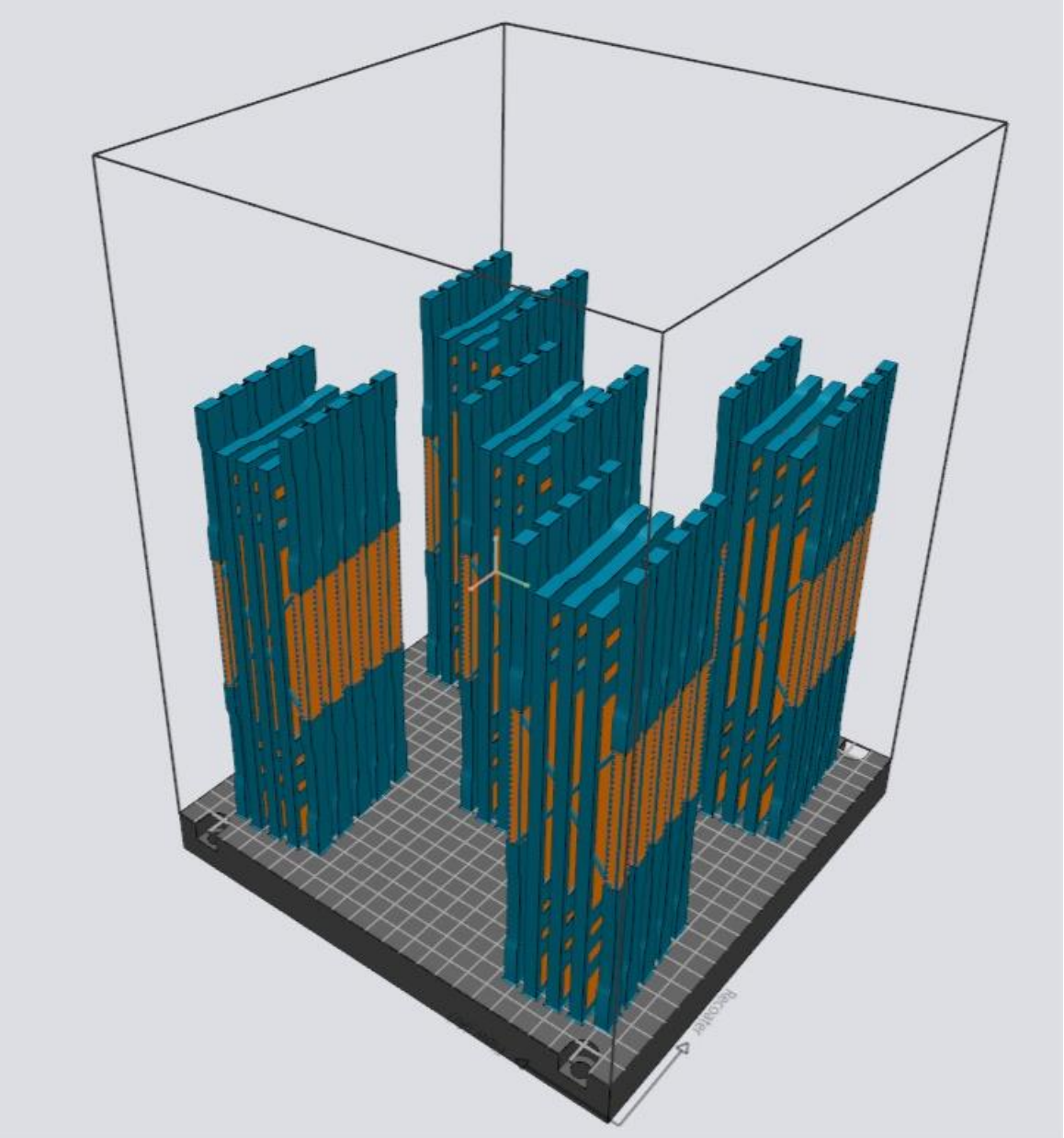

Fig. A.2.3: Oblique view of configuration 1. Build 1 and Build 6 (B1 and B6) will use the build design in this figure. Blue are parts or solid supports and orange are porous supports.

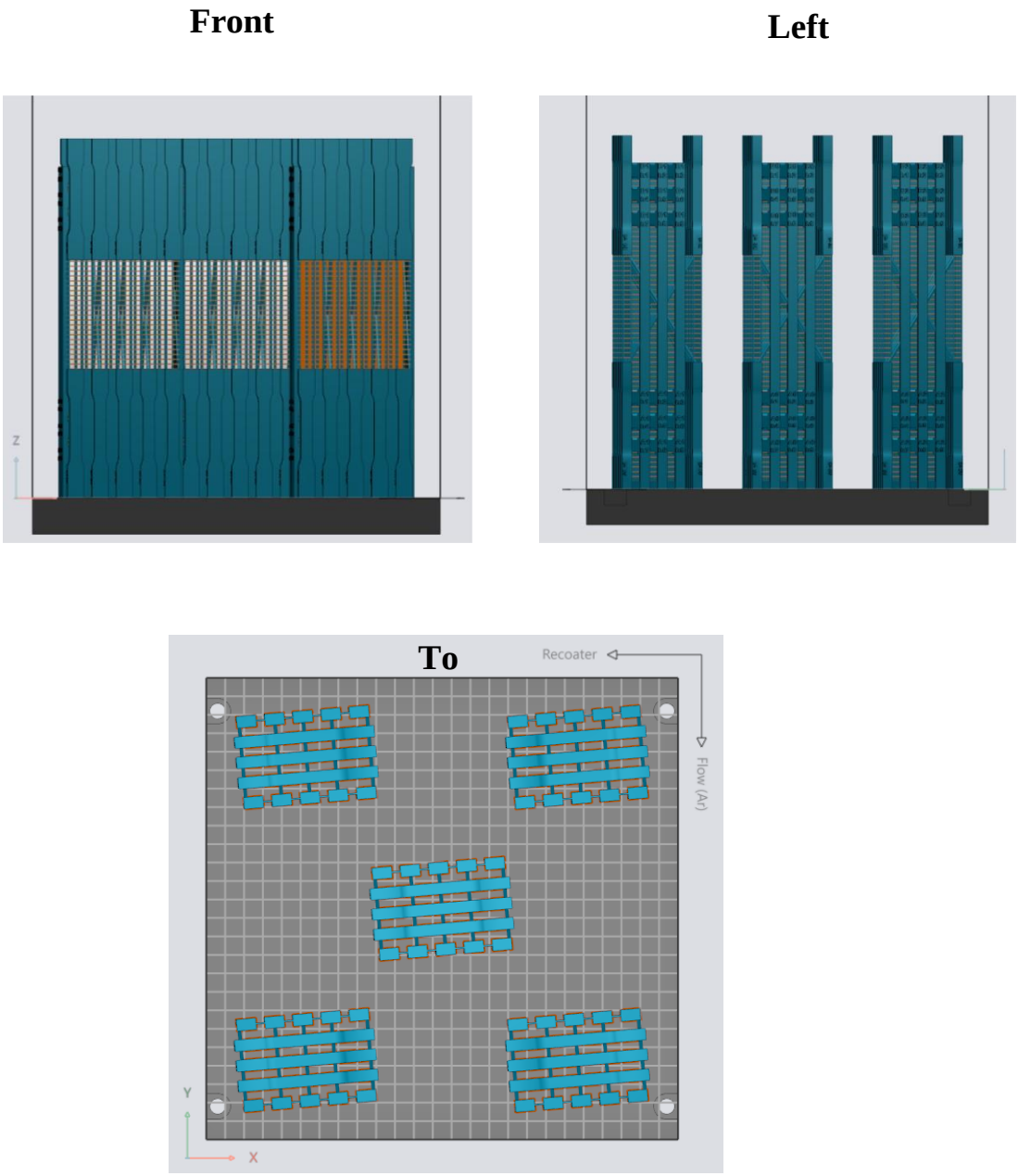

Fig. A.2.4**:** Front, right, and top view of the configuration 1 build design used for B1 and B6. Blue are parts or solid supports and orange are porous supports.

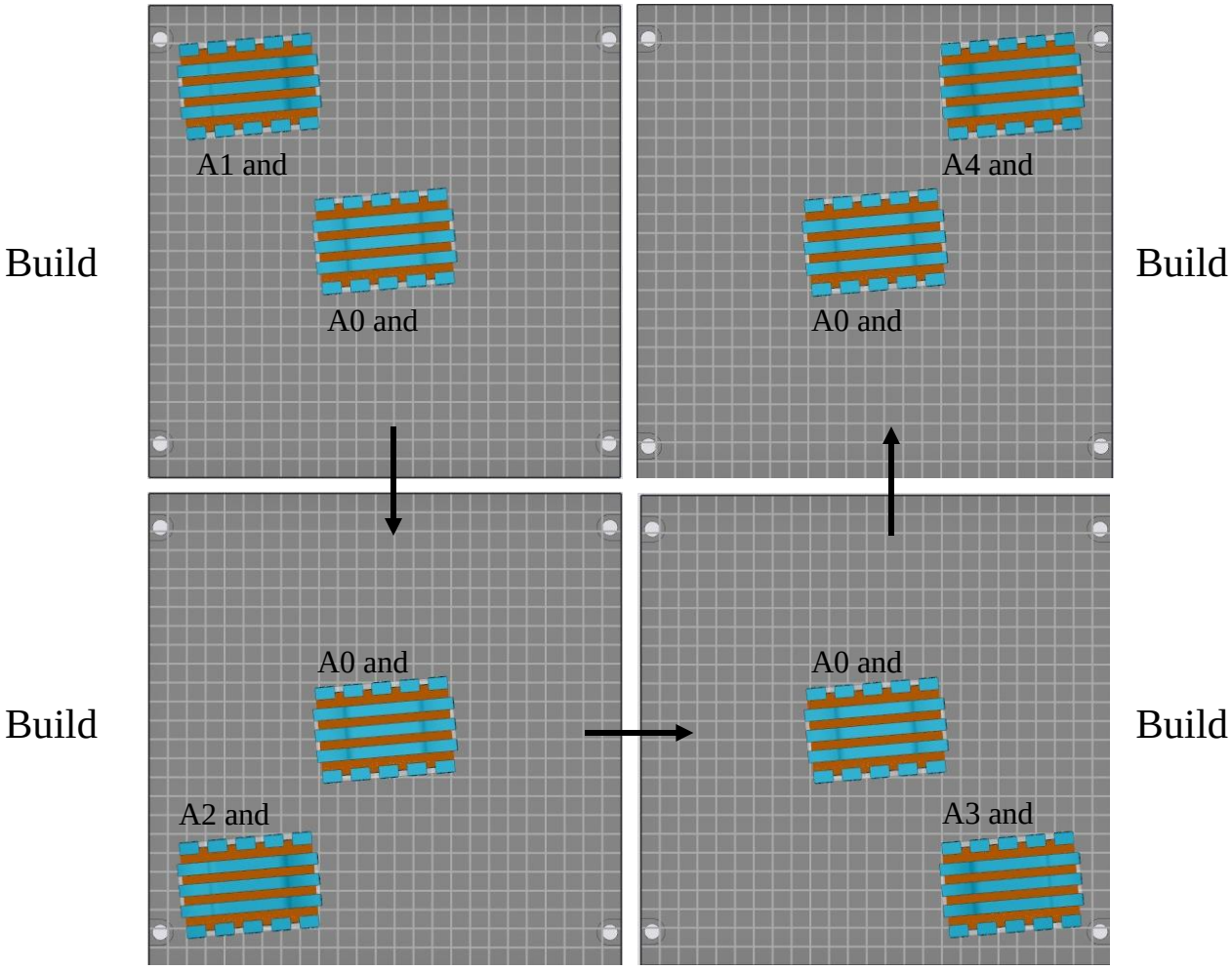

Fig. A.2.5: Sequence of Builds 2-5 (B2-B5), where the center cluster of parts (region 0) is always present and the outer region rotates between region 1 to 4.

Appendix A.3: Powder Certification

Inspection Certificate

EOS Titanium Ti64

Inspection certificate according to EN 10204, type 3.1

Trade name	EOS Titanium Ti64	Manufacturing method	Plasma atomized
EOS product no.	9011-0039	Date of manufacturing	11.12.2020
Lot number	A 482001		
Manufacturer	Electro Optical Systems Finland Oy Lemminkäisenkatu 36 FI-20520 Turku Finland Tel.: +358 (0)20 765 91 40 Quality_Control_FINLAND@eos.info	Supplier	EOS GmbH Electro Optical Systems Robert-Stirling-Ring 1 D-82152 Krailling Germany Tel.: +49 89 893 36 0

Declaration of conformance

As part of EOS quality assurance, the powder lot has been analyzed for powder properties and has been tested to work in EOS M machine. Parts built with this lot have been tested against EOS criteria and standard requirements.

Powder lot conforms to EOS requirements for powder, machine behavior, and solid part properties. The chemical composition and mechanical properties are in accordance with standards ISO 5832-3, ASTM F1472, ASTM F2924 and ASTM F3302.

Date: 11.12.2020

Approved by:

Marjaana Hovi

QA Specialist

Electro Optical Systems Finland Oy

Inspection Certificate

Analyses of Powder (see page 4 for analysis details)

Sampling and Analysis Sample Preparation

Sampling of the quality assurance test batch and analysis sample preparation done according to ASTM B215.

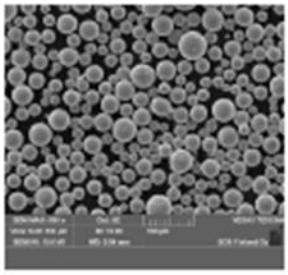

Cleanliness of Powder

Powder is visually free from foreign materials and uniform in condition.

Morphology

Powder is predominantly spherical with low levels of deformed particles.

Particle Size Distribution Analysis

Test method	Size characteristic	Limits	Result	✓/✗	Test Method	Size charateristic	Result
Laser diffraction	d10 [µm]	22 - 32	30	✓	Dynamic image analysis X_{Conv}	x10 [µm]	24
	d50 [µm]	34 - 44	41	✓		x50 [µm]	37
	d90 [µm]	49 - 61	57	✓		x90 [µm]	50

Sieve Analysis

Fraction retained	Test Method	Limits	Result	✓/✗
≥ 63 µm [wt%]	Laboratory sieving	Max. 0.5	0.0	✓

Powder Density Analysis

Property	Test Method	Limits	Result	✓/✗
Apparent density [g/cm³]	ASTM B212	2.40 - 2.80	2.59	✓
Skeletal density [g/cm³]	Gas displacement	N/A	4.416	N/A

Powder Water Content Analysis

Property	Test Method	Limits	Result	✓/✗
Water content [ppm]	Coulometric KF titration	Max. 125	40	✓

Chemistry Analysis (External ISO 17025 accredited laboratory)

Element	Test Method	Limits [wt.%]	Result	✓/✗	Element	Test Method	Limits [wt.%]	Result	✓/✗
Ti	ICP-OES	Balance	Bal.	✓	N	Fusion	Max. 0.04	0.02	✓
Al	ICP-OES	5.50 - 6.75	6.32	✓	H	Fusion	Max. 0.012	0.002	✓
V	ICP-OES	3.50 - 4.50	4.02	✓	Y	ICP-OES	Max. 0.005	<0.001	✓
Fe	ICP-OES	Max. 0.25	0.21	✓	OE, each	ICP-OES	Max. 0.10	<0.10	✓
O	Fusion	Max. 0.15	0.15	✓	OE, total	ICP-OES	Max. 0.40	<0.40	✓
C	Combustion	Max. 0.08	0.01	✓					

Inspection Certificate

Analyses of Solid Part Properties (see page 4 for analysis details)

Following properties for this lot have been determined on additively manufactured solid parts using following system setup:

EOS M Machine: EOS M 290 400W
EOS Parameter Set: Ti64_PerformanceM291 1.1
Post Processing: Heat treatment 2 hours at 800 °C

Chemistry Analysis (External ISO 17025 accredited laboratory)

Element	Test Method	Limits [wt.%]	Result	✓/✗	Element	Test Method	Limits [wt.%]	Result	✓/✗
Ti	ICP-OES	**Balance**	Bal.	✓	N	Fusion	**Max. 0.05**	0.04	✓
Al	ICP-OES	**5.50 - 6.75**	6.20	✓	H	Fusion	**Max. 0.015**	0.004	✓
V	ICP-OES	**3.50 - 4.50**	4.00	✓	Y	ICP-OES	**Max. 0.005**	<0.001	✓
Fe	ICP-OES	**Max. 0.30**	0.19	✓	OE, each	ICP-OES	**Max. 0.10**	<0.10	✓
O	Fusion	**Max. 0.20**	0.16	✓	OE, total	ICP-OES	**Max. 0.40**	<0.40	✓
C	Combustion	**Max. 0.08**	0.01	✓					

Density

Density	Test Method	Limit	Result	✓/✗
Solid density **[g/cm³]**	ISO 3369	**Min. 4.4**	4.4	✓

Mechanical Properties (External ISO 17025 accredited laboratory)

Property	Test Method	Limit	Result	✓/✗
Yield strength, Rp0.2 **[MPa]**	ISO 6892-1 A14	**Min. 860**	1018	✓
Tensile strength, Rm **[MPa]**		**Min. 930**	1123	✓
Elongation, A **[%]**		**Min. 10**	13	✓

Appendix A.4: Support Removal

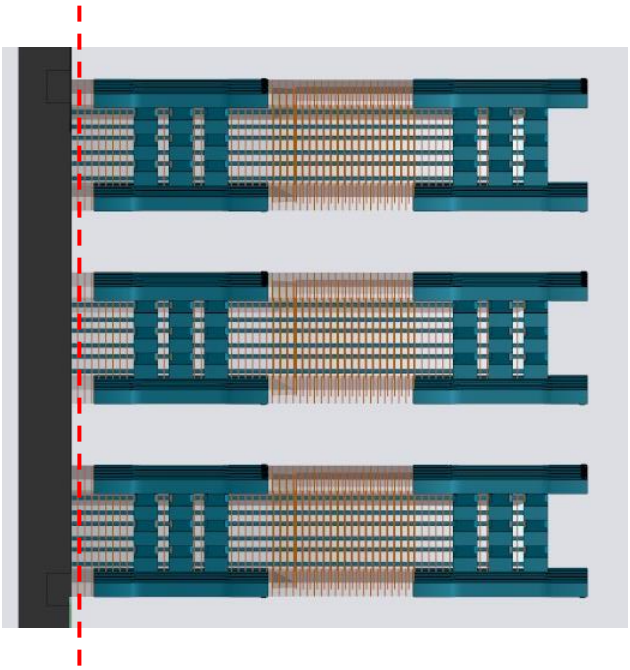

Fig. A.4.1: Approximate location of the cut each contributor shall make to separate the structures from the build plate.

Appendix A.5: Ti6Al4V Build Plate Drawing

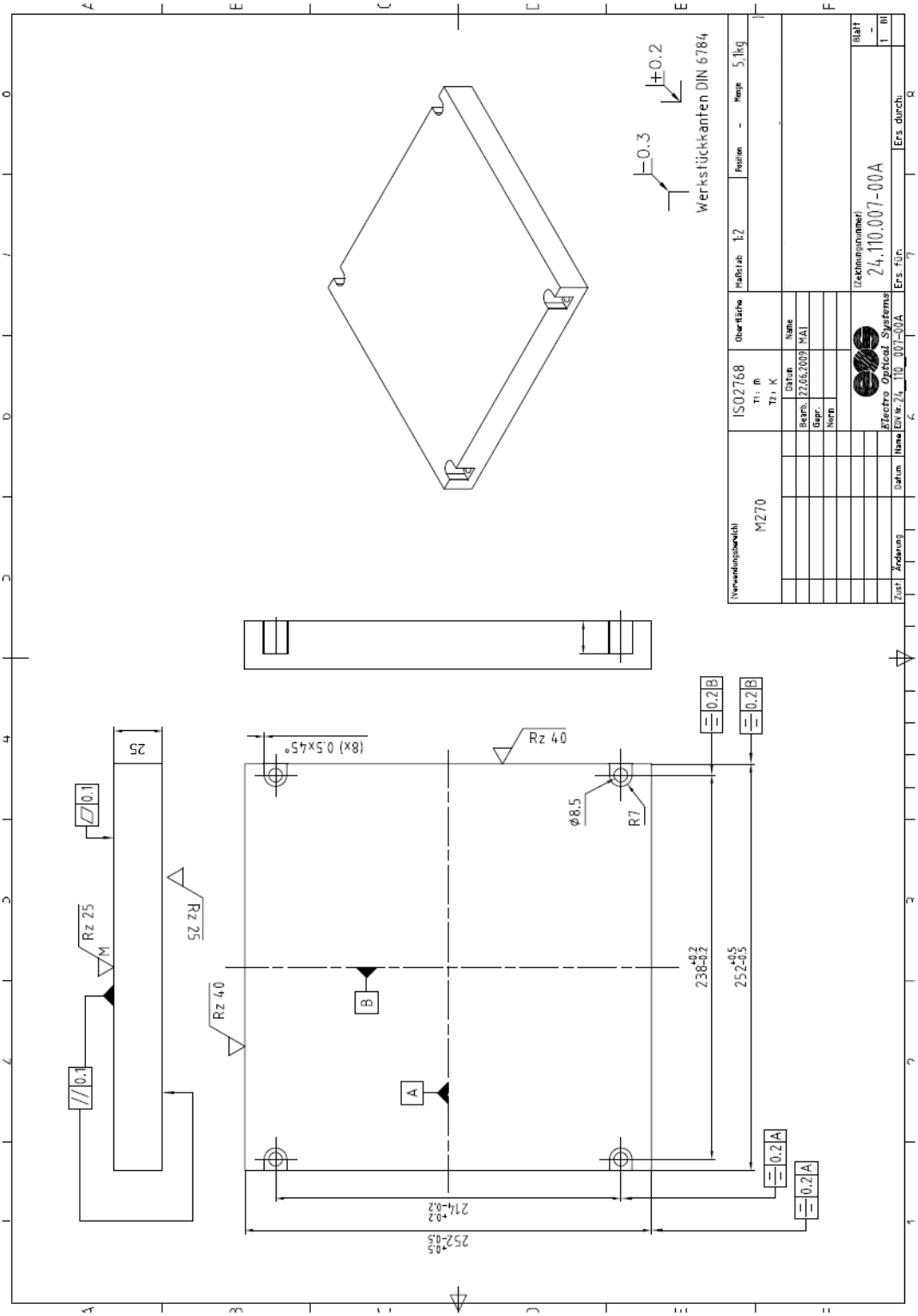

Appendix A.6: Build Plate Profilometer Line Scan Locations

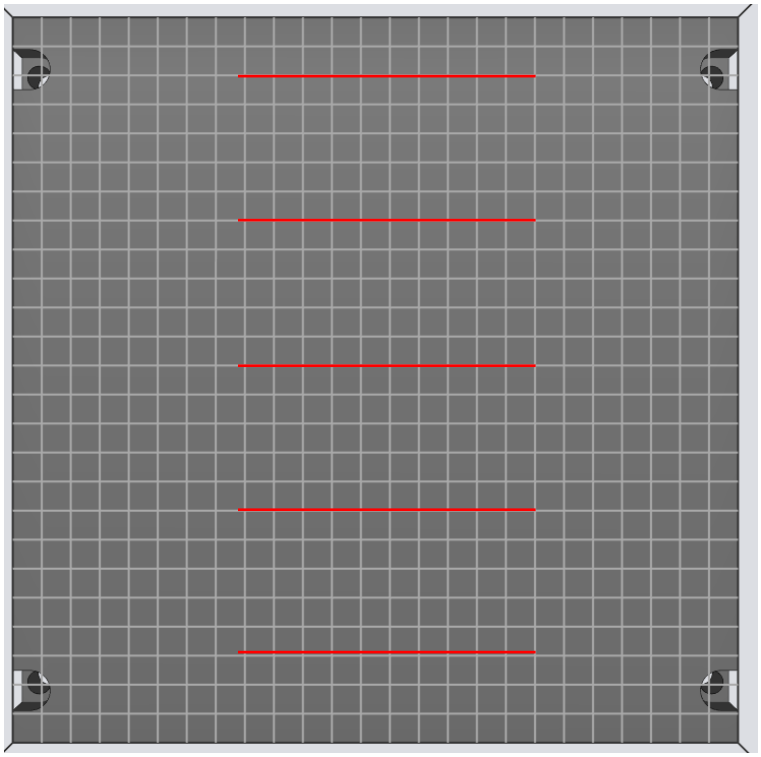

Fig. A.6.1**:** Approximate locations of the 5 contact profilometer line scans. 3 scans shall be made at each location.

Appendix A.7: Powder Mixing Schematics

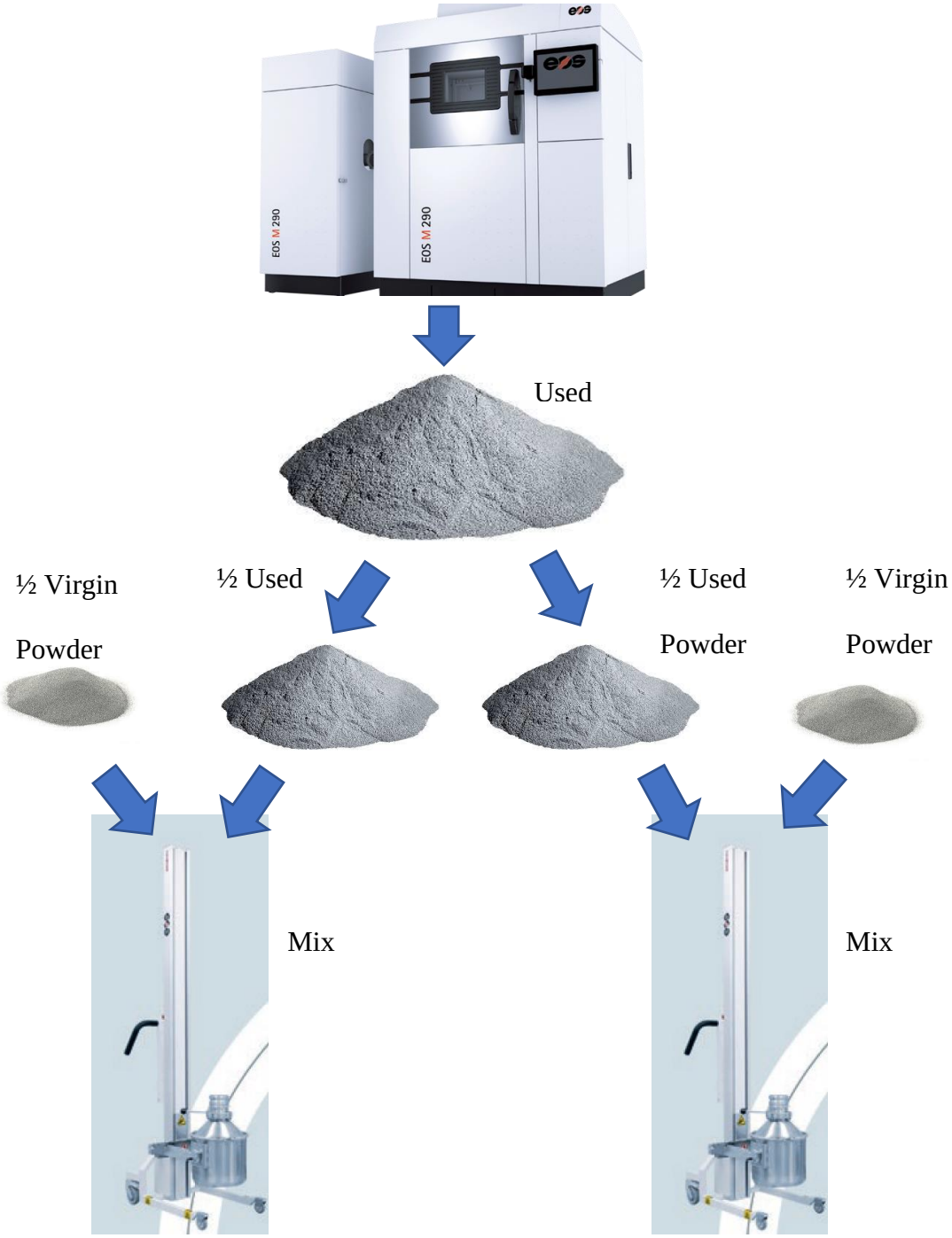

Fig. A.7.1: Flow chart outlining the powder collection and mixing process.

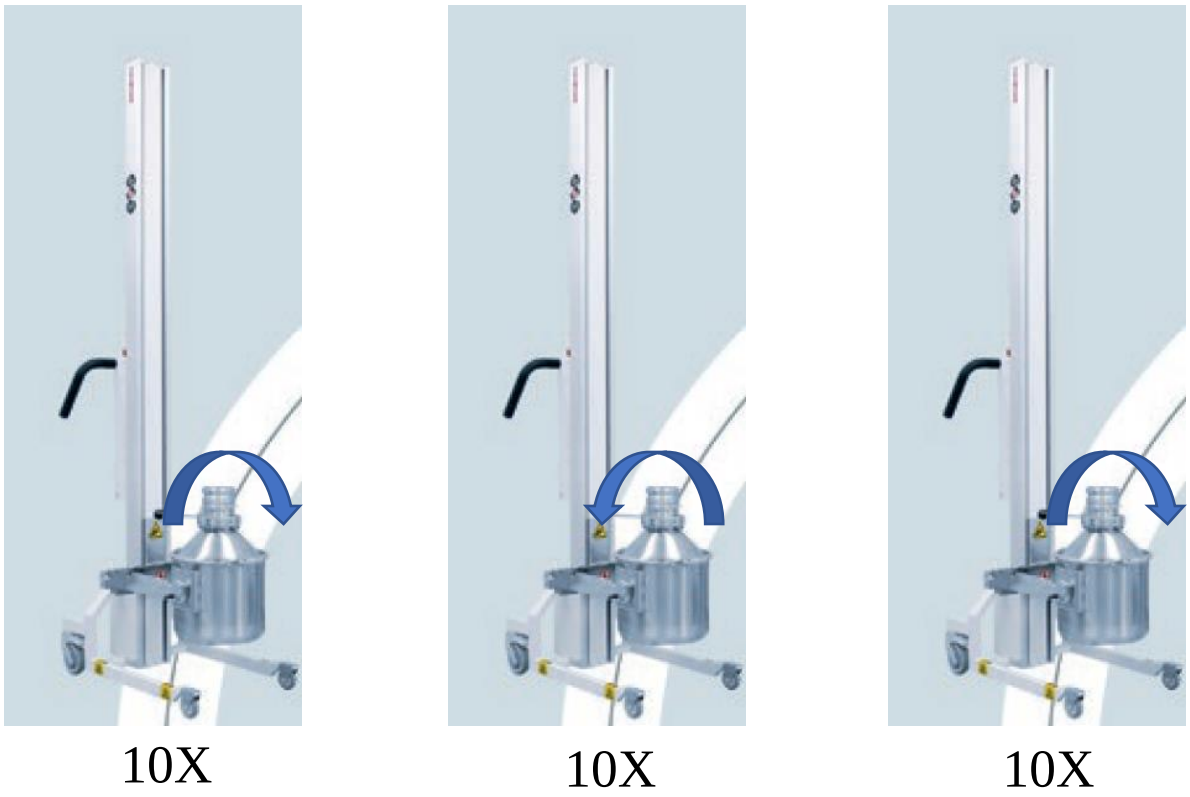

Fig. A.7.2: Schematic outlining the powder keg rotation as part of the powder mixing process. Keg is turned 10 times forwards, 10 times backwards, and 10 more times forwards.

Appendix B: Additional Figures

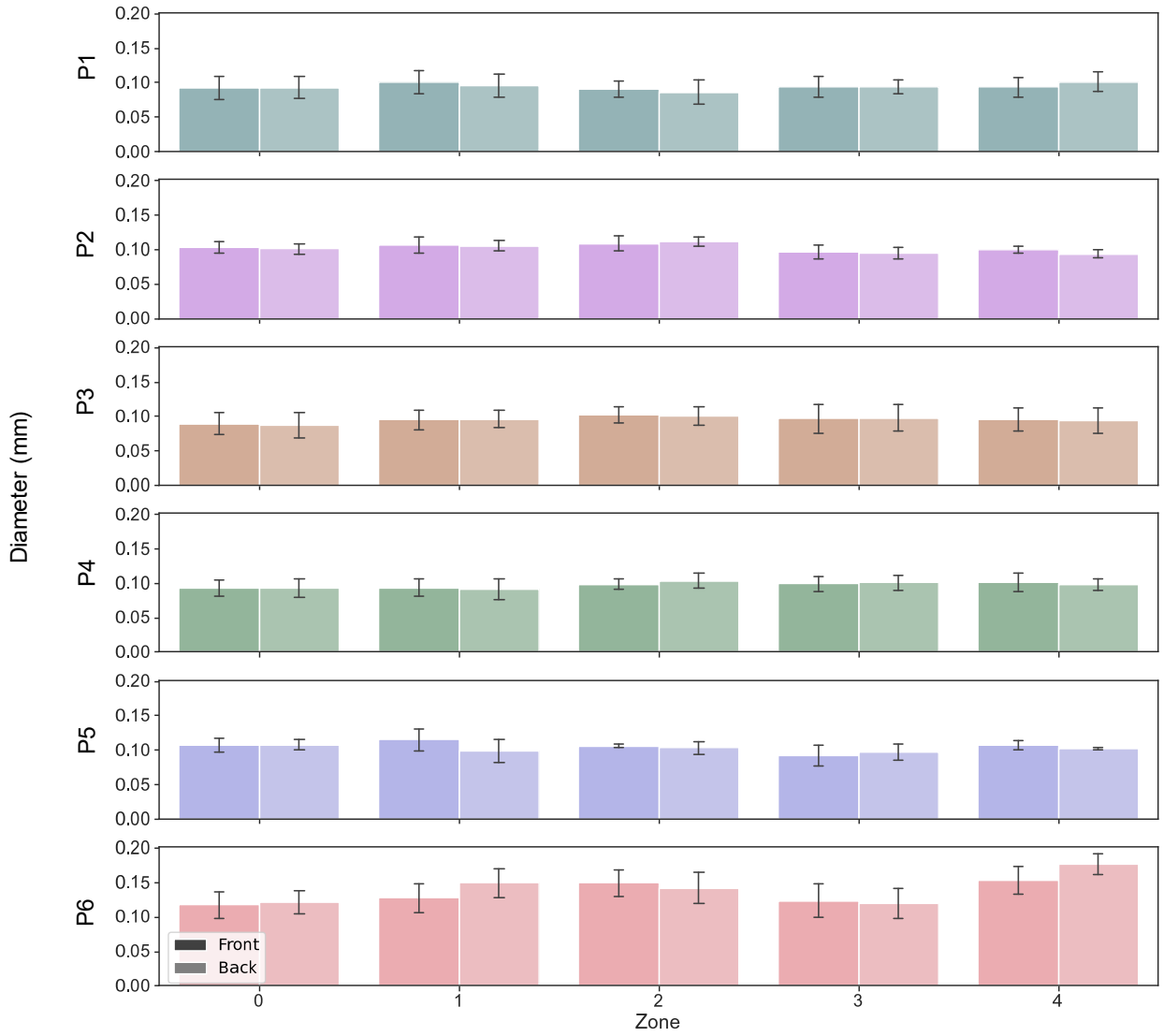

Fig. B.1: Average diameter of pores from each zone separated by the coupon location within each zone.

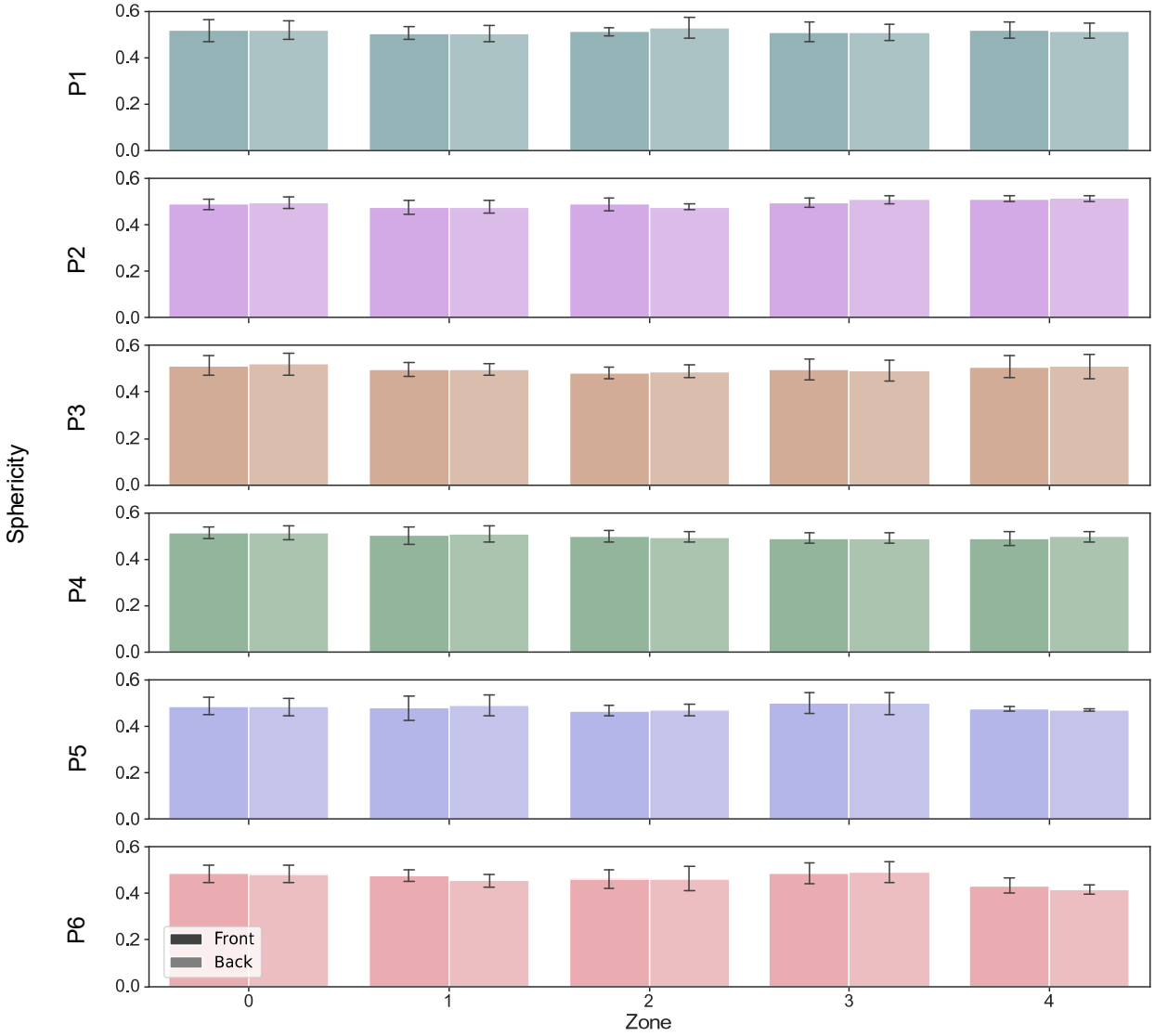

Fig. B.2: Average sphericity of pores from each zone separated by the coupon location within each zone.

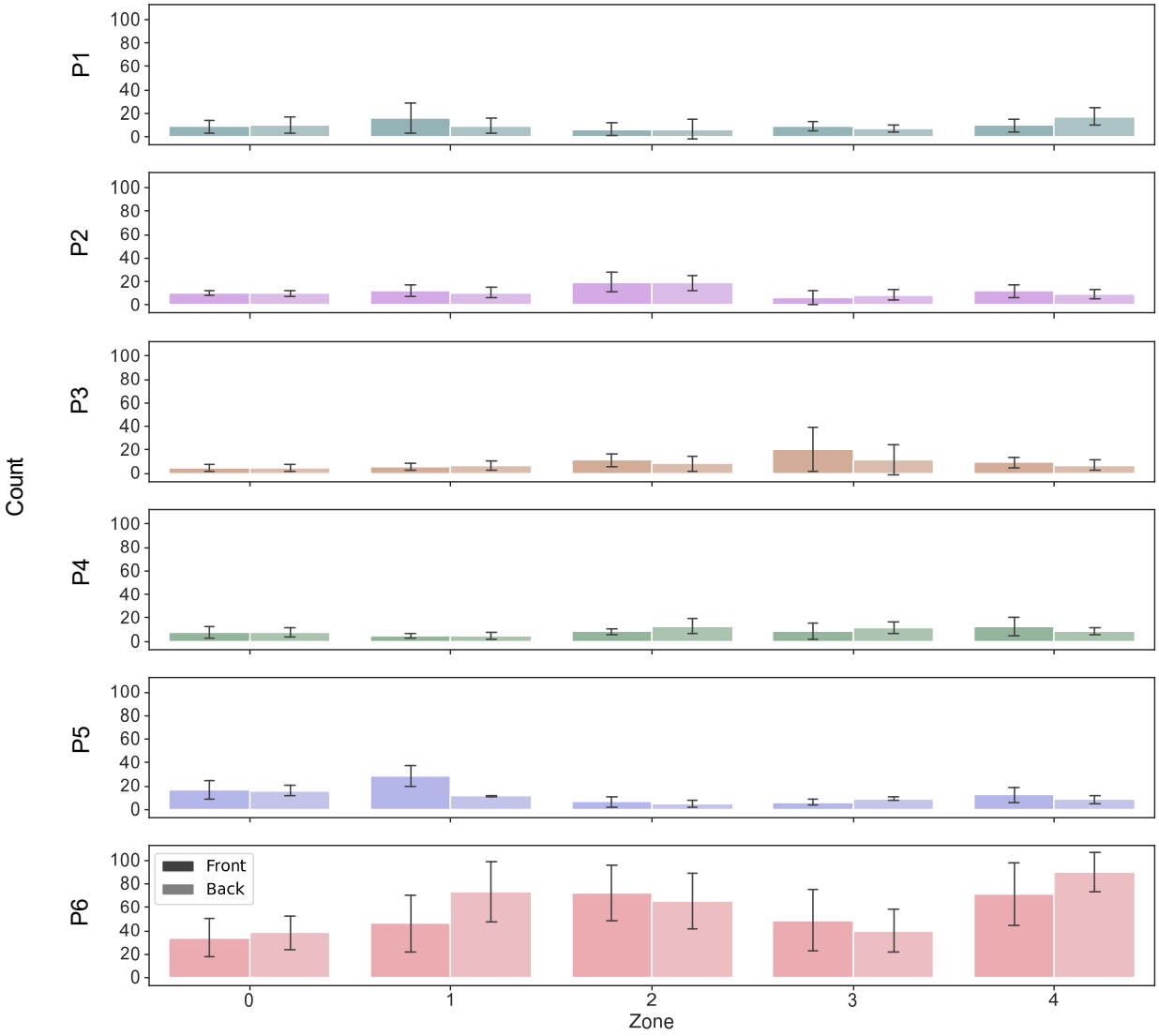

Fig. B.3: Average number of pores greater than 0.125 mm in diameter per coupon from each zone separated by the coupon location within each zone.

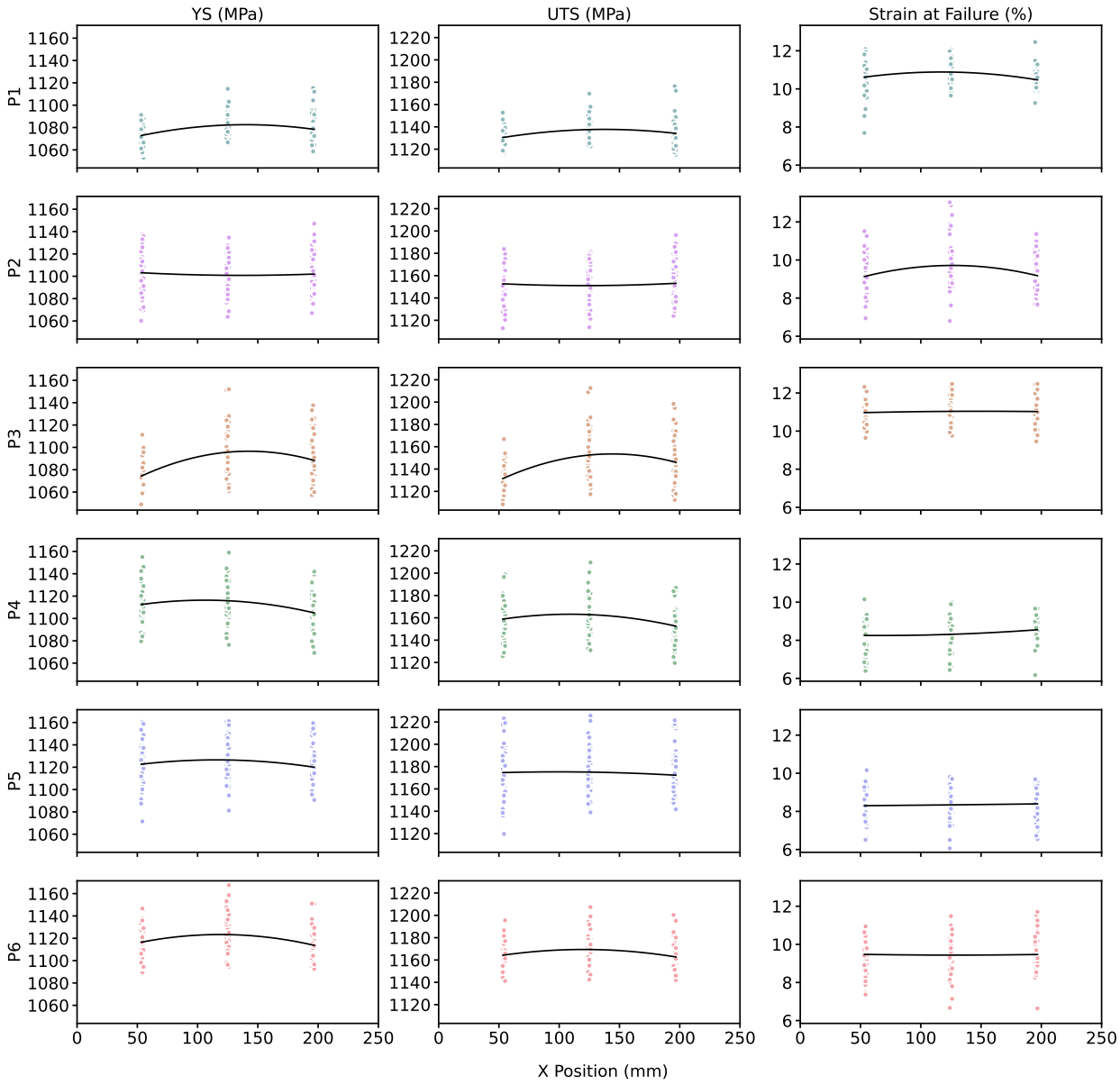

Fig. B.4: YS, UTS, and strain at failure as a function of the x-axis position of each horizontal coupon. Each row contains the data for one participant. Polynomial regression was applied, and the best fit line is shown.

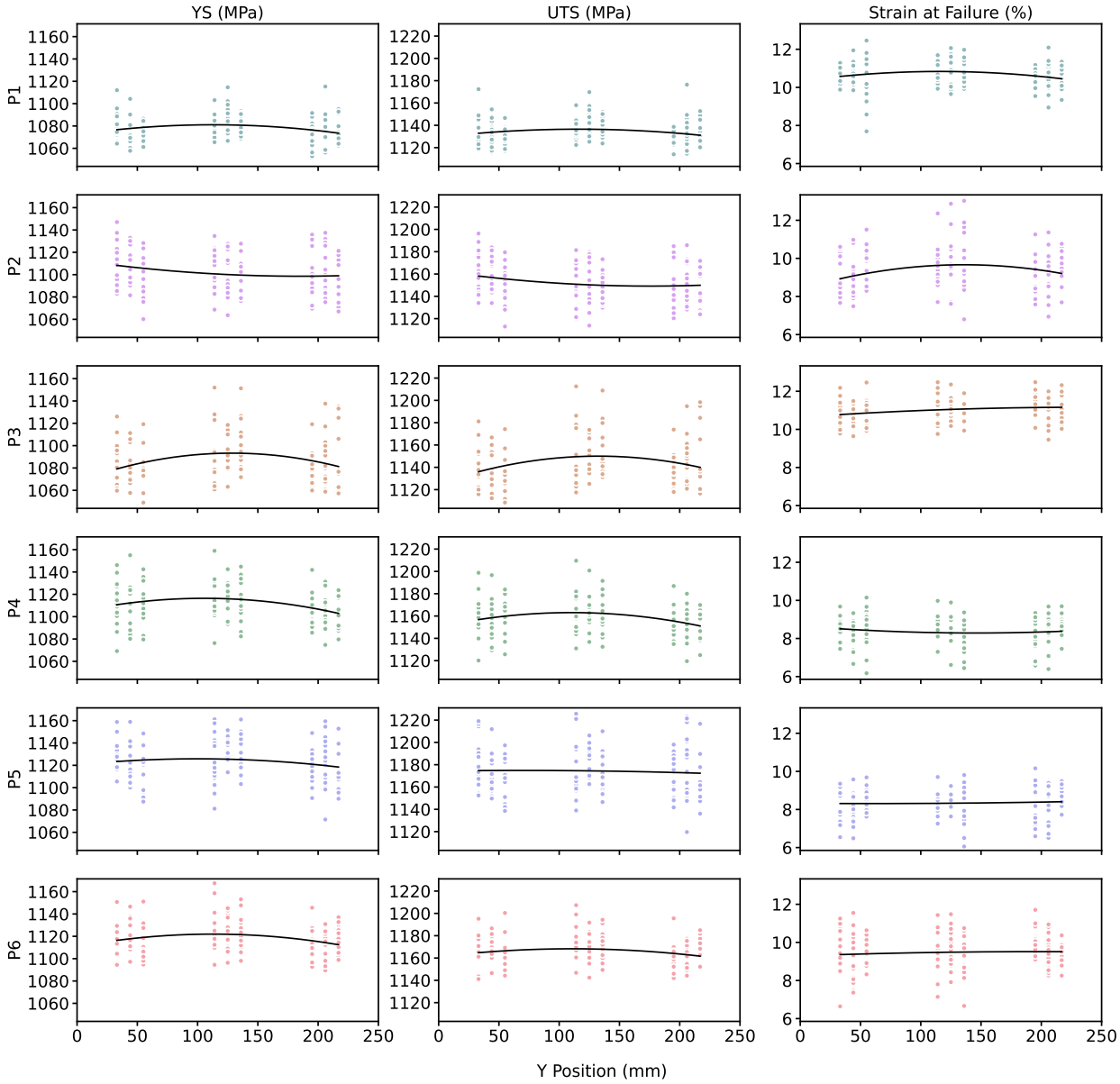

Fig. B.5: YS, UTS, and strain at failure as a function of the y-axis position of each horizontal coupon. Each row contains the data for one participant. Polynomial regression was applied, and the best fit line is shown.

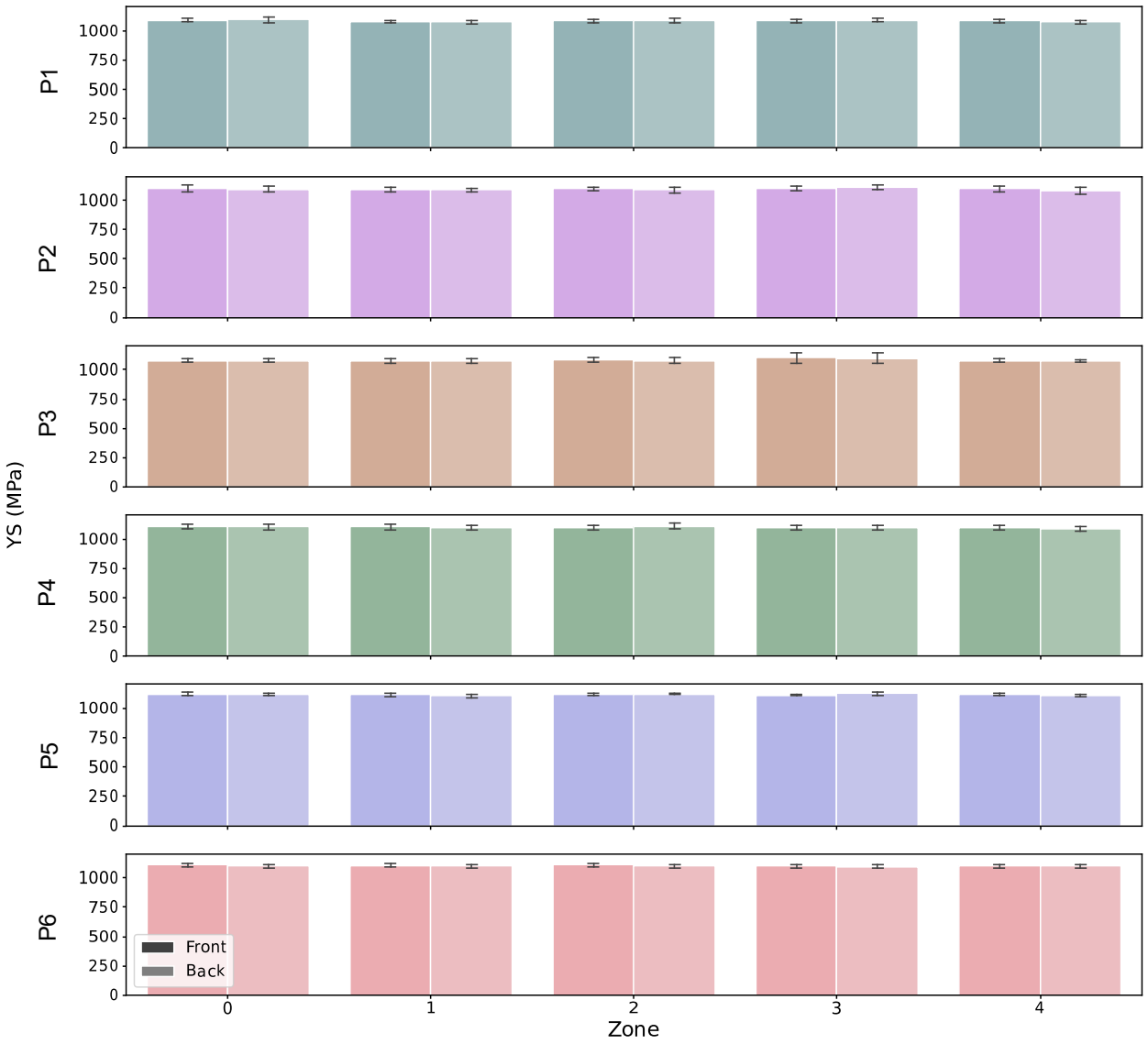

Fig. B.6: Vertical coupon YS in each zone, separated by the front and back rows of coupons.

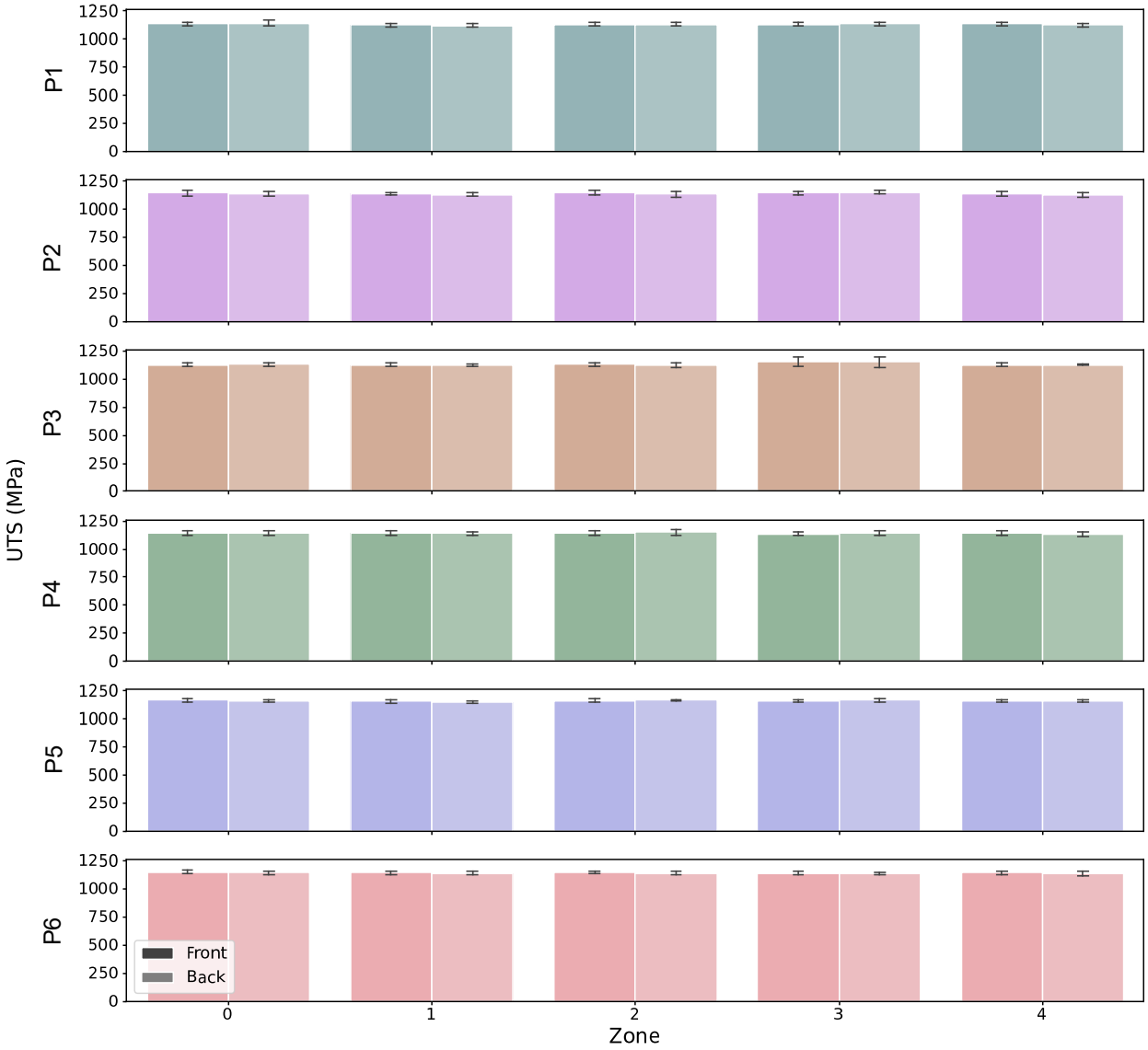

Fig. B.7: Vertical coupon UTS in each zone, separated by the front and back rows of coupons.

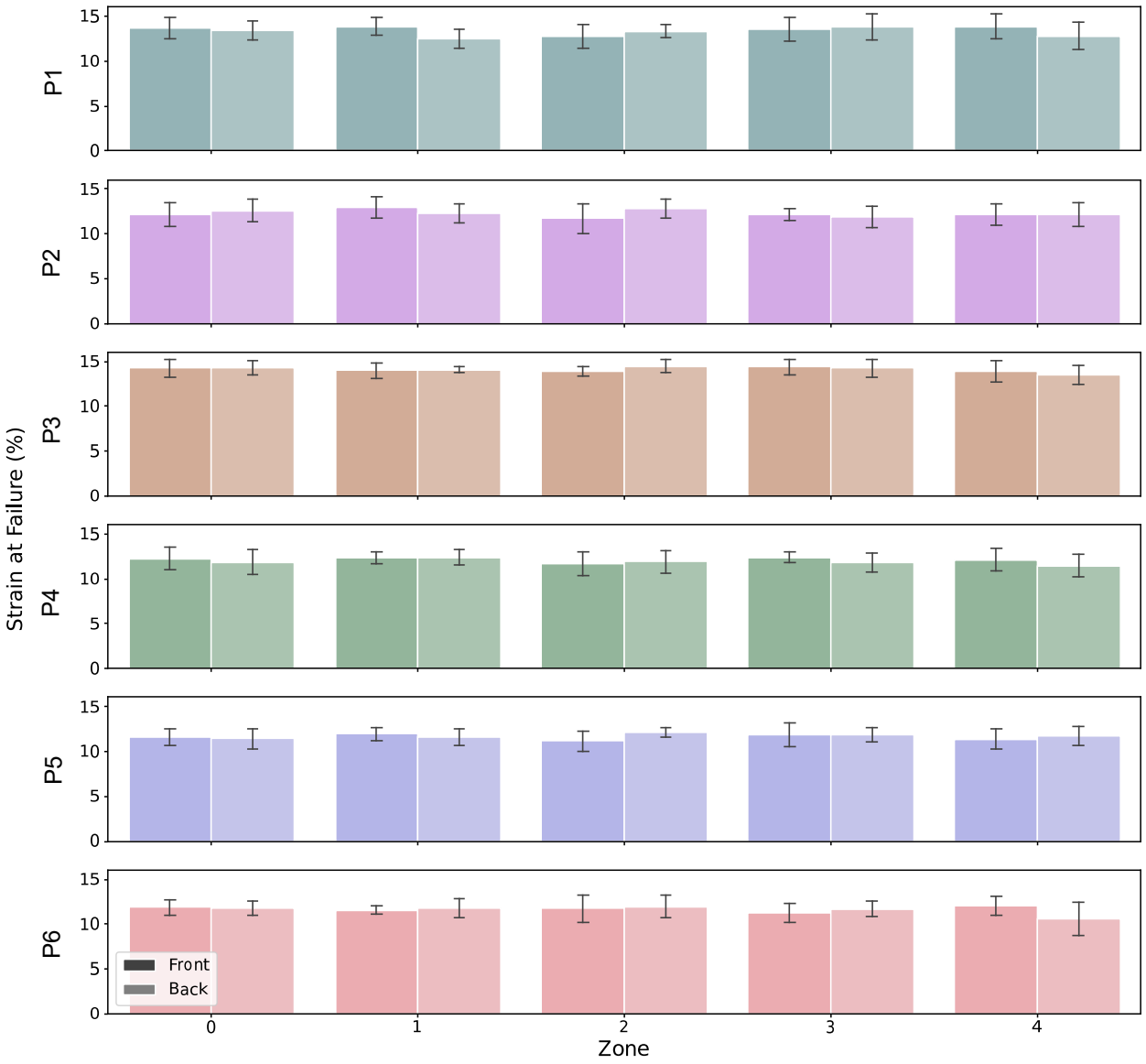

Fig. B.8: Vertical coupon strain at failure in each zone, separated by the front and back rows of coupons.

VITA

Reid Schur

Education:

Ph.D., University of Washington, Seattle, WA 2019-2023
Doctor of Philosophy in Materials Science and Engineering

Dissertation: Laser Powder Bed Fusion of Ti-6Al-4V: A Round Robin Analysis of Mechanical Property Variability

M.S., University of Washington, Seattle, WA 2017-2019
Master of Science in Materials Science and Engineering

Thesis: Effects of Powder Reuse on the Mechanical Properties of Electron Beam Additively Manufactured Ti-6Al-4V

B.S., Washington University, St. Louis, MO 2013-2017
Major: Mechanical Engineering
Minor: Materials Science and Engineering

Awards/Honors:

- Fotedar Fellowship
- Journal of Failure Analysis and Prevention Best Paper of the Year (2020) for "A Fractographic Analysis of Additively Manufactured Ti6Al4V by Electron Beam Melting: Effects of Powder Reuse"

Publications:

[1] S. Ghods, R. Schur, R. Schleusener, A. Montelione, R. Pahuja, C. Wisdom, D. Arola, M. Ramulu, Contributions of intra-build design parameters to mechanical properties in electron beam additive manufacturing of Ti6Al4V, Mater Today Commun. 30 (2022) 103190. https://doi.org/10.1016/j.mtcomm.2022.103190.

[2] S. Ghods, R. Schur, A. Montelione, R. Schleusener, D.D. Arola, M. Ramulu, Importance of Build Design Parameters to the Fatigue Strength of Ti6Al4V in Electron Beam Melting Additive Manufacturing, Materials. 15 (2022) 5617. https://doi.org/10.3390/ma15165617.

[3] R. Schur, S. Ghods, C. Wisdom, R. Pahuja, A. Montelione, D. Arola, M. Ramulu, Mechanical anisotropy and its evolution with powder reuse in Electron Beam Melting AM of Ti6Al4V, Mater Des. 200 (2021) 109450. https://doi.org/10.1016/j.matdes.2021.109450.

[4] S. Ghods, R. Schur, E. Schultz, R. Pahuja, A. Montelione, C. Wisdom, D. Arola, M. Ramulu, Powder Reuse and its Contribution to Porosity in Additive Manufacturing of Ti6Al4V, Materialia (Oxf). 15 (2021) 1–10. https://doi.org/10.1016/j.mtla.2020.100992.

[5] R. Schur, S. Ghods, E. Schultz, C. Wisdom, R. Pahuja, A. Montelione, D. Arola, M. Ramulu, A Fractographic Analysis of Additively Manufactured Ti6Al4V by Electron Beam Melting: Effects of Powder Reuse, Journal of Failure Analysis and Prevention. (2020). https://doi.org/DOI 10.1007/s11668-020-00875-0.

[6] S. Ghods, E. Schultz, C. Wisdom, R. Schur, R. Pahuja, A. Montelione, D. Arola, M. Ramulu, Electron Beam Additive Manufacturing of Ti6Al4V: Evolution of Powder Morphology and Part Microstructure with Powder Reuse, Materialia (Oxf). 9 (2020) 100631. https://doi.org/10.1016/j.mtla.2020.100631.

[7] A. Montelione, S. Ghods, R. Schur, C. Wisdom, D. Arola, M. Ramulu, Powder Reuse in Electron Beam Melting Additive Manufacturing of Ti6Al4V: Particle Microstructure, Oxygen Content and Mechanical Properties, Addit Manuf. 35 (2020) 101216. https://doi.org/10.1016/j.addma.2020.101216.

[8] J.O. Wright, N.W. Skelley, R.P. Schur, R.M. Castile, S.P. Lake, R.H. Brophy, Microstructural and mechanical properties of the posterior cruciate ligament: A comparison of the anterolateral and posteromedial bundles, Journal of Bone and Joint Surgery - American Volume. 98 (2016) 1656–1664. https://doi.org/10.2106/JBJS.16.00032.